Quantifying Earthquake Collapse Risk of Tall Steel Moment Frame Buildings Using Rupture-to-Rafters Simulations

Thesis by

Hemanth Siriki

In Partial Fulfillment of the Requirements
for the Degree of
Doctor of Philosophy

California Institute of Technology
Pasadena, California

2014

Defended December 30, 2014

© 2014

Hemanth Siriki

All Rights Reserved

Acknowledgements

Pursuing a doctoral degree is a rewarding endeavor that is often not possible without the support of numerous individuals. First, I would like to express my sincere gratitude to my advisor, Dr.Krishnan, for providing me an invaluable opportunity to conduct this research. During the course of my stay at Caltech, he has been a constant source of inspiration guiding me and allowing me to mature not just as a researcher but as an individual. His commitment to students and passion towards research allowed me to push my own boundaries further in conducting research in a clear and logical manner. It has been a privilege working under his guidance and I will incorporate the lessons I learnt from him in my professional and personal life to the best of my abilities. I also express my gratitude to Dr.Heaton, who was my advisor towards the end in guiding me to successfully finish my research. His wealth of knowledge always left me in awe and the innumerable discussions I had with him allowed me to continuously pursue various topics in an highly efficient and innovative manner. I will forever cherish the thought process he inculcated into me to address numerous problems during the course of these discussions.

I would also like to extend my gratitude to my thesis defense committee members - Dr.Hall and Dr.Beck. Their irreplaceable guidance and the knowledge they shared allowed me to pursue topics that otherwise wouldn't have been possible. This thesis wouldn't be complete for without the help of Dr.Rosakis, Dr.Bhat and Dr.Lu. They have generously allowed me to use their laboratory data for my research. A special thanks to Dr.Bhat for helping me understand topics that aren't my expertise and in guiding me to incorporate the same in my research. Thank you to the administrative staff in the Department of Mechanical and Civil Engineering, including, Oseguera Carolina, Cheryl Greer, Chris Silva and Lynn Seymour, in making my transition to life at Caltech a pleasurable one.

I thank fellow members of Caltech graduate community, Stephen Wu, Min Hei Cheng, Vanessa

Heckman, Shiyan Song, Gokcan Karakus, Pinaky Bhattacharya and Subhonmesh Bose for their friendship and the countless technical, ethical and philosophical discussions we had on various topics. Words cannot describe the pleasure of knowing Kaushik Dasgupta and Ramses Mourhatch through the course of my stay at Caltech and in US. Life wouldn't be the same without them. These are two people that I hold extremely close to my heart knowing that they are there whenever and whatever reason I need them for alongside my two other close friends Frances and Calyani Ganeshan. I also extend my warm regards to Arden, Erika and members of Quest Salchata Crew for allowing me to be a part of their lives that I dearly regard as home and family.

Last but not the least, I would like to dedicate this thesis and extend my gratitude towards my parents for their unconditional love and support in my pursuit of life. Their motivation and patience allowed me to reach heights that I have not imagined before. I would also like to thank my sister for her constant encouragement.

Abstract

There is a sparse number of credible source models available from large-magnitude past earthquakes. A stochastic source model generation algorithm thus becomes necessary for robust risk quantification using scenario earthquakes. We present an algorithm that combines the physics of fault ruptures as imaged in laboratory earthquakes with stress estimates on the fault constrained by field observations to generate stochastic source models for large-magnitude (M_w 6.0-8.0) strike-slip earthquakes. The algorithm is validated through a statistical comparison of synthetic ground motion histories from a stochastically generated source model for a magnitude 7.90 earthquake and a kinematic finite-source inversion of an equivalent magnitude past earthquake on a geometrically similar fault. The synthetic dataset comprises of three-component ground motion waveforms, computed at 636 sites in southern California, for ten hypothetical rupture scenarios (five hypocenters, each with two rupture directions) on the southern San Andreas fault. A similar validation exercise is conducted for a magnitude 6.0 earthquake, the lower magnitude limit for the algorithm. Additionally, ground motions from the $M_w 7.9$ earthquake simulations are compared against predictions by the Campbell-Bozorgnia NGA relation as well as the ShakeOut scenario earthquake. The algorithm is then applied to generate fifty source models for a hypothetical magnitude 7.9 earthquake originating at Parkfield, with rupture propagating from north to south (towards Wrightwood), similar to the 1857 Fort Tejon earthquake. Using the spectral element method, three-component ground motion waveforms are computed in the Los Angeles basin for each scenario earthquake and the sensitivity of ground shaking intensity to seismic source parameters (such as the percentage of asperity area relative to the fault area, rupture speed, and rise-time) is studied.

Under plausible San Andreas fault earthquakes in the next 30 years, modeled using the stochastic source algorithm, the performance of two 18-story steel moment frame buildings (UBC 1982 and 1997 designs) in southern California is quantified. The approach integrates rupture-to-rafters simulations into the PEER performance based earthquake engineering (PBEE) framework. Using stochastic sources and computational seismic wave propagation, three-component ground motion histories at 636 sites in southern California are generated for sixty scenario earthquakes on the San Andreas fault. The ruptures, with moment magnitudes in the range of 6.0-8.0, are assumed to occur at five locations on the southern section of the fault. Two unilateral rupture propagation directions are considered. The 30-year probabilities of all plausible ruptures in this magnitude range and in that section of the fault, as forecast by the United States Geological Survey, are distributed among these 60 earthquakes based on proximity and moment release. The response of the two 18-story buildings hypothetically located at each of the 636 sites under 3-component shaking from all 60 events is computed using 3-D nonlinear time-history analysis. Using these results, the probability of the structural response exceeding Immediate Occupancy (IO), Life-Safety (LS), and Collapse Prevention (CP) performance levels under San Andreas fault earthquakes over the next thirty years is evaluated.

Furthermore, the conditional and marginal probability distributions of peak ground velocity (PGV) and displacement (PGD) in Los Angeles and surrounding basins due to earthquakes occurring primarily on the mid-section of southern San Andreas fault are determined using Bayesian model class identification. Simulated ground motions at sites within 55-75km from the source from a suite of 60 earthquakes ($M_w 6.0 - 8.0$) primarily rupturing mid-section of San Andreas fault are considered for PGV and PGD data.

Contents

Acknowledgements iii

Abstract v

1 Motivation, Background and Scope 1

2 Stochastic Source Model Generation Algorithm for Strike-Slip Earthquakes 5

2.0.1 Slip Distribution 6

2.0.2 Rupture Speed Distribution 8

2.0.3 Slip velocity-time function 10

2.1 Methodology 11

2.1.1 Slip D 11

2.1.2 Rupture Speed (V_r) 16

2.1.3 Slip velocity-time function 20

2.2 Application to the Southern San Andreas Fault 22

2.3 Sensitivity of Ground Motions in the Los Angeles Basin to Source Parameters of Large Ruptures on the San Andreas Fault 39

2.4 Discussion 41

2.5 Data and Resources 45

3 Limit State Exceedance Probabilities of Building Performance Under Earthquake Excitation Using Rupture-to-Rafters Simulations 46

3.1 Methodology 48

3.1.1 Stochastic source models for scenario earthquakes 49

3.1.2 Probability of occurrence of scenario earthquakes using earthquake rupture forecasts [contribution by Ramses Mourhatch (21(Mourhatch 2015))] 49

3.1.3 Ground motion simulation for scenario earthquakes 50

3.1.4 3-D nonlinear dynamic analysis of target buildings under scenario earthquake ground motion 51

3.1.5 Applying the PEER PBEE framework to estimate probability of exceedance of FEMA356 performance limit states for target buildings 51

3.2 Application to performance quantification of tall steel moment frame buildings in southern California under San Andreas earthquakes . . 52

3.2.1 Target buildings, target fault, and time horizon 52

3.2.2 Scenario earthquakes on the southern San Andreas fault 55

3.2.3 30-year probability of occurrence of scenario earthquakes [contribution by Ramses Mourhatch ((Mourhatch 2015))] 55

3.2.4 Simulated ground motions for the scenario earthquakes 56

3.2.5 Structural response under the scenario earthquakes 72

3.2.6 **30-year exceedance probabilities of structural performance limit states** . . 84

4 Characterizing Long-Period Ground Motions Using Bayesian Model Class Selection. **88**

4.1 **Ground Motion Simulation** 90

4.2 **Bayesian Model Selection** 91

4.3 **Conditional and Unconditional Probability Distributions for PGV and PGD** 95

4.4 **Probability Distributions Used** 99

5 Conclusions **101**

5.1 Findings 101

5.2 **Future Work** 105

A Source Model Generation Algorithm Validation: $M_w6.05$, 2004 Parkfield-like Earthquake on Southern San Andreas Fault **107**

B Ground Motion Maps for $M_w7.9$ Denali Finite-Source Inversion and Stochastic Source Models Traveling at Sub-Rayleigh and Super-shear Regimes **116**

C Various Stochastic Source Models Generated Through the Algorithm and the Associated Ground Motion Maps **125**

List of Figures

2.1 Histograms of magnitudes of past earthquakes considered by (a) Somerville et al. (1999) and (b) Mai and Beroza (2002) for determining the spectral properties of the slip distribution on the fault. Source mechanisms of these earthquakes are not limited to strike-slip, but include reverse, thrust etc. Note the sparse number of large magnitude ($M_w \geq 7.0$) earthquakes included in either study. 7

2.2 Rise-time plotted as a function of slip observed in laboratory earthquakes (Lu 2009, 2010). The correlation between the two is in agreement with dynamic rupture studies conducted by Schmedes et al. (2010). 11

2.3 Blue circles show the standard deviation σ of log-normal PDF fits to the slip distribution from finite-source inversions of 56 strike-slip earthquakes as a function of earthquake magnitude M_w. The magenta line is the best-fitting linear least-squares fit described by Eq. 2.3. 11

2.4 Plane view of moment-preserving filter used to smoothen the slip distribution. The filter function is Gaussian along fault length (with width d) and parabolic along fault depth (with width 3/4d), where d is the depth of rupture. The parabola has a zero ordinate at the bottom and a peak at two-thirds height from the bottom. 13

2.5 Application of the stochastic source algorithm to a $M_w = 7.9$ strike-slip earthquake. Recursive divisions of fault area followed by assignment of random realizations of magnitude-dependent log-normal PDFs of slip lead to five hierarchical levels [(a) Level - 1 through (e) Level - 5] of the seismic source. The final step involves subdividing the parent segments to small daughter segments capable of producing the desired highest frequency wave in ground motion simulations. Assignment of random realizations of magnitude-dependent log-normal PDFs of slip to these daughter segments along with a smoothing filter leads to (f) the final filtered slip distribution. 14

2.6 Power Spectral Density (PSD) of a stochastic slip realization along (a) strike and (b) dip directions as shown in Fig.2.5(f) for M_w 7.9 earthquake. 16

2.7 Normalized histograms of slip(m) of a $M_w 7.90$ earthquake from: (a) a finite-source inversion of the 2002 Denali earthquake and (b) one stochastic source realization using the outlined method. 17

2.8 Locations along the southern San Andreas fault at which stress estimates are available from the World Stress Map project. Five data clusters are shown (magenta-, yellow-, blue-, green-, and red-colored points). 18

2.9 Slip velocity plotted as a function of time for a laboratory earthquake and the best fitting isosceles triangular slip velocity-time function. 20

2.10 Normalized histograms of slip-to-rise-time ratio observed in laboratory earthquakes and the associated lognormal fit. 20

2.11 Maximum rise-times in finite-source inversions of 56 past earthquakes plotted as a function of their magnitudes. The linear trend is best captured by Eq. 2.8, the straight line shown in red. 21

2.12 One of five stochastic source realizations (the median model) for the north-to-south rupture of a hypothetical $M_w = 7.9$ earthquake on the southern San Andreas fault. Two possible rupture locations, identified as rupture locations (a) 1 and (b) 3, are shown. Also shown on top of slip (color scale same as in Fig. 2.5(a)) is the rupture speed distribution. Blue indicates rupture propagating at the sub-Rayleigh speed of $0.87V_s$, while red indicates rupture propagating at the super-shear speed of $1.67V_s$. Rupture speed is held constant along fault depth. The model has a constant slip-velocity of 4.15 m/s. 22

2.13 One of five stochastic source realizations (the median model) for the south-to-north rupture of a hypothetical $M_w = 7.9$ earthquake on the southern San Andreas fault. Two possible rupture locations, identified as rupture locations (a) 2 and (b) 4, are shown. Also shown on top of slip (color scale same as in Fig. 2.5(a)) is the rupture speed distribution. Blue indicates rupture propagating at the sub-Rayleigh speed of $0.87V_s$, while red indicates rupture propagating at the super-shear speed of $1.67V_s$. Rupture speed is held constant along fault depth. The model has a constant slip-velocity of 4.15 m/s. 23

2.14 The geographical distribution of the 636 southern California sites (shown as triangles) where ground motions are computed. The spacing between the sites is 3.5 km approximately. The ellipses identify the basins in southern California: Simi valley, San Fernando valley, San Gabriel valley and Los Angeles basin. 24

2.15 (a) Slip (m) and (b) Rise-time (s) distributions from a finite source inversion of teleseismic, strong motion, and GPS data from the Mw = 7.9 Denali fault earthquake of 2002 (Krishnan et al. 2006a). Rupture-time (s) contours are overlaid on the slip distribution. . 25

2.16 Solid lines: Median PGV computed at 636 sites in southern California from ten rupture scenarios (five rupture locations along the southern San Andreas fault x two rupture directions) using each of five stochastic source realizations; Dashed lines: The corresponding median PGV from all fifty scenario earthquakes. All earthquakes are of magnitude $M_w = 7.9$. 26

2.17 Comparison of the “median” stochastic source model (top) located at rupture location 3 and the Denali fault earthquake finite-source model (bottom) also located at rupture location 3. Both (a) north-to-south and (b) south-to-north propagating ruptures are shown. Note the differences in the slip asperity locations in the two models. 26

2.18 EW and NS components of PGV (m/s) from a north-to-south propagating $M_w = 7.9$ rupture at location 3 on the southern San Andreas fault: (a) and (b) Stochastic median source model; (c) and (d) Denali earthquake finite-source inversion model (Krishnan et al. 2006a). The inset shows the fault trace and the hypocenter location. 27

2.19 EW and NS components of PGD (m) from a north-to-south propagating $M_w = 7.9$ rupture at location 3 on the southern San Andreas fault: (a) and (b) Stochastic median source model; (c) and (d) Denali earthquake finite-source inversion model (Krishnan et al. 2006a). The inset shows the fault trace and hypocenter location. 28

2.20 EW component of PGV (m/s) from a south-to-north propagating $M_w = 7.9$ rupture at location 3 on the southern San Andreas fault: (a) Stochastic median source model; (b) Denali earthquake finite-source inversion model (Krishnan et al. 2006a). 29

2.21 (a) and (b) Difference in the PGV (EW component) generated by the Denali source model and the modified Denali model [PGV (modified Denali) - PGV (Denali)] for north-to-south ruptures at rupture locations 1 and 3,respectively. The modified Denali model is obtained by making the rise-times from the original Denali model proportional to the slip using the stochastic source generation algorithm. 30

2.22 Five $M_w = 7.9$ north-to-south rupture scenarios (at locations 1–5) on the San Andreas fault using [(a)–(e)] the stochastic median model and [(f)–(j)] the Denali finite-source inversion model: Histograms and best-fit log-normal PDFs (insets) of PGV at 636 sites in southern California. The product of the listed scaling factor and the normalized histogram ordinate at a specific peak velocity gives the total number of sites for that velocity. 32

2.23 Five $M_w = 7.9$ south-to-north rupture scenarios (at locations 1–5) on the San Andreas fault using [(a)–(e)] the stochastic median model and [(f)–(j)] the Denali finite-source inversion model: Histograms and best-fit log-normal PDFs (insets) of PGV at 636 sites in southern California. The product of the listed scaling factor and the normalized histogram ordinate at a specific peak velocity gives the total number of sites for that velocity. 33

2.24 Median peak average horizontal velocity (m/s) [(red) Stochastic and (blue) Denali model] as a function of source-to-site distance, in southern California due to $M_w 7.90$ earthquake occurring along southern San Andreas fault. The shaded region corresponds to median plus/minus one standard deviation. A total of 10 rupture scenarios (5 rupture locations x 2 propagation directivity) are considered 34

2.25 Median peak average horizontal velocity (m/s) [(red, green) Stochastic and (violet, blue) Denali model] as a function of source-to-site distance for basin and non-basin sites, in southern California due to $M_w 7.90$ earthquake occurring along southern San Andreas fault. The shaded region corresponds to median plus/minus one standard deviation. A total of 10 rupture scenarios (5 rupture locations x 2 propagation directivity) are considered 35

2.26 (a) Median peak horizontal velocity (m/s) and (b) median peak horizontal displacement (m) as a function of source-to-site distance for ten $M_w 7.90$ earthquake scenarios on the southern San Andreas fault (five rupture locations and two rupture directions) using the median stochastic source model. Shown in red are the predictions by the Campbell-Bozorgnia NGA relation. The shaded region corresponds to median plus/minus one standard deviation. 35

2.27 (a) V_s^{30} (m/s) and (b) basin depth (km) maps for southern California. Black circles correspond to 48 stations at which PGV and PGD values are computed using Campbell-Bozorgnia attenuation relation for comparison against simulation predictions. Red triangles indicate the geographical distribution of the 636 southern California sites where stochastic ground motions are computed. The ellipses identify the basins in southern California: Simi valley, San Fernando valley, San Gabriel valley and Los Angeles basin. 36

2.28 Spectral acceleration (g) at $T = 3\ s$ as a function of source-to-site distance for ten $M_w 7.90$ earthquake scenarios on the southern San Andreas fault (five rupture locations and two rupture directions). Shown in green and blue are the simulated east-west and the north-south S_a^{3s} components at greater Los Angeles sites using the median stochastic source model, respectively. Shown in red are the predictions by the Campbell-Bozorgnia NGA relation. The shaded region corresponds to median plus/minus one standard deviation. 37

2.29 Slip (m) distribution and rupture time contours (1s intervals) for a $M_w 7.8$ earthquake of the ShakeOut earthquake source (Graves et al. 2011). The peak slip-rate for this source is 4.38 m/s. 38

2.30 (a) East-West and (b) North-South component of peak ground velocity (m/s) simulated using the median stochastic source model with epicenter at Bombay Beach. (c) and (d) The corresponding PGV maps for the ShakeOut scenario. 38

2.31 Results from simulating fifty $M_w = 7.9$ north-to-south rupture scenarios on the San Andreas fault (similar to the 1857 Fort Tejon earthquake) using stochastic seismic source models. [(a)–(c)] show the scatter-plots of the median PGV in Los Angeles basin as a function of the percentage of asperity area relative to the fault area, the maximum rise-time, and the percentage rupture propagating at sub-Rayleigh speeds. [(d)–(f)] show the corresponding histograms for the fifty scenarios. The product of the listed scaling factor and the normalized histogram ordinate gives the parameter frequency. 40

2.32 Median horizontal peak ground velocity (m/s) in southern California from a total of fifty $M_w 7.90$ earthquakes on the southern San Andreas fault (5 source realizations x 5 rupture locations x 2 propagation directions) as a function of the rise-time (s) for (a) north-to-south and (b) south-to-north propagating rupture. 42

2.33 Median horizontal peak ground velocity (m/s) in southern California from a total of fifty $M_w 7.90$ earthquakes on the southern San Andreas fault (5 source realizations x 5 rupture locations x 2 propagation directions) as a function of the percentage of rupture propagating at the sub-Rayleigh speed of $0.87 V_s$ for (a) north-to-south and (b) south-to-north propagating rupture. 42

3.1 Structural models of the two 18-story steel moment frame buildings: (a) Isometric view of the existing building (designed using the 1982 UBC). (b) Plan view of a typical floor of the existing building showing the location of columns and moment-frame (MF) beams. (c) Isometric view of the new building (redesigned using the 1997 UBC). (d) Plan view of a typical floor of the redesigned building. 54

3.2 Stochastic median slip (m) model with rupture time (s) contours for (a) $M_w 7.9$ (b) $M_w 7.6$ and (c) $M_w 7.2$ scenario earthquakes. The sources have constant peak slip-velocities of 4.14, 3.2, 2.59 m/s respectively. 57

3.3 Peak horizontal velocity (m/s) at 636 sites in southern California under north-to-south propagating (a)-(c) $M_w 7.9$, (d)-(f) $M_w 7.6$, and (g)-(i) $M_w 7.6$ scenario earthquakes at locations 1, 3 & 5. 60

3.4 Peak horizontal velocity (m/s) at 636 sites in southern California under south-to-north propagating (a)-(c) $M_w 7.9$, (d)-(f) $M_w 7.6$, and (g)-(i) $M_w 7.6$ scenario earthquakes at locations 1, 3 & 5. 61

3.5 Peak horizontal displacement (m) at 636 sites in southern California under north-to-south propagating (a)-(c) $M_w 7.9$, (d)-(f) $M_w 7.6$, and (g)-(i) $M_w 7.6$ scenario earthquakes at locations 1, 3 & 5. 62

3.6 Peak horizontal displacement (m/s) at 636 sites in southern California under south-to-north propagating (a)-(c) $M_w 7.9$, (d)-(f) $M_w 7.6$, and (g)-(i) $M_w 7.6$ scenario earthquakes at locations 1, 3 & 5. 63

3.7 Median peak east-west and north-south ground velocity (m/s) as a function of rupture location along the southern San Andreas fault for various magnitudes: (a),(c) north-to-south and (b),(d) south-to-north propagating rupture. Shaded region represents median PGV +/- one standard deviation. 64

3.8 Median peak east-west and north-south ground displacement (m) as a function of rupture location along the southern San Andreas fault for various magnitudes: (a),(c) north-to-south and (b),(d) south-to-north propagating rupture. Shaded region represents median PGD +/- one standard deviation. 65

3.9 Median geometric mean horizontal velocity (m/s) and displacement (m) simulated by (a, c) the stochastic median model and predicted by (b, d) the Campbell-Bozorgnia NGA relation at 636 sites in southern California as a function of source-to-site distance for various magnitude ruptures on the southern San Andreas fault. Both north-to-south and south-to-north propagating ruptures are included. Shaded region represents median value +/- one standard deviation. 66

3.10 Basin depth (km) map for southern California. Red triangles indicate the geographical distribution of the 636 southern California sites where ground motions from the scenario earthquakes are computed. The ellipses identify the basins in southern California: Simi valley, San Fernando valley, San Gabriel valley and Los Angeles basin. 67

3.11 Peak horizontal velocity (m/s) at 636 sites in southern California plotted as a function of basin depth (km) and distance to rupture (km) due to north-to-south propagating earthquakes on the southern San Andreas fault of varying magnitudes and rupture locations. . 67

3.12 Peak horizontal displacement (m) at 636 sites in southern California plotted as a function of basin depth (km) and distance to rupture (km) due to north-to-south propagating earthquakes on the southern San Andreas fault of varying magnitudes and rupture locations. 68

3.13 Median peak geometric mean horizontal velocity (m/s) map for ten ruptures (five locations and two rupture directions) of magnitudes $M_w \ 7.9, \ 7.6, \ 7.2, \ and \ 6.8$ using (a)-(d) simulations; and (e)-(h) Campbell-Bozorgnia NGA relation. 69

3.14 Median peak geometric mean horizontal displacement (m) map for ten ruptures (five locations and two rupture directions) of magnitudes $M_w \ 7.9, \ 7.6, \ 7.2, \ and \ 6.8$ using (a)-(d) simulations; and (e)-(h) Campbell-Bozorgnia NGA relation. 69

3.15 Median peak geometric mean horizontal (a) velocity (m/s) and (b) displacement (m) at 636 sites in southern California from simulations compared against that predicted by the Campbell-Bozorgnia NGA relation as a function of magnitude of earthquakes on the southern San Andreas fault. Two rupture propagation directions (north-to-south and south-to-north and five rupture locations are included. 70

3.16 Median peak horizontal ground velocity (m/s) in southern California for north-to-south propagating M_w 7.90, M_w 7.60, and M_w 7.20 ruptures as a function of (a) - (c) the percentage of rupture propagating at the sub-Rayleigh speed of $0.87V_s$ and (d) - (f) maximum rise-time (s) in the source. 71

3.17 Median peak horizontal ground velocity (m/s) in southern California for south-to-north propagating M_w 7.90, M_w 7.60, and M_w 7.20 ruptures as a function of (a) - (c) the percentage of rupture propagating at the sub-Rayleigh speed of $0.87V_s$ and (d) - (f) maximum rise-time (s) in the source. 72

3.18 Peak inter-story drift ratio (IDR) maps for the existing building with perfect connections under ground motion from north-to-south propagating (a) - (c) M_w 7.9, (d) - (f) M_w 7.6, and (g) - (i) M_w 7.2 earthquakes on the southern San Andreas fault at rupture locations 1, 3, & 5. 73

3.19 Peak inter-story drift ratio (IDR) maps for the redesigned building with brittle connections under ground motion from north-to-south propagating (a) - (c) M_w 7.9, (d) - (f) M_w 7.6, and (g) - (i) M_w 7.2 earthquakes on the southern San Andreas fault at rupture locations 1, 3, & 5. 74

3.20 Peak inter-story drift ratio (IDR) maps for the existing building with perfect connections under ground motion from south-to-north propagating (a) - (c) M_w 7.9, (d) - (f) M_w 7.6, and (g) - (i) M_w 7.2 earthquakes on the southern San Andreas fault at rupture locations 1, 3, & 5. 75

3.21 Peak inter-story drift ratio (IDR) maps for the redesigned building with brittle connections under ground motion from south-to-north propagating (a) - (c) M_w 7.9, (d) - (f) M_w 7.6, and (g) - (i) M_w 7.2 earthquakes on the southern San Andreas fault at rupture locations 1, 3, & 5. 76

3.22 Median peak interstory drift ratio in the (a) - (b) existing and (c) - (d) redesigned buildings as a function of rupture location for north-to-south and south-to-north propagating scenario earthquakes of various magnitudes on the southern San Andreas fault. Shaded region represents median +/- one standard deviation 77

3.23 Median peak IDR in the existing and redesigned buildings plotted as a function of San Andreas fault scenario earthquake magnitude. The bars correspond to median +/- one standard deviation. 78

3.24 Median pseudo-acceleration (g) spectra of (a) - (c) East-West and (d) - (f) North-South components of simulated ground motion histories from M_w 7.90, 7.60, and 7.20 scenario earthquakes (data from north-to-south and south-to-north ruptures are combined) for various source-to-site distances. Also shown in black for comparison is the UBC97 MCE spectrum (soil classification S_B, fault type A at 5 km distance). 79

3.25 X (EW) and Y (NS) peak interstory drift ratios in (a)-(b) the existing, and (c)-(d) the redesigned buildings as a function of predominant time-period (s) of EW and NS components of ground velocity histories and the corresponding PGV (m/s) from all 60 scenario earthquakes on the southern San Andreas fault (6 magnitudes, 5 rupture locations, 2 rupture directions). Peak IDR of 0.007, 0.025, and 0.05 correspond to the FEMA356 limits for IO, LS, and CP performance levels. 80

3.26 X (EW) and Y (NS) peak interstory drift ratios in (a)-(b) the existing and (c)-(d) the redesigned buildings as a function of PGD (m) and PGV (m/s) of EW and NS components ground motion histories from all 60 scenario earthquakes on the southern San Andreas fault (6 magnitudes, 5 rupture locations, 2 rupture directions). Peak IDR of 0.007, 0.025, and 0.05 correspond to the FEMA356 limits for IO, LS, and CP performance levels. . . 82

3.27 Fragility curves of the probability of the peak IDR for (a) the existing and (b) the redesigned building in the X (solid)- and Y (dashed)- directions exceeding FEMA limits for immediate occupancy (IO), life-safety (LS), and collapse prevention (CP) performance levels as a function of PGV in the corresponding direction. Two additional fragilities corresponding to peak IDR levels of 0.075 (red-tagged, RT) and 0.10 (model collapse, CO), are also shown. 83

3.28 Fragility curves of the probability of the peak IDR for (a) the existing and (b) the redesigned building exceeding FEMA limits for immediate occupancy (IO), life-safety (LS), and collapse prevention (CP) performance levels as a function of SA (g) at fundamental period. Two additional fragilities corresponding to peak IDR levels of 0.075 (red-tagged, RT) and 0.10 (model collapse, CO), are also shown. 84

4.1 The geographical distribution of the 636 southern California sites (shown as triangles) where scenario earthquake ground motions are computed. The spacing between the sites is 3.5 km approximately. The inset shows the southern San Andreas fault rupture extent of a M_w 7.9 earthquake at Location 3. 90

4.2 Horizontal (a), (b) peak ground velocity (m/s) and (c), (d) peak ground displacement (m) histograms for M_w $7.9, 7.6, 7.2, 6.8, 6.4,$ and 6.05 scenario earthquakes rupturing location 3 of southern San Andreas fault. Synthetic data from all sites within a source-to-site distance of 55 km-75 km in the Los Angeles and adjacent basins are included. The PGV and PGD data are collated into 1.25 m/s and 1.25 m bins, respectively. 92

4.3 Scatter plot of horizontal (a) peak ground velocity (m/s); and (b) peak ground displacement (m) as a function of magnitude simulated for M_w $7.9, 7.6, 7.2, 6.8, 6.4$, and 6.05 scenario earthquakes rupturing location 3 of southern San Andreas fault. Note that PGV and PGD are plotted on a log scale. Synthetic data from all sites within a source-to-site distance of 55 km-75 km in the Los Angeles and adjacent basins are included. The median value is indicated by a 'x' for each magnitude. The best fitting lines to the median PGD and PGV values are $log_{10}PGD = 0.98M_w - 7.62$ and $log_{10}PGV = 0.89M_w - 6.77$, respectively. 93

4.4 Combined histograms of the (a) PGV (m/s) and (b) PGD (m) for the 60 scenario earthquakes at location 3 on the southern San Andreas fault with magnitudes in the M_w $6.0 - 7.9$ range. Data from all sites at source-to-site distances of 55-75 km are included. The PGV and PGD data are collated into 1.25 m/s and 1.25 m bins, respectively. 94

4.5 Conditional (given earthquake magnitude, colored dashed lines) and unconditional (solid black line) probability distributions of (a) PGV (m/s) and (b) PGD (m) at basin sites at a distance of 55-75 km for earthquakes in the magnitude range of 6.04-7.90 identified through Bayesian model class selection. The grey dashed lines are the unconditional distributions derived by the summation of conditional distributions followed by normalization, equivalent to assuming an uniform distribution on magnitude. 98

A.1 (a) Stochastic median source model with slip in m for a $M_w = 6.05$ earthquake on the San Andreas fault. (b) Finite-source inversion model for the $M_w = 6.0$ Parkfield earthquake of 2004 (Ji 2004). Rupture time (s) contours are overlaid on the slip distribution. The maximum slip rate for the stochastic and inversion models is 1.99 m/s and 1.09 m/s respectively. 108

A.2 Solid lines: Median PGV computed at 636 sites in southern California from ten rupture scenarios (five rupture locations along the southern San Andreas fault x two rupture directions) using each of five stochastic source realizations; Dashed lines: The corresponding median PGV from all fifty scenario earthquakes. All earthquakes are of magnitude $M_w = 6.05$. 109

A.3 EW and NS components of PGV (cm/s) from a north-to-south propagating rupture at location 3 on the southern San Andreas fault: (a) and (b) $M_w = 6.05$ stochastic median source model; (c) and (d) $M_w = 6.0$ Parkfield earthquake finite-source inversion model (Ji 2004). 110

A.4 EW and NS components of PGD (cm) from a north-to-south propagating rupture at location 3 on the southern San Andreas fault: (a) and (b) $M_w = 6.05$ stochastic median source model; (c) and (d) $M_w = 6.0$ Parkfield earthquake finite-source inversion model (Ji 2004). 111

A.5 Five $M_w = 6.05$ north-to-south rupture scenarios (at locations $1-5$) on the San Andreas fault using [(a)$-$(e)] the stochastic median model and [(f)$-$(j)] the $M_w = 6.0$ Parkfield earthquake finite-source inversion model: Histograms and best-fit log-normal PDFs (insets) of PGV at 636 stations in southern California. The product of the listed scaling factor and the normalized histogram ordinate at a specific peak velocity gives the total number of stations for that velocity. 112

A.6 Five $M_w = 6.05$ south-to-north rupture scenarios (at locations $1-5$) on the San Andreas fault using [(a)$-$(e)] the stochastic median model and [(f)$-$(j)] the $M_w = 6.0$ Parkfield earthquake finite-source inversion model: Histograms and best-fit log-normal PDFs (insets) of PGV at 636 stations in southern California. The product of the listed scaling factor and the normalized histogram ordinate at a specific peak velocity gives the total number of stations for that velocity. 113

A.7 Median peak average horizontal velocity (m/s) [(red) Stochastic and (blue) Parkfield model] as a function of source-to-site distance, in southern California due to $M_w 6.05$ earthquake occurring along southern San Andreas fault. The shaded region corresponds to median plus/minus one standard deviation. A total of 10 rupture scenarios (5 rupture locations x 2 propagation directivity) are considered. 114

A.8 (a) Median peak horizontal velocity (m/s) and (b) median peak horizontal displacement (m) as a function of source-to-site distance for ten $M_w 6.05$ earthquake scenarios on the southern San Andreas fault (five rupture locations and two rupture directions) using the median stochastic source model. Shown in red are the predictions by the Campbell-Bozorgnia NGA relation. The shaded region corresponds to median plus/minus one standard deviation. 114

A.9 Spectral acceleration (g) at T = 3 s as a function of source-to-site distance for ten Mw 6.05 earthquake scenarios on the southern San Andreas fault (five rupture locations and two rupture directions). Shown in green and blue are the simulated east-west and the north-south Sa3s components at greater Los Angeles sites using the median stochastic source model, respectively. Shown in red are the predictions by the Campbell-Bozorgnia NGA relation. The shaded region corresponds to median plus/minus one standard deviation. 115

B.1 EW and NS components of (a) and (b) PGV (m/s); (c) and (d) PGD (m) from a north-to-south propagating rupture at location 1 on the southern San Andreas fault for Denali earthquake finite-source inversion model (Krishnan et al. 2006a) with rupture speed modified to travel in pure sub-Rayleigh mode. 117

B.2 EW and NS components of (a) and (b) PGV (m/s); (c) and (d) PGD (m) from a north-to-south propagating rupture at location 1 on the southern San Andreas fault for Denali earthquake finite-source inversion model (Krishnan et al. 2006a) with rupture speed modified to travel in pure super-shear mode. 118

B.3 EW and NS components of (a) and (b) PGV (m/s); (c) and (d) PGD (m) from a north-to-south propagating rupture at location 1 on the southern San Andreas fault for a Stochastic source realization (refer to as model-1) of $M_w 7.9$ earthquake with rupture traveling in pure sub-Rayleigh mode. 119

B.4 EW and NS components of (a) and (b) PGV (m/s); (c) and (d) PGD (m) from a north-to-south propagating rupture at location 1 on the southern San Andreas fault for a Stochastic source realization (model-1) of $M_w 7.9$ earthquake with rupture traveling in pure super-shear mode. 120

B.5 EW and NS components of (a) and (b) PGV (m/s); (c) and (d) PGD (m) from a north-to-south propagating rupture at location 1 on the southern San Andreas fault for a Stochastic source realization (refer to as model-2) of $M_w 7.9$ earthquake with rupture traveling in pure sub-Rayleigh mode. 121

B.6 EW and NS components of (a) and (b) PGV (m/s); (c) and (d) PGD (m) from a north-to-south propagating rupture at location 1 on the southern San Andreas fault for a Stochastic source realization (model-2) of $M_w 7.9$ earthquake with rupture traveling in pure super-shear mode. 122

B.7 EW and NS components of (a) and (b) PGV (m/s); (c) and (d) PGD (m) from a north-to-south propagating rupture at location 1 on the southern San Andreas fault for a Stochastic source realization (refer to as model-3) of $M_w 7.9$ earthquake with rupture traveling in pure sub-Rayleigh mode. 123

B.8 EW and NS components of (a) and (b) PGV (m/s); (c) and (d) PGD (m) from a north-to-south propagating rupture at location 1 on the southern San Andreas fault for a Stochastic source realization (model-3) with rupture traveling in pure super-shear mode. 124

C.1 (a)-(e) Stochastic median source models (here on referred to as models-1, 2, 3, 4, 5) with slip in m for a $M_w = 7.9$ earthquake on the San Andreas fault. Rupture time (s) contours are overlaid on the slip distribution. The rupture contours shown correspond to the stochastic stress conditions at location 1 of the rupture staring at Parkfield. Note that the rupture time contours change for a different location. 126

C.2 EW component of PGV (m/s) from a north-to-south propagating rupture at (a) - (e) locations 1 - 5 respectively on the southern San Andreas fault for stochastic $M_w7.9$ model-1 source model. The NS component of PGV has similar characteristics as EW component and the PGD is proportional to PGV in most cases. 127

C.3 EW component of PGV (m/s) from a south-to-north propagating rupture at (a) - (e) locations 1 - 5 respectively on the southern San Andreas fault for stochastic $M_w7.9$ model-1 source model. The NS component of PGV has similar characteristics as EW component and the PGD is proportional to PGV in most cases. 128

C.4 EW component of PGV (m/s) from a north-to-south propagating rupture at (a) - (e) locations 1 - 5 respectively on the southern San Andreas fault for stochastic $M_w7.9$ model-2 source model. The NS component of PGV has similar characteristics as EW component and the PGD is proportional to PGV in most cases. 129

C.5 EW component of PGV (m/s) from a south-to-north propagating rupture at (a) - (e) locations 1 - 5 respectively on the southern San Andreas fault for stochastic $M_w7.9$ model-2 source model. The NS component of PGV has similar characteristics as EW component and the PGD is proportional to PGV in most cases. 130

C.6 EW component of PGV (m/s) from a north-to-south propagating rupture at (a) - (e) locations 1 - 5 respectively on the southern San Andreas fault for stochastic $M_w7.9$ model-3 source model. The NS component of PGV has similar characteristics as EW component and the PGD is proportional to PGV in most cases. 131

C.7 EW component of PGV (m/s) from a south-to-north propagating rupture at (a) - (e) locations 1 - 5 respectively on the southern San Andreas fault for stochastic $M_w 7.9$ model-3 source model. The NS component of PGV has similar characteristics as EW component and the PGD is proportional to PGV in most cases. 132

C.8 EW component of PGV (m/s) from a north-to-south propagating rupture at (a) - (e) locations 1 - 5 respectively on the southern San Andreas fault for stochastic $M_w 7.9$ model-4 source model. The NS component of PGV has similar characteristics as EW component and the PGD is proportional to PGV in most cases. 133

C.9 EW component of PGV (m/s) from a south-to-north propagating rupture at (a) - (e) locations 1 - 5 respectively on the southern San Andreas fault for stochastic $M_w 7.9$ model-4 source model. The NS component of PGV has similar characteristics as EW component and the PGD is proportional to PGV in most cases. 134

C.10 EW component of PGV (m/s) from a north-to-south propagating rupture at (a) - (e) locations 1 - 5 respectively on the southern San Andreas fault for stochastic $M_w 7.9$ model-5 source model. The NS component of PGV has similar characteristics as EW component and the PGD is proportional to PGV in most cases. 135

C.11 EW component of PGV (m/s) from a south-to-north propagating rupture at (a) - (e) locations 1 - 5 respectively on the southern San Andreas fault for stochastic $M_w 7.9$ model-5 source model. The NS component of PGV has similar characteristics as EW component and the PGD is proportional to PGV in most cases. 136

C.12 (a)-(e) Stochastic median source models (here on referred to as models-1, 2, 3, 4, 5) with slip in m for a $M_w = 7.6$ earthquake on the San Andreas fault. Rupture time (s) contours are overlaid on the slip distribution. The rupture contours shown correspond to the stochastic stress conditions at location 1 of the rupture staring at Parkfield. Note that the rupture time contours change for a different location. 137

C.13 EW component of PGV (m/s) from a north-to-south propagating rupture at (a) - (e) locations 1 - 5 respectively on the southern San Andreas fault for stochastic $M_w 7.6$ model-1 source model. The NS component of PGV has similar characteristics as EW component and the PGD is proportional to PGV in most cases. 138

C.14 EW component of PGV (m/s) from a south-to-north propagating rupture at (a) - (e) locations 1 - 5 respectively on the southern San Andreas fault for stochastic $M_w 7.6$ model-1 source model. The NS component of PGV has similar characteristics as EW component and the PGD is proportional to PGV in most cases. 139

C.15 EW component of PGV (m/s) from a north-to-south propagating rupture at (a) - (e) locations 1 - 5 respectively on the southern San Andreas fault for stochastic $M_w 7.6$ model-2 source model. The NS component of PGV has similar characteristics as EW component and the PGD is proportional to PGV in most cases. 140

C.16 EW component of PGV (m/s) from a south-to-north propagating rupture at (a) - (e) locations 1 - 5 respectively on the southern San Andreas fault for stochastic $M_w 7.6$ model-2 source model. The NS component of PGV has similar characteristics as EW component and the PGD is proportional to PGV in most cases. 141

C.17 EW component of PGV (m/s) from a north-to-south propagating rupture at (a) - (e) locations 1 - 5 respectively on the southern San Andreas fault for stochastic $M_w 7.6$ model-3 source model. The NS component of PGV has similar characteristics as EW component and the PGD is proportional to PGV in most cases. 142

C.18 EW component of PGV (m/s) from a south-to-north propagating rupture at (a) - (e) locations 1 - 5 respectively on the southern San Andreas fault for stochastic $M_w 7.6$ model-3 source model. The NS component of PGV has similar characteristics as EW component and the PGD is proportional to PGV in most cases. 143

C.19 EW component of PGV (m/s) from a north-to-south propagating rupture at (a) - (e) locations 1 - 5 respectively on the southern San Andreas fault for stochastic $M_w 7.6$ model-4 source model. The NS component of PGV has similar characteristics as EW component and the PGD is proportional to PGV in most cases. 144

C.20 EW component of PGV (m/s) from a south-to-north propagating rupture at (a) - (e) locations 1 - 5 respectively on the southern San Andreas fault for stochastic $M_w 7.6$ model-4 source model. The NS component of PGV has similar characteristics as EW component and the PGD is proportional to PGV in most cases. 145

C.21 EW component of PGV (m/s) from a north-to-south propagating rupture at (a) - (e) locations 1 - 5 respectively on the southern San Andreas fault for stochastic $M_w 7.6$ model-5 source model. The NS component of PGV has similar characteristics as EW component and the PGD is proportional to PGV in most cases. 146

C.22 EW component of PGV (m/s) from a south-to-north propagating rupture at (a) - (e) locations 1 - 5 respectively on the southern San Andreas fault for stochastic $M_w 7.6$ model-5 source model. The NS component of PGV has similar characteristics as EW component and the PGD is proportional to PGV in most cases. 147

C.23 (a)-(e) Stochastic median source models (here on referred to as models-1, 2, 3, 4, 5) with slip in m for a $M_w = 7.2$ earthquake on the San Andreas fault. Rupture time (s) contours are overlaid on the slip distribution. The rupture contours shown correspond to the stochastic stress conditions at location 1 of the rupture staring at Parkfield. Note that the rupture time contours change for a different location. 148

C.24 EW component of PGV (m/s) from a north-to-south propagating rupture at (a) - (e) locations 1 - 5 respectively on the southern San Andreas fault for stochastic $M_w 7.2$ model-1 source model. The NS component of PGV has similar characteristics as EW component and the PGD is proportional to PGV in most cases. 149

C.25 EW component of PGV (m/s) from a south-to-north propagating rupture at (a) - (e) locations 1 - 5 respectively on the southern San Andreas fault for stochastic $M_w 7.2$ model-1 source model. The NS component of PGV has similar characteristics as EW component and the PGD is proportional to PGV in most cases. 150

C.26 EW component of PGV (m/s) from a north-to-south propagating rupture at (a) - (e) locations 1 - 5 respectively on the southern San Andreas fault for stochastic $M_w 7.2$ model-2 source model. The NS component of PGV has similar characteristics as EW component and the PGD is proportional to PGV in most cases. 151

C.27 EW component of PGV (m/s) from a south-to-north propagating rupture at (a) - (e) locations 1 - 5 respectively on the southern San Andreas fault for stochastic $M_w 7.2$ model-2 source model. The NS component of PGV has similar characteristics as EW component and the PGD is proportional to PGV in most cases. 152

C.28 EW component of PGV (m/s) from a north-to-south propagating rupture at (a) - (e) locations 1 - 5 respectively on the southern San Andreas fault for stochastic $M_w 7.2$ model-3 source model. The NS component of PGV has similar characteristics as EW component and the PGD is proportional to PGV in most cases. 153

C.29 EW component of PGV (m/s) from a south-to-north propagating rupture at (a) - (e) locations 1 - 5 respectively on the southern San Andreas fault for stochastic $M_w 7.2$ model-3 source model. The NS component of PGV has similar characteristics as EW component and the PGD is proportional to PGV in most cases. 154

C.30 EW component of PGV (m/s) from a north-to-south propagating rupture at (a) - (e) locations 1 - 5 respectively on the southern San Andreas fault for stochastic $M_w 7.2$ model-4 source model. The NS component of PGV has similar characteristics as EW component and the PGD is proportional to PGV in most cases. 155

C.31 EW component of PGV (m/s) from a south-to-north propagating rupture at (a) - (e) locations 1 - 5 respectively on the southern San Andreas fault for stochastic $M_w 7.2$ model-4 source model. The NS component of PGV has similar characteristics as EW component and the PGD is proportional to PGV in most cases. 156

C.32 EW component of PGV (m/s) from a north-to-south propagating rupture at (a) - (e) locations 1 - 5 respectively on the southern San Andreas fault for stochastic $M_w 7.2$ model-5 source model. The NS component of PGV has similar characteristics as EW component and the PGD is proportional to PGV in most cases. 157

C.33 EW component of PGV (m/s) from a south-to-north propagating rupture at (a) - (e) locations 1 - 5 respectively on the southern San Andreas fault for stochastic $M_w 7.2$ model-5 source model. The NS component of PGV has similar characteristics as EW component and the PGD is proportional to PGV in most cases. 158

List of Tables

2.1 Quality factor and the corresponding error in measurement of θ_a. 17

3.1 UCERF3 time-independent 30-year occurrence probabilities for each scenario earthquake. Half of these probabilities are assigned to north-to-south propagating ruptures and the other half to south-to-north propagating ruptures. 57

3.2 Properties of stochastic "median" kinematic source models for the scenario earthquakes. 59

3.3 PGV thresholds for the exceedance of IO, LS, CP, RT, & CO performance levels in the existing and the redesigned building models with probabilities of 2%, 5%, 10%, and 50%. 85

3.4 S_a (at the two horizontal fundamental translational periods) thresholds for the exceedance of IO, LS, CP, RT, & CO performance levels in the existing [along X (Y)] and the redesigned [along X+Y- (X+Y+)] building models with probabilities of 2%, 5%, 10%, and 50%. 85

3.5 Exceedance probability (%) of IO, LS, and CP performance levels in existing (redesigned) building model(s) conditioned on earthquake magnitude. 86

3.6 30-year exceedance probability (%) of FEMA356 limits for IO, LS, and CP performance levels of existing and redesigned buildings in the greater Los Angeles region due to southern San Andreas fault earthquakes in the magnitude range of M_w $6.0 - 8.0$ based on scenario simulations 86

4.1 Maximum a Posteriori (MAP) estimates of mean (standard deviation) of the model classes considered for the conditional distributions of PGV and PGD at a distance of 55-75 km given earthquake magnitude. In the case of levy distribution, the values correspond to location (shape) parameters. Bold values correspond to the distribution with greatest posterior probability. 96

4.2 Posterior probability of the model classes considered for the conditional distributions of PGV and PGD at a distance of 55-75 km given earthquake magnitude. The largest probabilities corresponding to each magnitude are shown in bold. 97

4.3 Maximum a Posteriori (MAP) estimates of the parameters of the model classes considered for the unconditional distributions of PGV and PGD at a distance of 55-75 km for earthquakes in the magnitude range of 6.05-7.90. Bold values correspond to the distribution with greatest posterior probability. 97

4.4 Posterior probability of the model classes considered for the unconditional distributions of PGV and PGD at basin sites at a distance of 55-75 km for earthquakes in the magnitude range of 6.04-7.90. The largest probabilities corresponding to each magnitude are shown in bold. 97

4.5 Posteriori probability (%) of the model class exceeding specified peak ground velocity (displacement) value. 99

Chapter 1

Motivation, Background and Scope

Until recently, collapse and major damage of steel buildings in earthquakes wasn't an anticipated notion. However, the damage sustained by tall steel buildings during recent earthquakes such as the 1985, $M_w 7.8$, Mexico city, and the 1994, $M_w 6.7$, Northridge, and the 1995, $M_w 6.9$, Kobe earthquakes brought forth the possibility of collapse in mid-rise and high-rise structures. This can be attributed to a multitude of reasons from ground motion characteristics such as the large amplitude, long period and duration shaking resulting from basin response to structural characteristics such as the susceptibility of beam-column connections, drastic tapering columns in upper stories. Many of the existing buildings in densely populated areas (e.g., Los Angeles, USA) with active seismic zones nearby are designed according to codes when there was inadequate understanding on the nature and impact of earthquakes capable of producing large ground motions. The newer buildings on the other hand are designed according to codes that are modified based on lessons from past earthquakes. While most of these buildings are designed to withstand seismic forces, the code based design process based on low-rise building performance and extended to tall buildings doesn't provide an insight into the performance of the structure during actual earthquakes. Furthermore, the modifications to the code are primarily done through the observations in past earthquakes and in consideration that there are few large magnitude earthquakes for which tenable data is available, it might not provide the best possible way for seismic risk assessment of buildings in future earthquakes. In order to gain true insights into the structural performance and henceforth seismic risk assessment, a thorough analysis on dynamic response of the structure has to be conducted under various levels of ground motion intensities from different earthquakes and estimates of these intensities for a given site under these earthquakes. Ground motion prediction equations (or attenuation relationships, GMPE) that describe the median ground motion intensity such as spectral acceleration, peak velocity/displacement, along with its standard deviation, based on source-to-site distance, magnitude, source type (e.g., normal fault, strike-slip fault) and site conditions (e.g., basin depth) can be used for this purpose. However, empirical relationships such as GMPE are based on global earthquake database and are inadequate in large magnitude range due to lack of sufficient data. Additionally, they do not factor in seismic source features such as slip distribution, rupture speed and directivity of the rupture etc., alongside geological features such as geometry of the fault, topography of basins, mountains etc. that play a pivotal role in the nature of regional ground shaking pattern.

Under these circumstances, rupture-to-rafters simulations that combine the advancements in the fields of seismology and structural engineering over the past few years form the perfect vessel to conduct structural performance and corresponding seismic risk studies in an accurate and versatile manner using a probabilistic framework. These simulations include seismic source modeling and determining their occurrence probabilities on the given fault of interest, simulating associated regional ground motion maps and using the same in the non-linear dynamic analysis of buildings post design to ultimately quantify the seismic performance of the considered structures. An analysis such as this involves an active interaction between scientists and engineers enabling each other for a precise understanding on the earthquake process and seismic response of structures. Furthermore, rupture-to-rafters simulations present an ideal way to answer intriguing questions pertaining to strong ground motions and related tall building response such as:

1. How can one quantify and understand the variation in seismic sources especially for large magnitude earthquakes (for which there is limited understanding) that are capable of producing high ground motion intensities?

2. What is the nature of ground motion from such sources at distances varying from tens to hundreds of kilometers? What is the sensitivity of these ground motions to seismic source parameters such as slip, rupture speed and others?

3. How are the ground motions influenced at a given site influenced by hypocenter location, rupture directivity, location and related parameters? How do they compare against empirical relations that are extensively used for code based design process?

4. What is the nature of tall building response to these ground motions and what are the ground motion characteristics that impact this response?
5. What are the damage mechanisms of tall buildings and would retrofitting help in mitigating this damage?
6. What are the regional expected losses due to earthquakes that occur frequently or otherwise?

It has to be noted that rupture-to-rafters simulations provides answers to many other questions in the field of earthquake engineering and not limited to the ones presented earlier. This study aims to present the rupture-to-rafters simulations framework and establish a proof-of-concept using extensive numerical studies on how such simulations can be used to establish the seismic performance of structures addressing numerous other issues in a meticulous manner.

Modeling seismic sources of various magnitudes and calculating the associated regional ground motion intensities forms the back-bone of rupture-to-rafters simulations. Seismic source models of past earthquakes can be used for this. However in view of the fact that credible data from very few large earthquakes is available, this study presents a new algorithm based on understanding of historic earthquakes and laboratory earthquake data to define stochastic seismic source models of large magnitude ($M_w 6.0-8.0$) strike-slip earthquakes in its entirety. This algorithm has been extensively validated using source models of past earthquakes such as the 2002 $M_w 7.9$ Denali, and 2004 $M_w 6.0$ Parkfield earthquakes. Fortunately in the recent years, the computational tools for regional ground motion simulations using seismic sources such as the ones mentioned here have been profusely developed. One such advancement is the use of spectral element method based programs that incorporate the regional crustal velocity structure. These programs have been extensively validated and became an indispensable arsenal for researchers to simulate regional ground motion maps (Frankel and Stephenson 2000; Pratt et al. 2003; Horikawa et al. 2003; Kagawa et al. 2004; Landes et al. 2004; Raileanu et al. 2005; Furumura 2005; Aagaard 2006; Graves 2006; Li et al. 2007; Lee et al. 2008; Plesch et al. 2011). Chapter-2 of this study provides an in depth look into these topics and other related information.

One such spectral element based program has been used to simulate ground motions in southern California from sixty large stochastic earthquakes generated through the algorithm on San Andreas fault with varying magnitude, rupture-directivity and -location. The simulated ground motions have been analyzed carefully to gauge their sensitivity to the modeling of source parameters and site characteristics. Moreover, the simulated ground motions have been incorporated to conduct nonlinear dynamic analysis of two 18-story moment frame buildings using three-dimensional finite element based models. The corresponding building response has been investigated thoroughly to evaluate the damage extent and sensitivity of the response to ground motion parameters such as peak ground velocity/displacement through fragility curve and other data analysis techniques. Adjacently, a probabilistic framework and the necessary computations are presented to calculate the likelihood of these buildings exceeding various limit states like Immediate Occupancy, Life Safety due to large earthquakes. Chapter-3 of this study extensively discusses the rupture-to-rafters simulations framework. To enable the reader for a thorough understanding on how the simulations are conducted, this is presented in context on how it is used to quantify seismic performance of tall buildings in southern California due to large San Andreas fault earthquakes.

Finally, Chapter-4 highlights the characteristics of long-period ground motions and on how ground motion simulations through rupture-to-rafters simulations in conjunction with a Bayesian model class identification form an alternative to understand ground motion nature of future earthquakes. These results influence the representation of the national/regional seismic hazard maps that are judiciously used by engineers and safety regulatory agencies. The author sincerely hopes that the reader through the course of this thesis gains an invaluable perspective on the highlights of rupture-to-rafters simulations while simultaneously learning more about the existing methodologies and their limitations in quantifying seismic sources, associated ground motions, the seismic response and performance of tall buildings under such ground motions.

e

Chapter 2

Stochastic Source Model Generation Algorithm for Strike-Slip Earthquakes

Rupture-to-rafters simulations offer an alternative (and perhaps more realistic) approach for risk quantification and design of new structures (Krishnan et al. 2006a; Krishnan et al. 2011). Generating stochastic seismic source models for these simulations is a crucial step, given the limited number of credible source models from large historical earthquakes. The seismic source model is a mathematical representation of the earthquake rupture process. Two types of source models are used in earthquake physics:

1. “kinematic” models, which prescribe the spatial and temporal evolution of the rupture speed, the slip, and the slip velocity on the fault, inferred from seismic, geodetic, and geological observations.
2. “dynamic” models, which prescribe the fault pre-stress, fracture energy, and stress drop. An earthquake is nucleated at a point in the model by artificially increasing the pre-stress to a value greater than the shear strength. The rupture process is then allowed to evolve dynamically as dictated by an assumed fault friction law. The development of dynamic source models is an active area of research in earthquake source physics (e.g., Madariaga and Olsen 2002; Schmedes et al. 2010; Bizzarri 2011).

While dynamics source models may better characterize earthquake source physics and there are efforts underway to validate them against empirical data (e.g., Dalguer et al. 2008; Harris et al. 2009; Olsen et al. 2009; Andrews and Barall 2011; Shi and Day 2013; Baumann and Dalguer 2014), the theory is more complex and less mature when compared to kinematic source modeling (e.g., the state of stress in the earth and the fault friction law are not known; they are not as well-constrained as kinematic source parameters such as slip). Here, we represent an earthquake source using a kinematic model. Kinematic source description involves dividing the fault rupture plane(s) into a number of smaller sub-events. Each sub-event (considered as a point source) is characterized by three parameters: slip, rupture speed and slip velocity-time function. Brune (1970) proposed one of the earliest earthquake source models, in which near- and far-field displacement spectra are calculated from a fault dislocation model accelerated by an effective stress. Significant progress has been made in kinematic source modeling since then with the help of data collected by modern seismic networks (Zeng et al. 1994; Somerville et al. 1999; Hartzell et al. 1999; Mai and Beroza 2002; Nielsen and Madariaga 2003; Guatteri et al. 2004; Tinti et al. 2005; Lavallée et al. 2006; Liu et al. 2006; Graves and Pitarka 2010; Aagaard et al. 2010; Aagaard et al. 2010). We start with a brief description of current approaches to prescribing the three source parameters for each sub-event.

2.0.1 Slip Distribution

Spatial variation of kinematic slip in a rupture is perhaps the best understood amongst the three source parameters. This is partly due to the fact that surface slip can be constrained in a finite-source inversion of an earthquake using geodetic observations. Rupture speed and slip velocity-time function, on the other hand, are inferred completely through inversions. The power spectral density (PSD) of the two-dimensional slip distribution from these inversions typically decays with wave number according to a power law. On this basis, a PSD function, inferred from finite-source inversion of past earthquakes, could be inverted back to the spatial domain to produce a stochastic slip model (e.g., Somerville et al. 1999; Mai and Beroza 2002). Because finite-source inversions are typically able to resolve longer wavelengths only, their PSDs do not properly characterize the spectral dropoff with wave-number. Graves and Pitarka (2010) overcome this deficiency by augmenting the long-wavelength portion of the PSDs from finite-source inversions (or uniform/random slip distributions) with a band-limited PSD function that accurately captures the spectral decay inferred from seismic data. It should be noted that in developing the PSD function, slip inversions of only a limited number of large magnitude earthquakes were used (e.g., see Fig. 2.1) and the slip models are often interpolated to facilitate a direct comparison. In a study of seven earthquakes including the 1994 Northridge earthquake, Lavallée et al.

(2006) discussed the negative effects of this interpolation on PSD decay. Moreover, this approach anchors the sources to a specific power-spectral decay and may not capture the degree of variability perhaps inherent to seismic sources.

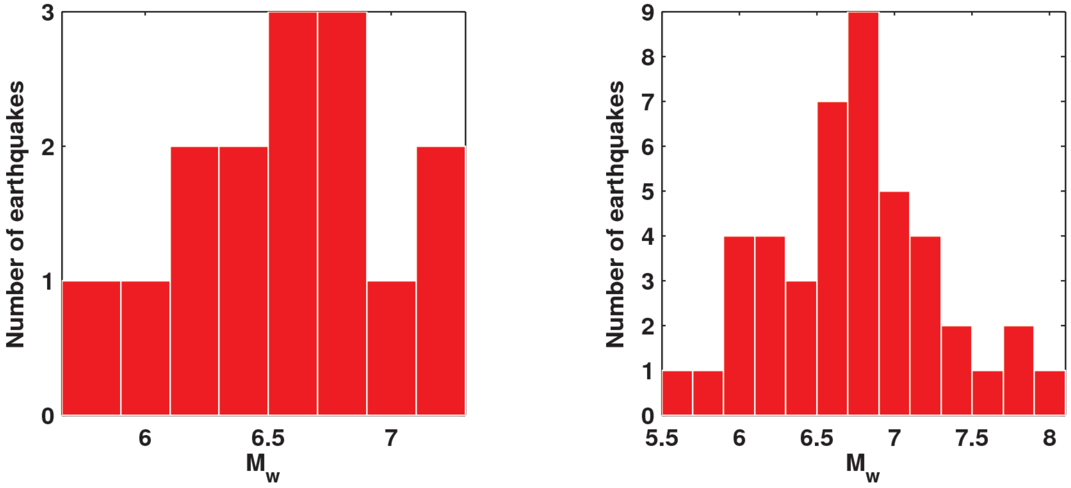

(a) (b)

Figure 2.1: Histograms of magnitudes of past earthquakes considered by (a) Somerville et al. (1999) and (b) Mai and Beroza (2002) for determining the spectral properties of the slip distribution on the fault. Source mechanisms of these earthquakes are not limited to strike-slip, but include reverse, thrust etc. Note the sparse number of large magnitude ($M_w \geq 7.0$) earthquakes included in either study.

An alternate approach is to generate spatial distribution of slips for an earthquake of given magnitude stochastically and accept or reject each model by one of two methods:

1. comparing spectra of the resulting synthetic ground motions (assuming a rupture-speed and slip velocity-time function distribution) against that of recorded ones (e.g., Zeng et al. 1994).

2. comparing the spectral decay as a function of wave-number against the broad range of the corresponding decays found in finite-source inversions of past earthquakes.

Whereas in the former approach, the spectra of synthetic ground motions are influenced by the choice of rupture speed, slip velocity-time function, Green's function etc., the latter has no such concerns. Accordingly, the latter approach is adopted here. Our algorithm divides the rupture area recursively along length, until each daughter segment has a dimensional aspect ratio close to unity. The mean slip on each daughter segment is characterized using lognormal probability distributions. The mean and standard deviation of these distributions depend upon the magnitude of its parent segment. Slip on each daughter segment is assigned a value that is a single realization of the corresponding probability distribution, with the slip vector oriented along strike (i.e., rake = 180°). To introduce slip variation along depth, each (approximately square) daughter segment is subdivided into four segments using one subdivision along depth and one along length. The assignment of slip for this penultimate generation of daughter segments is based on the same method as the previous generations of daughter segments. Finally, these penultimate generation segments are subdivided along length and depth to the resolution needed for wave propagation simulations. Slips are assigned to the final generation of segments as realizations of the lognormal probability distribution corresponding to the magnitude of the parent segment from the penultimate generation. A filter is applied to smoothen the resulting slip distribution eliminating sharp spatial variations. Additionally, at each step, the mean slips are scaled linearly to that of the parent segment such that the net seismic moment M_o is conserved. The resulting slip distribution is accepted if the average power spectra, along the length and the depth of the rupture, decay with wave number according to a power law with decay coefficient between 2.0 and 4.0. This is the range of values for the decay observed in finite-source inversions of past earthquakes (e.g., Somerville et al. 1999; Mai and Beroza 2002). The use of 1-D spectra along length and depth rather than a 2-D spectrum over the area of rupture is based on the assumption that slip along fault is statistically independent of slip along depth. While this assumption may not strictly hold true, the use of a circular PSD criterion for model acceptance is not likely to be significantly different from the use of two 1-D spectra along length and depth (Lavallée et al. 2006).

2.0.2 Rupture Speed Distribution

The initiation time of slip at any given location along the rupture depends upon the rupture speed V_r. Rupture speed can have a significant influence on the character of the radiated seismic waves, the resulting ground motions, and the impact on the built environment. Even though theoretical models (e.g., Burridge 1973; Andrews 1976) have shown that ruptures could travel at speeds higher than the Rayleigh wave speed, rupture speeds in ground motion simulations have traditionally been assumed to be lower. This is due, in part, to the sparsity of such strong ground motion data. However, evidence from recent earthquakes such as the 1999 M_w7.6 Izmit (e.g., Bouchon et al. 2002), the 2001 M_w7.8 Kunlun (e.g.,Bouchon and Vallée 2003; Bhat et al. 2007), the 2002 M_w7.9 Denali (e.g., Frankel 2004; Dunham and Archuleta 2004), and the 1979 M_w6.4 Imperial Valley (e.g., Archuleta 1984; Das 2010) earthquakes, point to rupture speeds exceeding the Rayleigh wave speed. Based in part on this evidence, several new models have been developed with an underlying principle that the secant rupture speed (the average rupture speed from the hypocenter to a given subfault location) or local rupture speed is correlated with slip on the fault (e.g., Guatteri et al. 2004; Liu et al. 2006; Graves and Pitarka 2010; Aagaard et al. 2010; Aagaard et al. 2010; Song and Somerville 2010; Song et al. 2014) . Others correlate rupture initiation with slip (e.g., Graves and Pitarka 2010). However, Schmedes et al. (2010) found no evidence for such correlation from dynamic rupture models of 315 earthquakes. They further cautioned that assuming any such correlation could lead to over-prediction of simulated ground motions. In addition to field observations and theoretical models, laboratory earthquakes have yielded important insights into the fault rupture process. Stable pulse-like ruptures have been realized in the laboratory under controlled conditions (Rosakis et al. 1999; Rosakis et al. 2007; Lu 2009; Lu et al. 2010; Mello et al. 2010). Both sub-Rayleigh and super-shear ruptures have been realized. The sub-Rayleigh ruptures have been observed to propagate at speeds in the vicinity of 0.87V_S, where V_S is the shear wave speed in the medium. Under special normal stress and fault roughness conditions, the ruptures have been observed to transition to super-shear speeds in the vicinity of 1.67V_S. In our source representation, we assume that all ruptures initiate at a sub-Rayleigh speed of 0.87V_S. Using estimates of pre-stress on the fault from paleoseismic, focal mechanisms, borehole breakouts, and other in-situ observations catalogued in the World Stress Map project (Heidbach et al.), we assess whether conditions exist for rupture to transition to super-shear speeds as it progresses along the fault. If such conditions do exist for any sub-event along the rupture, we prescribe a rupture speed of 1.67V_S for that sub-event. We noted previously when discussing dynamic source models that the state of stress in the earth is not known accurately. Yet, we continue to use estimates of the same in characterizing our kinematic source models. This is justifiable because only the rupture speed in kinematic source models is dependent upon the state of stress. On the other hand, the evolution of all three source parameters (slip, slip velocity and rupture speed) in dynamic source models are affected by the state of stress.

2.0.3 Slip velocity-time function

The slip velocity-time function describes the temporal evolution of slip during an earthquake and is characterized by slip magnitude, rise-time (time taken for peak slip to be attained) and peak time (time taken for peak slip velocity to be attained). Variation of slip velocity with time in a source model affects the frequency and amplitude characteristics of the resulting ground motions. It is specified either as a single function (single time window) or as a series of overlapping time-shifted functions (multiple time windows). Commonly assumed functional forms include Gaussian, triangular, trigonometric, and modified Yoffe (Tinti et al. 2005). Function coefficients are typically determined from dynamic rupture simulations (e.g., Cotton and Campillo 1995; Guatteri et al. 2004; Tinti et al. 2005; Liu et al. 2006) or finite-source inversions of past earthquakes (e.g., Hartzell et al. 1996; Somerville et al. 1999). Unfortunately, dynamic rupture simulations have been seen to be quite sensitive to the choice of modeling parameters making it difficult to constrain these coefficients. Furthermore, seismic data that could be useful in determining these coefficients is rather sparse. Thus, there is limited understanding of these source characteristics. Laboratory earthquakes could serve to bridge this knowledge gap as the slip-velocity time function can be directly measured in the laboratory.

In the laboratory earthquakes generated by Lu (2009, 2010), rise-time (measured in μs) has been found to be linearly correlated with slip (measured in μm) as shown in Fig. 2.2. The rise-times shown are the basal widths of the best-fitting isosceles triangles to the slip velocity-time functions measured in the laboratory. This is in agreement with dynamic rupture studies (e.g., Schmedes et al. 2010) and similar to Graves and Pitarka (2010), where they postulate rise-time being proportional to the square root of the slip. We fit a lognormal probability density function (PDF) to the slip to rise-time ratio measured in the laboratory earthquakes. Assuming self-similarity of the slip-to-rise-time ratio between the laboratory scale and the earth scale, we equate the mean and variance of this ratio at the earth scale to that observed in the laboratory. Independent realizations of this PDF are assigned as the slip-to-rise-time ratios for all the subfaults comprising the rupture. A slip proportional rise-time is thus prescribed to each segment. This incorporates the physics of temporal characteristics of slip as we best know it. It should be noted that Andrews and Barall (2011) make a comparable self-similarity assumption. They assume that the ratio of initial shear stress to the initial normal stress on the fault is scale independent and that the mean and variance of a PDF describing this ratio are scale invariant.

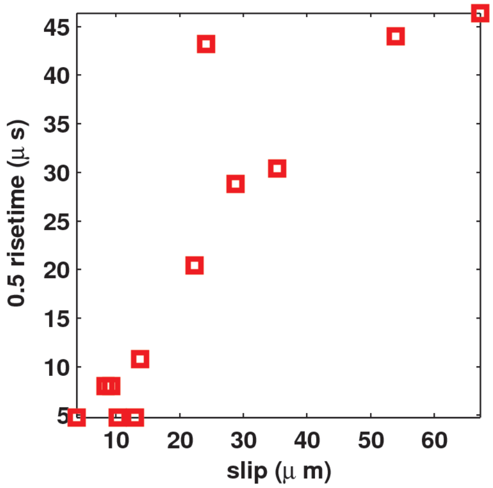

Figure 2.2: Rise-time plotted as a function of slip observed in laboratory earthquakes (Lu 2009, 2010). The correlation between the two is in agreement with dynamic rupture studies conducted by Schmedes et al. (2010).

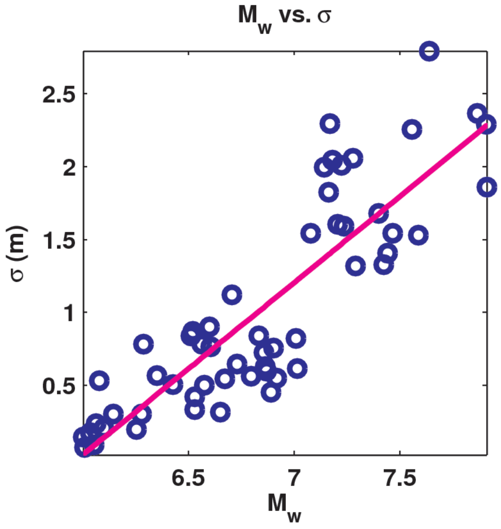

Figure 2.3: Blue circles show the standard deviation σ of log-normal PDF fits to the slip distribution from finite-source inversions of 56 strike-slip earthquakes as a function of earthquake magnitude M_w. The magenta line is the best-fitting linear least-squares fit described by Eq. 2.3.

2.1 Methodology

2.1.1 Slip D

For a target earthquake magnitude M_w, the rupture area A of a stochastic source model is estimated using the Hanks & Bakun (2002, 2008) relationship given by:

$$A = \begin{cases} 10^{Mw-3.98} & A \leq 537km^2 \\ 10^{\frac{3}{4}(Mw-3.07)} & A > 537km^2 \end{cases} \tag{2.1}$$

With area of rupture known and the seismogenic depth d inferred from seismicity on the fault, the length of rupture l can be determined. If d exceeds l, the rupture dimensions are re-calculated assuming a square rupture area (i.e. $l == d$). Seismic Moment M_o and mean slip $\bar{D}$ of the earthquake are estimated from magnitude M_w using:

$$M_o = GA\bar{D} = 10^{\frac{3}{2}M_w + 10.7} \tag{2.2}$$

where G is the average shear modulus of the earth ($\sim$ 30 GPa). To arrive at a realistic slip distribution with this mean slip, we recursively divide the rupture area lengthwise in half, each parent segment being subdivided into two daughter segments. This segmentation is continued until each fault segment attains a dimensional aspect ratio close to unity. In order to develop a credible methodology to assign realistic slips to these segments, we have carefully studied finite-source inversions of 56 past strike-slip earthquakes (refer to the Data and Resources section for details) with magnitude $M_w = 6.0 - 8.0$. We observe that a series of log-normal PDFs can be used to reasonably describe the slip distribution in these sources. Furthermore, the standard deviation of log-normal PDF fits to the slip distribution in these models scales linearly with their magnitudes (Fig. 2.3). This linear scaling can be expressed by the regression relation:

$$\sigma = 1.1827M_w - 7.0754 \tag{2.3}$$

Now, from the parent segment magnitude and Eq. 2.3, we determine the standard deviation of the log-normal PDF that is to be used to characterize the slip of the daughter segments. The mean for this PDF is taken to be the average slip of the parent segment. Two independent realizations of this PDF are generated and assigned as the mean slips on the two daughter segments. They are subsequently scaled uniformly such that the sum of the seismic moments of the daughter segments matches that of the parent segment. If parent segment M_w is less than 6.0 (the lower magnitude limit in Fig. 2.3), the standard deviation corresponding to $M_w = 6.0$ is used.

To introduce variation of slip along the depth of the fault, each segment is subdivided into four daughter segments in the penultimate step, two along length and two along depth. Random mean slips are assigned as before. In the final step, each fault segment is further discretized to the resolution required for generating the desired highest frequency wave in ground motion simulations. Slip assignment is based on independent realizations of a log-normal PDF with the mean slip and the standard deviation determined from Eqs. 2.2 and 2.3, respectively, both using the magnitude of the parent segment. Finally, a unit 2-D filter that is Gaussian along length and parabolic along depth is applied to

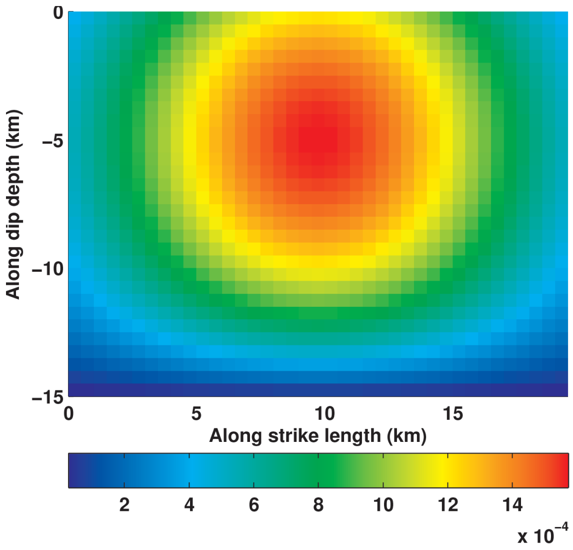

Figure 2.4: Plane view of moment-preserving filter used to smoothen the slip distribution. The filter function is Gaussian along fault length (with width d) and parabolic along fault depth (with width 3/4d), where d is the depth of rupture. The parabola has a zero ordinate at the bottom and a peak at two-thirds height from the bottom.

smoothen the slip distribution (Fig. 2.4). Dimensions of the filter are d and $3/4d$ along length and depth, respectively. In order to ensure that maximum moment release occurs within the upper-third portion of the fault (Fialko et al. 2005), the parabola has a peak at two-thirds height from the bottom. The ordinate at the bottom of the filter is assigned zero value to ensure zero moment release below the seismogenic depth.

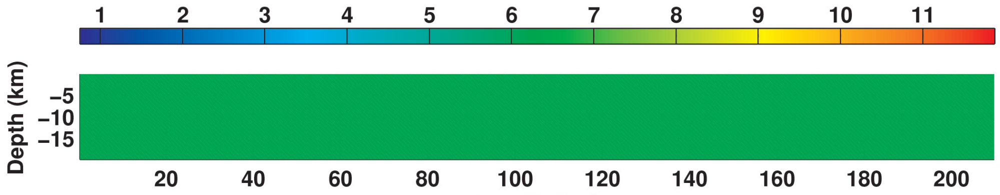

(a) Hierarchy level - 1

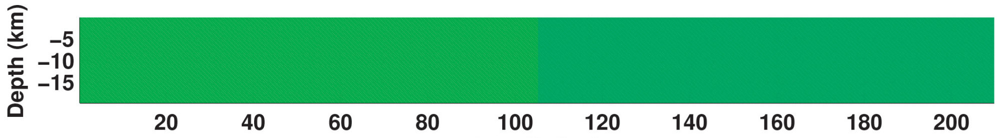

(b) Hierarchy level - 2

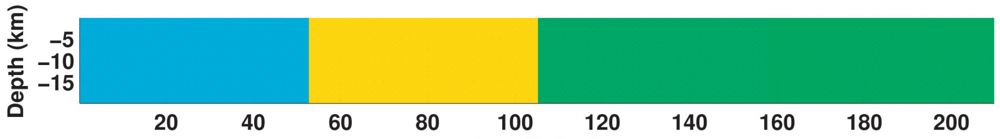

(c) Hierarchy level - 3

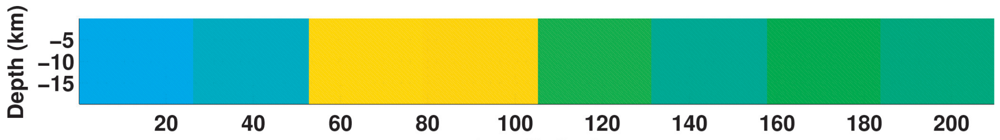

(d) Hierarchy level - 4

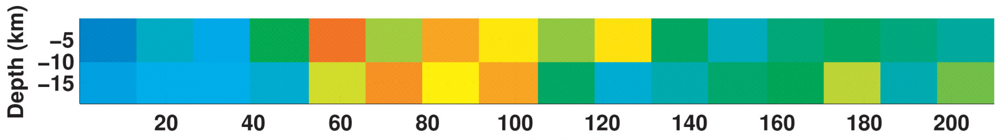

(e) Hierarchy level - 5

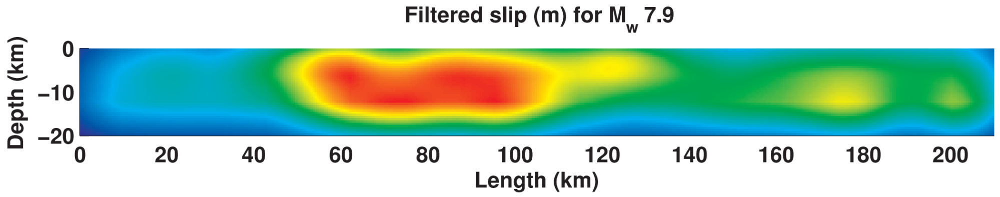

(f) Final filtered slip distribution

Figure 2.5: Application of the stochastic source algorithm to a $M_w = 7.9$ strike-slip earthquake. Recursive divisions of fault area followed by assignment of random realizations of magnitude-dependent log-normal PDFs of slip lead to five hierarchical levels [(a) Level - 1 through (e) Level - 5] of the seismic source. The final step involves subdividing the parent segments to small daughter segments capable of producing the desired highest frequency wave in ground motion simulations. Assignment of random realizations of magnitude-dependent log-normal PDFs of slip to these daughter segments along with a smoothing filter leads to (f) the final filtered slip distribution.

For example, suppose a stochastic source model is to be generated for a magnitude $M_w = 7.9$ earthquake on the San Andreas fault. From Eq. 2.1, the rupture area is 4200 km^2. The average seismogenic depth of the San Andreas fault may be assumed to be 20 km (i.e., rupture depth $d = 20$) based on observations. Therefore, the length of the rupture L is 210 km. Average slip from Eq. 2.2 is 6.30 m. Fig. 2.5(a) shows the hierarchy level 1 model. Recursive division of the level 1 model along fault length leads to hierarchy levels 2, 3, and 4 [Figs. 2.5(b), 2.5(c), and 2.5(d), respectively]. The average slips on the two daughter segments at hierarchy level 2 are drawn from a log-normal PDF with mean slip of 6.30 m and standard deviation of 2.26 m (from Eq. 2.3 corresponding to $M_w = 7.9$). To preserve the seismic moment, the average slips of the daughter segments are scaled to 6.65 m ($M_w = 7.71$) and 5.95 m ($M_w = 7.68$), respectively. The average slips on the first two daughter segments at hierarchy level 3 are drawn from a log-normal PDF with mean slip of 6.65 m and standard deviation of 2.05 m (from Eq. 2.3 corresponding to $M_w = 7.71$). Again, these are scaled to 3.83 m ($M_w = 7.35$) and 9.47 m ($M_w = 7.62$), respectively, to preserve moment. The two daughter segments at level 3 arising from the $M_w 7.68$ parent segment have average slips of 5.91 m and 5.99 m (realizations drawn from a log-normal PDF with mean 5.95 and standard deviation 2.01 and scaled to match moment of $M_w = 7.68$). Similarly, hierarchy level 4 results in eight approximately 20 km square segments, with average slips 3.40 m ($M_w = 7.11$), 4.27 m ($M_w = 7.18$), 9.46 m ($M_w = 7.41$), 9.48 m ($M_w = 7.41$), 6.73 m ($M_w = 7.31$), 5.10 m ($M_w = 7.23$), 6.48 m ($M_w = 7.30$), and 5.51 m ($M_w = 7.26$). At the next hierarchy level, the fault is subdivided along both length and depth [Fig. 2.5(e)]. Coincidentally, the area of 10 km square segments at hierarchy level 5 corresponds approximately to a magnitude 6 rupture from Eq. 2.1, the lower magnitude limit of the finite-source inversions used in the development of Eq. 2.3. At the final step, the hierarchy level 5 segments are subdivided into 0.5 km squares. This is the resolution needed to generate a 2 sec wave in ground motion simulations [Fig. 2.5(f)]. The slips for each of these segments are generated as independent realizations of log-normal PDFs with mean slips from the scaled average slips of parent segments from hierarchy level 5, and standard deviations determined from Eq. 2.3 using the magnitudes corresponding to these parent segments. The power-spectral density of the slip along fault length and depth as a function of the wave number are shown in Figs. 2.6(a) and 2.6(b), respectively. The average PSD decays with wavenumber as a power law with decay coefficients of 2.24 and 2.13 along length and depth respectively. Because these values lie between 2 and 4, this stochastic source model is an acceptable realization and can be reliably used for ground motion simulations.

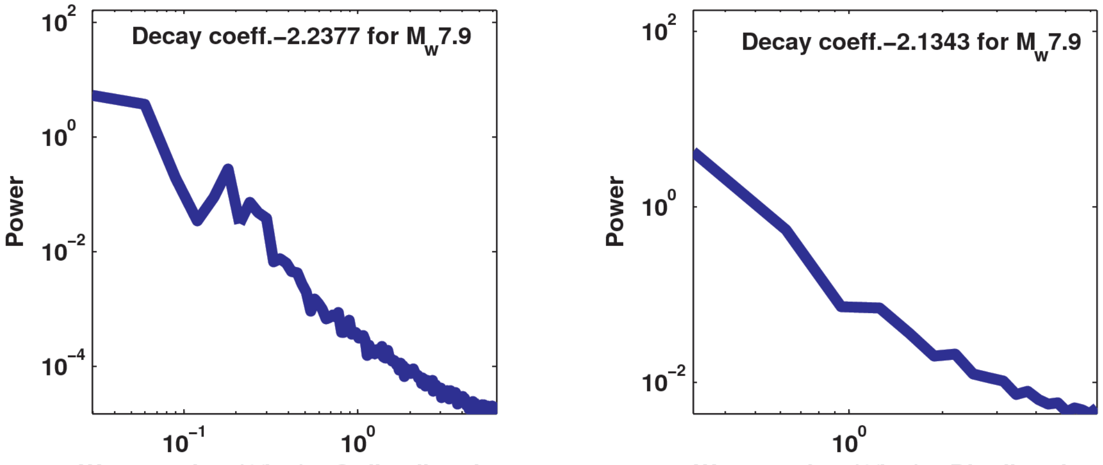

(a) (b)

Figure 2.6: Power Spectral Density (PSD) of a stochastic slip realization along (a) strike and (b) dip directions as shown in Fig.2.5(f) for M_w 7.9 earthquake.

Shown in Fig. 2.7 are the normalized histograms of slip (m) in a finite-source inversion model of the magnitude 7.9 Denali earthquake of 2002 (Krishnan et al. 2006a) and one stochastic source realization using the outlined method. The similarity in the two distributions (with the exception of the frequency of sub-faults with zero slip) suggests that a series of log-normal PDFs can indeed be used to define slip distribution in stochastic source models. The large concentration of zero slip sub-faults in the finite-source inversion model is due to the greater length assumed in the inversion (about 290 km) as compared to about 210 km for the stochastic model.

2.1.2 Rupture Speed (V_r)

Laboratory earthquakes (Rosakis et al. 2007; Lu 2009; Lu et al. 2010; Mello et al. 2010) show the influence of initial fault shear stress on the rupture speed (in addition to the influence of other parameters). Initial shear stress, in the case of a strike-slip fault, can be determined using the orientation (θ) between the maximum principal stress (σ_1) and the fault strike. The maximum and minimum principal stresses (σ_1 and σ_3) on a strike-slip fault lie on the plane perpendicular to that of the fault. The intermediate principal stress (σ_2) is hydrostatic, acts normal to the fault plane, and varies linearly with

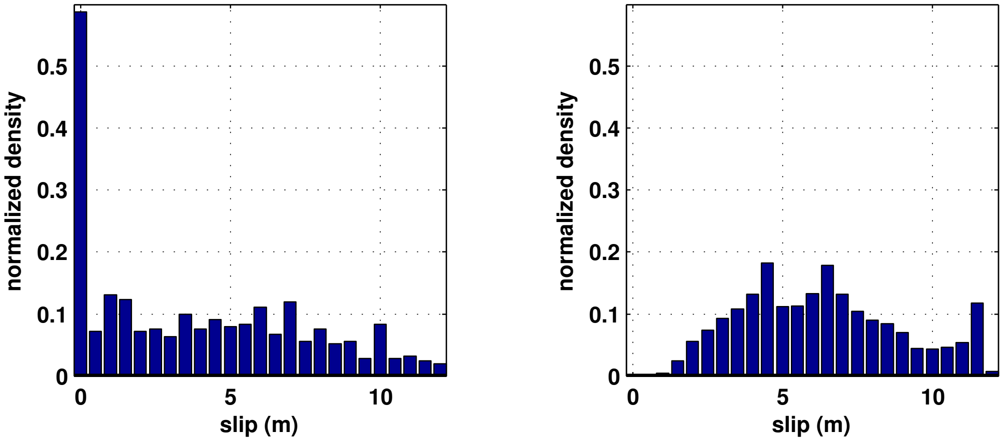

(a) (b)

Figure 2.7: Normalized histograms of slip(m) of a $M_w 7.90$ earthquake from: (a) a finite-source inversion of the 2002 Denali earthquake and (b) one stochastic source realization using the outlined method.

fault depth. Evaluating θ along the fault forms an important step in estimating the initial shear stress (τ), and in further determining the rupture speed distribution for a seismic source.

The World Stress Map (WSM) project (Heidbach et al. 2008) compiles the azimuth of maximum principal stress (θ_a) at near-fault locations worldwide. The angles are derived from field observations (including paleoseismic estimates of slip, borehole breakouts and hydraulic fractures) and theoretical investigations (including focal mechanisms of past earthquakes). Based on the quality of underlying data, an estimate of the maximum measurement error is also provided (Table 2.1).

Quality	Error
A	±15°
B	±20°
C	±25°
D	±40°
E	un-reliable

Table 2.1: Quality factor and the corresponding error in measurement of θ_a.

To account for the uncertainty in the measurement of θ_a, we add a randomly generated fraction of the measurement error from Table 2.1 to the reported estimate of θ_a. We use this estimate of θ_a in computing the orientation of the maximum principal stress σ_1 relative to the fault:

$$\theta = 180° - |\phi - \theta_a| \tag{2.4}$$

where ϕ is the strike at the closest point on the fault. These near-fault data locations typically occur in clusters (e.g., data points on the southern San Andreas fault are clustered at five locations as shown in Fig. 2.8).

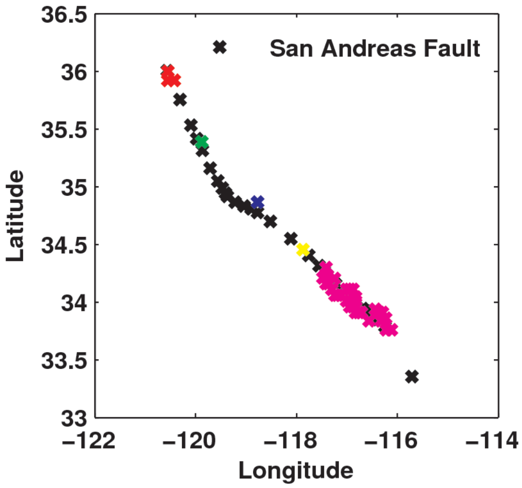

Figure 2.8: Locations along the southern San Andreas fault at which stress estimates are available from the World Stress Map project. Five data clusters are shown (magenta-, yellow-, blue-, green-, and red-colored points).

We assume θ at each cluster location to be characterized by a lognormal distribution with mean equal to the arithmetic mean of θ for all the locations within the cluster and standard deviation calculated from the cluster with the highest number of WSM data points. We further assume that θ is constant along fault depth, i.e., rupture speed varies along fault length alone. All the sub-events on the fault that lie in the zone tributary to a data cluster are assigned randomized θs drawn from the corresponding lognormal distribution. All the sub-events within distances equal to the seismogenic depth d in a given tributary zone are assigned the same randomly generated realization of θ. Assuming ambient stresses in the crust adjacent to the fault are maintained by the frictional stability of small, high-friction fractures, and that fluid pressures in the crust are hydrostatic (Townend and Zoback 2000; Zoback and Townend 2001; Townend and Zoback 2004; Townend 2006; Townend, personal communication, 2008) initial shear (τ) and normal (σ_n) stresses on the sub-event are calculated using:

$$\begin{aligned} &\bar{\sigma} = \frac{\sigma_1 + \sigma_3}{2} \simeq \sigma_2 = \rho_r g z \ ; \ p = \rho_w g z \ ; \ \Delta\sigma = \frac{2\mu_p(\bar{\sigma} - p)}{\sqrt{\mu_p^2 + 1}} \\ &\tau = \frac{\Delta\sigma}{2} sin2\theta \ ; \ \sigma_n = \bar{\sigma} - p - \frac{\Delta\sigma}{2} cos2\theta \end{aligned} \tag{2.5}$$

where p is the hydrostatic fluid pressure, $\bar{\sigma}$ and $\Delta\sigma$ are the mean and differential stress, respectively, ρ_r and ρ_w are the density of rock and water, respectively, τ and σ_n are the initial shear and normal stresses acting on the sub-fault respectively, and, g is the acceleration due to gravity. In our algorithm, z corresponds to half the seismogenic depth and $\mu_p(= 0.6)$ is the static Coulomb friction coefficient. Our assumption that the stress orientation is uniform with depth but variable along strike is primarily motivated by the lack of data along depth. If, in the future, such data becomes available, the algorithm could be modified to incorporate variations along depth as well.

Loading factor (S) at any given location along the fault is calculated as:

$$\begin{aligned} &S = \frac{(\tau_p - \tau_r)}{(\tau - \tau_r)} \\ &\tau_p = \mu_p \sigma_n \ ; \ \tau_r = \mu_r \sigma_n \end{aligned} \tag{2.6}$$

where $\mu_p(= 0.6)$ and $\mu_r(= 0.1)$ (Goldsby and Tullis 2002; Di Toro et al. 2004) are the static and dynamic friction coefficients, respectively, and, τ_p and τ_r are the static and dynamic friction strength of the fault at that location, respectively. If S $\geq$ 1.77, rupture is assumed to propagate at sub-Rayleigh speeds (Andrews 1976) and a rupture speed of $0.87 V_S$ is assigned for all sub-events along depth at that location based on laboratory observations. If S $\leq$ 1.77, it is assumed that stress conditions exist for rupture to be able to transition to super-shear speeds. The transition length (L_t) is given by Rosakis et al. (2007) as:

$$\begin{aligned} &L_t = L_c f(S) \\ &L_c = \frac{G(\tau_p - \tau_r) d_o}{\pi(1 - \nu)(\tau - \tau_r)^2} \ ; \ f(S) = 9.8(1.77 - S)^{-3} \end{aligned} \tag{2.7}$$

where L_c is the critical crack length, d_o is the characteristic slip chosen randomly from a uniform distribution between 0.5 m and 1 m (Ide and Takeo 1997), and $\nu(= 0.25)$ is the Poisson's ratio. If

L_t is less than the along-length distance from hypocenter to the location under consideration, a local rupture speed of $1.67V_S$ is assigned for all the sub-faults along depth at that location on the fault; else rupture speed is set at $0.87V_S$. Thus, rupture is assumed to propagate at one of two speeds, either a sub-Rayleigh speed of $0.87V_S$ or a super-shear speed of $1.67V_S$. Although shear wave speed may vary locally along the fault, here, we assume a constant V_S of 3.29 km/s, resulting in a bimodal distribution of two rupture speeds, 2.86 km/s and 5.49 km/s. It should be noted that the changing strike on faults such as the San Andreas may affect rupture speeds. Here, we assume that the effect of the changing strike on the principal stress orientations on the fault fully accounts for its effect on rupture speed. We do not explicitly consider fault geometry in the determination of the rupture speed distribution.

2.1.3 Slip velocity-time function

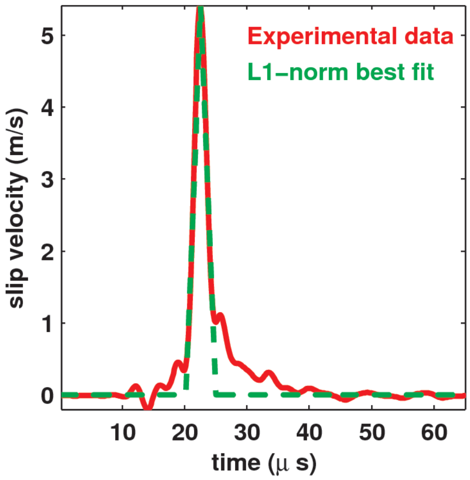

Figure 2.9: Slip velocity plotted as a function of time for a laboratory earthquake and the best fitting isosceles triangular slip velocity-time function.

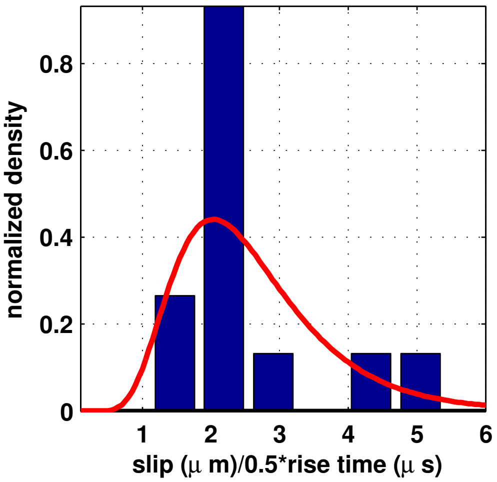

Figure 2.10: Normalized histograms of slip-to-rise-time ratio observed in laboratory earthquakes and the associated lognormal fit.

We use triangular slip velocity-time functions in our stochastic sources. The parameters are determined using data from a catalog of pulse-like laboratory earthquakes. Using an L_1 norm, we fit isosceles triangles to the slip velocity-time functions measured in the laboratory (e.g., see Fig. 2.9). It turns out that the slip-to-rise-time ratios so obtained for all available laboratory earthquakes can be reasonably well characterized by a log-normal distribution (see Fig. 2.10) with mean 2.605 and standard deviation 1.167.

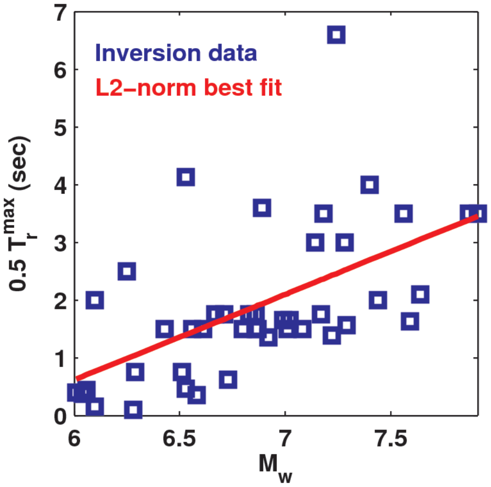

Figure 2.11: Maximum rise-times in finite-source inversions of 56 past earthquakes plotted as a function of their magnitudes. The linear trend is best captured by Eq. 2.8, the straight line shown in red.

For a given slip model, we generate a realization of slip to rise-time ratio using this distribution. Since fault slip is known within each sub-event, we can compute the rise-time and hence the slip velocity within each sub-event. It is possible that the random realization of the slip-to-rise-time ratio can result in extremely large unrealistic rise times. In order to avoid such anomalous realizations, we once again turn to the finite-source inversions of the 56 earthquakes cataloged in the ETH database. Shown in Fig. 2.11 is the maximum rise time (T_r^{max}) as a function of earthquake magnitude for these events. A linear trend is observed and the best-fitting relation is given by:

$$0.5T_r^{max} = 1.5M_w - 8.3 \tag{2.8}$$

For a stochastic source of a given magnitude, if the maximum rise-time in the model exceeds T_r^{max} from Eq. 2.8, we discard this rise-time distribution and generate a new realization for the slip-to-rise-time ratio.

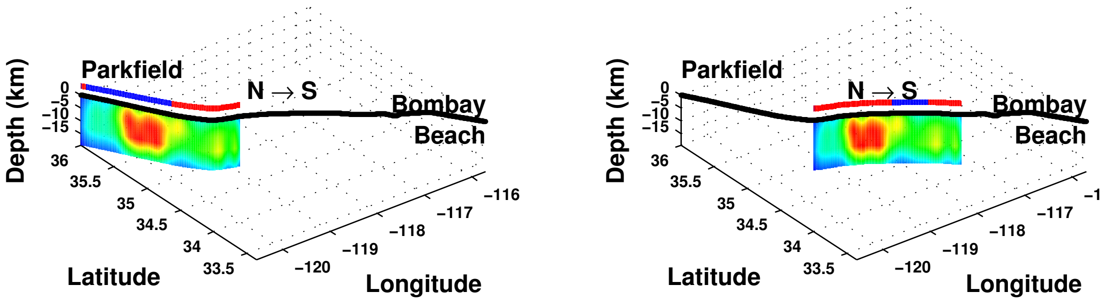

(a) (b)

Figure 2.12: One of five stochastic source realizations (the median model) for the north-to-south rupture of a hypothetical $M_w = 7.9$ earthquake on the southern San Andreas fault. Two possible rupture locations, identified as rupture locations (a) 1 and (b) 3, are shown. Also shown on top of slip (color scale same as in Fig. 2.5(a)) is the rupture speed distribution. Blue indicates rupture propagating at the sub-Rayleigh speed of $0.87V_s$, while red indicates rupture propagating at the super-shear speed of $1.67V_s$. Rupture speed is held constant along fault depth. The model has a constant slip-velocity of 4.15 m/s.

2.2 Application to the Southern San Andreas Fault

Using the recursive division algorithm, we generate a suite of five stochastic source model realizations each for a $M_w = 7.9$ and a $M_w = 6.05$ earthquake along the Southern San Andreas Fault. Each source realization is placed at five uniformly spaced locations starting at Parkfield in central California and terminating at Bombay Beach in southern California (e.g., see Figs. 2.12 and 2.13). Two rupture directions are considered for each location – north-to-south and south-to-north. This leads to ten rupture scenarios for each of the five source realizations and a total of fifty unilaterally propagating earthquakes (five source realizations x five rupture locations x two rupture propagation directions) for either magnitude level.

In reversing the rupture directions, the slip distributions are also reversed, while maintaining the right-lateral strike slip nature of the source. The hypocenter is chosen to be at the beginning of each rupture at a depth $\frac{d}{2}$, where d is the seismogenic depth. Rupture initiation time at each sub-fault is computed assuming a circular rupture front. Here, we use the open source package SPECFEM3D (V2.0 SESAME, Kellogg 2011) that is based on the spectral element method (Komatitsch and Tromp 1999; Tromp et al. 2008) to compute three-component waveforms at 636 sites [Fig. 2.14] in Southern California for all 50 scenarios. SPECFEM3D accounts for 3-D variations of seismic wave speeds and density, topography and bathymetry, and attenuation as dictated by the SCEC Community Velocity

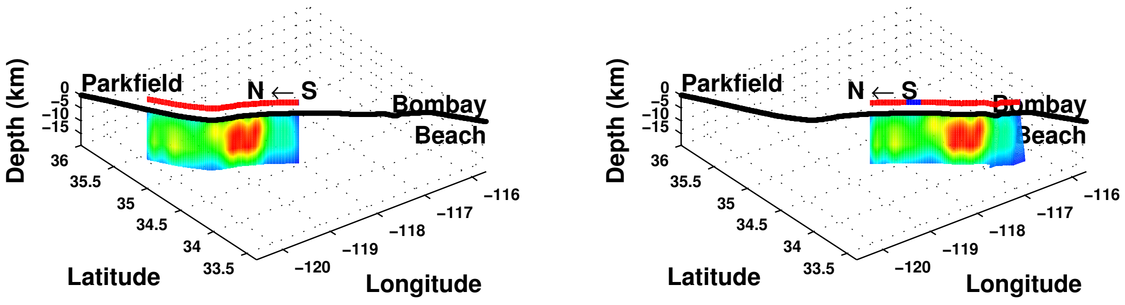

(a) (b)

Figure 2.13: One of five stochastic source realizations (the median model) for the south-to-north rupture of a hypothetical $M_w = 7.9$ earthquake on the southern San Andreas fault. Two possible rupture locations, identified as rupture locations (a) 2 and (b) 4, are shown. Also shown on top of slip (color scale same as in Fig. 2.5(a)) is the rupture speed distribution. Blue indicates rupture propagating at the sub-Rayleigh speed of $0.87V_s$, while red indicates rupture propagating at the super-shear speed of $1.67V_s$. Rupture speed is held constant along fault depth. The model has a constant slip-velocity of 4.15 m/s.

Model (CVM-H 11.9). This model is based on current research, and incorporates tens of thousands of direct velocity measurements that describe the Los Angeles basin and other geologic structures in southern California (Plesch et al. 2011; Suss and Shaw 2003). The model includes background crustal tomography (Hauksson 2000; Lin et al. 2007) enhanced using 3-D adjoint waveform methods (Tape et al. 2009), the Moho surface (Plesch et al. 2011), and a teleseismic upper mantle wave-speed description (Prindle and Tanimoto 2006). Earlier versions of this wave-speed model have been used to reliably model the basin response accurately down to a shortest period of approximately 2 s (Komatitsch et al. 2004; Liu et al. 2004; Quinay et al. 2013). Casarotti et al. (2008) have created a spectral element mesh of the Southern California region, compatible with the wave-speed model using an advanced unstructured mesher, CUBIT, developed by the Sandia National Laboratory, USA (Sandia National Laboratory 2011), and adapted as GeoCUBIT for large-scale geological applications. The simulated waveforms are lowpass-filtered with a corner at 2 seconds [the underlying SCEC CVM-H 11.9 wave-speed model (Plesch et al. 2011) is capable of resolving waves with periods longer than 2s only].

To ensure that the source models generated by the recursive division algorithm are credible, we make qualitative and statistical comparisons of the peak ground velocities (PGV) generated by these models against the peak velocities generated by finite-source inversions of comparable earthquakes with similar magnitudes (also simulated using SPECFEM3D). The finite source inversions selected

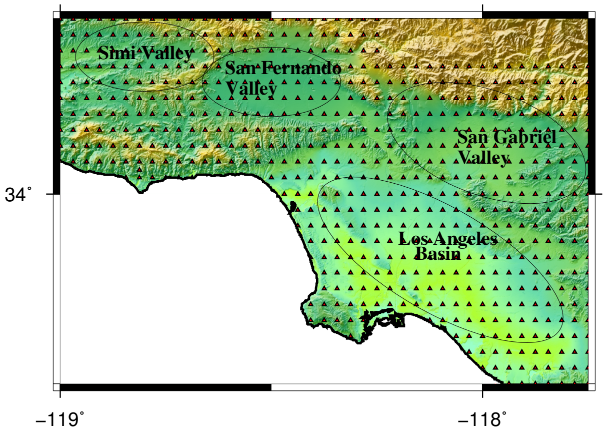

Figure 2.14: The geographical distribution of the 636 southern California sites (shown as triangles) where ground motions are computed. The spacing between the sites is 3.5 km approximately. The ellipses identify the basins in southern California: Simi valley, San Fernando valley, San Gabriel valley and Los Angeles basin.

for this exercise include that of the 2002 $M_w = 7.9$ Denali fault earthquake (Krishnan et al. 2006a, Fig. 2.15) and the 2004 $M_w = 6.0$ Parkfield earthquake (Ji 2004). Whereas the Parkfield earthquake occurred on the San Andreas fault, the last big earthquake (magnitude greater than 7.5) to occur there was the magnitude 7.9 Fort Tejon earthquake in 1857. In the absence of data from a large earthquake on the San Andreas fault, the next best alternative for validation is a big earthquake on a geometrically similar fault such as the Denali fault in Alaska. Fortunately, the 2002 earthquake was reasonably well-recorded and a joint finite-source inversion using teleseismic body and strong-motion waveforms as well as GPS vectors is available (Krishnan et al. 2006a). It has been common practice to simulate ground motions using finite-source inversions and it would be important to compare and contrast ground motions generated by such sources and the stochastic source models from our algorithm. The results of the validation exercise for the $M_w = 7.9$ earthquake are presented here, whereas the results corresponding to the $M_w = 6.0$ earthquake are available in the Appendix A. We select the median source model from the stochastic model set for the validation exercise, considering that most engineering applications are concerned with median (plus/minus one standard deviation) ground motions as opposed to extreme ground motions. However, it should be pointed out that in the absence of greater data from large earthquakes such as the Denali, it is hard to judge whether the ground motions from the Denali event are typical of such events or whether they are on the high or low side. This, unfortunately, is the best we can do presently as far as validation is concerned. The method for selecting the median

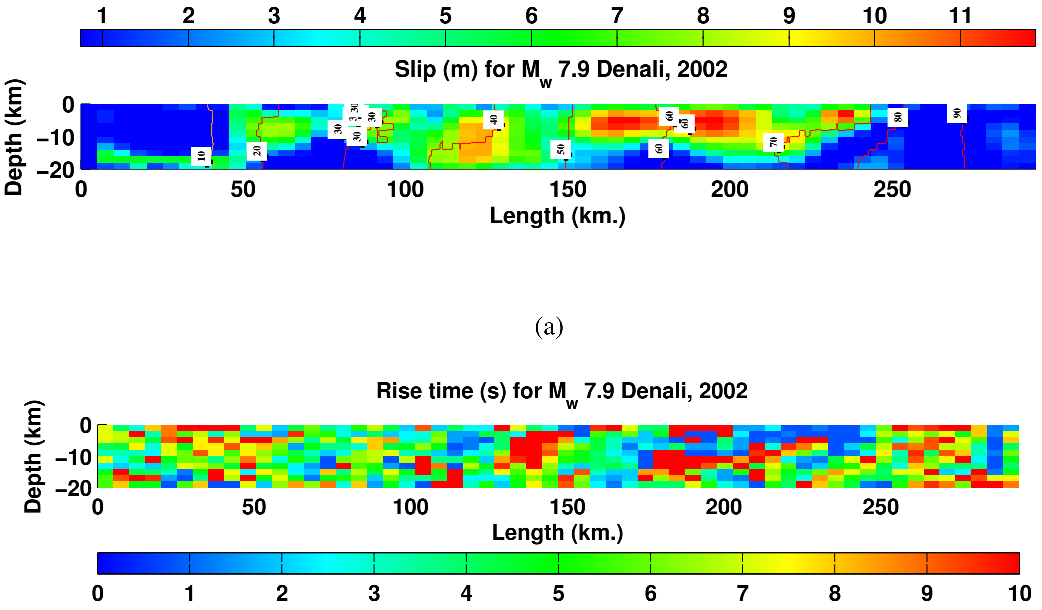

(a)

(b)

Figure 2.15: (a) Slip (m) and (b) Rise-time (s) distributions from a finite source inversion of teleseismic, strong motion, and GPS data from the Mw = 7.9 Denali fault earthquake of 2002 (Krishnan et al. 2006a). Rupture-time (s) contours are overlaid on the slip distribution.

source is as follows:

1. For each of the five stochastic source realizations, we compute the median PGV for the two horizontal components of the synthetic ground motion waveforms at 636 sites from each of the ten rupture scenarios (five rupture locations x two rupture directions).

2. For each of the five stochastic source realizations, we compute the median value of the ten median PGVs for the ten rupture scenarios from (i), separately for the two horizontal components. The solid lines in Fig. 2.16 illustrate this median PGV for each of the five stochastic source realizations for the hypothetical $M_w = 7.9$ San Andreas fault earthquake.

3. To identify the median source model, we compute the median PGV of the ground motions produced at the 636 sites by all fifty scenario earthquakes. The dashed lines in Fig. 2.16 correspond to this median value of PGV for the NS and EW ground motion components for the hypothetical $M_w = 7.9$ San Andreas fault earthquake.

4. Of the five stochastic source realizations, the source whose median PGV (SRSS of EW and

NS PGVs) is closest to the corresponding median PGV produced by all five source realizations [computed in (iii)] is taken to be the median model and the ground motions produced by this model are used in the validation exercise. Note that the rupture speed within the median model varies depending upon the location of rupture, while the distribution of slip and rise-time remain unchanged.

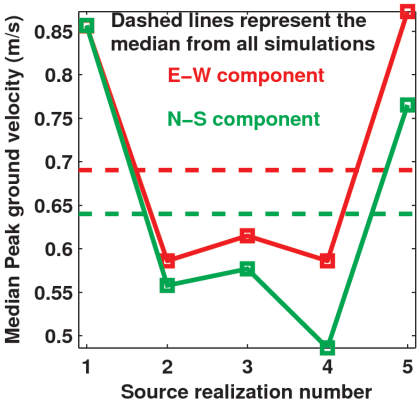

Figure 2.16: Solid lines: Median PGV computed at 636 sites in southern California from ten rupture scenarios (five rupture locations along the southern San Andreas fault x two rupture directions) using each of five stochastic source realizations; Dashed lines: The corresponding median PGV from all fifty scenario earthquakes. All earthquakes are of magnitude $M_w = 7.9$.

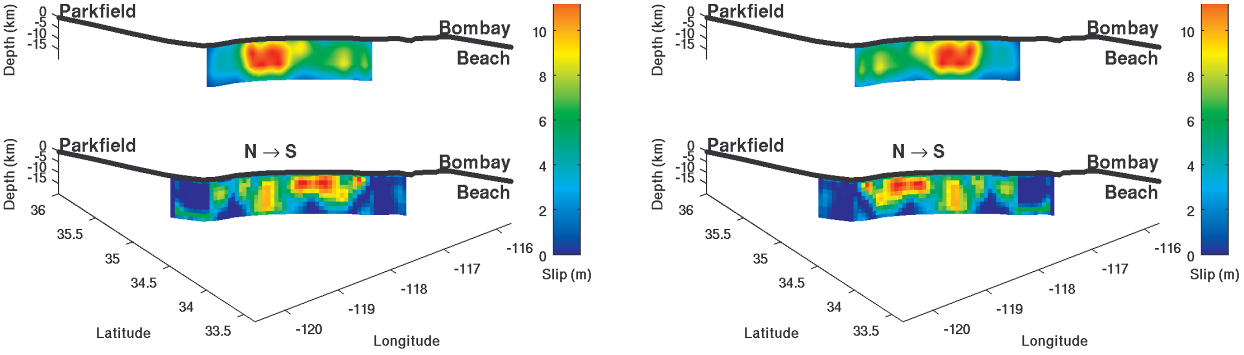

(a)

(b)

Figure 2.17: Comparison of the "median" stochastic source model (top) located at rupture location 3 and the Denali fault earthquake finite-source model (bottom) also located at rupture location 3. Both (a) north-to-south and (b) south-to-north propagating ruptures are shown. Note the differences in the slip asperity locations in the two models.

In order to study qualitative differences between the ground motion generated by the stochastic median model and the Denali finite-source inversion model, we map these models onto the San Andreas fault at rupture location 3, approximately mid-way between Parkfield and Bombay Beach (Fig.

2.17), and directly due north of the Los Angeles basin. Both north-to-south and south-to north rupture propagation directions are simulated. The location of the largest asperity in the stochastic mean model is offset from that of the Denali model by about 100 km. This has a significant influence on the nature of the resulting ground motion. It should be the noted that even though the length of the Denali source is longer (about 290 km.) than the stochastic source (about 210 km), there is a large concentration of sub-faults with zero slip toward the end of the rupture (see Figs. 2.5(f) and 2.15). Slip is predominantly concentrated within a length of about 200 km (between 50-250 km).

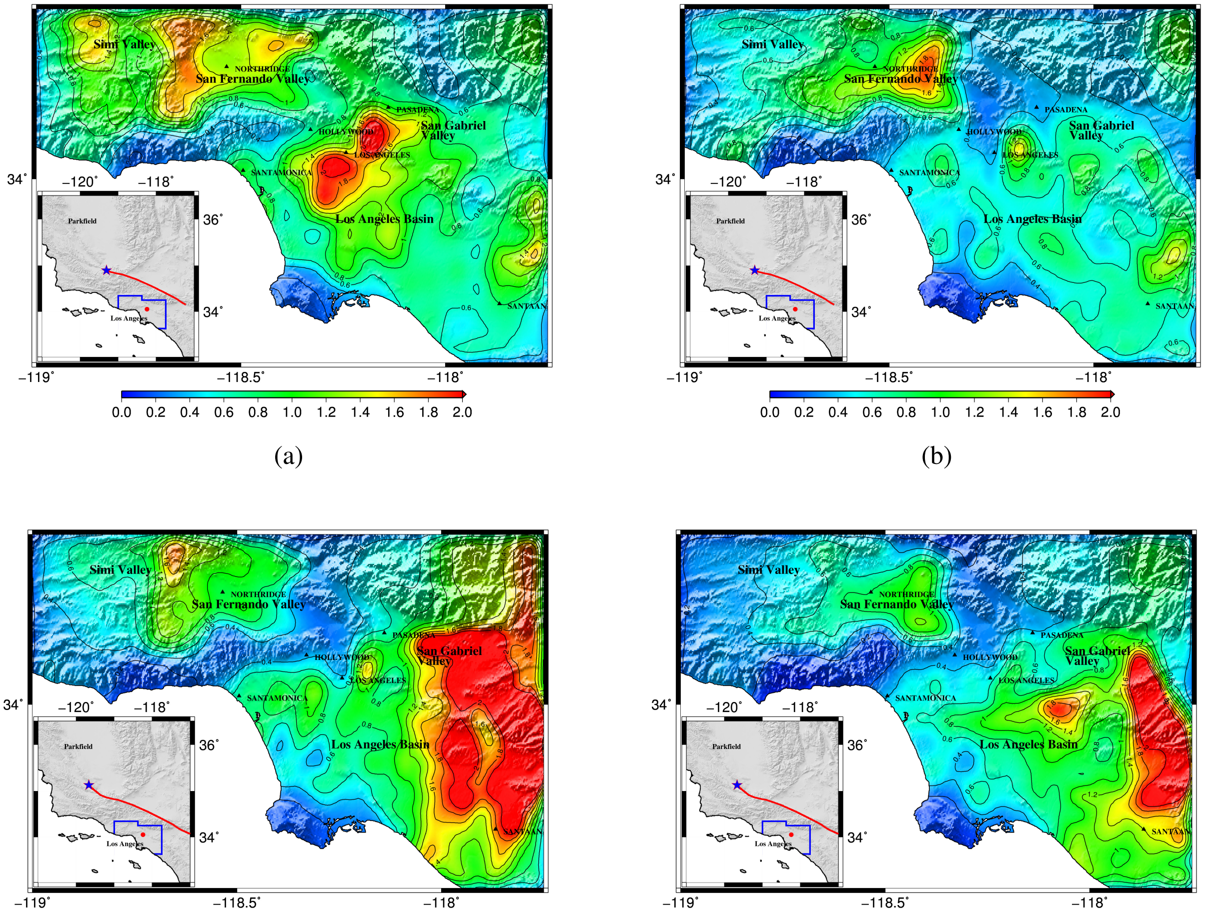
Simi Valley
NORTHRIDGE
San Fernando Valley
PASADENA
HOLLYWOOD
San Gabriel Valley
LOS ANGELES
SANTAMONICA
Los Angeles Basin
SANTAAN
Parkfield
Los Angeles
34°
36°
−120°
−118°
−119°
−118.5°
−118°
0.0
0.2
0.4
0.6
0.8
1.0
1.2
1.4
1.6
1.8
2.0

(a) (b)

(c) (d)

Figure 2.18: EW and NS components of PGV (m/s) from a north-to-south propagating $M_w = 7.9$ rupture at location 3 on the southern San Andreas fault: (a) and (b) Stochastic median source model; (c) and (d) Denali earthquake finite-source inversion model (Krishnan et al. 2006a). The inset shows the fault trace and the hypocenter location.

Shown in Figs. 2.18(a) and 2.18(b) are the PGV of the EW and NS components of ground motion

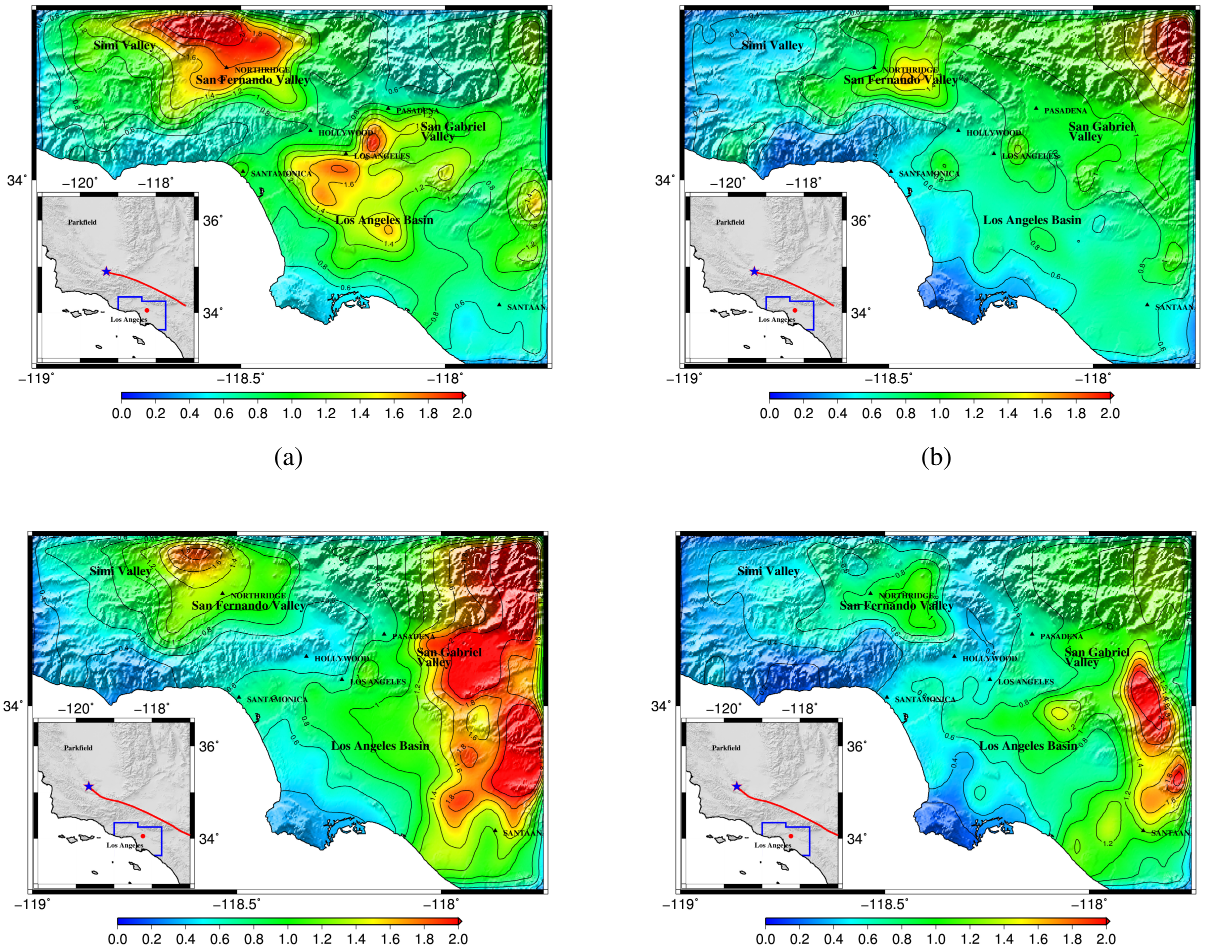
Simi Valley
NORTHRIDGE
San Fernando Valley
PASADENA
San Gabriel Valley
HOLLYWOOD
LOS ANGELES
SANTAMONICA
Los Angeles Basin
SANTAAN
Parkfield
Los Angeles
34˚
36˚
−120˚
−118˚
−119˚
−118.5˚
−118˚
0.0
0.2
0.4
0.6
0.8
1.0
1.2
1.4
1.6
1.8
2.0

(a) (b) (c) (d)

Figure 2.19: EW and NS components of PGD (m) from a north-to-south propagating $M_w = 7.9$ rupture at location 3 on the southern San Andreas fault: (a) and (b) Stochastic median source model; (c) and (d) Denali earthquake finite-source inversion model (Krishnan et al. 2006a). The inset shows the fault trace and hypocenter location.

simulated using the stochastic median model. Figs. 2.18(c) and 2.18(d) show similar maps generated using the Denali source model. The corresponding peak ground displacement (PGD) maps are given in Figure 2.19. The peak motions produced by the stochastic median model are far more intense in the Los Angeles (LA) basin than in the San Gabriel valley which is located east of the LA basin. The reverse is true for the motions generated by the Denali source model. This is directly attributable to the location of the largest asperity in the two models. In the north-to-south rupture, the largest slip asperity in the stochastic median model occurs to the west of the midpoint of the source, whereas the same occurs to the east of the midpoint in the Denali source. Thus, ground motions from the Denali model are stronger in the east, whereas ground motions from the stochastic model are stronger in the mid-section of the greater Los Angeles region. The PGD maps are strongly correlated with the PGV maps in both cases.

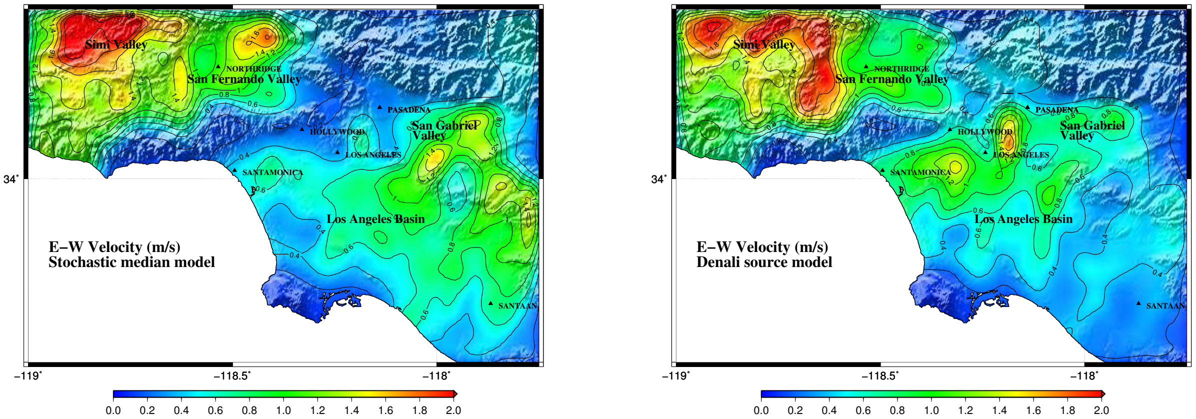
Simi Valley
NORTHRIDGE
San Fernando Valley
PASADENA
San Gabriel Valley
HOLLYWOOD
LOS ANGELES
SANTAMONICA
Los Angeles Basin
SANTAAN
34˚
E–W Velocity (m/s)
Stochastic median model
Denali source model
–119˚
–118.5˚
–118˚
0.0
0.2
0.4
0.6
0.8
1.0
1.2
1.4
1.6
1.8
2.0

(a) Median model (b) Denali model

Figure 2.20: EW component of PGV (m/s) from a south-to-north propagating $M_w = 7.9$ rupture at location 3 on the southern San Andreas fault: (a) Stochastic median source model; (b) Denali earthquake finite-source inversion model (Krishnan et al. 2006a).

In the case of a rupture propagating south-to-north, the large asperity in the Denali model is further northwest compared to the asperity in the stochastic median model. As a result, ground motions from the Denali model are more intense in the LA basin and less intense in the San Gabriel valley, while the reverse is true for the ground motions from the stochastic median model (Fig. 2.20).

In general, peak ground motion distribution from the stochastic median and Denali source models located at various sections along the southern San Andreas fault seems to be dictated strongly by the relative location of the slip asperities. The location of these asperities along the fault are further dictated by rupture directivity for the given source model. For north-to-south propagating ruptures, the location of intense ground motions moves gradually from Simi valley to San Fernando valley, on to Los Angeles basin, and finally to San Gabriel valley as the hypocenter location is progressively changed from Parkfield towards Bombay Beach. Intense ground motions from the Denali model occur further southeast compared to that from the stochastic median model, consistent with the fact that the largest slip asperity in the former model is further southeast. These observations are reversed for south-to-north propagating ruptures, i.e., the location of intense ground motion moves gradually from the San Gabriel valley to the LA basin, on to the San Fernando valley, and finally to the Simi valley; and strong ground motion from the Denali model occurs further northwest when compared to that generated by the stochastic median model.

In addition to asperity location, another factor leading to differences in the ground motions from the Denali source model and the stochastic median source model is the assumed correlation between rise-time and slip in the stochastic model and the lack of the same in the Denali model, even though the maximum rise-time for both models is approximately 6 s. The effect of this correlation can be estimated by comparing the ground motions from the Denali model against that from a "modified Denali" model. In this modified model, the rise-times from the original Denali model are made proportional to the slip using the stochastic source generation algorithm. All other parameters remain the same as the original model. Figs. 2.21(a) and 2.21(b) show the difference in the PGV (EW component) generated by these two source models [PGV (modified Denali) - PGV (Denali)] for north-to-south ruptures at rupture locations 1 and 3, respectively. While, the differences are not significant in most of the region, clearly, there are a few locations where significant differences are seen.

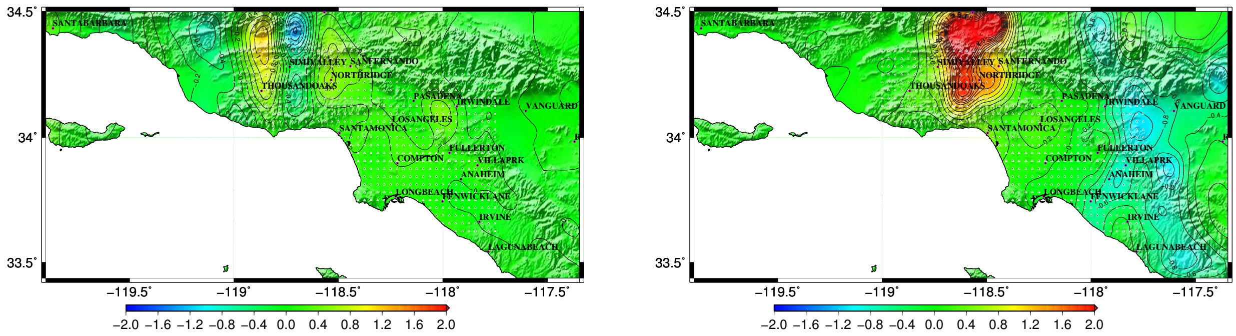
34.5˚
34˚
33.5˚
SANTABARBARA
SIMIVALLEY
SANFERNANDO
NORTHRIDGE
THOUSANDOAKS
PASADENA
IRWINDALE
VANGUARD
LOSANGELES
SANTAMONICA
FULLERTON
COMPTON
VILLAPRK
ANAHEIM
LONGBEACH
TENWICKLANE
IRVINE
LAGUNABEACH
−119.5˚
−119˚
−118.5˚
−118˚
−117.5˚
−2.0 −1.6 −1.2 −0.8 −0.4 0.0 0.4 0.8 1.2 1.6 2.0

(a) Rupture Location - 1

(b) Rupture Location - 3

Figure 2.21: (a) and (b) Difference in the PGV (EW component) generated by the Denali source model and the modified Denali model [PGV (modified Denali) - PGV (Denali)] for north-to-south ruptures at rupture locations 1 and 3,respectively. The modified Denali model is obtained by making the rise-times from the original Denali model proportional to the slip using the stochastic source generation algorithm.

Despite the differences in the modeling of source parameters, the overall intensities of ground motion from the stochastic median model are not vastly different from that produced by the Denali finite-source inversion model. This can be seen in the statistical comparisons shown in Figs. 2.22 and 2.23. Fig. 2.22 includes the histograms (and PDFs) of PGV for each of the five north-to-south rupture scenarios (at locations 1 through 5). The histograms and the best-fitting log-normal PDFs for the PGVs from the stochastic median model are quite similar to those for the PGVs from the Denali finite-source inversion model. Fig. 2.23 includes the same, but for the five south-to-north rupture scenarios. Once again, there is reasonably good agreement between the two lending credibility to the source generation algorithm. It is interesting to note that the south-to-north ruptures produce less intense ground motions for all rupture scenarios using the Denali source and the stochastic median model alike when compared to the north-to-south ruptures. The comparison of attenuation of ground motion (median peak average horizontal velocity) with distance from source is shown in Fig. 2.24. Furthermore, the attenuation of ground motion for both the basin and non-basin sites are illustrated in Fig. 2.25. Once again the agreement between the attenuation of ground motion produced by the stochastic source and the Denali finite-source inversion models is quite good. The median values are computed by collating data in 2 km wide bins. Source-to-site distance is taken to be the shortest distance from the site to any point on the rupture extent. The lack of data beyond 100 km in the case of the Denali source is because of the fact that the Denali source is about 80 km longer than the stochastic sources.

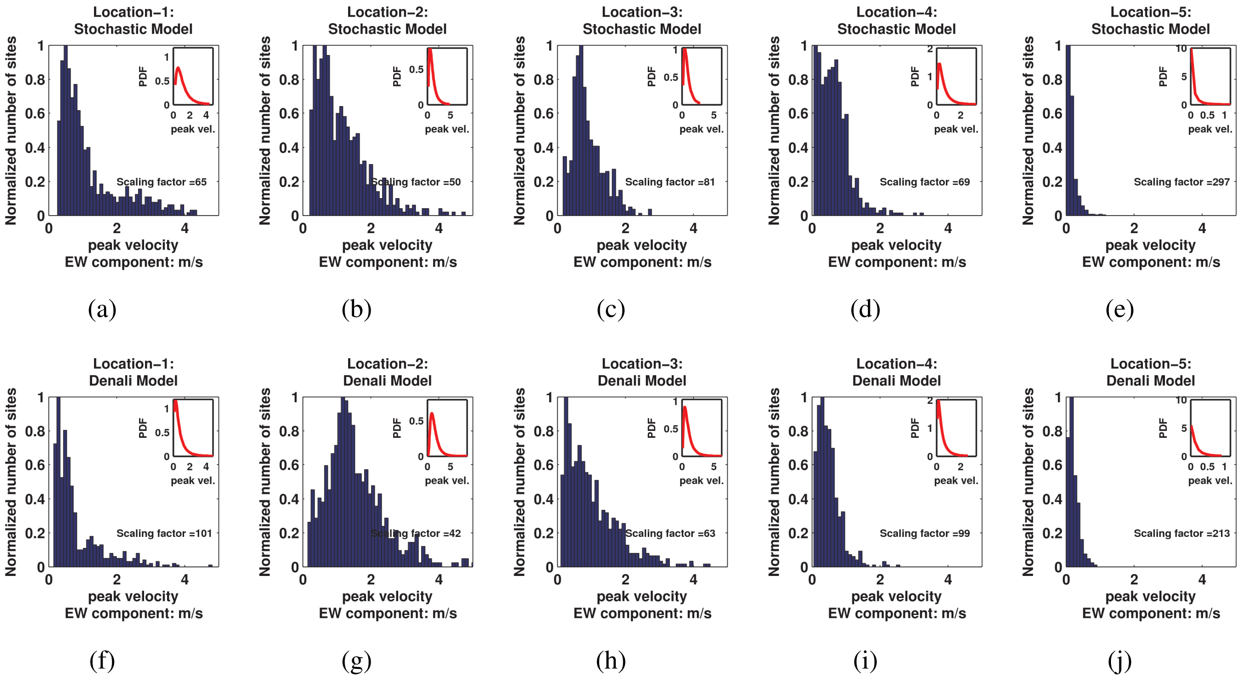

(a) (b) (c) (d) (e)

(f) (g) (h) (i) (j)

Figure 2.22: Five $M_w = 7.9$ north-to-south rupture scenarios (at locations 1–5) on the San Andreas fault using [(a)–(e)] the stochastic median model and [(f)–(j)] the Denali finite-source inversion model: Histograms and best-fit log-normal PDFs (insets) of PGV at 636 sites in southern California. The product of the listed scaling factor and the normalized histogram ordinate at a specific peak velocity gives the total number of sites for that velocity.

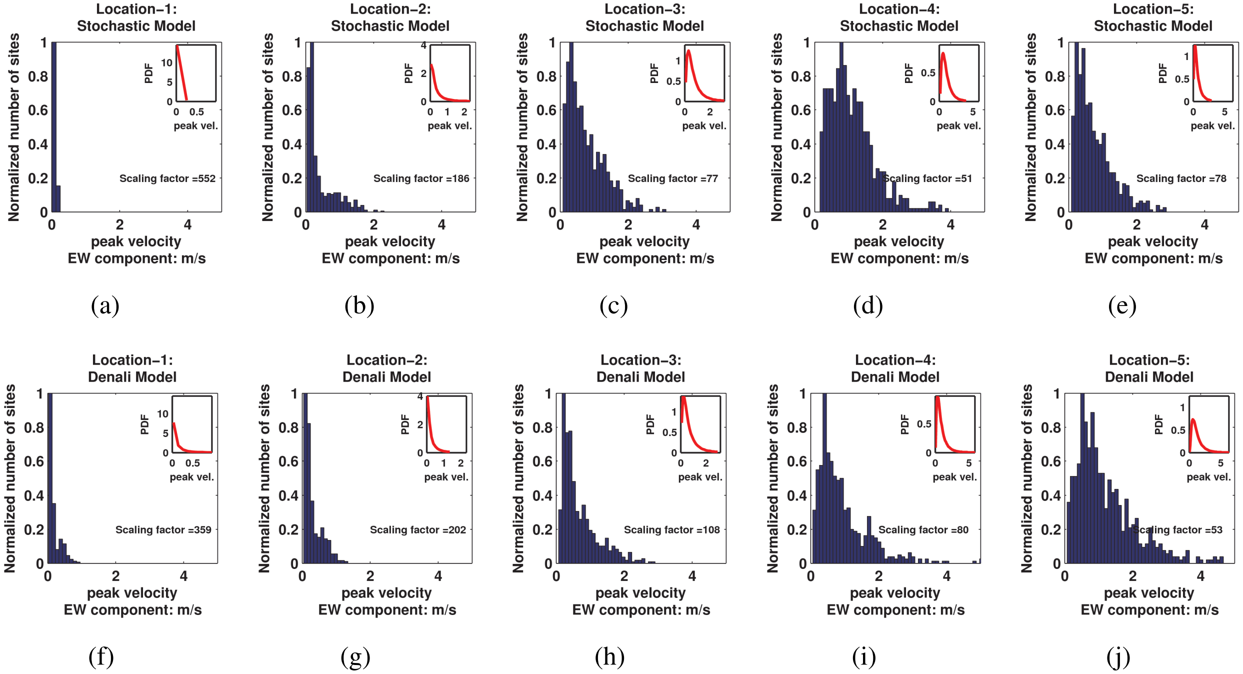

Figure 2.23: Five $M_w = 7.9$ south-to-north rupture scenarios (at locations 1–5) on the San Andreas fault using [(a)–(e)] the stochastic median model and [(f)–(j)] the Denali finite-source inversion model: Histograms and best-fit log-normal PDFs (insets) of PGV at 636 sites in southern California. The product of the listed scaling factor and the normalized histogram ordinate at a specific peak velocity gives the total number of sites for that velocity.

Ground motion prediction equations (GMPEs), developed on the basis of data collected from global earthquakes, have been used extensively in engineering applications including the design of buildings. It would be useful to understand how the ground motions generated by the median stochastic source model compare against the median motions predicted by GMPEs. Olsen and Mayhew (2010) have outlined a wide array of goodness of fit metrics for use in broadband ground motion simulation validation (Baker et al. 2014). Of these, peak ground velocity (PGV), peak ground displacement (PGD), and spectral acceleration (S_a) at 3s are the most relevant metrics for the comparison of long-period motions, the primary focus of this study. Shown in Fig. 2.26 are the median peak horizontal velocity and displacement (and median plus/minus one standard deviation) as a function of distance from source simulated at sites in the greater Los Angeles region that are within 100 km of the median stochastic source model ($M_w 7.9$) for the ten rupture scenarios described previously (rupture locations 1 through 5, and rupture directions north-to-south and south-to-north). The median values are computed by collating data in 2 km wide bins. Also shown for comparison is the corresponding ground motion prediction by the Campbell-Bozorgnia Next Generation Attenuation (NGA) relation (Campbell and Bozorgnia 2008). V_s^{30} (the average shear-wave velocity between 0 and 30 m depth) and basin depth for these stations (Fig. 2.27) are

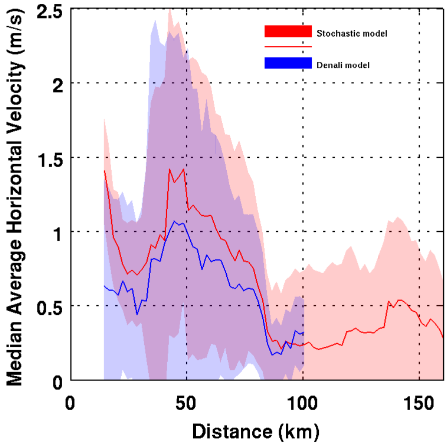

Figure 2.24: Median peak average horizontal velocity (m/s) [(red) Stochastic and (blue) Denali model] as a function of source-to-site distance, in southern California due to $M_w 7.90$ earthquake occurring along southern San Andreas fault. The shaded region corresponds to median plus/minus one standard deviation. A total of 10 rupture scenarios (5 rupture locations x 2 propagation directivity) are considered

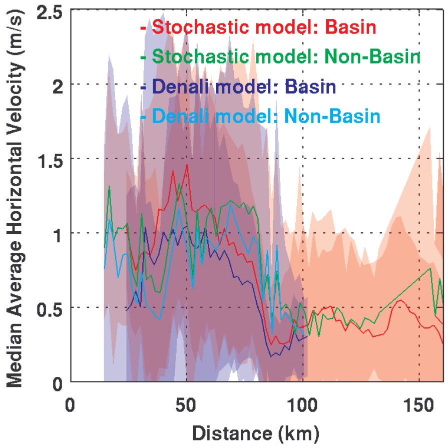

Figure 2.25: Median peak average horizontal velocity (m/s) [(red, green) Stochastic and (violet, blue) Denali model] as a function of source-to-site distance for basin and non-basin sites, in southern California due to $M_w 7.90$ earthquake occurring along southern San Andreas fault. The shaded region corresponds to median plus/minus one standard deviation. A total of 10 rupture scenarios (5 rupture locations x 2 propagation directivity) are considered

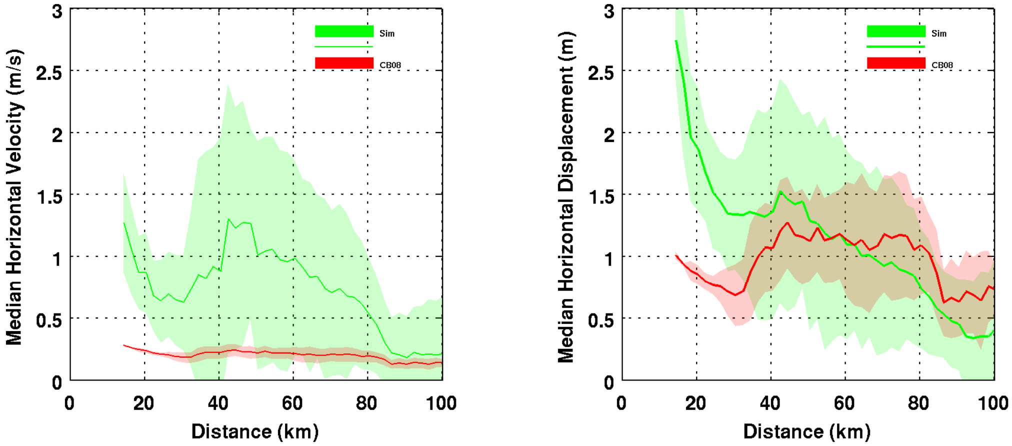

(a) (b)

Figure 2.26: (a) Median peak horizontal velocity (m/s) and (b) median peak horizontal displacement (m) as a function of source-to-site distance for ten $M_w 7.90$ earthquake scenarios on the southern San Andreas fault (five rupture locations and two rupture directions) using the median stochastic source model. Shown in red are the predictions by the Campbell-Bozorgnia NGA relation. The shaded region corresponds to median plus/minus one standard deviation.

taken from Wald and Allen (2007) and the SCEC Community Velocity Model - Harvard (Plesch et al. 2011), respectively. In addition to the source and path effects, the other important factors that dictate

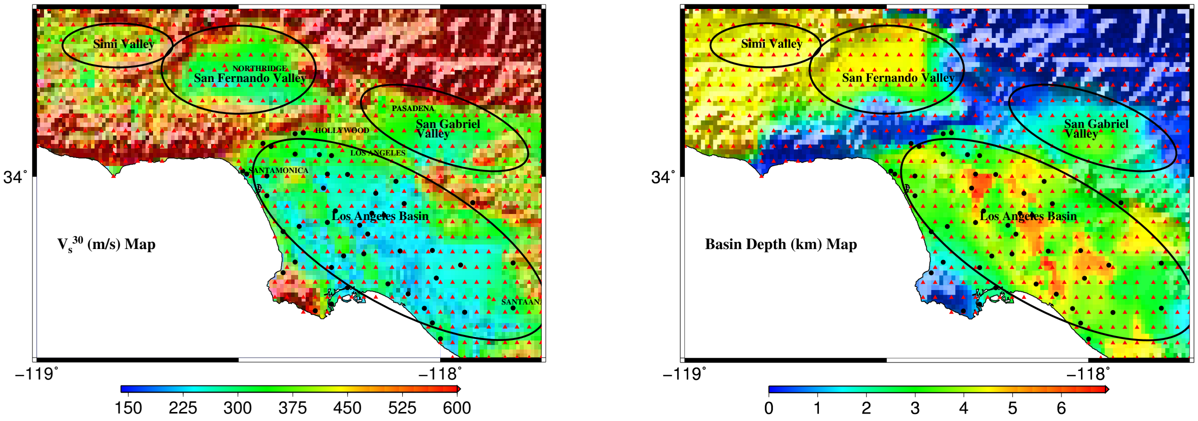
Simi Valley
NORTHRIDGE
San Fernando Valley
PASADENA
San Gabriel Valley
HOLLYWOOD
LOS ANGELES
SANTAMONICA
Los Angeles Basin
SANTAAN
34°
V_s^{30} (m/s) Map
–119°
–118°
150
225
300
375
450
525
600
Simi Valley
San Fernando Valley
San Gabriel Valley
Los Angeles Basin
34°
Basin Depth (km) Map
–119°
–118°
0
1
2
3
4
5
6

(a)

(b)

Figure 2.27: (a) V_s^{30} (m/s) and (b) basin depth (km) maps for southern California. Black circles correspond to 48 stations at which PGV and PGD values are computed using Campbell-Bozorgnia attenuation relation for comparison against simulation predictions. Red triangles indicate the geographical distribution of the 636 southern California sites where stochastic ground motions are computed. The ellipses identify the basins in southern California: Simi valley, San Fernando valley, San Gabriel valley and Los Angeles basin.

ground motion intensities are the basin depth and shear-wave velocities in the top-soil or geotechnical layer (V_S^{30}). In general, greater basin depths and/or lower V_S^{30} values lead to stronger ground motion. For the five rupture locations considered here, basin sites are located at distances no smaller than 40 km. This leads to significant amplification in the simulations at distances greater than 40 km. The NGA relations also show the amplification due to the presence of basins. The peak displacements in the basins predicted by the simulations match quite well with the GMPE predictions. However, the same cannot be said of the peak ground velocities or spectral accelerations at 3s (Fig. 2.28). Median PGVs in the basins from the simulations are three to six times of that predicted by the Campbell-Bozorgnia NGA relation. The same holds true for S_a^{3s} as well. It is possible that the bimodal rupture speed in our source model combined with the coherence in the source parameters (constant slip rate) may be causing stronger directivity effects. However, the good agreement in the NGA and simulation predictions for PGD seems to indicate otherwise.

There has been a concerted effort at the Southern California Earthquake Center toward the simulation of broadband ground motion. Recent large scenario earthquake simulations on the southern San Andreas fault include Terashake (e.g., Olsen et al. 2008; Ely et al. 2010), ShakeOut (e.g., Bielak et al. 2010; Graves et al. 2011) and M8 (e.g., Cui et al. 2010). All these simulations were carried

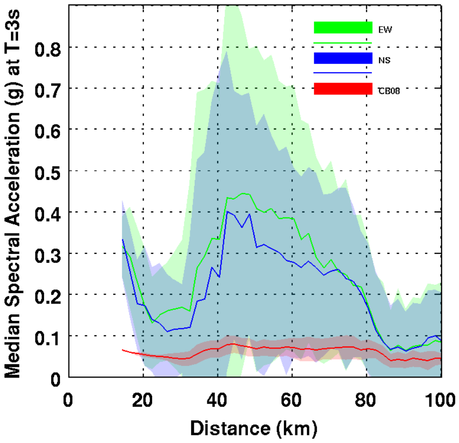

Figure 2.28: Spectral acceleration (g) at $T = 3\ s$ as a function of source-to-site distance for ten $M_w 7.90$ earthquake scenarios on the southern San Andreas fault (five rupture locations and two rupture directions). Shown in green and blue are the simulated east-west and the north-south S_a^{3s} components at greater Los Angeles sites using the median stochastic source model, respectively. Shown in red are the predictions by the Campbell-Bozorgnia NGA relation. The shaded region corresponds to median plus/minus one standard deviation.

out using the SCEC-CVM (Kohler et al. 2003) seismic wave-speed model whereas the simulations in this study have been carried out using the SCEC-CVMH model. So it may not be possible to make a secular comparison. It is nonetheless useful to understand the variability in the ground motions resulting from the combined effect of different source models and wave-speed models. Here, we compare the $M_w 7.8$ ShakeOut scenario earthquake ground motions against the ground motions produced by the median stochastic source model, described earlier in the section, with epicenter at Bombay Beach and propagating north. The ShakeOut earthquake slip model is shown in Fig. 2.29. The peak slip (∼15 m) and the peak slip rate (∼4.8 m/s) are similar to that of the median source model (11.9 m and 4.15 m/s, respectively). The two horizontal components of the peak ground velocity from the two source models are shown in Fig. 2.30 . The ranges of PGVs observed in the greater Los Angeles region from the two sources is quite similar. The differences in the extent and location of "hot-spots" can be attributed to the differences in the underlying wave-speed models used for the two simulations, the location, size, and intensity of the primary slip asperity, and the differences in the rupture speed distribution. The stochastic source has a bimodal rupture speed distribution (0.87V_S or 1.67V_S) whereas the ShakeOut source has a peak rupture speed of 1.4V_S at the location of maximum slip, a rupture speed of 0.85V_S at locations of average slip, and a rupture speed of 0.2V_S at locations with zero slip.

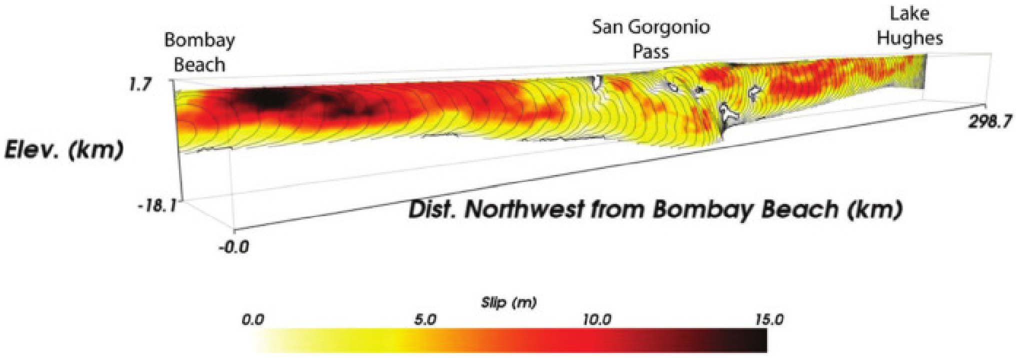

Figure 2.29: Slip (m) distribution and rupture time contours (1s intervals) for a $M_w 7.8$ earthquake of the ShakeOut earthquake source (Graves et al. 2011). The peak slip-rate for this source is 4.38 m/s.

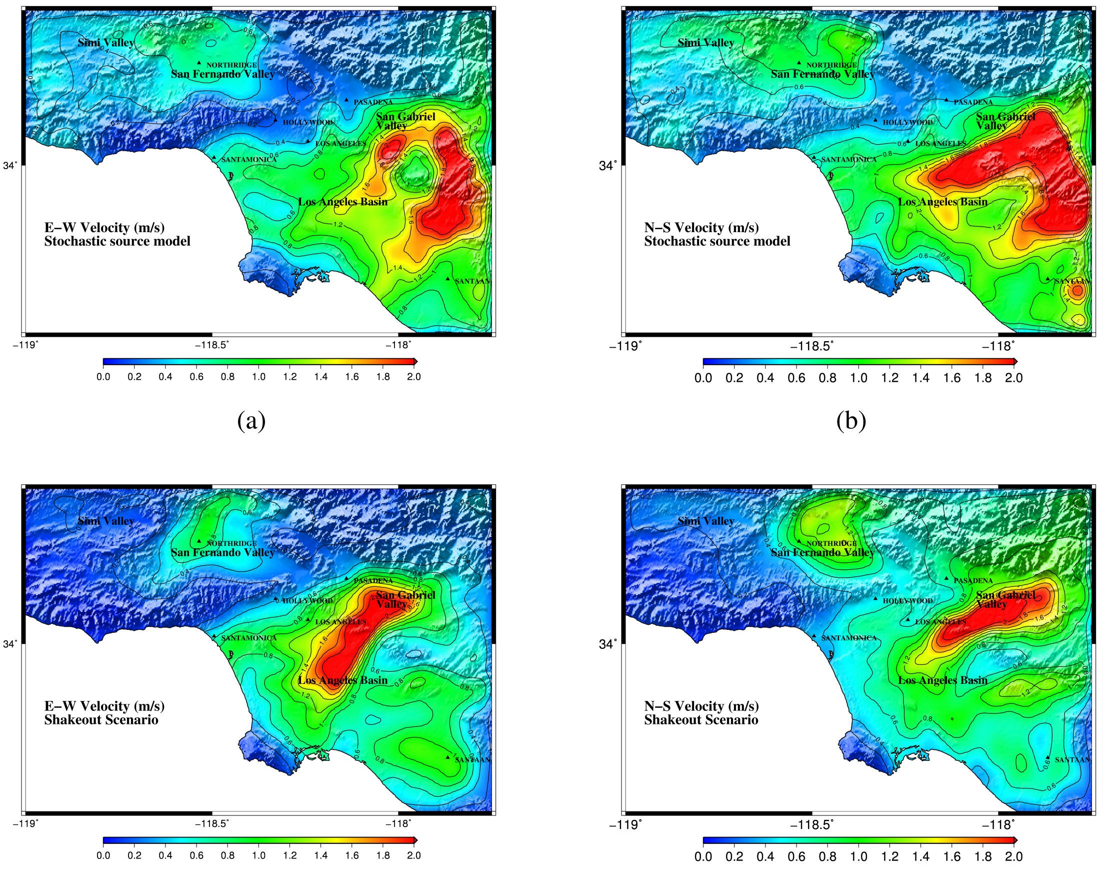
Simi Valley
NORTHRIDGE
San Fernando Valley
PASADENA
HOLLYWOOD
LOS ANGELES
San Gabriel Valley
SANTAMONICA
Los Angeles Basin
SANTAANA
34°
–119°
–118.5°
–118°
0.0
0.2
0.4
0.6
0.8
1.0
1.2
1.4
1.6
1.8
2.0
E–W Velocity (m/s)
Stochastic source model
N–S Velocity (m/s)
Stochastic source model
E–W Velocity (m/s)
Shakeout Scenario
N–S Velocity (m/s)
Shakeout Scenario

(a) (b)

(c) (d)

Figure 2.30: (a) East-West and (b) North-South component of peak ground velocity (m/s) simulated using the median stochastic source model with epicenter at Bombay Beach. (c) and (d) The corresponding PGV maps for the ShakeOut scenario.

2.3 Sensitivity of Ground Motions in the Los Angeles Basin to Source Parameters of Large Ruptures on the San Andreas Fault

To understand the sensitivity of ground motions in the LA basin to the source parameters of large ruptures on the San Andreas fault, the recursive division algorithm is applied to generate 50 stochastic seismic source models of an $M_w = 7.9$ earthquake. All ruptures are assumed to initiate at Parkfield and propagate south toward Wrightwood, similar to the Fort Tejon earthquake of 1857, the last big earthquake on the southern San Andreas fault. Source parameters of interest include the percentage of asperity area relative to the fault area (an asperity in our model is defined as a minimum of two continuous subfaults where the magnitude of slip in each subfault is greater than or equal to the mean slip), maximum rise-time in the source model, and the percentage of the rupture propagating at sub-Rayleigh speeds (alternately percentage of the rupture propagating at super-shear speeds). For each scenario earthquake, the peak horizontal ground velocity is calculated at each of the 211 sites in the Los Angeles basin [Fig. 2.14] as the maximum of the square root of the sum of the squares of the N-S and E-W ground velocity histories. The median of this set of peak ground velocities is used for the sensitivity analysis.

Fig. 2.31 shows scatter-plots of the median PGV as a function of the percentage of asperity area, the maximum rise-time, and the percentage of the rupture propagating at sub-Rayleigh speeds. Also shown are the histograms for each of these quantities. The following observations can be made: (i) there is a relatively low correlation (correlation coefficient = -0.30) between median PGV and percentage of asperity area. Reader should note here that a seismic source model with a single large asperity might have the same percentage of asperity area as one with several smaller asperities; however, the resulting ground motions from the two models may be significantly different. (ii) A moderate correlation (correlation coefficient = -0.57) can be observed between the median PGV and the maximum rise-time in the source model, with median PGV gradually declining with increasing values of maximum rise time. (iii) An unexpected finding, however, is that the median PGV in the LA basin is generally larger when a greater proportion of the rupture propagates at sub-Rayleigh speeds and smaller when a greater proportion of the rupture propagates at super-shear speeds. Incidentally, Aagaard and Heaton (2004) too reported a similar observation in their near-source ground motion sim-

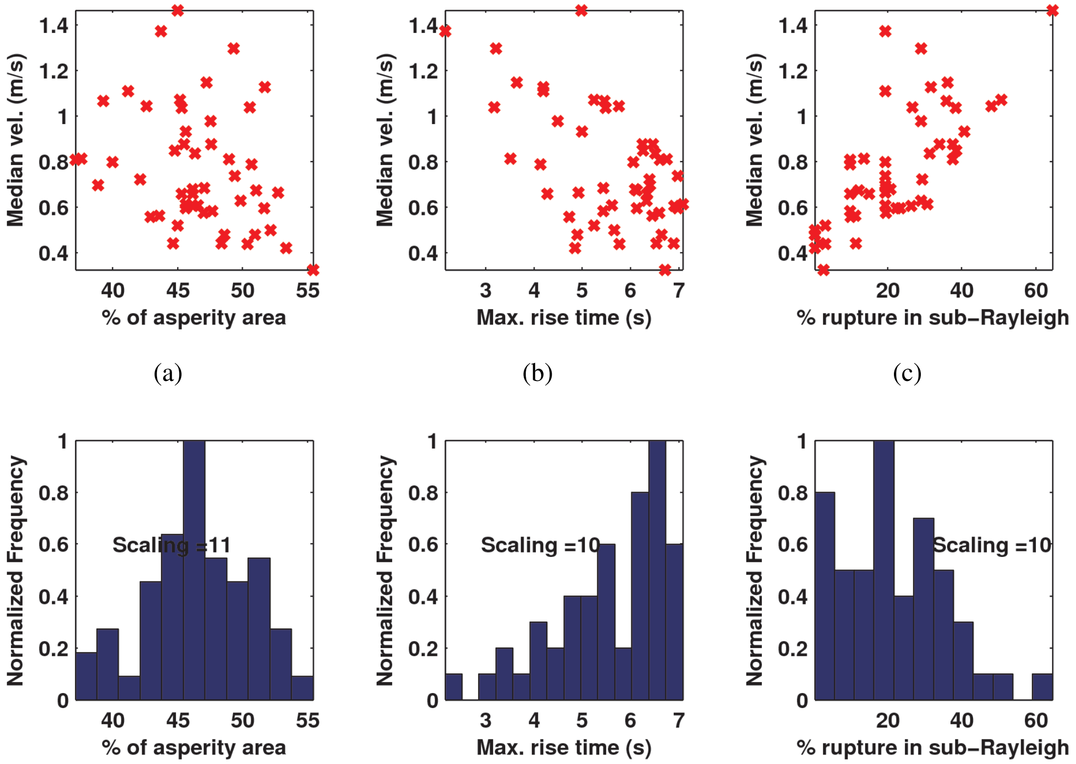

(a) (b) (c)

(d) (e) (f)

Figure 2.31: Results from simulating fifty $M_w = 7.9$ north-to-south rupture scenarios on the San Andreas fault (similar to the 1857 Fort Tejon earthquake) using stochastic seismic source models. [(a)–(c)] show the scatter-plots of the median PGV in Los Angeles basin as a function of the percentage of asperity area relative to the fault area, the maximum rise-time, and the percentage rupture propagating at sub-Rayleigh speeds. [(d)–(f)] show the corresponding histograms for the fifty scenarios. The product of the listed scaling factor and the normalized histogram ordinate gives the parameter frequency.

ulation. A high correlation coefficient of 0.74 is observed between median PGV and percentage of rupture propagating at sub-Rayleigh speed. Additional ground motion maps for ruptures traveling in either pure super-shear or sub-Rayleigh regime for stochastic and finite-source inversion models are shown in Appendix B. (iv) The mean of the median PGV at the 211 Los Angeles basin sites from all fifty 1857 Fort Tejon-like stochastic sources of $M_w = 7.9$ is 0.77 m/s and the standard deviation is 0.26 m/s. In comparison, the corresponding mean and standard deviation of the PGV predicted by the Campbell-Bozorgnia (2008) NGA relation are 0.16 m/s and 0.03 m/s, respectively. (v) The mean of the median PGD at the 211 southern California sites in the Los Angeles basin from all 50 stochastic sources of $M_w = 7.9$ is 1.09 m and the standard deviation is 0.40 m. The corresponding mean and standard deviation of the PGD predicted by the Campbell-Bozorgnia NGA relation are 0.94 m and 0.29 m, respectively.

It is clear that while the mean and standard deviation of the PGD predicted by the attenuation relationship is in close agreement with that predicted by the simulations, the same cannot be said about PGV. It is important that this disagreement between NGA relations and the simulations is reconciled as building codes utilize the NGA relations to characterize seismic hazard for the design of buildings. This is especially critical for tall buildings as their response is quite sensitive to PGV (Krishnan and Muto 2013).

To ensure that findings (ii) and (iii) are not limited to ground motions from earthquakes occurring at Location 1 alone and hold more broadly, we plot the median PGV in the east-west and north-south directions at all sites in the greater Los Angeles area (not just LA basin sites) from the fifty earthquakes described in the last section as a function of rise-time (Fig. 2.32), and percentage of the rupture propagating at the sub-Rayleigh speed of $0.87V_s$ (Fig. 2.33). It is quite clear that the greater the percentage of rupture propagating at sub-rayleigh speeds, the stronger are the ground motions. PGV drops marginally with increasing rise-time, although this anti-correlation is weaker than the correlation with respect to rupture speed. Findings (ii) and (iii) thus appear to hold true for all rupture locations and all southern California sites (when considered collectively). However, we are not sure whether the number of source models used in the sensitivity study are enough to capture the variability of sources on a fault such as the San Andreas. Further studies are needed to quantify the sample size necessary to ensure statistical significance.

2.4 Discussion

The recursive division algorithm outlined here can be implemented for any strike-slip fault in the world given good estimates of principal stress orientations. Principal stress orientation data is currently available for most major fault systems in the world (http://dc-app3-14.gfz-potsdam.de), although the quality of the data may not be uniformly good. In the absence of such data an assumption would have to be made on the rupture speed in order for this algorithm to be used (e.g., a constant rupture speed of, say, $0.8V_s$, across the fault). In making this assumption, the finding that the greater the

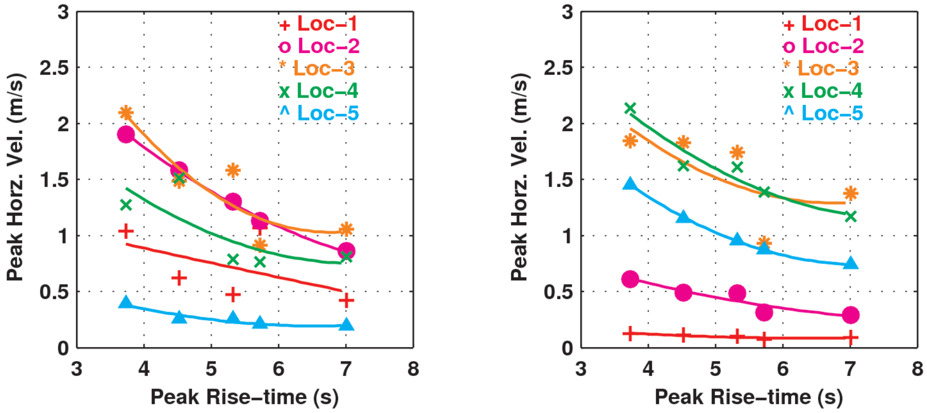

(a) (b)

Figure 2.32: Median horizontal peak ground velocity (m/s) in southern California from a total of fifty $M_w7.90$ earthquakes on the southern San Andreas fault (5 source realizations x 5 rupture locations x 2 propagation directions) as a function of the rise-time (s) for (a) north-to-south and (b) south-to-north propagating rupture.

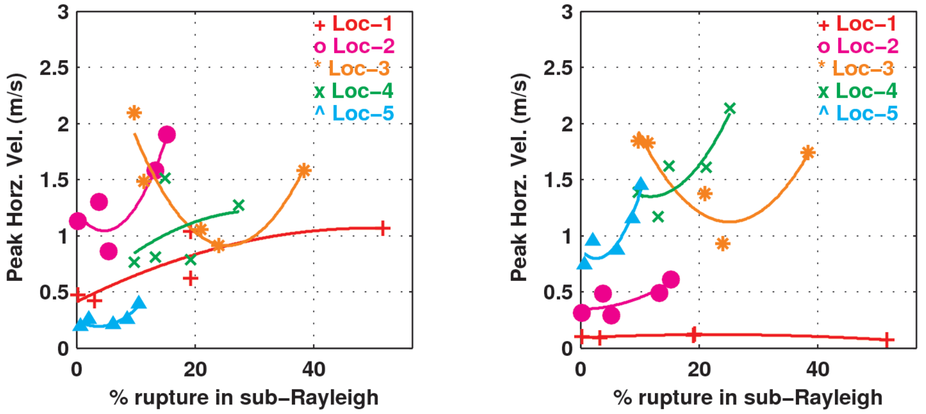

(a) (b)

Figure 2.33: Median horizontal peak ground velocity (m/s) in southern California from a total of fifty $M_w7.90$ earthquakes on the southern San Andreas fault (5 source realizations x 5 rupture locations x 2 propagation directions) as a function of the percentage of rupture propagating at the sub-Rayleigh speed of $0.87V_s$ for (a) north-to-south and (b) south-to-north propagating rupture.

percentage of the rupture propagating at sub-Rayleigh speeds the stronger is the resulting ground motion must be considered. The presented algorithm augments known aspects of seismic sources from finite-source inversions with observations from laboratory earthquakes to model kinematic parameters of strike-slip sources, thus incorporating physics of the rupture process as we best know it. There are three distinguishing features of the recursive division algorithm that sets it apart from other existing methodologies:

1. Deviating from the common approach of defining a 2-D power spectral density (PSD) function that usually decays with increasing wave number and inverting it back into the spatial domain to generate the slip distribution, the recursive division algorithm generates stochastic slip distributions in the spatial domain. A subsequent check is made to ensure that the slip power spectrum decays as a function of the wave number in accordance with a power law whose exponent is between 2 and 4, the range of values observed in finite-source inversions of past earthquakes. Allowing such a range for this exponent rather than imposing a fixed value (as is done in existing methods) would likely produce a more diverse set of seismic source models, more closely emulating the broad spectrum of seismic sources inferred from earthquake data. In addition, this approach would produce distinct power spectra of slip along the length and the depth of the fault. One questionable feature of our algorithm is that it prescribes smoothly varying slip across kinks and bends of non-planar faults. The effects of this feature of the resulting stochastic source models need to be studied in the future.

2. Based on the observation in laboratory earthquakes that rupture speed is dependent upon initial stress conditions on the fault, the recursive division algorithm uses initial stress to judge whether rupture proceeds at sub-Rayleigh speeds or at super-shear speeds. Rather than assigning a constant average rupture propagation speed, the algorithm assigns sub-Rayleigh and super-shear propagation speeds of $0.87V_S$ and $1.67V_S$, respectively, as observed in the laboratory. Thus, the resulting kinematic source models are physics-based and more realistic. Some existing models do specify a varying slip-proportional rupture speed. However, dynamic rupture simulations have not conclusively shown this to be true.

   It should be mentioned that calculating the initial stress on the fault is a non-trivial problem, especially in the face of limited data. The key assumption that goes into the determination of the normal and shear stresses using the principal stress orientations along the fault is that the fault is in a critical state and that the pore pressure in the crust surrounding the fault is hydrostatic. This assumption is based on in-situ measurements, core samples, and inferences from seismicity. Given that the measurements are made at shallow depths of the earth's crust, it is an open question whether this assumption holds true over the entire seismogenic depth of the fault. Nevertheless, in the absence of evidence to the contrary, it is assumed that the stress across the depth of the fault is uniform. This results in rupture speeds that are variable along fault length, but constant along fault depth.

3. Both laboratory earthquakes and dynamic rupture simulations indicate that there exists a correlation between slip and rise-time. Empirical relations characterizing this correlation determined from dynamic rupture simulations can be quite sensitive to the choice of parameters used in the simulations. Accordingly, slip-to-rise-time ratios from the laboratory earthquakes are directly used to characterize the rise-times (and hence slip velocity) in the recursive division algorithm. The slip-to-rise-time ratio (i.e., slip velocity) is assumed to be constant for a given stochastic source realization. The maximum rise-time observed in finite-source inversions of past earthquakes is used to constrain rise-times in the algorithm as well.

   The extension and applicability of laboratory observations to the real earth is still an open question. The issue of scaling is far from resolved. We must reiterate, however, that the self-similarity assumption for the slip-to-rise-time ratio between the laboratory scale and the earth scale is as plausible (or not) as the self-similarity assumptions on initial stresses on faults made in dynamic rupture propagation simulations. In this work, we have studied long-period ground motions at distances greater than 15 km or so. Long-period ground motion at these distances may not be sensitive to the detailed shape of the source-time function. So the use of triangular slip velocity-time functions in our stochastic sources may be acceptable. However, more realistic (dynamically compatible) Kostrov type or modified Yoffe type source time functions (Tinti et al. 2005) may be needed for broadband and/or near-source ground motion simulations.

The characterization of the underlying probability distributions of earthquake source parameters (and/or their correlations) in the proposed approach may possibly be improved by incorporating statistics from dynamic rupture simulations (rather than from finite source inversions in the case of slip, for instance). Such an approach is used by "pseudo-dynamic" stochastic rupture model generators (e.g., Song and Somerville 2010; Mena et al. 2012; Trugman and Dunham 2014a; Song et al. 2014). They typically represent final slip, rupture speed, and slip rate as spatial random fields that are statistically characterized (and/or correlated) by synthetic data from dynamic rupture simulations. Because dynamic models are physically self-consistent, they may be able to better characterize the relationship between earthquake source parameters. However, they too suffer from a lack of knowledge of the spatial heterogeneity of the background stress field and the frictional failure law for the fault. As more data to better constrain these aspects becomes available, our algorithm may be adapted to incorporate earthquake source parameter statistics from dynamic rupture simulations.

2.5 Data and Resources

The database of global finite-source rupture models of past earthquakes was searched using `http://www.seismo.ethz.ch/static/srcmod/Events.html` (last updated July 23, 2007. Last accessed September 16, 2014). Using `http://dc-app3-14.gfz-potsdam.de/index.html` (last updated August, 20 -09. Last accessed October 21, 2014), the world stress map project database was accessed. The ground motion plots were made using the Generic Mapping Tools version 4.5.7 found at `http://gmt.soest.hawaii.edu/projects/gmt` (last accessed October 20, 2014).

in this chapter, the stochastic algorithm presented has been applied to several $M_w 7.9$ and $M_w 6.05$ earthquakes occurring along southern San Andreas fault and the associated ground motion characteristics are discussed. However, it is crucial that the algorithm is used to model earthquakes in between $Mw6.0 - 7.9$ and the nature of corresponding ground motions are analyzed thoroughly for use in rupture-to-rafters simulations. The following chapter addresses this issue along with rupture-to-rafters simulations methodology and its application to evaluate seismic performance of two 18-story moment frame buildings.

Chapter 3

Limit State Exceedance Probabilities of Building Performance Under Earthquake Excitation Using Rupture-to-Rafters Simulations

The right-lateral strike-slip San Andreas fault is the active boundary that accommodates much of the motion between the North American and Pacific plates with an average slip rate of 2.5 - 3.5 cm/yr (Fialko 2006; Lindsey and Fialko 2013). The southern section of the fault, starting at Parkfield and ending at Bombay Beach near the Salton Sea, has the potential to produce earthquakes up to about magnitude 8.3. Ground motions generated from earthquakes on this section of the fault may be strong enough to cause damage to tall buildings in greater Los Angeles. In addition to the San Andreas fault, these buildings may be at risk from earthquakes on blind-thrust faults such as the Northridge and Puente Hills faults, and other smaller strike-slip fault systems such as the Newport-Inglewood, the San Jacinto, the Elsinore, and the Santa Monica-Hollywood-Raymond fault systems, that have the potential to produce magnitude $\sim$7 earthquakes. Here we attempt to characterize building performance under earthquakes on the San Andreas fault alone over the next thirty years using physics-based simulations of earthquakes and structural response. The approach can be easily extended to incorporate risk from all the other known fault systems.

The last big earthquake on the southern section of the San Andreas fault was the $M_w 7.9$ Fort Tejon earthquake of 1857. Paleoseismic investigations by Sieh and others (e.g., Sieh 1978; Weldon et al. 2005) points to the rupture having initiated at Parkfield in central California, propagating roughly 360 km in a southeasterly direction down to Wrightwood in southern California. A prototype rupture-to-rafters simulation by the third author (with others) of an earthquake similar to the Fort Tejon earthquake on San Andreas fault, pointed to significant damage to the two moment frame buildings considered in this study (kri ; Krishnan et al. 2006b) as well as extensive repair/replacement costs to the structures (hypothetically located) at several sites in the greater Los Angeles region (Muto et al. 2008). That study demonstrated that it may be possible to conduct risk assessment more quantitatively using rupture-to-rafters simulations of scenario earthquakes. Here, we introduce our physics-based rupture-to-rafters simulations into the performance based earthquake engineering (PBEE) framework (Porter 2003) developed by the Pacific Earthquake Engineering Research (PEER) center to assess the risk to the same buildings under southern San Andreas fault earthquakes that may occur in the next 30 years. Such a study, when conducted for all known faults, may better inform decision-making in urban planning and design, disaster mitigation and management, insurance and reinsurance, and risk management.

While the PEER PBEE framework has four stages (hazard analysis, structural analysis, damage analysis, and loss analysis), we focus in this study only on the first two stages to estimate limit states of structural performance [Immediate Occupancy (IO), Life Safety (LS), and Collapse Prevention (CP)]. PBEE has been successfully used in assessing the seismic collapse safety/risk of buildings (e.g., Haselton et al. 2010; Miyamoto et al. 2010; Eads et al. 2013; Raghunandan et al. 2014; Mathiasson and Medina 2014) as well as in estimating losses (e.g., Mitrani-Reiser et al. 2006; Goulet et al. 2007; Ramirez et al. ; Ramirez et al. 2012). However, hazard analysis, for the development of ground motion time-histories, has typically involved the adoption of a spectrum (or spectra) for design basis earthquake (DBE) and/or maximum considered earthquake (MCE), selection of suitable recorded ground motion records based on the nature of hazard, and scaling of the records in some manner to make them compatible with the DBE/MCE spectrum. Selection and scaling ground motions for use in PBEE is an active area of research (see special issue on the topic in the Journal of Structural Engineering Huang et al. 2011). Several challenges exist, the most important being the lack of records from large events at reasonable source-to-site distances (Applied Technology Council 2009), especially in sedimentary basins such as Los Angeles. 3-component synthetic ground motion histories, generated by computationally propagating seismic waves under scenario earthquakes (e.g., Olsen et al. 1995; Heaton et al. 1995; Graves 1998; Aagaard and Heaton 2004; Graves 2006; Aagaard 2006; kri ; Krishnan et al. 2006b; Olsen et al. 2008; Cui et al. 2010; Bielak et al. 2010; Graves and Pitarka 2010; Aagaard et al. 2010; Aagaard et al. 2010; Graves et al. 2011; Olsen et al. 2014), may be used to circumvent the difficulties associated with ground motion selection and scaling. Regional seismic wave-speed models, incorporating 3-D variations of seismic wave speeds and density, topography and bathymetry, and attenuation, capable of resolving long period waves ($> 2\ s$) are being developed for many parts of the world (e.g., Frankel and Stephenson 2000; Pratt et al. 2003; Suss and Shaw 2003; Magistrale et al. 2000; Magistrale et al. 1996; Kohler et al. 2003; Prindle and Tanimoto 2006; Tape et al. 2009; Tape et al. 2010; Ely et al. 2010; Plesch et al. 2011; Horikawa et al. 2003; Kagawa et al. 2004; Furumura 2005; Lee et al. 2008; Aagaard 2006; Graves 2006; Landes et al. 2004; Raileanu et al. 2005; Li et al. 2007). Concurrently, wave propagation codes (e.g., Olsen et al. 1995; Bao et al. 1998; Graves 1998; Komatitsch and Tromp 1999; Liu et al. 2004; Komatitsch et al. 2010; Komatitsch 2011) have sufficiently matured for use in tackling real-world problems, at least for the study of long-period structures such as tall buildings and long-span bridges. In the next section, we outline the methodology for incorporating rupture-to-rafters simulations into the modular PEER PBEE approach for probabilistically quantifying performance.

3.1 Methodology

The methodology consists of 5 steps:

1. Generating stochastic source models for scenario earthquakes on the target fault.
2. Computing probabilities of occurrence over the targeted time horizon of all plausible ruptures on the target fault and distributing these probabilities to the scenario earthquakes.
3. Simulating 3-component ground motion histories at chosen sites from the scenario ruptures using seismic wave propagation through a regional finte-element, finite-difference, or spectral-element model of the earth.
4. Performing 3-D nonlinear analysis of the target buildings at each site under ground motions from each scenario rupture.
5. Applying the PEER PBEE framework to estimate exceedance probabilities of structural performance levels over the targeted time horizon from earthquakes on the target fault.

3.1.1 Stochastic source models for scenario earthquakes

An earthquake rupture (source) is characterized by the distribution of slip, slip velocity (or rise time) and rupture propagation speed across the rupture area. Two options, kinematic and dynamic approach, exist for the modeling of an earthquake source as described at the beginning of Chapter 2. Pseudo-earthquakes created in the laboratory have further augmented our understanding with insights into the rupture process. This has led to the development of kinematic [e.g., Graves and Pitarka 2010 (`http://scec.usc.edu/scecpedia/Broadband_Platform`), Schmedes et al. 2013, RupGen-eQuake-RC (`http://equake-rc.info/CERS-software/rupgen/`), Siriki et al. 2014] as well as pseudodynamic (e.g., Trugman and Dunham 2014b) rupture generators.

A computationally tractable set of earthquake rupture scenarios (characterized by magnitude, rupture location, hypocenter location and rupture direction) that span the range of earthquakes that may lead to some damage in the target structure at any of the target sites is devised. Using a rupture generator, kinematic source model realizations are generated for this set of rupture scenarios. Several realizations may be generated for a given scenario. Here we adopt the Siriki et al. (2014) stochastic source algorithm (as described in Chapter 2) for earthquake rupture generation.

3.1.2 Probability of occurrence of scenario earthquakes using earthquake rupture forecasts [contribution by Ramses Mourhatch (Mourhatch 2015)]

The Working Group on California Earthquake Probabilities (WGCEP), a group comprised of scientists and engineers from the U.S. Geological Survey (USGS), the California Geological Survey (CGS), and the Southern California Earthquake Center (SCEC), has been developing the Uniform California Earthquake Rupture Forecast (UCERF, Field et al. 2009; Field et al. 2013). Using fault models that specify fault geometry, deformation models that specify slip-rate and creep for each fault section, earthquake rate models that specify the long-term rate of all earthquakes in the region (at some spatial resolution), and earthquake probability models that specify the likelihood of a given event occurring during a specified time horizon, perhaps conditioned on additional information such as date of last event, yearly rupture rates for all possible rupture scenarios in California are forecast. All major faults are divided into segments of 2 km to 13 km length. The rupture extent of each forecast earthquake spans two or more of these segments. Whereas version 3 (UCERF3) gives time-independent rates alone (where the assumed Poisson probability model depends only on long-term rates), the previous version (UCERF2) provides both time-dependent and time-independent rates. The models in the framework are constrained by geologic, geodetic (e.g., GPS), seismic (earthquake catalogues), and paleoseismic data. The framework itself has a logic tree structure wherein model (epistemic) uncertainty is accounted for by the allocation of likelihood-dependent weights to all branches. The weighted average of the earthquake rates from all pathways of UCERF's logic tree is used to assign probabilities to all rupture scenarios that may occur within the spatial extent of the simulated earthquake scenarios. These probabilities of all plausible ruptures (which may be many more in number than the set of simulated earthquakes) are distributed amongst the smaller set of simulated earthquake scenarios on the basis of location and seismic moment (energy) release by Mourhatch (2015). This is illustrated by way of an example in a later section on the application of the method to the southern San Andreas fault. Henceforth, plausible ruptures from UCERF will be referred to as "forecast earthquakes" to distinguish them from the simulated earthquakes which will be referred to as "scenario earthquakes".

3.1.3 Ground motion simulation for scenario earthquakes

For each rupture scenario, the seismic source is modeled as a patchwork of smaller sources, each small source being represented by a double-couple and mathematically quantified by a centroidal moment tensor. The energy from each little source is released sequentially at rupture times as dictated by the rupture speed distribution of the overall source model. The disturbance at the source propagates to the site through the earth model in the form of P and S waves whose interactions lead to Rayleigh and Love waves as well. As mentioned previously, several methods exist for the generation and propagation of seismic waves. Here, we simulate ground motions using an open source package SPECFEM3D as discussed in Section 2.2. Although hybrid methods to synthesize broadband ground motion, that combine low-frequency synthetic ground motion from wave propagation simulations with high-frequency stochastically (e.g., Graves and Pitarka 2010) or deterministically (e.g., Mourhatch and Krishnan 2014) generated ground motion, exist, we limit ourselves to using long-period ground motion alone in this study. Our target buildings are long-period structures structures as well and are not affected substantially by high-frequency ground motion (Krishnan et al. 2006b).

3.1.4 3-D nonlinear dynamic analysis of target buildings under scenario earthquake ground motion

3-D structural models of the target buildings are subjected to the 3-component ground motion from the scenario earthquakes at each of the target sites of interest. Structural performance is measured by the peak interstory drift (IDR) over the height of the building. FEMA 356 (FEMA 2000) relates peak IDR to the building performance limits states of Immediate Occupancy (IO), Life Safety (LS), and Collapse Prevention (CP) for various types of structures. For example, the peak IDR limits for exceedance of IO, LS, and CP levels are 0.007, 0.025 and 0.05, respectively, for steel moment frame buildings and 0.005, 0.015, and 0.02, respectively, for steel braced-frame buildings (American Society of Civil Engineers 2007). Several programs for nonlinear analysis of buildings exist [e.g., OpenSEES (McKenna et al. 2000), PERFORM3D (Computers and Structures), Drain3DX (Powell and Campbell), Ruaumoko (Carr 2001), etc.]. Here, we use FRAME3D (Krishnan 2003; Krishnan 2009) to conduct nonlinear dynamic analysis of the target buildings. It is a special-purpose program for the analysis of steel structures that handles accurately many phenomena specific to these structures and critical for capturing their failure mechanisms, such as the nonlinear shear behavior of joints comprising panel zones in two orthogonal directions, buckling and fracture of braces, fracture of moment-connections etc. It has been extensively validated against experimental data and has been used for analysis of many tall steel buildings (Krishnan and Hall 2006a; Krishnan and Hall 2006b; Krishnan 2007; Krishnan and Hall 2006b; Krishnan 2010).

3.1.5 Applying the PEER PBEE framework to estimate probability of exceedance of FEMA356 performance limit states for target buildings

At this stage, ground motion histories at several target sites under several realizations of a suite of earthquake scenarios, the structural response to these motions, and the probability of occurrence of these scenarios are known. To compute performance limit states for the target buildings, it is necessary to condense the continuous-time ground motion histories into discrete scalar or vector intensity measures. Here, we choose to use the intensity measure of peak ground velocity (PGV) which has been shown to be related to the input energy imparted to the structure by ground shaking (Uang and Bertero

1988; Krishnan and Muto 2012; Krishnan and Muto 2013) and may best correlate with region wide damage. Collating PGVs at all the target sites due to a scenario earthquake of a given magnitude and location into suitable bins and fitting a log-normal distribution to the data, the conditional probability density function of PGV, conditioned upon earthquake magnitude and location, $p(PGV|M_w, loc)$, may be computed. Collating the peak IDR response of the target buildings under all earthquake scenarios into suitable bins, the cumulative probability of exceedance of a given performance limit state conditioned upon PGV, $P(IDR > Limit\ State|PGV)$, i.e., the building fragility, may be determined as well (by fitting a log-normal distribution to the data). If the conditional probability of occurrence of a given magnitude scenario earthquake within a specified time horizon, conditioned on location, $P(M_w|loc)$, is known, the probability of exceedance of a building performance limit state in that time horizon, $P(IDR > Limit\ State)$, may be written as:

$$P(IDR > Limit\ State) = \sum_{M_w} \sum_{loc} \int_{PGV} P(IDR > Limit\ State|PGV)\ p(PGV|M_w, loc)\ dPGV\ P(M_w/loc) \tag{3.1}$$

3.2 Application to performance quantification of tall steel moment frame buildings in southern California under San Andreas earthquakes

In this section, we illustrate the workings of the methodology by applying it to a real-world older existing structure in southern California and a hypothetical modern redesign of the same using a newer building code.

3.2.1 Target buildings, target fault, and time horizon

The existing building is an 18-story office building, located within five miles of the epicenter of the 1994 Northridge earthquake. An isometric view of its FRAME3D model is shown in Figure 3.1(a). It was designed according to the 1982 Uniform Building Code (UBC) and completed in 1986-87. The height of the building above ground is 75.7 m (248’ 4”) with a typical story height of 3.96 m (13’ 0”) and taller first, seventeenth, and penthouse stories. The lateral force-resisting system consists of two-bay welded steel moment-frames, two apiece in either principal direction of the structure as shown in Figure 3.1(b). The location of the north frame one bay inside of the perimeter gives rise to some torsional eccentricity. Many moment-frame beam-column connections in the building fractured during the 1994 M_w 6.7 Northridge earthquake, and the building has been extensively investigated since then by engineering research groups (Krishnan and Muto ; Chi et al. 1998; Carlson). Fundamental periods, computed assuming 100% dead load and 30% live load contribution to the mass, are 4.52s (X-translation), 4.26s (Y-translation) and 2.69s (torsion). We model the connection susceptibility to fracture probabilistically [modeling details can be found in Krishnan and Muto (2012)].

The redesigned building, a FRAME3D model of which is shown in Figure 3.1(c), is similar to the existing building, but the lateral force-resisting system has been redesigned according to the 1997 UBC. It has been designed for larger earthquake forces and greater redundancy in the lateral force-resisting system, with 8 bays of moment-frames in either direction [although lateral resistance will likely be dominated by the three-bay moment frames shown in Figure 3.1(d) as opposed to the single-bay moment frames]. The frame located in the interior of the existing building has been relocated to the exterior, eliminating the torsional eccentricity. Fundamental periods, computed assuming 100% dead load and 30% live load contribution to the mass, are 4.06s ([X+Y-] translation), 3.85s ([X+Y+] translation) and 2.60s (torsion). The positive (+) directions of the X and Y axes are shown on the plans (Figure 3.1). Note that the fundamental translational modes are oriented approximately along the floor plate diagonals. This is because the L-shaped layout of the moment frames at opposite corners of the building, the use of box columns at the corners along one diagonal and I-sections for columns at the corners along the other diagonal, and the absence of X-direction beams in two bays located at diagonally opposite corners create two axes of symmetry (one strong and one weak) that are oriented roughly along the floor plate diagonals. Detailed floor plans, beam and column sizes, and the gravity, wind and seismic loading criteria for the two buildings can be found in (Krishnan et al. 2005). The redesigned building is modeled assuming perfect connections, i.e., connections not susceptible to fracture.

The target fault is the southern section of the San Andreas fault that runs from Parkfield in central California to Bombay Beach in southern California, distance of roughly 586 km. The time horizon of

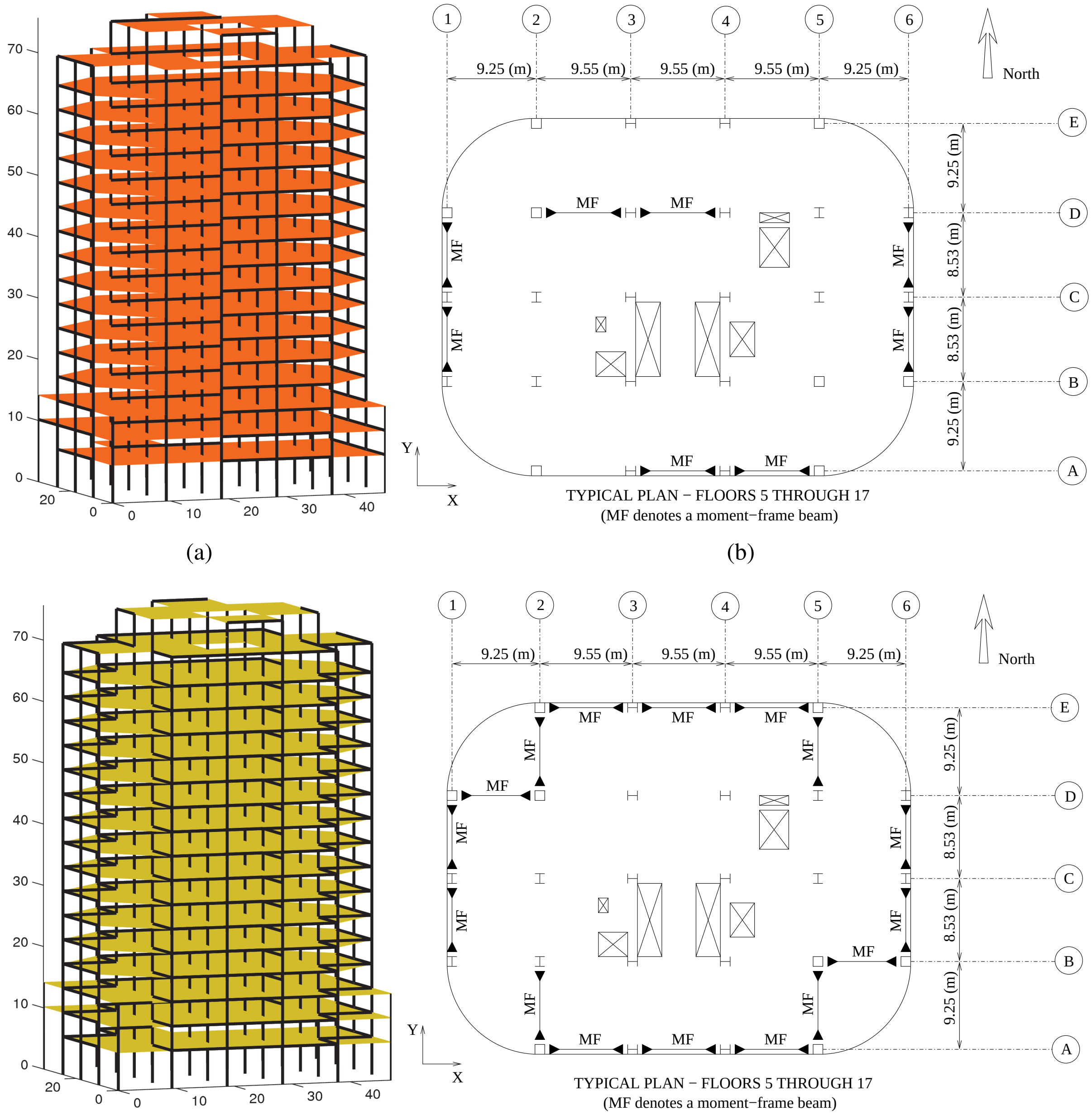

70
60
50
40
30
20
10
0
20
0
0
10
20
30
40
Y
X
1
2
3
4
5
6
9.25 (m)
9.55 (m)
9.55 (m)
9.55 (m)
9.25 (m)
North
E
D
C
B
A
9.25 (m)
8.53 (m)
8.53 (m)
9.25 (m)
MF
TYPICAL PLAN − FLOORS 5 THROUGH 17
(MF denotes a moment−frame beam)

(a) (b)

(c) (d)

Figure 3.1: Structural models of the two 18-story steel moment frame buildings: (a) Isometric view of the existing building (designed using the 1982 UBC). (b) Plan view of a typical floor of the existing building showing the location of columns and moment-frame (MF) beams. (c) Isometric view of the new building (redesigned using the 1997 UBC). (d) Plan view of a typical floor of the redesigned building.

interest is the next 30 years.

3.2.2 Scenario earthquakes on the southern San Andreas fault

We are interested in the performance of the target buildings hypothetically located at 636 sites in southern California. These sites, shown in Fig. 2.14, are located in three distinct basin structures marked by ellipses, the centrally located Los Angeles basin, the Simi and the San Fernando valleys to the northwest, and the San Gabriel valley to the east. Earthquakes on the San Andreas fault with magnitudes below about 6 are not likely to produce ground motions strong enough to cause damage to the target buildings hypothetically located at any of the 636 sites. Accordingly, a suite of sixty earthquakes with six different magnitudes exceeding 6 (M_w 6.05, 6.40, 6.80, 7.20, 7.60, 7.90), rupturing five locations on the target fault, with rupture propagating unilaterally in one of two directions (north-to-south or south-to-north), comprises the set of scenario earthquakes upon which building performance quantification will be based. Figs. 2.12 and 2.13 shows four of the ten scenario earthquakes with magnitude 7.9.

3.2.3 30-year probability of occurrence of scenario earthquakes [contribution by Ramses Mourhatch (Mourhatch 2015)]

WGCEP has divided the southern section of the San Andreas fault (from Parkfield to Bombay Beach) into approximately 100 segments ranging in length from about 4.6 km to about 8.8 km. Of all the plausible earthquakes on the San Andreas fault forecast in UCERF3, 118,000-140,000 forecast earthquakes (actual number depends upon the logic tree branch considered) rupture at least one of these segments. Rupture probabilities assigned by WGCEP to these ruptures have to be (partially or wholly) collectively redistributed to the 60 scenario earthquakes (6 magnitudes x 5 locations x 2 rupture directions) simulated in this study in order to fully account for the associated seismic risk. Half of these probabilities are assigned to north-to-south propagating ruptures and half to south-to-north propagating ruptures. Accordingly, Mourhatch (2015) classifies the forecast earthquakes into six bins depending upon moment magnitude: [5.90 - 6.27], (6.27 - 6.66], (6.66 - 7.06], (7.06 - 7.46], (7.46 - 7.79], (7.79 - 8.34]. Note that the seismic moments of the M_w 6.05, 6.40, 6.80, 7.20, 7.60, 7.90 scenario earthquakes correspond to the average of the seismic moments of the upper and lower magnitude limits of these six bins, respectively. Each bin will thus be associated with five scenario earthquakes (corresponding to the five locations) of a given magnitude. The upper limit of the last bin is assumed higher to include all forecast earthquakes with magnitude greater than 7.9. This, of course, implies that the building performance limit state exceedance probabilities would be underestimated. Now, the probabilities of all forecast earthquake in a given bin are to be distributed amongst the five scenario earthquakes associated with that bin. For this, the earthquake occurrence rate (number of earthquakes per year) of each forecast earthquake in that bin is multiplied by its seismic moment to arrive at a seismic moment release rate. This rate is distributed to the fault segments participating in that forecast earthquake in proportion to their areas. The contributions of seismic moment release rates of each fault segment from all the forecast earthquakes in that magnitude bin are summed. This cumulative moment release rate is assigned to the most closely located scenario earthquake out of the five scenario earthquakes corresponding to that bin. It is possible that the rupture extents of larger magnitude scenario earthquakes may overlap such that two or more scenario earthquakes may extend over the same fault segment(s). The moment release rates on such segments (lying within the scenario earthquake overlap) are evenly distributed among the overlapping scenario earthquakes. Next, the contributions of moment release rates to each of the five scenario earthquakes from all the fault segments are summed to arrive at their seismic moment release rates. Dividing these rates by the corresponding seismic moments of the scenario earthquakes gives the scenario earthquake rates (number of earthquakes per year), r. The probability of occurrence of the scenario earthquake over a period of ΔT years is then given by $P(M_w/loc) = 1 - e^{-r\Delta T}$ (assuming Poisson distribution).

Shown in Table. 3.1 are the 30-year occurrence probabilities of the 30 scenario earthquakes determined using this approach. Half of these probabilities will be assigned to the north-to-south propagating ruptures and the other half to the south-to-north propagating ruptures.

3.2.4 Simulated ground motions for the scenario earthquakes

For each scenario earthquake magnitude, five source realizations are generated using the Siriki et al. (2014) stochastic source algorithm. We are interested in determining the probability of structural performance limit states being exceeded under "median" ground motion, rather than "extreme" ground motion. Accordingly, from the five source realizations, we identify the median source model (whose ground motions will be used in structural performance quantification) as described in Section 2.2.

M_w [Bin]	Location 1 (Parkfield)	Location 2	Location 3	Location 4	Location 5 (Bombay Beach)	Total Probability (All Locations)
6.05 [5.90 - 6.27]	0.5785	0.0009	0.0000	0.0428	0.0179	0.6041
6.40 (6.27 - 6.66]	0.0096	0.0202	0.1978	0.1965	0.0133	0.3828
6.80 (6.66 - 7.06]	0.0141	0.0257	0.0088	0.1106	0.0306	0.1792
7.20 (7.06 - 7.46]	0.0266	0.0255	0.0084	0.0292	0.0476	0.1302
7.60 (7.47 - 7.79]	0.0116	0.0144	0.0072	0.0096	0.0185	0.0598
7.90 (7.79 - 8.34]	0.0317	0.0273	0.0260	0.0212	0.0178	0.1180
Total Probability M_w [5.90 - 8.34]	0.6165	0.1089	0.2375	0.3562	0.1375	0.8553

Table 3.1: UCERF3 time-independent 30-year occurrence probabilities for each scenario earthquake. Half of these probabilities are assigned to north-to-south propagating ruptures and the other half to south-to-north propagating ruptures.

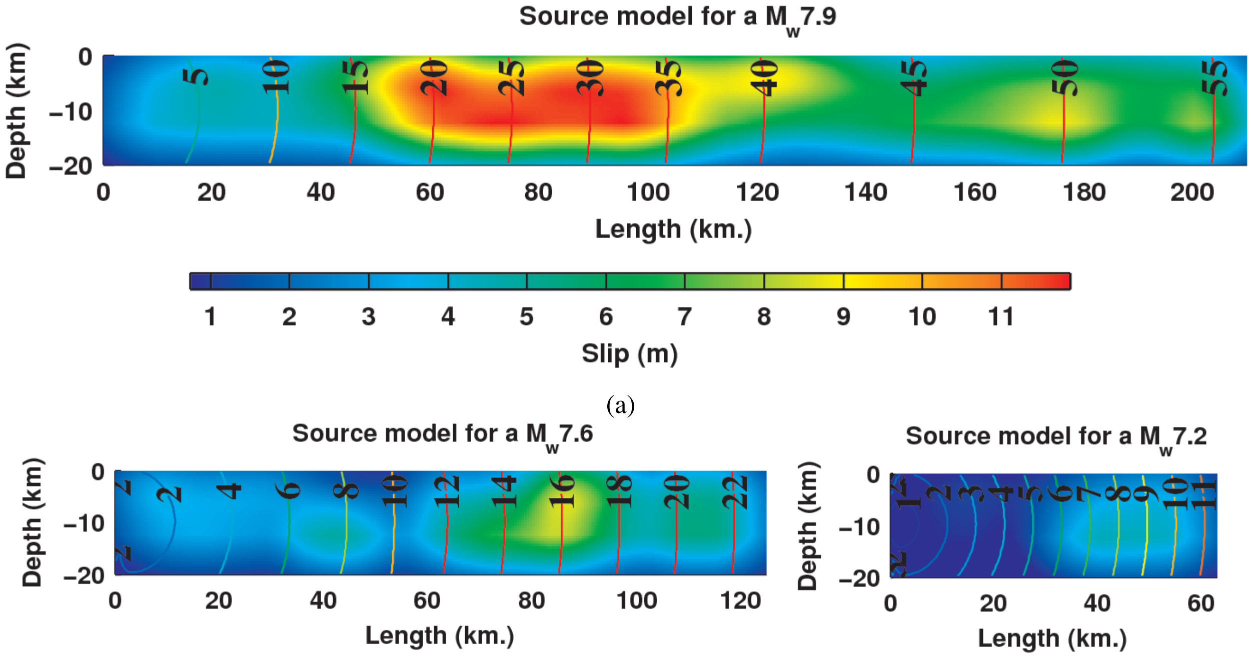

(a)

(b)

(c)

Figure 3.2: Stochastic median slip (m) model with rupture time (s) contours for (a) M_w7.9 (b) M_w7.6 and (c) M_w7.2 scenario earthquakes. The sources have constant peak slip-velocities of 4.14, 3.2, 2.59 m/s respectively.

Shown in Fig. 3.2 are the “median” stochastic sources for the magnitude 7.9, 7.6, and 7.2 scenario earthquakes. Additional stochastic source models and the associated ground motions are shown in Appendix C. The kinematic source properties of the median models for scenario earthquakes of all six magnitudes (7.9, 7.6, 7.2, 6.8, 6.4, and 6.0) are listed in Table. 3.2. The peak slips are close to those observed from finite-source inversions of past earthquakes of similar magnitude. For example, peak slips in the stochastic median models of $M_w7.9$, $M_w7.6$ and $M_w7.2$ scenario earthquakes are 13 m, 9 m and 4.5 m, respectively. In comparison, peak slips in the finite-source inversions of the $M_w7.9$ Denali earthquake of 2002, the $M_w7.56$ Izmit earthquake of 1999, and the $M_w7.28$ Landers earthquake of 1992 are 12 m (kri), 8 m (Delouis et al. 2002), amd 7 m (Wald and Heaton 1994), respectively. The Siriki et al. (2014) algorithm forces the peak slips to occur in the top two-thirds of rupture depth ensuring greatest seismic moment release there (consistent with Fialko et al. 2005) with slips gradually tapering to zero at the seismogenic depth. Additionally, on the average, asperities, where the greatest energy release occurs, constitute roughly a quarter of the fault rupture area (Tab. 3.2). Here, an asperity is defined as two or more continuous subfaults with slip greater than or equal to 1.25 times the average slip. Slip-to-rise-time ratio (slip velocity) is constant in the Siriki et al. (2014) stochastic models. Thus, rise-time is forced to be proportional to slip. Slip velocities vary between 1.7 m/s - 4.14 m/s for the scenario earthquakes. One point of comparison is the finite-source inversion model by kri () for the M_w 7.9, 2002 Denali earthquake where the peak slip-velocity is 2.98 m/s. An interesting feature of the stochastic models at the higher end of the magnitude spectrum of the scenario earthquakes is that ruptures predominantly travel at super-shear speeds. It has been observed in simulations that ruptures propagating at super-shear speeds tend to produce weaker ground motions than those propagating predominantly at sub-Rayleigh speeds (Aagaard and Heaton 2004; Siriki et al. 2014). On the other hand,rupture speeds in the stochastic source models at the lower end of the magnitude spectrum of the scenario earthquakes take values in the sub-Rayleigh as well as the super-shear regime.

The distribution of peak ground motion from the stochastic median model located at various sections along the southern San Andreas fault is strongly influenced by the location of the rupture, the location of slip asperities within the rupture, as well as rupture direction. For north-to-south propagating ruptures, the location of intense ground motions moves gradually from Simi valley to San Fernando valley, on to Los Angeles basin, and finally to San Gabriel valley as the rupture location is changed from Parkfield (Location 1) towards Bombay Beach (Location 5). In general, these observations are reversed for south-to-north propagating ruptures, i.e., the location of intense ground motion moves gradually from the San Gabriel valley to the LA basin, on to the San Fernando valley, and finally to the Simi valley, as the rupture location is varied from Location 5 to Location 1. In the case of the $M_w7.9$ earthquake starting midway along the southern San Andreas fault (i.e., rupture location 3) and propagating north-to-south [Figs. 3.3(b) & 3.5(b)], the peak motions produced by the stochas-

M_w	**rupture area** (km^2) **(Length, Depth)**	**mean slip (m)**	**% total asperity area**	**slip** (m) **(min, max)**	**0.5*rise time** (s) **(min, max)**	V_r**% in SR**[a] **(min, max)**
7.90	4200 (210, 20)	6.30	26.64	0.74, 11.87	0.18, 2.86	0.23, 51.67
7.60	2500 (125, 20)	3.75	24.98	0.50, 8.61	0.16, 2.69	0.40, 40.40
7.20	1260 (63, 20)	1.87	36.17	0.09, 4.47	0.03, 1.72	0.79, 32.53
6.80	640 (32, 20)	0.92	32.89	0.04, 1.96	0.02, 0.84	1.56, 85.93
6.40	280.5 (17, 16.5)	0.53	27.54	0.13, 0.82	0.07, 0.48	2.94, 100.00
6.05	121 (11, 11)	0.36	25.61	0.08, 0.56	0.04, 0.28	4.54, 100.00

Table 3.2: Properties of stochastic "median" kinematic source models for the scenario earthquakes.

---

[a] SR:subRayleigh

tic median model are far more intense in the Los Angeles (LA) basin than in the San Gabriel valley which is located east of the LA basin. The reverse is true for the motions generated by the rupture propagating south-to-north [Figs. 3.4(b) & 3.6(b)]. In the north-to-south rupture, the largest slip asperity in the stochastic median model occurs to the west of the mid-point of the source, whereas its location moves to the east of the mid-point in the south-to-north rupture. Accordingly, ground motions in the north-to-south rupture [Figs. 3.4(b) & 3.6(b)] are stronger in the central portion of the LA basin, whereas ground motions in the south-to-north rupture are stronger in the eastern section of the LA basin. Similar observations can be made in the case of other magnitudes as well. For M_w 7.60 and M_w 7.20 north-to-south propagating ruptures at location 3, ground motions are more intense in the San Gabriel Valley than in the LA basin [Figs. 3.3(e), 3.3(h), 3.5(e), & 3.5(h)]. The largest slip asperity in these cases lies east of the mid-point of the source [Figs. 3.2(b) & 3.2(c)]. The reverse holds true [Figs. 3.4(e), 3.4(h), 3.6(e), & 3.6(h)] for the south-to-north propagating ruptures. The effect of rupture directivity can be seen in the sharply contrasting peak ground motions from the north-to-south and south-to-north propagating M_w 7.9 ruptures at Location 1 [compare Figs. 3.3(a) and 3.5(a) against Figs. 3.4(a) and Fig. 3.6(a), respectively]. M_w 7.60 and smaller magnitude ruptures at locations 1 & 5 are too far away to cause significant shaking in the greater LA region. Peak ground displacement is

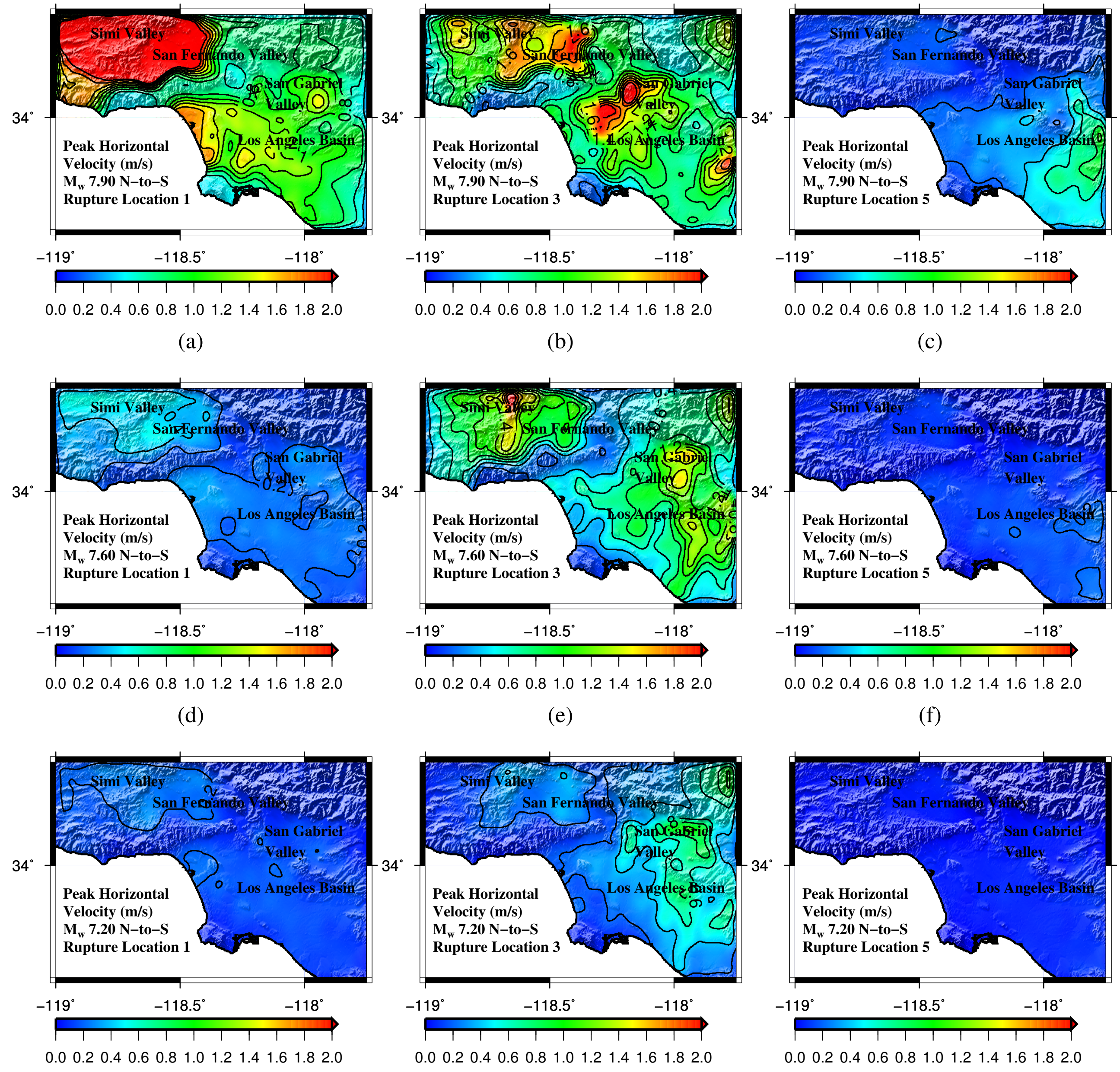
Simi Valley
San Fernando Valley
San Gabriel Valley
Los Angeles Basin
34˚
–119˚
–118.5˚
–118˚
0.0 0.2 0.4 0.6 0.8 1.0 1.2 1.4 1.6 1.8 2.0
Peak Horizontal Velocity (m/s) M$_w$ 7.90 N–to–S Rupture Location 1
Peak Horizontal Velocity (m/s) M$_w$ 7.90 N–to–S Rupture Location 3
Peak Horizontal Velocity (m/s) M$_w$ 7.90 N–to–S Rupture Location 5
Peak Horizontal Velocity (m/s) M$_w$ 7.60 N–to–S Rupture Location 1
Peak Horizontal Velocity (m/s) M$_w$ 7.60 N–to–S Rupture Location 3
Peak Horizontal Velocity (m/s) M$_w$ 7.60 N–to–S Rupture Location 5
Peak Horizontal Velocity (m/s) M$_w$ 7.20 N–to–S Rupture Location 1
Peak Horizontal Velocity (m/s) M$_w$ 7.20 N–to–S Rupture Location 3
Peak Horizontal Velocity (m/s) M$_w$ 7.20 N–to–S Rupture Location 5

(a) (b) (c)

(d) (e) (f)

(g) (h) (i)

Figure 3.3: Peak horizontal velocity (m/s) at 636 sites in southern California under north-to-south propagating (a)-(c) M_w7.9, (d)-(f) M_w7.6, and (g)-(i) M_w7.6 scenario earthquakes at locations 1, 3 & 5.

strongly correlated with the peak ground velocity in all cases.

The median value of the peak east-west and north-south ground velocity and displacement histories at the 636 sites in southern California (shaded region represents +/- one standard deviation) for each scenario earthquake magnitude are shown as a function of rupture location in Figs. 3.7 and 3.8, respectively. The influence of directivity is strongest for the ground motions produced by ruptures at

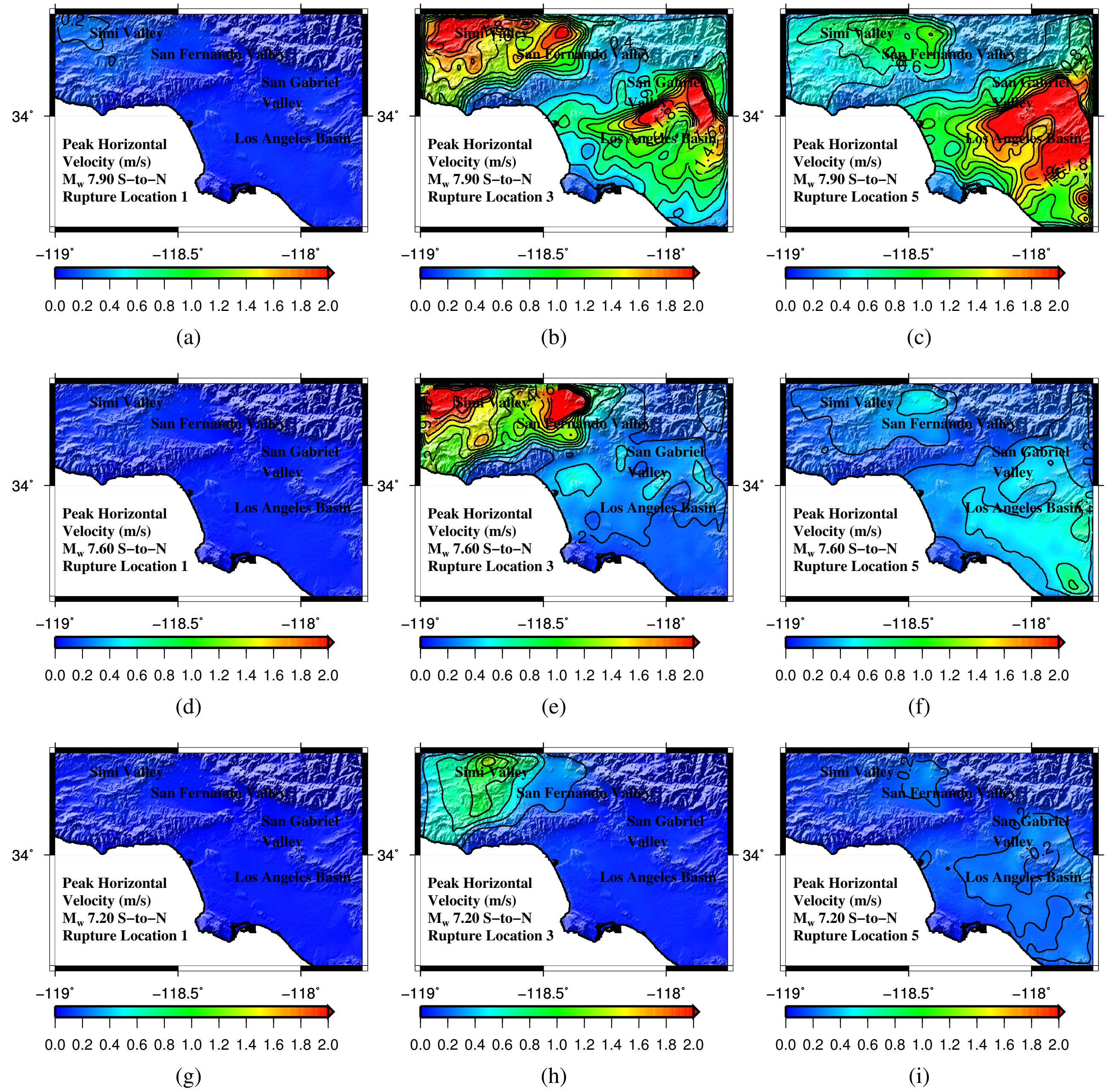

Simi Valley
San Fernando Valley
San Gabriel Valley
Los Angeles Basin
34˚
–119˚
–118.5˚
–118˚
0.0 0.2 0.4 0.6 0.8 1.0 1.2 1.4 1.6 1.8 2.0
Peak Horizontal Velocity (m/s) M$_w$ 7.90 S–to–N Rupture Location 1
Peak Horizontal Velocity (m/s) M$_w$ 7.90 S–to–N Rupture Location 3
Peak Horizontal Velocity (m/s) M$_w$ 7.90 S–to–N Rupture Location 5
Peak Horizontal Velocity (m/s) M$_w$ 7.60 S–to–N Rupture Location 1
Peak Horizontal Velocity (m/s) M$_w$ 7.60 S–to–N Rupture Location 3
Peak Horizontal Velocity (m/s) M$_w$ 7.60 S–to–N Rupture Location 5
Peak Horizontal Velocity (m/s) M$_w$ 7.20 S–to–N Rupture Location 1
Peak Horizontal Velocity (m/s) M$_w$ 7.20 S–to–N Rupture Location 3
Peak Horizontal Velocity (m/s) M$_w$ 7.20 S–to–N Rupture Location 5

(a) (b) (c)

(d) (e) (f)

(g) (h) (i)

Figure 3.4: Peak horizontal velocity (m/s) at 636 sites in southern California under south-to-north propagating (a)-(c) M_w7.9, (d)-(f) M_w7.6, and (g)-(i) M_w7.6 scenario earthquakes at locations 1, 3 & 5.

locations 1 and 5 on the fault, followed by those at locations 2 and 4. The influence of proximity to the dominant slip asperity and the seismic source more broadly is strongest for the ground motions produced by the ruptures at location 3, followed by those at locations 2 and 4. The sources at locations 2 and 4 have the most favorable combinations of source proximity and source-to-site rupture directivity configuration for north-to-south and south-to-north propagation, respectively, and result in the highest

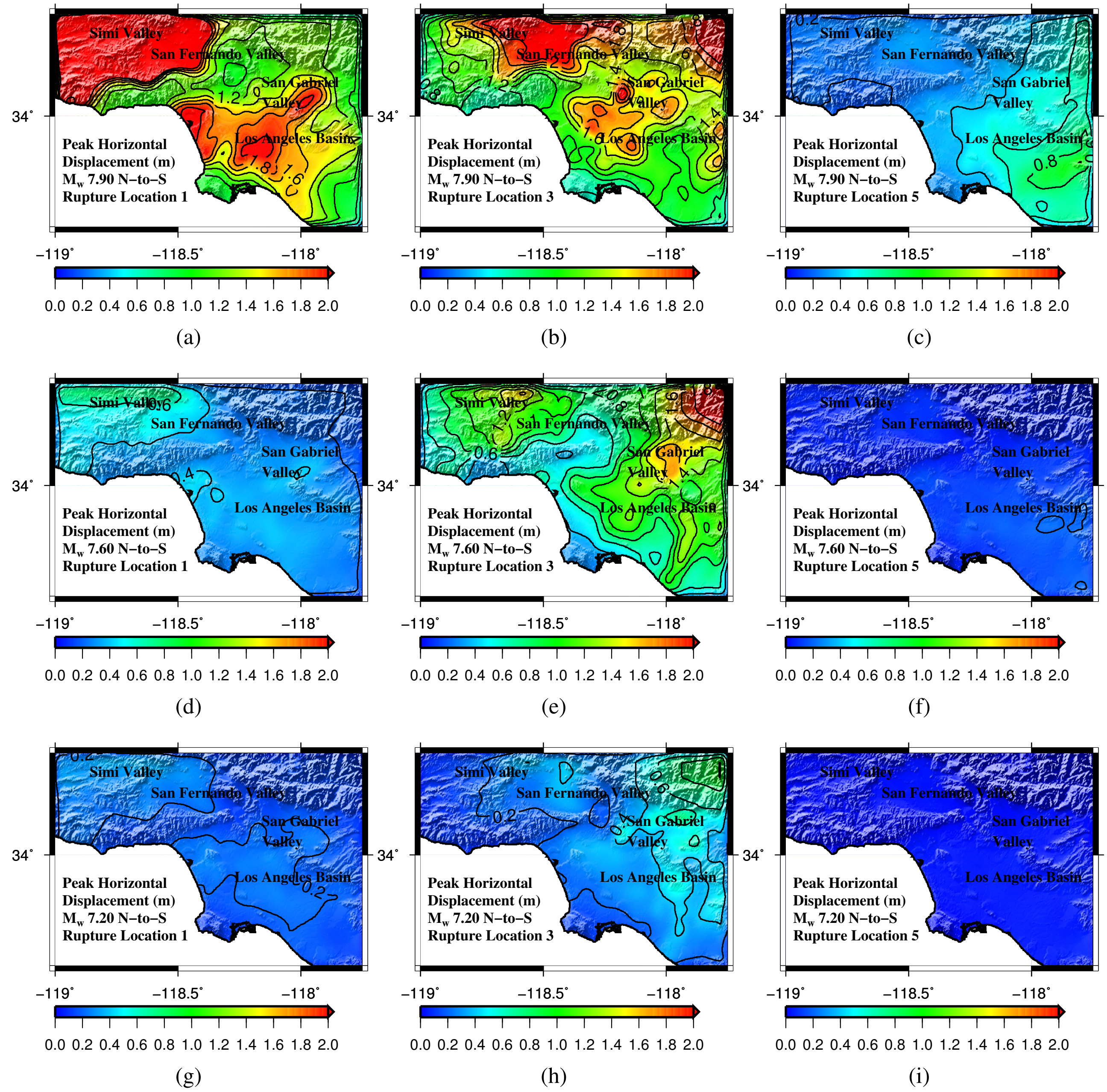
Simi Valley
San Fernando Valley
San Gabriel Valley
Los Angeles Basin
Peak Horizontal Displacement (m)
M$_w$ 7.90 N–to–S
Rupture Location 1
Rupture Location 3
Rupture Location 5
M$_w$ 7.60 N–to–S
M$_w$ 7.20 N–to–S
34˚
–119˚
–118.5˚
–118˚
0.0 0.2 0.4 0.6 0.8 1.0 1.2 1.4 1.6 1.8 2.0
(a)
(b)
(c)
(d)
(e)
(f)
(g)
(h)
(i)

Figure 3.5: Peak horizontal displacement (m) at 636 sites in southern California under north-to-south propagating (a)-(c) $M_w 7.9$, (d)-(f) $M_w 7.6$, and (g)-(i) $M_w 7.6$ scenario earthquakes at locations 1, 3 & 5.

median values of shaking intensities (PGV and PGD). Peak median and median plus one standard deviation values of PGV are about 1 m/s and 1.75 m/s, respectively. The corresponding values of PGD are 1.25 m and 2 m, respectively.

Ground motion prediction equations (GMPEs) or attenuation relations are extensively used in

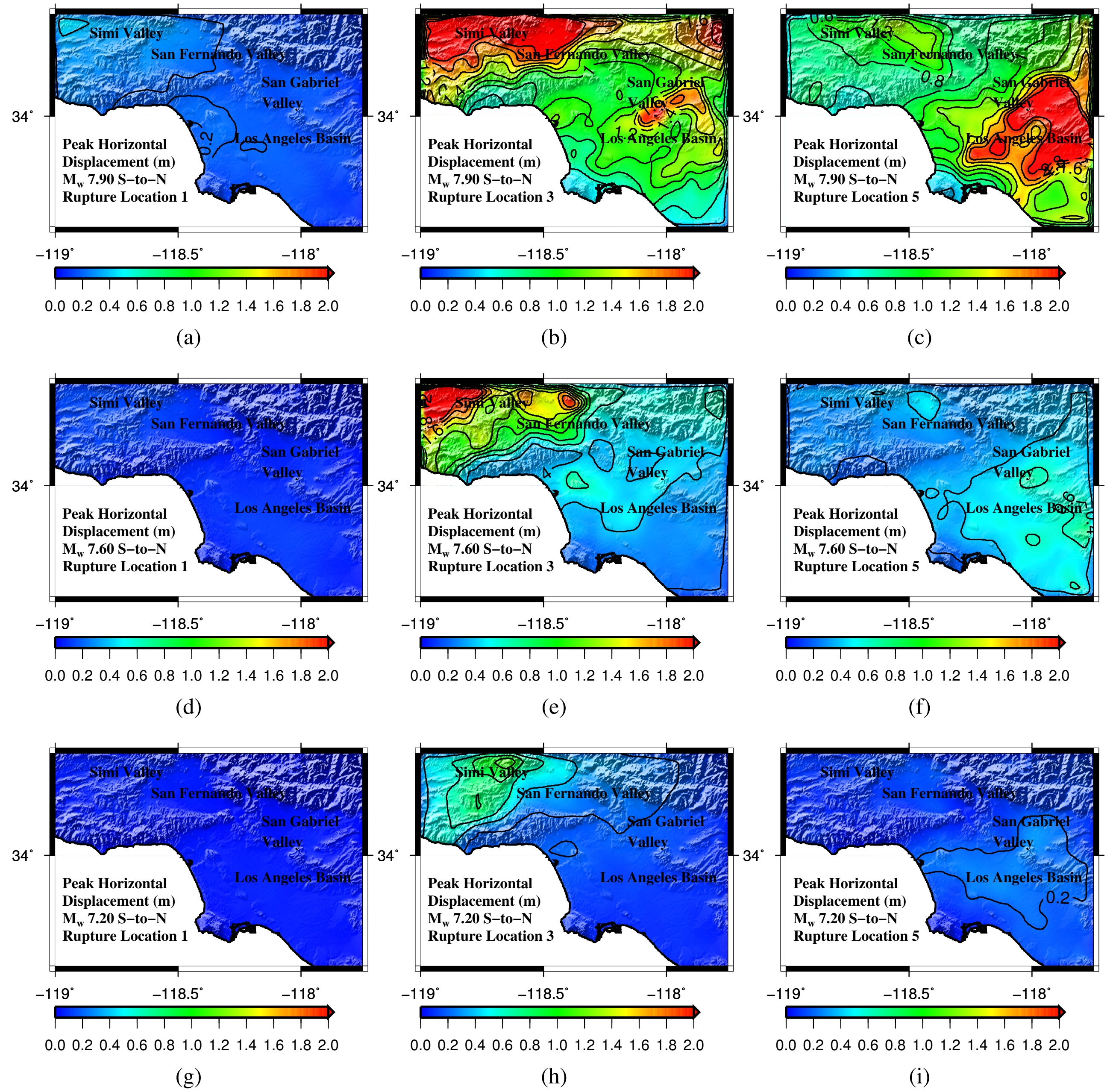
Simi Valley
San Fernando Valley
San Gabriel Valley
Los Angeles Basin
34˚
–119˚
–118.5˚
–118˚
0.0 0.2 0.4 0.6 0.8 1.0 1.2 1.4 1.6 1.8 2.0
Peak Horizontal Displacement (m) M_w 7.90 S–to–N Rupture Location 1
Peak Horizontal Displacement (m) M_w 7.90 S–to–N Rupture Location 3
Peak Horizontal Displacement (m) M_w 7.90 S–to–N Rupture Location 5
Peak Horizontal Displacement (m) M_w 7.60 S–to–N Rupture Location 1
Peak Horizontal Displacement (m) M_w 7.60 S–to–N Rupture Location 3
Peak Horizontal Displacement (m) M_w 7.60 S–to–N Rupture Location 5
Peak Horizontal Displacement (m) M_w 7.20 S–to–N Rupture Location 1
Peak Horizontal Displacement (m) M_w 7.20 S–to–N Rupture Location 3
Peak Horizontal Displacement (m) M_w 7.20 S–to–N Rupture Location 5
0.2
1.2
0.8
1.6
0.2

(a) (b) (c)

(d) (e) (f)

(g) (h) (i)

Figure 3.6: Peak horizontal displacement (m/s) at 636 sites in southern California under south-to-north propagating (a)-(c) $M_w 7.9$, (d)-(f) $M_w 7.6$, and (g)-(i) $M_w 7.6$ scenario earthquakes at locations 1, 3 & 5.

the development of hazard maps for the design and evaluation of structures. Attenuation relationships provide estimates of ground shaking intensity measures such as PGV as a function of distance for various magnitude earthquakes. Here, we compare the geometric mean horizontal velocity (GMHV) and displacement (GMHD), defined as the geometric mean of the maximum of the two horizontal compo-

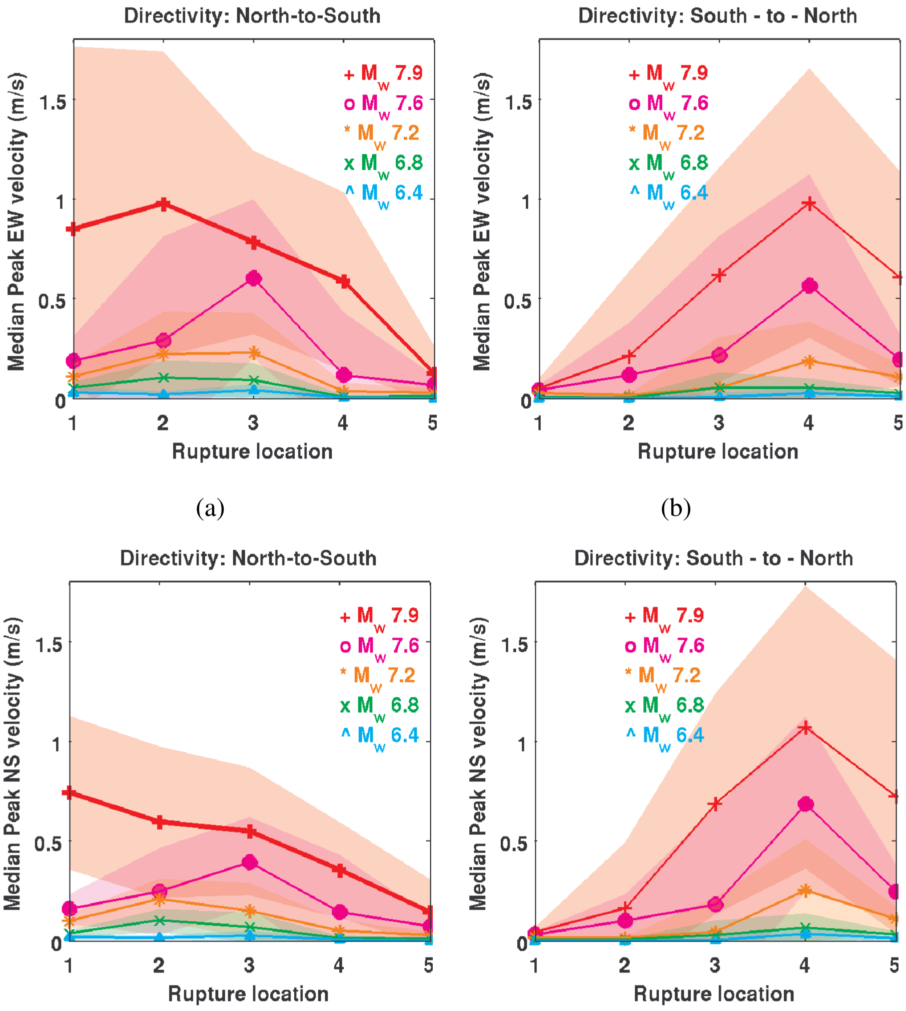

(a)

(b)

(c)

(d)

Figure 3.7: Median peak east-west and north-south ground velocity (m/s) as a function of rupture location along the southern San Andreas fault for various magnitudes: (a),(c) north-to-south and (b),(d) south-to-north propagating rupture. Shaded region represents median PGV +/- one standard deviation.

nents (which may not occur at the same time), predicted by the Campbell-Bozorgnia (C-B, 2008) next generation attenuation (NGA) relation against that from the scenario earthquake simulations. Two site parameters for the Campbell-Bozorgnia NGA relation, the average shear-wave velocity of the top 30 m soil layer (V_s^{30}) and the basin depth, are taken from from Wald and Allen (2007) and the SCEC CVM-H (Plesch et al. 2011), respectively. Shallow V_s^{30} values and deep basins generally lead to stronger ground motion intensities. Rupture directivity is not accounted for in the C-B NGA relation.

Shown in Figs. 3.9(a) – 3.9(d) are the peak median geometric mean horizontal velocity and displacement at 636 sites in southern California as a function of distance for earthquakes with six different magnitudes (6.05, 6.40, 6.80, 7.20, 7.60, 7.90) simulated using the stochastic median model

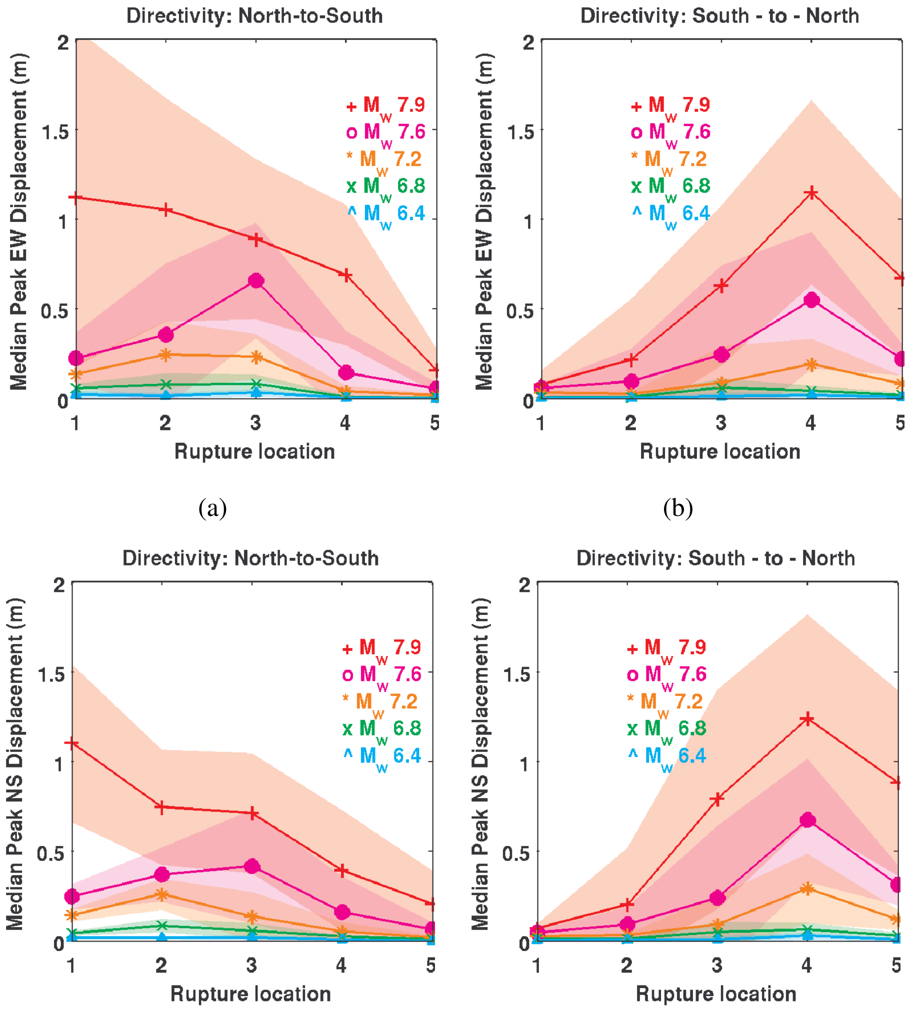

(a) (b)

(c) (d)

Figure 3.8: Median peak east-west and north-south ground displacement (m) as a function of rupture location along the southern San Andreas fault for various magnitudes: (a),(c) north-to-south and (b),(d) south-to-north propagating rupture. Shaded region represents median PGD +/- one standard deviation.

and predicted by the C-B NGA relation. Data from five rupture locations and two rupture propagation directions are included. Source-to-site distance is taken to be the shortest distance from a site to the surface projection of the rupture. Median values are computed by collating data in 2 km wide bins. It may be noted that while the median GMHV predicted by the M_w 6.0, 6.4, and 6.8 earthquake simulations lie close to that predicted by the attenuation relation, the same is not true for the M_w 7.2, 7.6, and 7.9 earthquake simulations. The simulated median GMHV values are significantly higher than that predicted by the NGA relation. For the M_w 7.90 earthquake, simulations produce GMHVs as high as 1.5 m/s, whereas, the C-B NGA relation produces a fifth of that value. However, it is interesting to note that median GMHD predicted by the C-B NGA relation is higher than that predicted by the

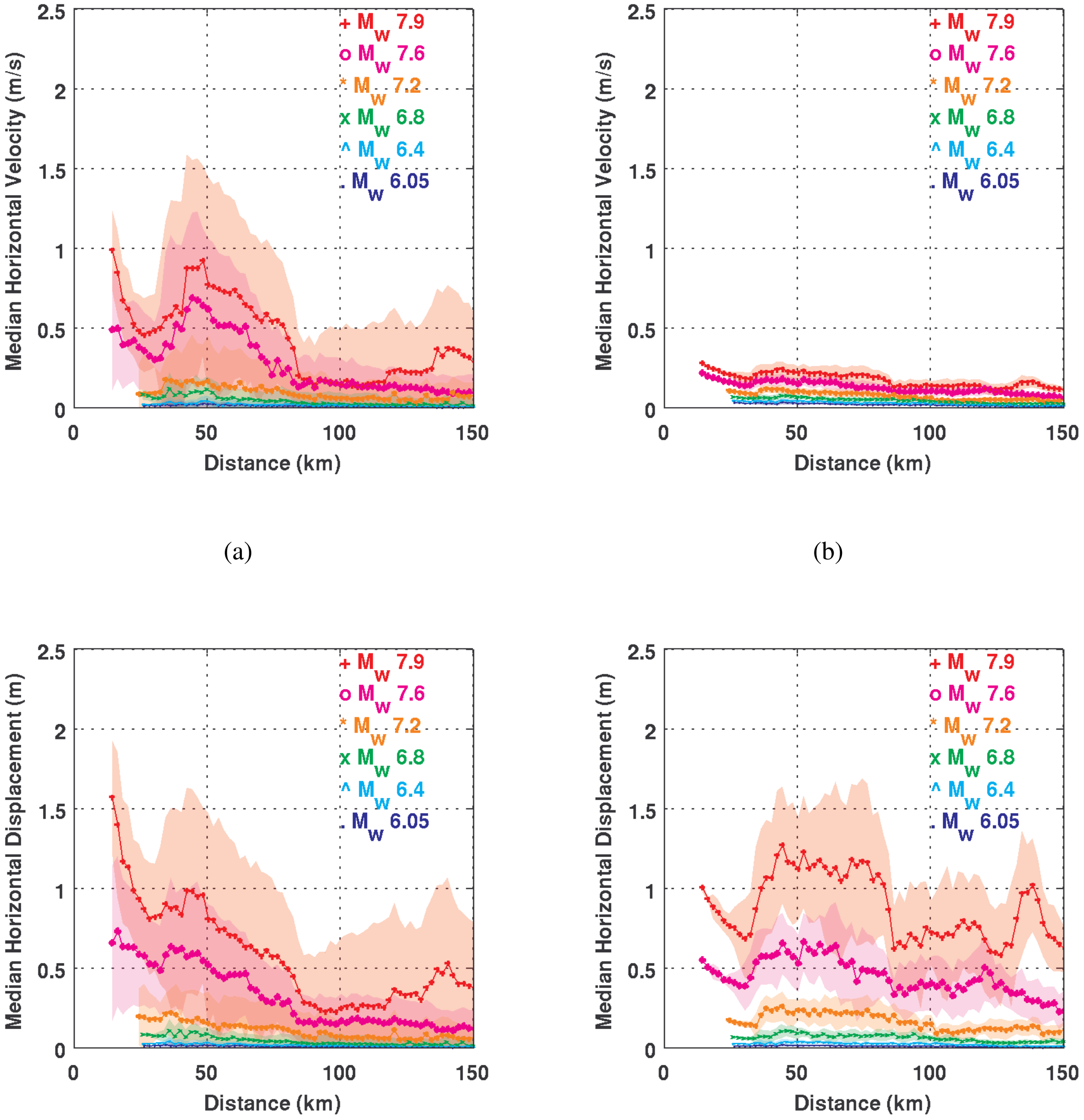

(a) (b)

(c) (d)

Figure 3.9: Median geometric mean horizontal velocity (m/s) and displacement (m) simulated by (a, c) the stochastic median model and predicted by (b, d) the Campbell-Bozorgnia NGA relation at 636 sites in southern California as a function of source-to-site distance for various magnitude ruptures on the southern San Andreas fault. Both north-to-south and south-to-north propagating ruptures are included. Shaded region represents median value +/- one standard deviation.

stochastic median model, especially for source-to-site distances greater than 50 km.

The primary reason for the ground motion intensities in Fig. 3.9 not monotonically decreasing with distance is the presence of four basins (Simi valley, San Fernando valley, Los Angeles basin, and

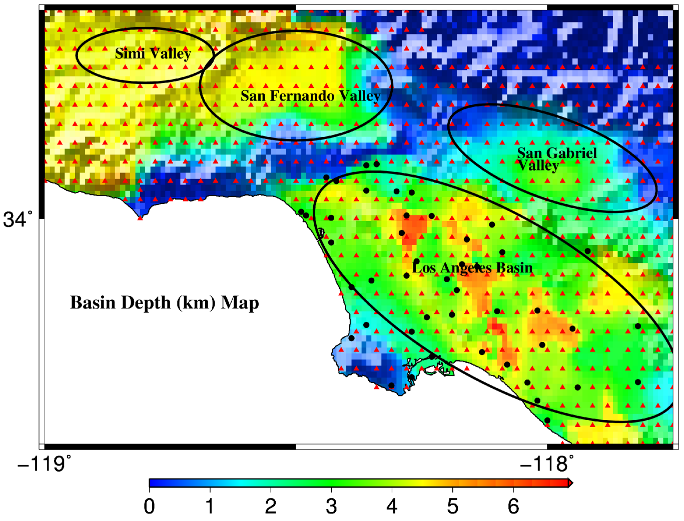
Simi Valley
San Fernando Valley
San Gabriel Valley
Los Angeles Basin
Basin Depth (km) Map
34˚
–119˚
–118˚
0
1
2
3
4
5
6

Figure 3.10: Basin depth (km) map for southern California. Red triangles indicate the geographical distribution of the 636 southern California sites where ground motions from the scenario earthquakes are computed. The ellipses identify the basins in southern California: Simi valley, San Fernando valley, San Gabriel valley and Los Angeles basin.

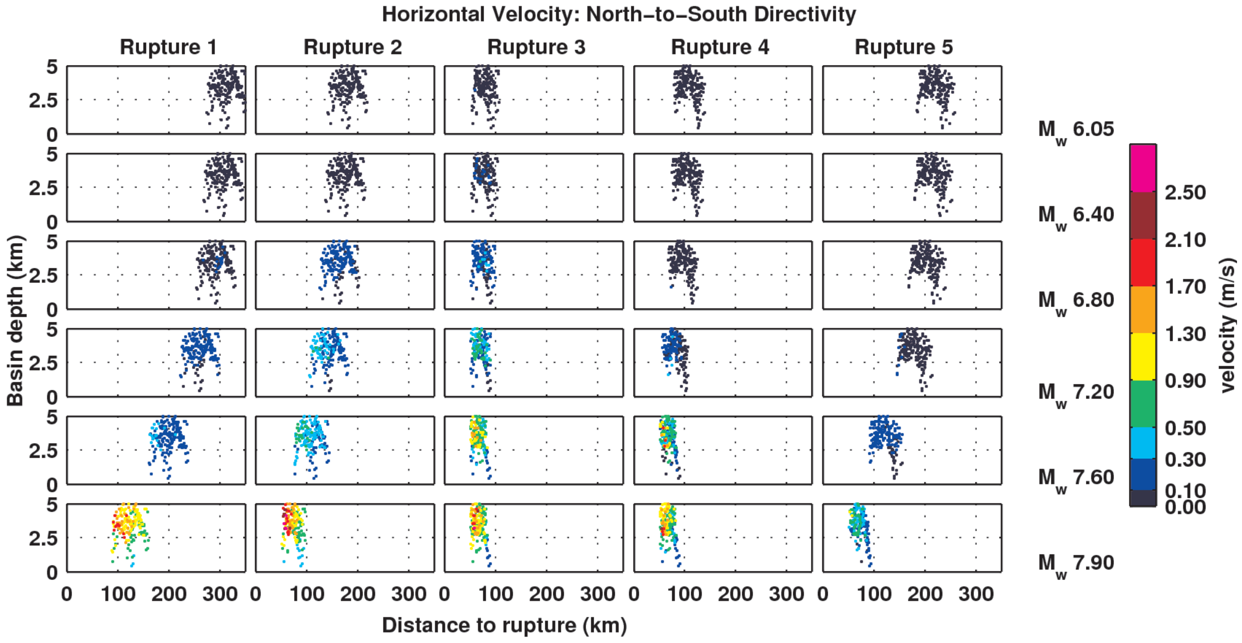

Figure 3.11: Peak horizontal velocity (m/s) at 636 sites in southern California plotted as a function of basin depth (km) and distance to rupture (km) due to north-to-south propagating earthquakes on the southern San Andreas fault of varying magnitudes and rupture locations.

San Gabriel valley; see Fig. 3.10 for basin depths in southern California) at various distances from the fault. The combined effect of basins and site-to-source distance on the peak horizontal velocity (PHV)

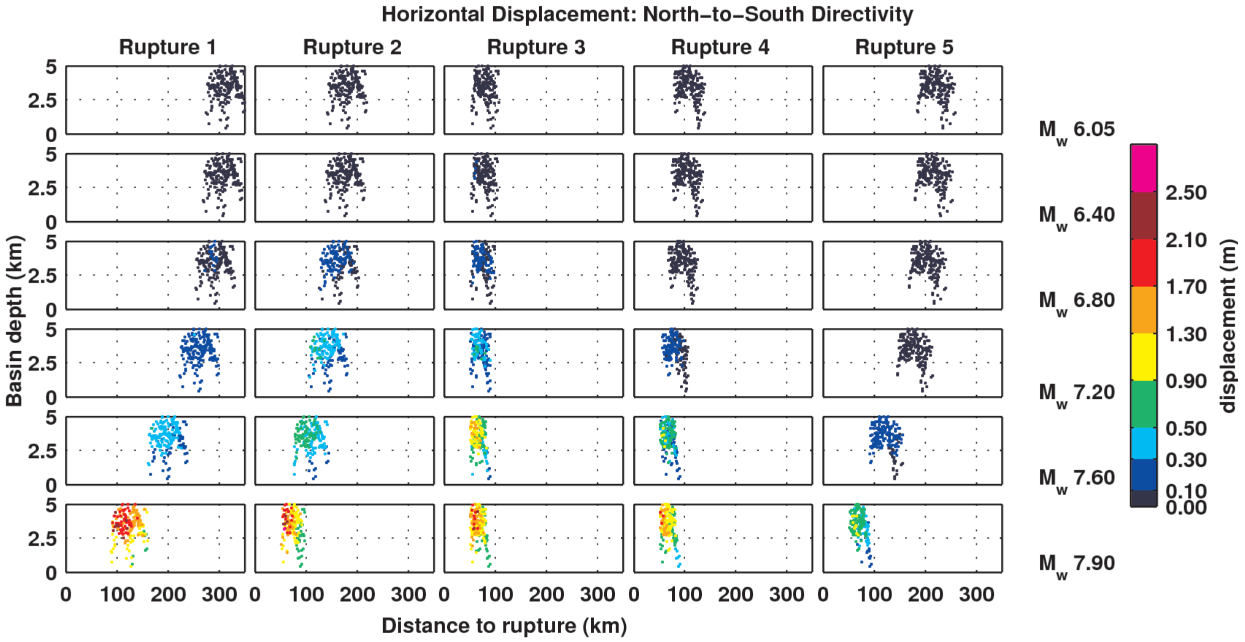

Figure 3.12: Peak horizontal displacement (m) at 636 sites in southern California plotted as a function of basin depth (km) and distance to rupture (km) due to north-to-south propagating earthquakes on the southern San Andreas fault of varying magnitudes and rupture locations.

and displacement (PHD) can be seen in Figs. 3.11 and 3.12, respectively. PHV and PHD are the peak values of the amplitudes of the velocity and displacement vectors over time, respectively. Here, these are plotted as a function of basin depth and site-to-source distance for the North-to-South ruptures of all six magnitudes. In general, PHV and PHD values are higher for deep basin sites that are close to the rupture. However, several anomalous cases can be found: e.g., a site situated at shallower basin depth than another site that is located at the same distance from the source experiences stronger ground motions; a site situated farther from the source than a site with the same basin depth experiences stronger ground motion. These are artifacts of the manner in which source-to-site distance is defined. While the closest distance from a site to the rupture may be short, the distance to the dominant slip asperity may happen to be quite large and vice-versa. Such oddities may result in the discrepancies observed in Figs. 3.11 and 3.12.

To try and isolate the effect of basin depth (from site-to-source distance and rupture propagation direction), we combine the data from all scenario earthquake simulations of a given magnitude (ten ruptures for each magnitude: five rupture locations and two rupture directions). This "stacking" should have an averaging effect, eliminating to a large extent the anomalies associated with distance deter-

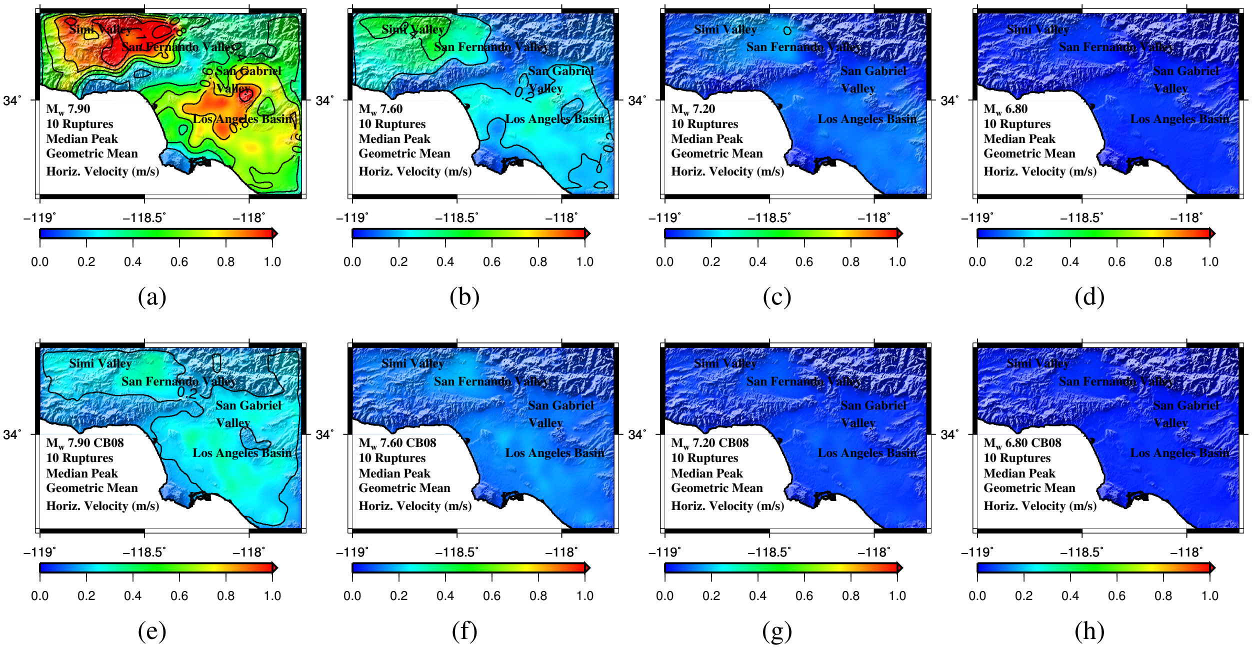
Simi Valley
San Fernando Valley
San Gabriel Valley
Los Angeles Basin
34˚
–119˚
–118.5˚
–118˚
M_w 7.90
M_w 7.60
M_w 7.20
M_w 6.80
M_w 7.90 CB08
M_w 7.60 CB08
M_w 7.20 CB08
M_w 6.80 CB08
10 Ruptures
Median Peak
Geometric Mean
Horiz. Velocity (m/s)
0.0
0.2
0.4
0.6
0.8
1.0
(a)
(b)
(c)
(d)
(e)
(f)
(g)
(h)

Figure 3.13: Median peak geometric mean horizontal velocity (m/s) map for ten ruptures (five locations and two rupture directions) of magnitudes M_w $7.9,\ 7.6,\ 7.2,\ and\ 6.8$ using (a)-(d) simulations; and (e)-(h) Campbell-Bozorgnia NGA relation.

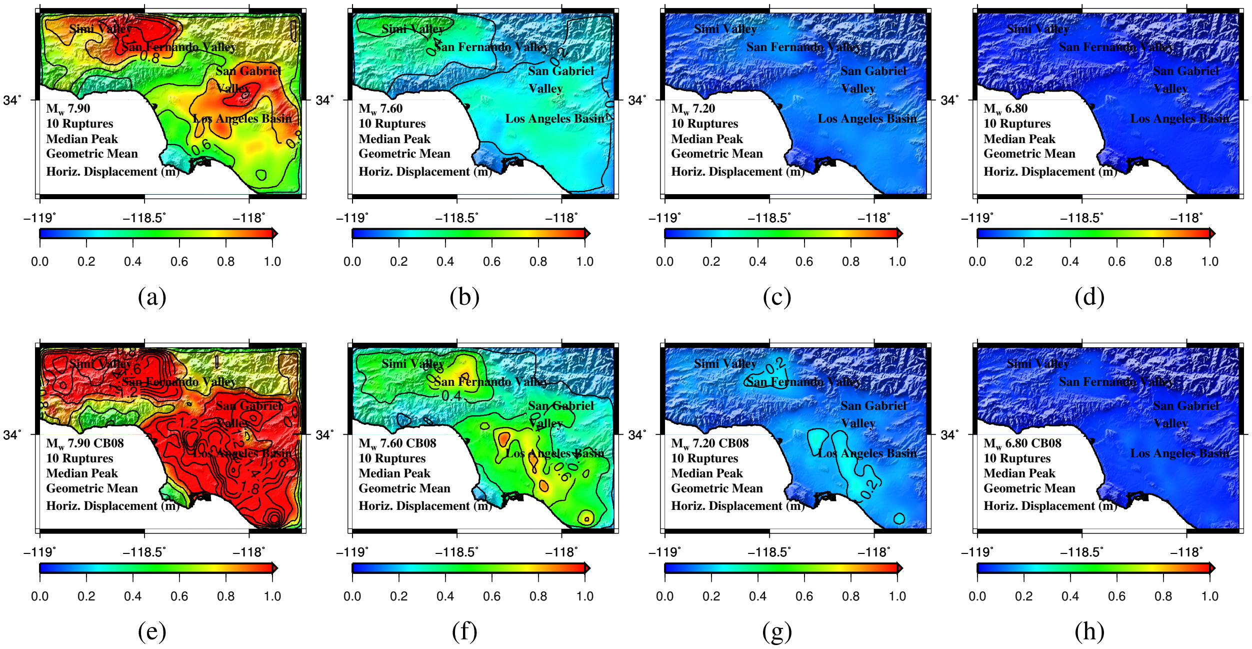
Simi Valley
San Fernando Valley
San Gabriel Valley
Los Angeles Basin
34˚
–119˚
–118.5˚
–118˚
M_w 7.90
M_w 7.60
M_w 7.20
M_w 6.80
M_w 7.90 CB08
M_w 7.60 CB08
M_w 7.20 CB08
M_w 6.80 CB08
10 Ruptures
Median Peak
Geometric Mean
Horiz. Displacement (m)
0.0
0.2
0.4
0.6
0.8
1.0
(a)
(b)
(c)
(d)
(e)
(f)
(g)
(h)

Figure 3.14: Median peak geometric mean horizontal displacement (m) map for ten ruptures (five locations and two rupture directions) of magnitudes M_w $7.9,\ 7.6,\ 7.2,\ and\ 6.8$ using (a)-(d) simulations; and (e)-(h) Campbell-Bozorgnia NGA relation.

mination and the effect of rupture propagation direction. Illustrated in Figs. 3.13 and 3.14 are maps of median peak geometric mean horizontal velocity (m/s) and displacement (m), respectively, of all 10 ruptures of a given magnitude from the simulations and from the Campbell-Bozorgnia attenuation relations. The following observations may be readily made: (i) the ground motion maps from both simulations and NGA relations correlate well with the basin depth map of Fig. 3.10; (ii) median peak GMHVs from simulation are far greater than the predictions by the C-B NGA relation; (iii) median peak GMHDs from simulation are somewhat lower than the predictions by the C-B NGA relation; The comparison of peak GMHVs and GMHDs from the simulations against that predicted by the C-B NGA relation is summarized in Fig. 3.15, where median values of the peak GMHV and GMHD from the two methods are shown plotted as a function of magnitude without consideration to the source-to-site distance.

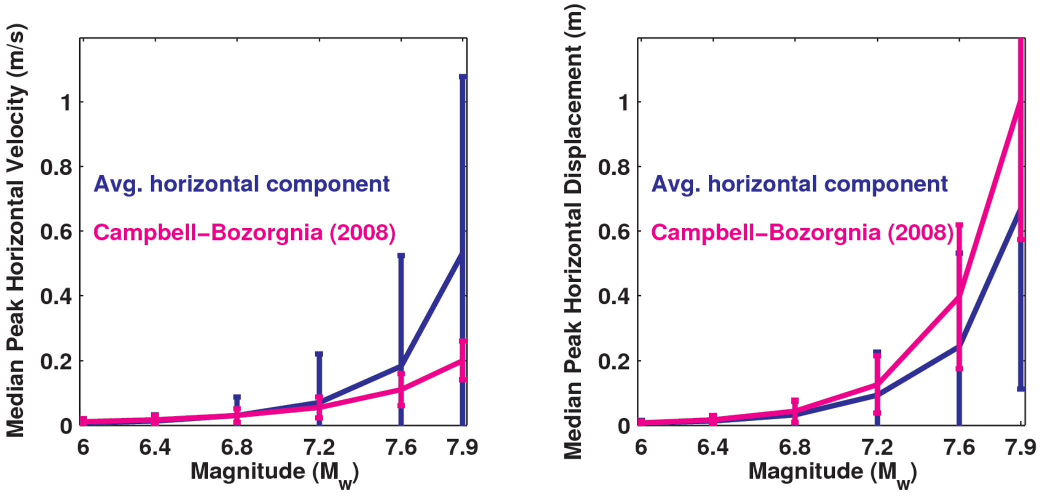

(a) (b)

Figure 3.15: Median peak geometric mean horizontal (a) velocity (m/s) and (b) displacement (m) at 636 sites in southern California from simulations compared against that predicted by the Campbell-Bozorgnia NGA relation as a function of magnitude of earthquakes on the southern San Andreas fault. Two rupture propagation directions (north-to-south and south-to-north and five rupture locations are included.

In addition to slip distribution, source/asperity proximity, rupture directivity, and the presence of basins, other factors that have a strong influence on ground motions are the source parameters of rupture speed and peak rise-time. The median horizontal PGV at all sites in the greater Los Angeles area for north-to-south and south-to-north propagating M_w 7.20, M_w 7.60 and M_w 7.90 earthquakes as a function of the percentage of the rupture propagating at the sub-Rayleigh speed of $0.87\ V_s$ are shown in Figs. 3.16(a) - 3.16(c) and 3.17(a) - 3.17(c), respectively. The corresponding plots of median PGV as

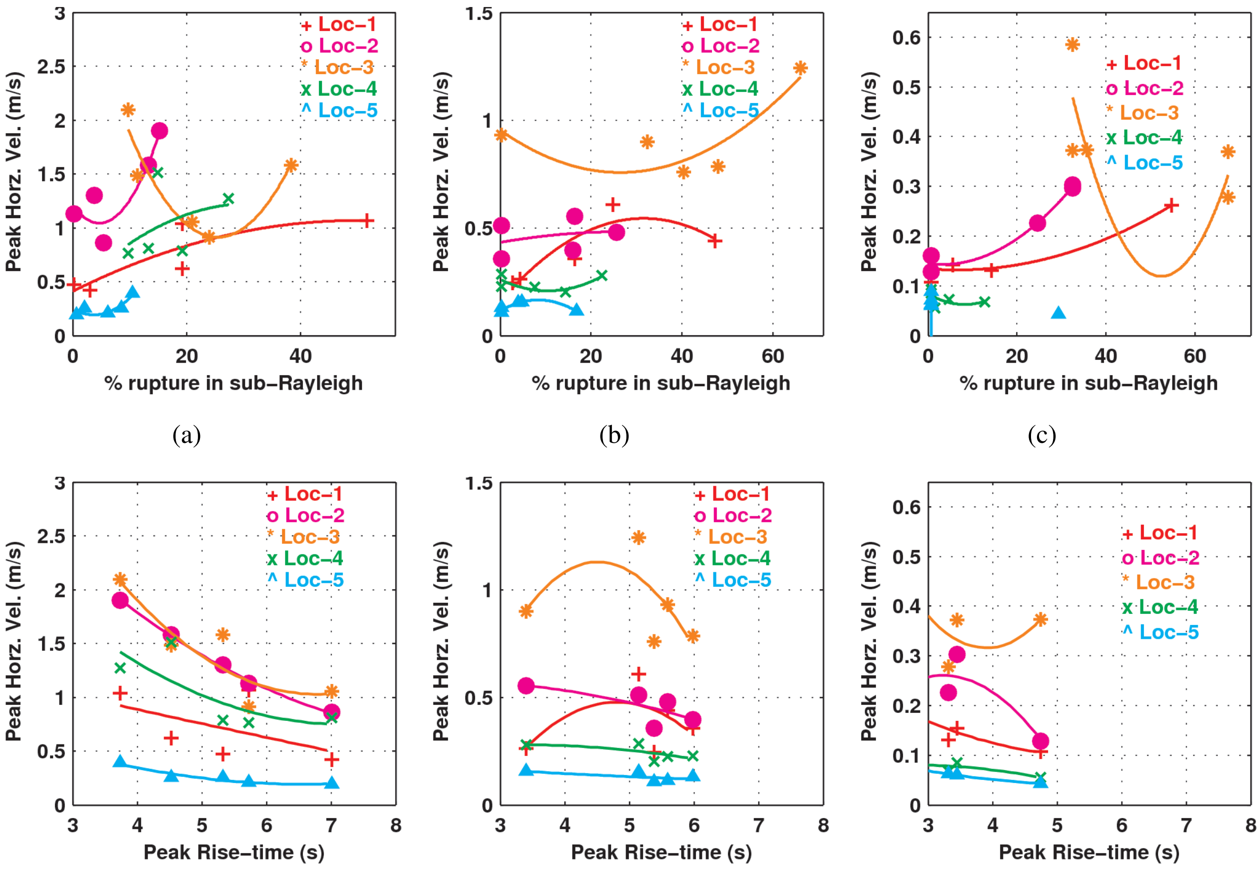

(a) (b) (c)

(d) (e) (f)

Figure 3.16: Median peak horizontal ground velocity (m/s) in southern California for north-to-south propagating M_w 7.90, M_w 7.60, and M_w 7.20 ruptures as a function of (a) - (c) the percentage of rupture propagating at the sub-Rayleigh speed of $0.87V_s$ and (d) - (f) maximum rise-time (s) in the source.

a function of the peak rise-time are shown in Figs. 3.16(d) - 3.16(f) and 3.17(d) - 3.17(f), respectively. In the case of M_w 7.20 and M_w 7.60 earthquakes, significant correlation cannot be seen between the ground motion intensities and rupture speed or peak rise-time. However, for the M_w 7.90 ruptures, it is observed that the greater the percentage of rupture propagating at the sub-Rayleigh speed of $0.87\ V_s$, the stronger are the ground motions. Exceptions to this finding are the N-to-S and S-to-N ruptures at location 3 where this effect is possibly overridden by the stronger influence of the distribution of slip (location and intensity of the main slip asperity, in particular). Median PGV also drops with increasing peak rise-time. No clear difference could be found between the median PGVs generated by the stochastic source models which assume constant slip velocity (or rise-times being proportional to slip) and finite-source inversion models with similar peak rise-times but not proportional to slip (Siriki et al. 2014). We should note that the sources used here may or may not capture the full range of

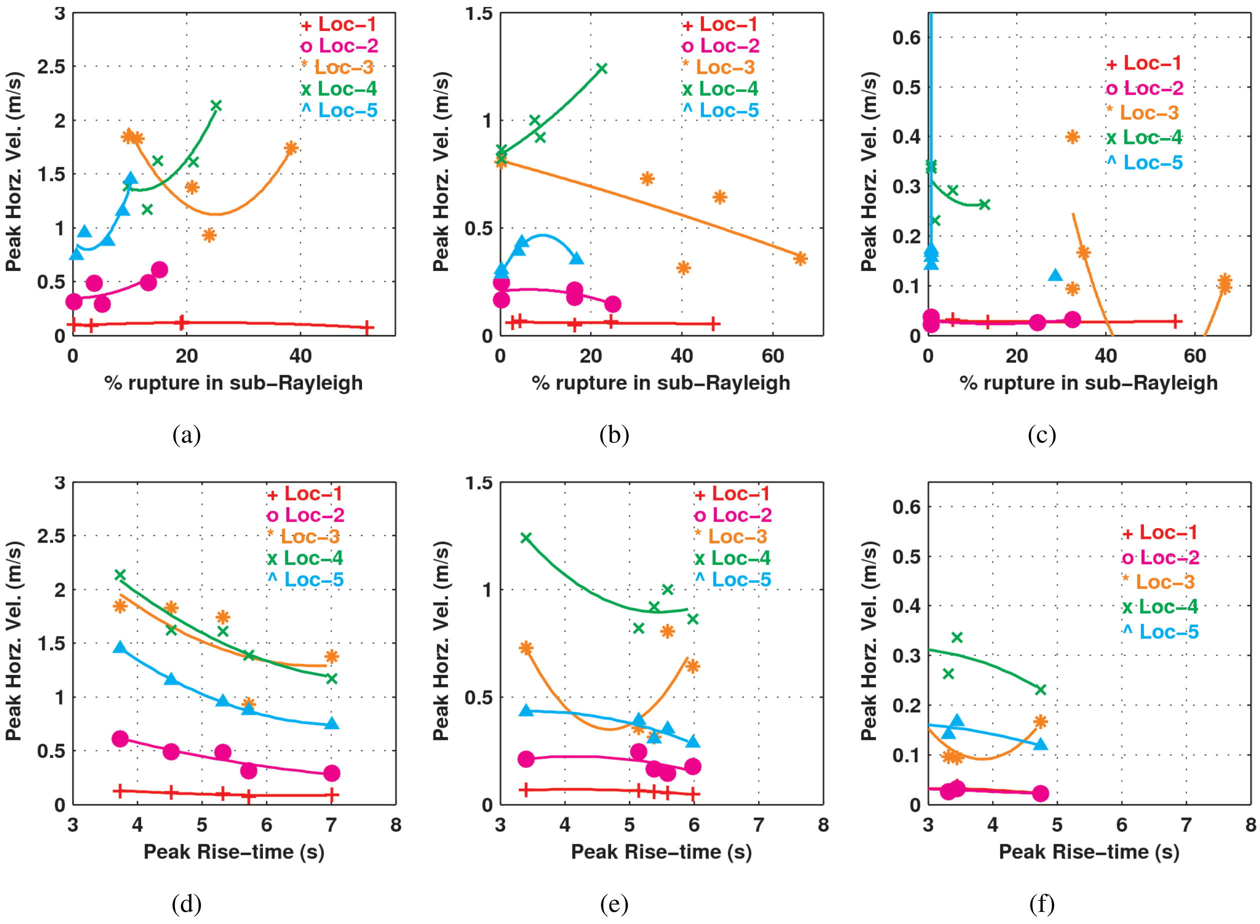

(a) (b) (c)

(d) (e) (f)

Figure 3.17: Median peak horizontal ground velocity (m/s) in southern California for south-to-north propagating M_w 7.90, M_w 7.60, and M_w 7.20 ruptures as a function of (a) - (c) the percentage of rupture propagating at the sub-Rayleigh speed of $0.87V_s$ and (d) - (f) maximum rise-time (s) in the source.

plausible sources on faults such as the San Andreas and/or the ground motions produced by them. A statistical study may be necessary to quantify the number of stochastic models needed to capture this variability with the desired statistical significance.

3.2.5 Structural response under the scenario earthquakes

The target buildings shown in Fig. 3.1 are analyzed under the 3-component ground motion histories simulated at the 636 sites in southern California for the 60 scenario earthquakes (6 magnitudes x 5 rupture locations x 2 rupture propagation directions). As described previously, the 3-D nonlinear dynamic analysis program FRAME3D is used for this purpose. Structural performance is quantified in terms of the peak inter-story drift ratio (IDR).

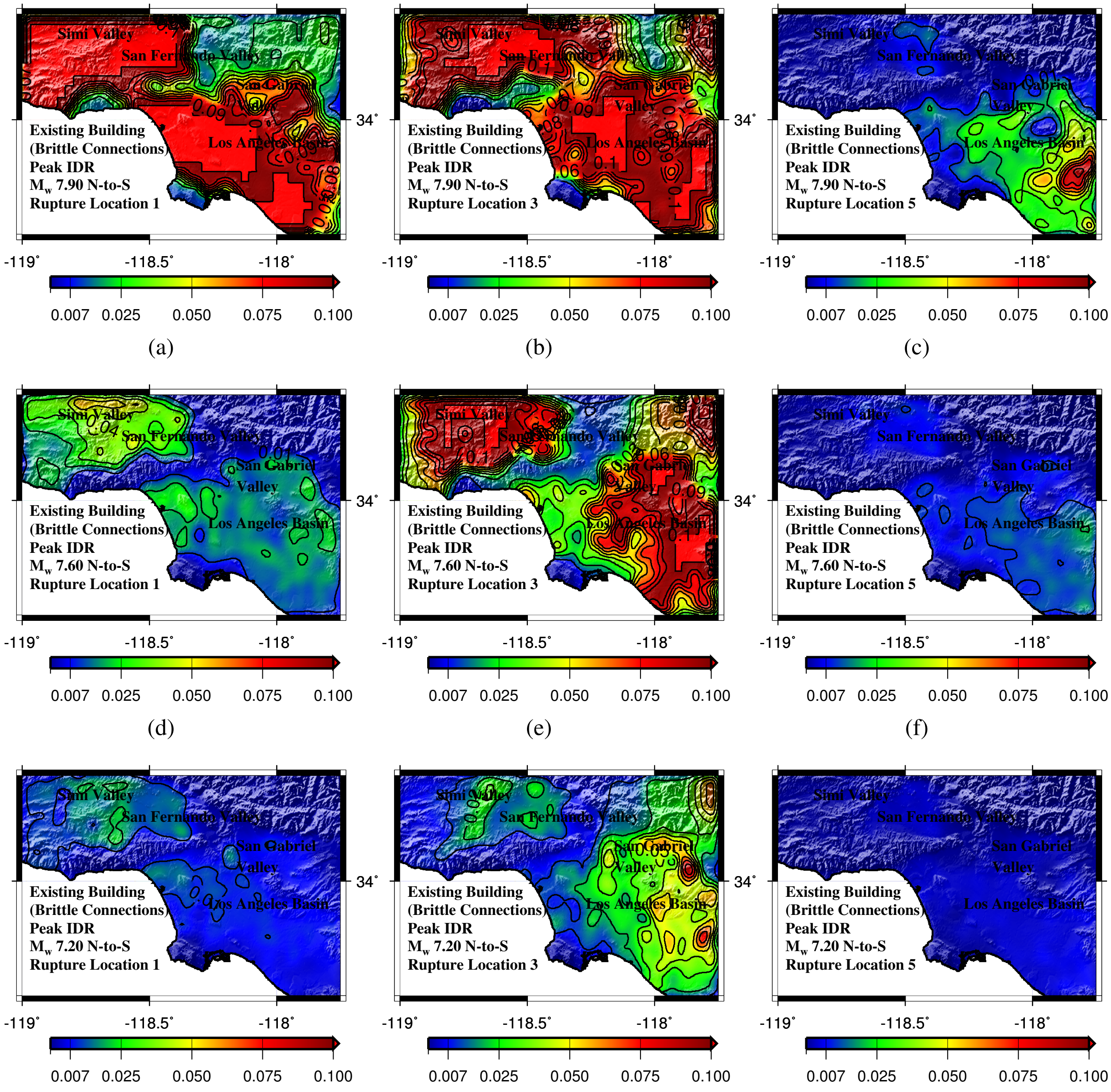
Simi Valley
San Fernando Valley
San Gabriel Valley
Los Angeles Basin
34˚
-119˚
-118.5˚
-118˚
0.007
0.025
0.050
0.075
0.100
Existing Building (Brittle Connections) Peak IDR M_w 7.90 N-to-S Rupture Location 1
Existing Building (Brittle Connections) Peak IDR M_w 7.90 N-to-S Rupture Location 3
Existing Building (Brittle Connections) Peak IDR M_w 7.90 N-to-S Rupture Location 5
Existing Building (Brittle Connections) Peak IDR M_w 7.60 N-to-S Rupture Location 1
Existing Building (Brittle Connections) Peak IDR M_w 7.60 N-to-S Rupture Location 3
Existing Building (Brittle Connections) Peak IDR M_w 7.60 N-to-S Rupture Location 5
Existing Building (Brittle Connections) Peak IDR M_w 7.20 N-to-S Rupture Location 1
Existing Building (Brittle Connections) Peak IDR M_w 7.20 N-to-S Rupture Location 3
Existing Building (Brittle Connections) Peak IDR M_w 7.20 N-to-S Rupture Location 5

(a) (b) (c)

(d) (e) (f)

(g) (h) (i)

Figure 3.18: Peak inter-story drift ratio (IDR) maps for the existing building with brittle connections under ground motion from north-to-south propagating (a) - (c) M_w 7.9, (d) - (f) M_w 7.6, and (g) - (i) M_w 7.2 earthquakes on the southern San Andreas fault at rupture locations 1, 3, & 5.

The peak IDR in the existing and redesigned building models for the median north-to-south propagating M_w 7.9, 7.6, and 7.2 scenario earthquake ruptures at locations 1, 3, and 5 are illustrated in Figs. 3.18 and 3.19, respectively. The corresponding maps for south-to-north propagating ruptures are

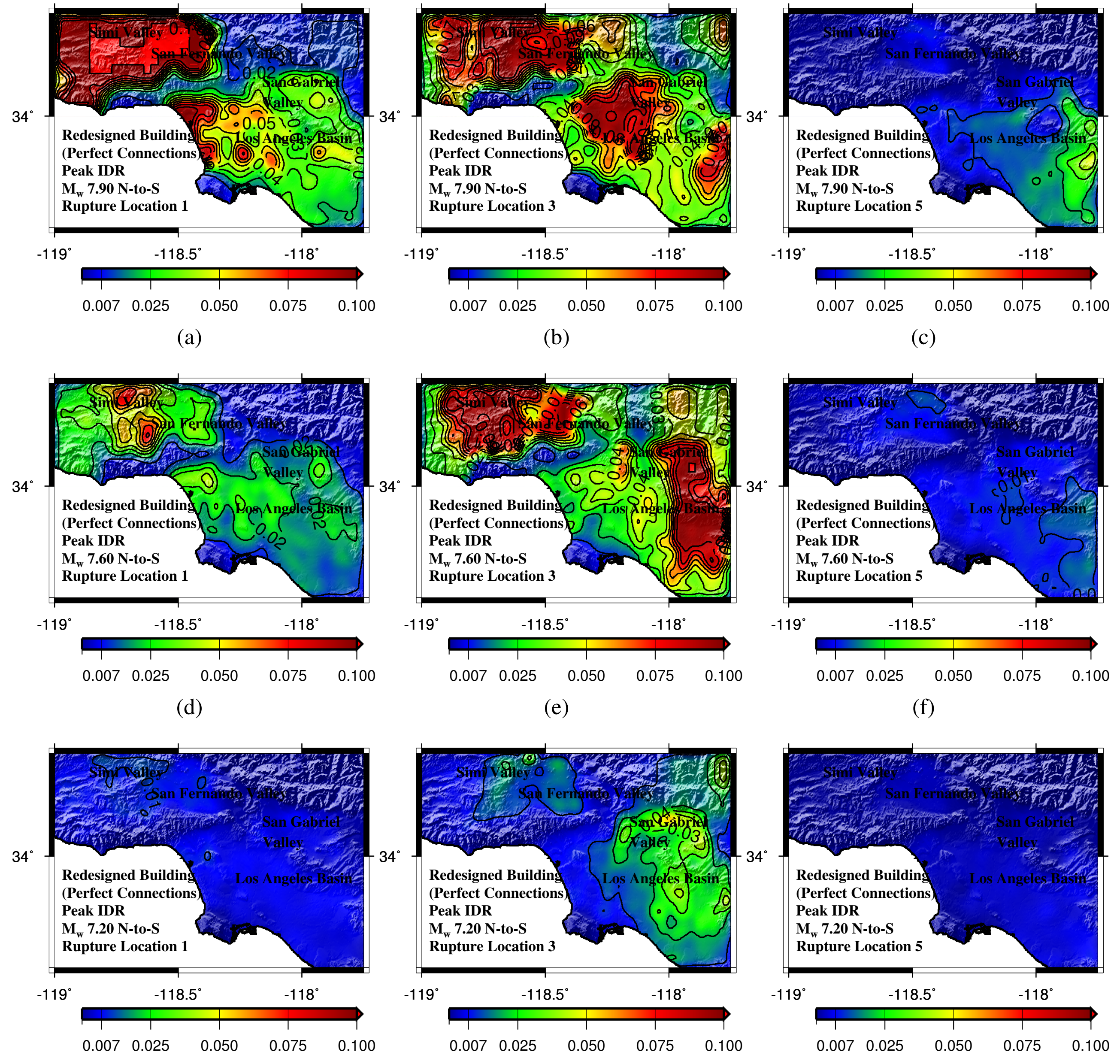
Simi Valley
San Fernando Valley
San Gabriel Valley
Los Angeles Basin
Redesigned Building (Perfect Connections) Peak IDR M_w 7.90 N-to-S Rupture Location 1
Redesigned Building (Perfect Connections) Peak IDR M_w 7.90 N-to-S Rupture Location 3
Redesigned Building (Perfect Connections) Peak IDR M_w 7.90 N-to-S Rupture Location 5
Redesigned Building (Perfect Connections) Peak IDR M_w 7.60 N-to-S Rupture Location 1
Redesigned Building (Perfect Connections) Peak IDR M_w 7.60 N-to-S Rupture Location 3
Redesigned Building (Perfect Connections) Peak IDR M_w 7.60 N-to-S Rupture Location 5
Redesigned Building (Perfect Connections) Peak IDR M_w 7.20 N-to-S Rupture Location 1
Redesigned Building (Perfect Connections) Peak IDR M_w 7.20 N-to-S Rupture Location 3
Redesigned Building (Perfect Connections) Peak IDR M_w 7.20 N-to-S Rupture Location 5
34°
-119°
-118.5°
-118°
0.007
0.025
0.050
0.075
0.100

(a) (b) (c)

(d) (e) (f)

(g) (h) (i)

Figure 3.19: Peak inter-story drift ratio (IDR) maps for the redesigned building with perfect connections under ground motion from north-to-south propagating (a) - (c) M_w 7.9, (d) - (f) M_w 7.6, and (g) - (i) M_w 7.2 earthquakes on the southern San Andreas fault at rupture locations 1, 3, & 5.

given in Figs. 3.20 and 3.21, respectively. For the existing building, peak IDR values beyond 0.05 are indicative of severe damage, whereas values below 0.01 are indicative of minimal damage not requiring any significant repair. For the redesigned building, peak IDRs beyond 0.06 are indicative of severe damage. As observed for ground motions, the performance of both existing and redesigned moment

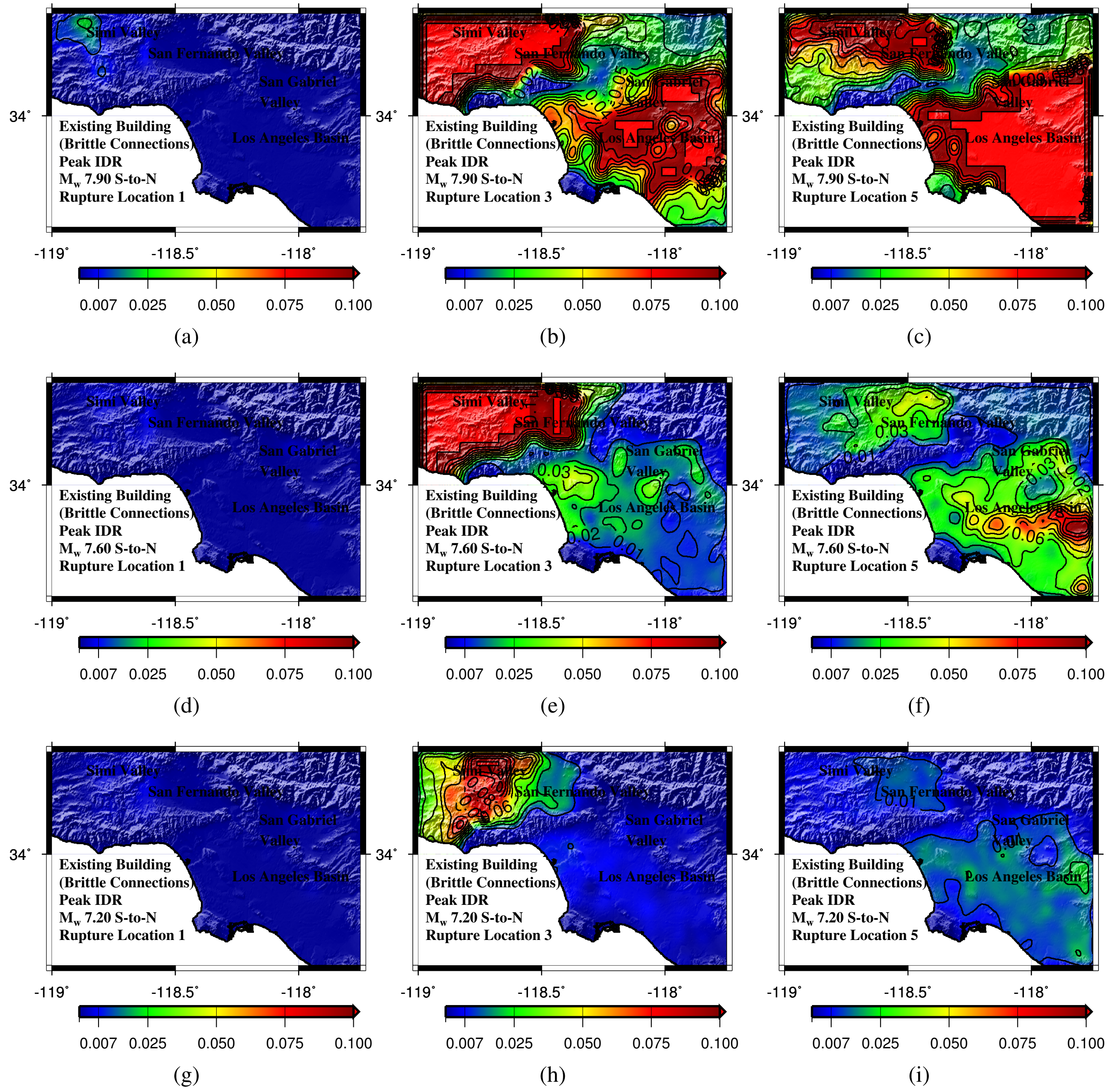
Simi Valley
San Fernando Valley
San Gabriel Valley
Los Angeles Basin
34˚
-119˚
-118.5˚
-118˚
0.007
0.025
0.050
0.075
0.100
Existing Building (Brittle Connections) Peak IDR M_w 7.90 S-to-N Rupture Location 1
Existing Building (Brittle Connections) Peak IDR M_w 7.90 S-to-N Rupture Location 3
Existing Building (Brittle Connections) Peak IDR M_w 7.90 S-to-N Rupture Location 5
Existing Building (Brittle Connections) Peak IDR M_w 7.60 S-to-N Rupture Location 1
Existing Building (Brittle Connections) Peak IDR M_w 7.60 S-to-N Rupture Location 3
Existing Building (Brittle Connections) Peak IDR M_w 7.60 S-to-N Rupture Location 5
Existing Building (Brittle Connections) Peak IDR M_w 7.20 S-to-N Rupture Location 1
Existing Building (Brittle Connections) Peak IDR M_w 7.20 S-to-N Rupture Location 3
Existing Building (Brittle Connections) Peak IDR M_w 7.20 S-to-N Rupture Location 5
0.01
0.02
0.03
0.06
(a)
(b)
(c)
(d)
(e)
(f)
(g)
(h)
(i)

Figure 3.20: Peak inter-story drift ratio (IDR) maps for the existing building with brittle connections under ground motion from south-to-north propagating (a) - (c) M_w 7.9, (d) - (f) M_w 7.6, and (g) - (i) M_w 7.2 earthquakes on the southern San Andreas fault at rupture locations 1, 3, & 5.

frame buildings depend upon the direction of propagation and location of the rupture. For instance, amongst earthquakes rupturing location 1, the north-to-south propagating ruptures cause far greater damage than the south-to-north propagating ruptures. The opposite holds true for ruptures occurring at location 5. For north-to-south propagating ruptures, the hot-spots (regions of high peak IDR) tend

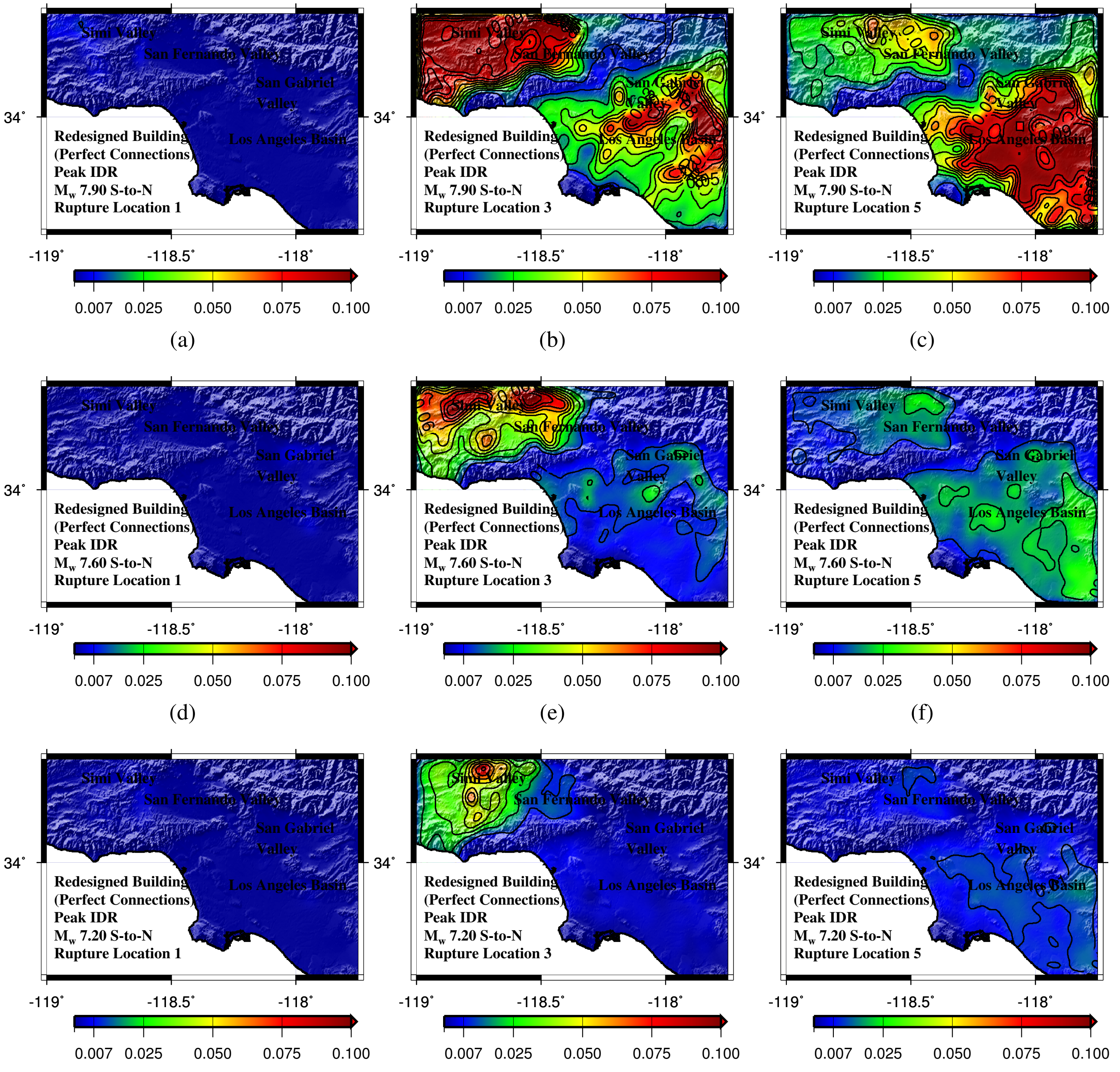
Simi Valley
San Fernando Valley
San Gabriel Valley
Los Angeles Basin
34˚
-119˚
-118.5˚
-118˚
0.007
0.025
0.050
0.075
0.100
Redesigned Building (Perfect Connections) Peak IDR M_w 7.90 S-to-N Rupture Location 1
Redesigned Building (Perfect Connections) Peak IDR M_w 7.90 S-to-N Rupture Location 3
Redesigned Building (Perfect Connections) Peak IDR M_w 7.90 S-to-N Rupture Location 5
Redesigned Building (Perfect Connections) Peak IDR M_w 7.60 S-to-N Rupture Location 1
Redesigned Building (Perfect Connections) Peak IDR M_w 7.60 S-to-N Rupture Location 3
Redesigned Building (Perfect Connections) Peak IDR M_w 7.60 S-to-N Rupture Location 5
Redesigned Building (Perfect Connections) Peak IDR M_w 7.20 S-to-N Rupture Location 1
Redesigned Building (Perfect Connections) Peak IDR M_w 7.20 S-to-N Rupture Location 3
Redesigned Building (Perfect Connections) Peak IDR M_w 7.20 S-to-N Rupture Location 5

(a) (b) (c)

(d) (e) (f)

(g) (h) (i)

Figure 3.21: Peak inter-story drift ratio (IDR) maps for the redesigned building with perfect connections under ground motion from south-to-north propagating (a) - (c) M_w 7.9, (d) - (f) M_w 7.6, and (g) - (i) M_w 7.2 earthquakes on the southern San Andreas fault at rupture locations 1, 3, & 5.

to migrate east-southeast as rupture is shifted from location 1 to location 5. The opposite is true for south-to-north propagating ruptures, with the hot-spots migrating west-northwest as rupture is shifted from location 5 to location 1. Across all magnitudes, no hotspots occur in the greater Los Angeles region for for location 1 ruptures propagating towards Parkfield and location 5 ruptures propagating towards Bombay Beach. The performance of the redesigned building is generally better than that of the existing building. Nevertheless, certain ruptures do place significant demands on it at several sites.

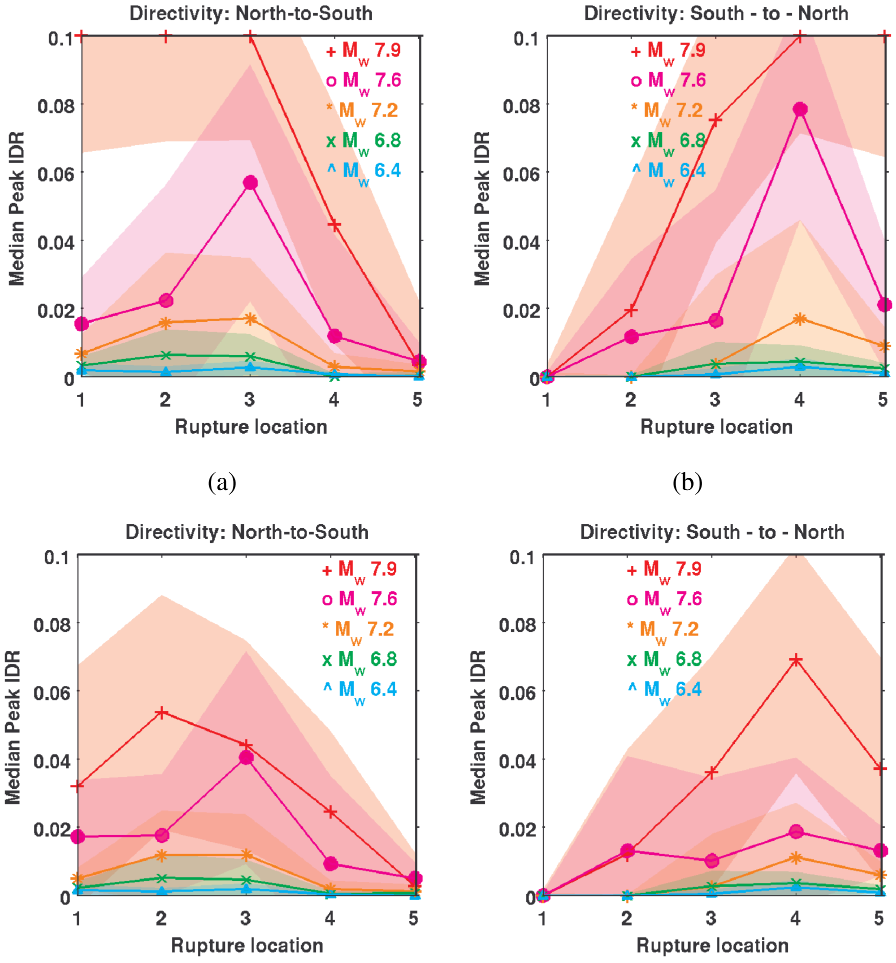

(a) (b)

(c) (d)

Figure 3.22: Median peak interstory drift ratio in the (a) - (b) existing and (c) - (d) redesigned buildings as a function of rupture location for north-to-south and south-to-north propagating scenario earthquakes of various magnitudes on the southern San Andreas fault. Shaded region represents median +/- one standard deviation

Fig. 3.22 shows the median peak IDR (shaded region represents median +/- one standard deviation) in the existing and redesigned buildings for all scenario earthquakes as a function of rupture location. Responses under north-to-south and south-to-north ruptures are shown separately. Irrespective of location and propagation direction, M_w $6.0 - 6.8$ ruptures do not impose significant drift demands on either building. Median response for both buildings falls below the peak IDR limit for the IO performance level. Median response under M_w 7.2 ruptures suggests building closure for repairs may be necessary, but life-safety may not be compromised in either building. Magnitudes 7.6

and 7.9 lead to a significant increase in the demands on both structures, with median IDRs exceeding CP performance levels in both buildings. In fact, the existing building model collapses in quite a few instances. Shown in Fig. 3.23 is the median value of the peak IDR for the existing and redesigned buildings as a function of scenario earthquake magnitude. In a significant number of cases, collapse is initiated in our models once peak IDR reaches 0.10. However, our models do not include local flange buckling in beams or columns. Local buckling of column flanges will likely hasten collapse initiation. In a study on seismic performance evaluation of 20-story steel moment frame buildings with brittle connections, Lee and Foutch (2002) found a median drift capacity of 0.07 for pre-Northridge steel moment frame buildings. Here, the median peak IDR in the existing building model under a M_w 7.90 earthquake is 0.055 (greater than the collapse prevention performance limit state), suggesting a state of imminent collapse, perhaps necessitating red tagging. A median peak IDR value of 0.025 for the redesigned building points to the significant improvements that have been made in seismic codes after the Northridge earthquake. Of course, our redesigned building model assumes that the connections behave in a ductile manner. Whether this will hold true remains to be seen.

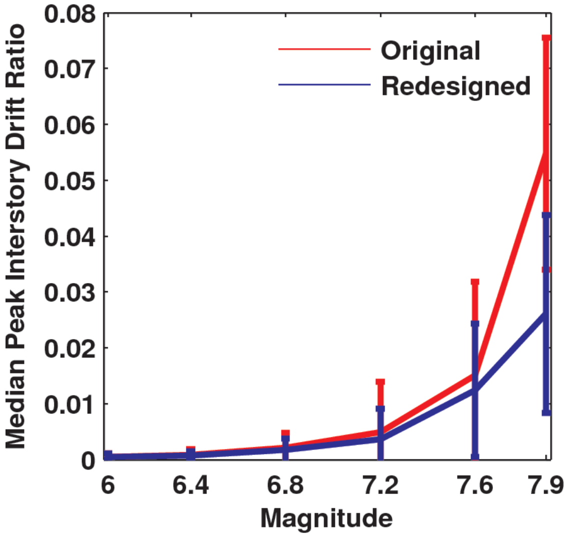

Figure 3.23: Median peak IDR in the existing and redesigned buildings plotted as a function of San Andreas fault scenario earthquake magnitude. The bars correspond to median +/- one standard deviation.

The median acceleration spectra of the EW and NS components of the simulated long period ($\geq$ 2 s) ground motion histories from M_w 7.2, M_w 7.6, and M_w 7.6 scenario earthquakes (data from both propagation directions included) are shown in Fig. 3.24. The shaded region represents the median +/- one standard deviation. The data have been combined into three bins with median source-to-site distances of 25 km, 65 km, and 105 km. The UBC97 design spectrum corresponding to soil type S_B and Fault Type A at a distance of 5 km is also shown for comparison. From the figure, it is clear that code-prescribed hazard fully accounts for the ground shaking intensities from M_w 7.20 earthquakes. However, median spectral accelerations in basin sites (at an average distance of 65 km) from M_w 7.9 earthquakes and median + one standard deviation spectral accelerations from M_w 7.6 earthquakes exceed the UBC97 spectral accelerations, on the average, by a factor of 2 in the long period regime ($\geq$ 2 s). In determining the median acceleration spectrum for a given source-to-site distance, the scenario earthquake data are collated into 6 km bins.

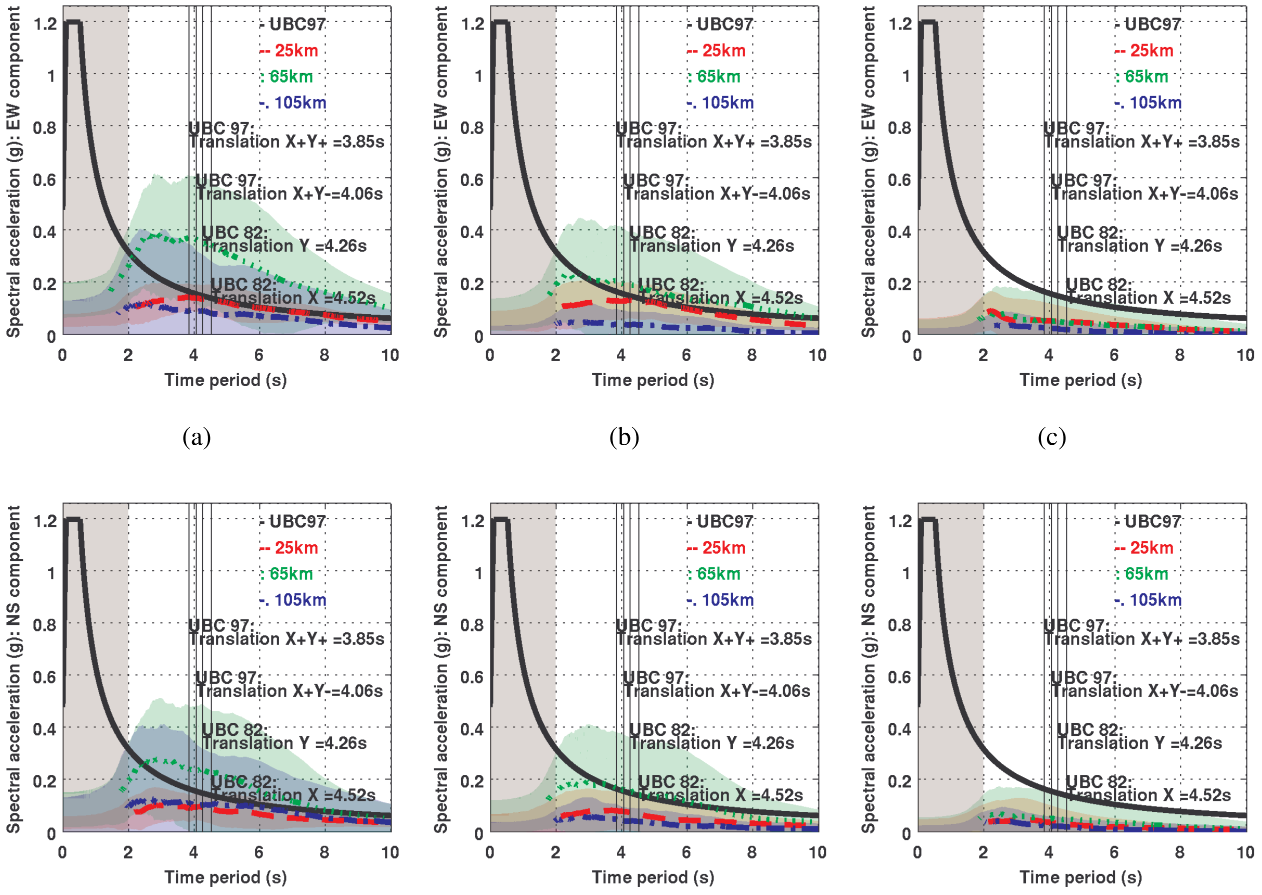

(a) (b) (c)

(d) (e) (f)

Figure 3.24: Median pseudo-acceleration (g) spectra of (a) - (c) East-West and (d) - (f) North-South components of simulated ground motion histories from M_w $7.90, 7.60$, and 7.20 scenario earthquakes (data from north-to-south and south-to-north ruptures are combined) for various source-to-site distances. Also shown in black for comparison is the UBC97 MCE spectrum (soil classification S_B, fault type A at 5 km distance).

In their study using idealized sawtooth-like ground motion waveforms, Krishnan and Muto

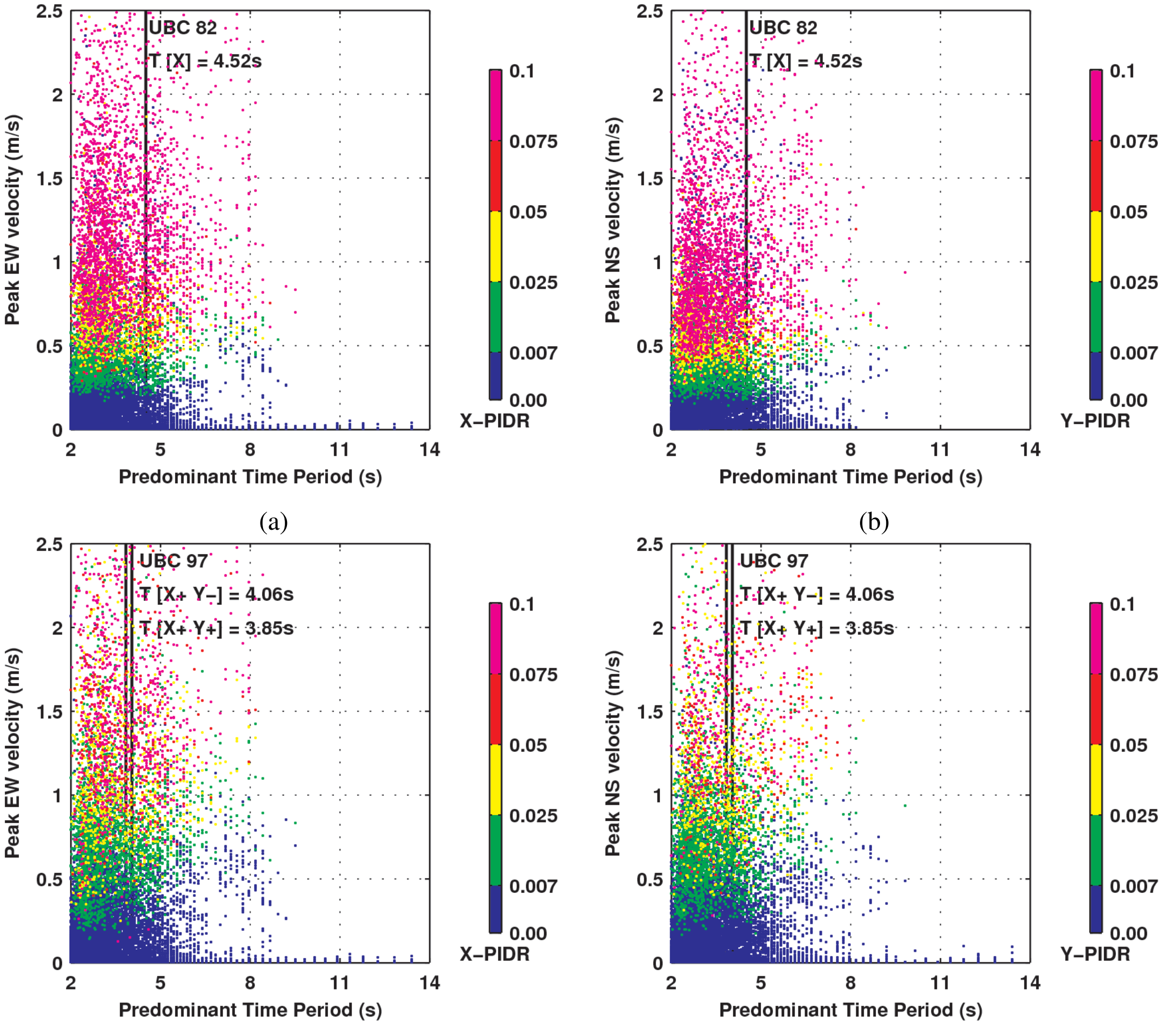

(a) (b)

(c) (d)

Figure 3.25: X (EW) and Y (NS) peak interstory drift ratios in (a)-(b) the existing, and (c)-(d) the redesigned buildings as a function of predominant time-period (s) of EW and NS components of ground velocity histories and the corresponding PGV (m/s) from all 60 scenario earthquakes on the southern San Andreas fault (6 magnitudes, 5 rupture locations, 2 rupture directions). Peak IDR of 0.007, 0.025, and 0.05 correspond to the FEMA356 limits for IO, LS, and CP performance levels.

(2013) pointed out that the response of the existing and redesigned buildings are sensitive to peak ground velocity, waveform period, and number of cycles. Shown in Fig. 3.25 are the peak IDR response of the two structures under all sixty scenario earthquakes on the southern San Andreas fault as a function of the predominant ground motion period (s) and PGV (m/s). Predominant ground motion period is taken to be the period at which the pseudo-acceleration spectrum peaks. The following observations can be made: (i) Peak IDRs largely remain below the IO performance limit when the PGV is below 0.2 m/s or so, indicating little or no disruption to building function. (ii) The existing building is under a significant risk for collapse (PIDR > 0.075) under ground motions with PGV greater than about 0.6 m/s. (iii) The redesigned building is more robust and is at significant risk of collapse only under ground motions with PGV greater than about 0.9 m/s. This shows that the performance of the stiffer and stronger redesigned building with perfect connections is far better than that of the torsionally eccentric, softer and weaker existing building with brittle connections. (iv) Both buildings are more susceptible to long period ground motion, particularly ground motion with dominant period greater than about the fundamental period of the building (consistent with Uang and Bertero 1988; Krishnan and Muto 2012). But the existing building is susceptible to a broader range of ground motions (predominant period in the [2 s, 7 s] range) than the redesigned building (predominant period in the [3 s, 6 s] range). (v) Relatively fewer cases exist where the peak IDR falls between the Life-Safety (LS) and Collapse Prevention (CP) limits in the existing building when compared to the redesigned building. This is the effect of the lack of redundancy in the existing building (two 2-bay frames in either direction). A little damage takes the building disproportionately closer to collapse. It should be pointed out that duration of ground motion has not been considered in making these observations. Also, it is possible that a time-history may have have two well-separated peaks in its pseudo-acceleration spectrum. The period associated with only one peak is accounted for in the foregoing analysis.

In addition to studying the building response as a function of ground motion predominant period and PGV, it may also be useful to map the peak IDR response of the buildings on to the PGV-PGD plane (Fig. 3.26). This approach has been taken by Olsen et al. (2014) in identifying the ground motions that collapse 20-story steel moment frame buildings or render them irreparable. The ground motion histories from the scenario earthquakes have PGV and PGD that do not cover the entire PGV-PGD plane. Large PGVs result in large PGDs as well, so no cases exist where the PGV is high, but the PGD is low. On this plane, the collapse regime takes a distinct "V" shape similar to Olsen et al. (2014) and Krishnan and Muto (2013). It may be concluded from this figure that PGV-PGD combinations of at least 0.4 m/s-0.3 m and 0.8 m/s-0.8 m, approximately, may be necessary to collapse the existing and redesigned buildings, respectively.

The vast amounts of synthetic data generated for the response of the two buildings under a vast suite of synthetic ground motion records may be used for the development of fragility curves [probability of the peak IDR exceeding, say, the FEMA356 limits for the performance levels of immediate

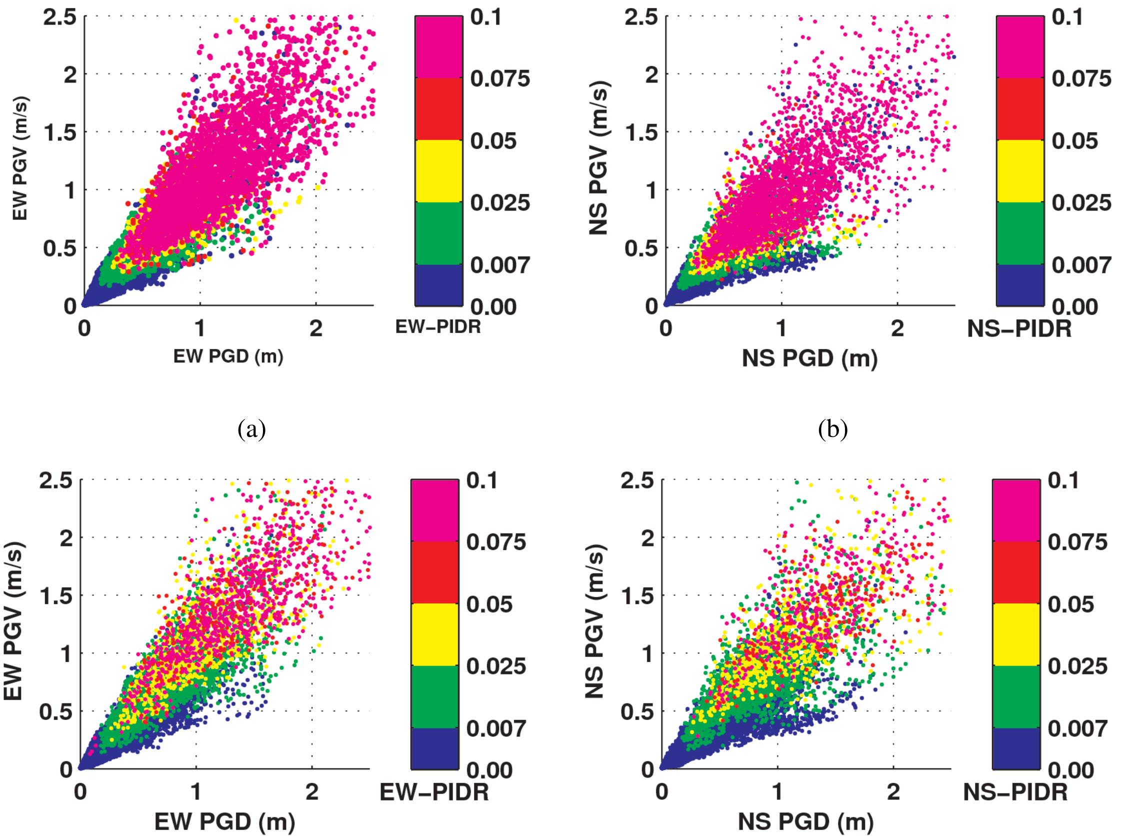

(a) (b) (c) (d)

Figure 3.26: X (EW) and Y (NS) peak interstory drift ratios in (a)-(b) the existing and (c)-(d) the redesigned buildings as a function of PGD (m) and PGV (m/s) of EW and NS components ground motion histories from all 60 scenario earthquakes on the southern San Andreas fault (6 magnitudes, 5 rupture locations, 2 rupture directions). Peak IDR of 0.007, 0.025, and 0.05 correspond to the FEMA356 limits for IO, LS, and CP performance levels.

occupancy (IO), life-safety (LS), and collapse prevention (CP)] as a function of ground motion intensities such as PGV and S_a at the two horizontal building translational fundamental periods. Fig. 3.27 shows fragility curves in the X and Y directions for the two buildings for exceedance of the FEMA356 performance levels of IO, LS, and CP, as well as two empirical performance levels, red-tagged (RT, peak IDR > 0.075) and model collapse (CO, peak IDR > 0.10), proposed by Krishnan and Muto (Muto and Krishnan 2011), as a function of PGV. The improved performance of the redesigned building is apparent. Model collapse probability for the redesigned building in the X (EW) direction is lower by factors of 1.75, 1.25, and 1.11 for PGVs of 1.0 m/s, 1.5 m/s, and 2.0 m/s, respectively. The corresponding factors in the Y (NS) direction are 4.33, 1.51, and 1.13 for PGVs of 1.0 m/s, 1.5 m/s, and 2.0 m/s, respectively. The redesigned building appears to perform better than a chevron-braced

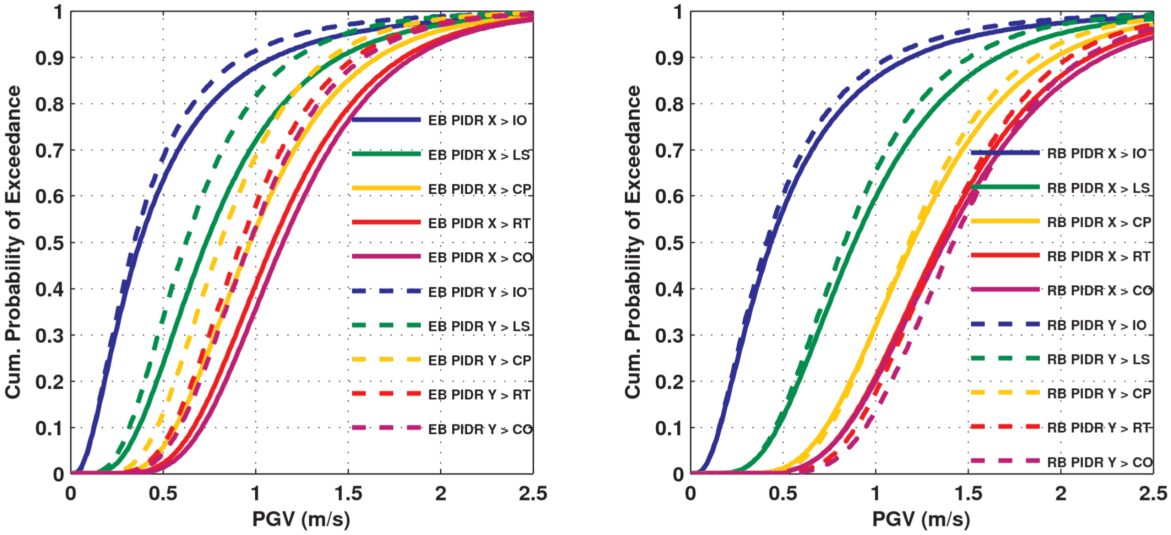

(a) (b)

Figure 3.27: Fragility curves of the probability of the peak IDR for (a) the existing and (b) the redesigned building in the X (solid)- and Y (dashed)- directions exceeding FEMA limits for immediate occupancy (IO), life-safety (LS), and collapse prevention (CP) performance levels as a function of PGV in the corresponding direction. Two additional fragilities corresponding to peak IDR levels of 0.075 (red-tagged, RT) and 0.10 (model collapse, CO), are also shown.

retrofit solution for the existing building Bjornsson and Krishnan (2012) where a 13% reduction in exceedance probability of the CP limit state was achieved at a PGV of 1 m/s. Reductions of 20% and 40% along EW and NS directions, respectively, are seen in the corresponding probability for the redesigned building. The fragility curves for the two buildings as a function of S_a at the two horizontal translational fundamental periods is shown in Fig. 3.28.

The PGV and S_a (at the two horizontal translational fundamental periods) thresholds for the 2%, 5%, 10%, and 50% exceedance probabilities of the limits for various performance levels for the two buildings are summarized in Tabs. 3.3 and 3.4. There is a 10% probability of collapse that earthquake records with a PGV of 0.71 m/s in the EW direction or a PGV of 0.59 m/s in the NS direction would collapse the existing building model. Similarly, there is a 10% probability of collapse that earthquake records with a PGV of 0.85 m/s in the EW direction or a PGV of 0.94 m/s in the NS direction would collapse the redesigned building model. Likewise, there is a 10% probability of collapse with a S_a of 0.22 g in the X (EW) direction or a S_a of 0.19 g in the Y (NS) direction for the existing building model. For the redesigned building model, there is a 10% probability of collapse with a S_a of 0.33 g in

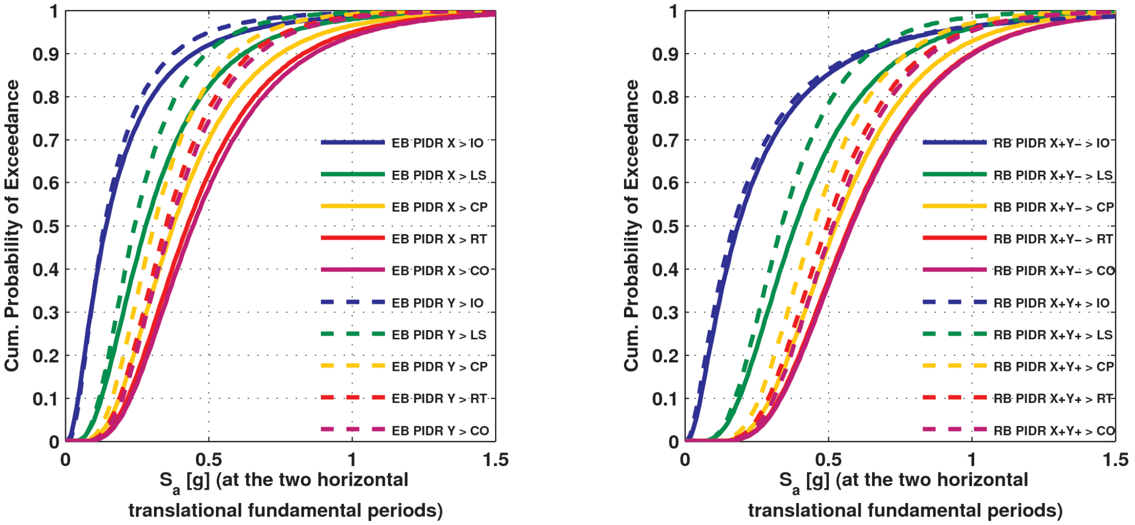

(a)

(b)

Figure 3.28: Fragility curves of the probability of the peak IDR for (a) the existing and (b) the redesigned building exceeding FEMA limits for immediate occupancy (IO), life-safety (LS), and collapse prevention (CP) performance levels as a function of SA (g) at fundamental period. Two additional fragilities corresponding to peak IDR levels of 0.075 (red-tagged, RT) and 0.10 (model collapse, CO), are also shown.

the X+Y- direction or a S_a of 0.31 g in the X+Y+ direction . The intent of building codes is to limit the probability of collapse to under 10%. It may thus be inferred that these are the intensities of ground motion that the two buildings have effectively been designed for.

3.2.6 30-year exceedance probabilities of structural performance limit states

The final step in the risk quantification of the two buildings using rupture-to-rafters simulations of scenario earthquakes is to compute the 30-year exceedance probabilities of the structural performance limit states using Eq. 3.1. Shown in Tab. 3.5 are the conditional probabilities of exceedance given an earthquake of magnitude 7.9 or 7.6 or 7.2 or 6.8 or 6.4 or 6.0, without consideration to the probability of occurrence of such an earthquake (i.e., without the $P(M_w/loc)$ term and the summation over M_w in Eq. 3.1). The probability of collapse of the existing model given a magnitude 7.9 earthquake on the southern San Andreas fault is as high as 39% whereas that of the redesigned building is less so, but still serious at 25%.

Building	Exceedance Probability	PGV (m/s) Threshold - EW (NS) components				
		IO	LS	CP	RT	CO
Existing	2%	0.07 (0.06)	0.24 (0.21)	0.41 (0.33)	0.49 (0.40)	0.53 (0.43)
Existing	5%	0.09 (0.10)	0.30 (0.26)	0.48 (0.40)	0.58 (0.48)	0.62 (0.51)
Existing	10%	0.12 (0.12)	0.36 (0.31)	0.56 (0.46)	0.66 (0.55)	0.71 (0.59)
Existing	50%	0.38 (0.34)	0.73 (0.62)	0.97 (0.81)	1.10 (0.92)	1.15 (0.97)
Redesigned	2%	0.08 (0.08)	0.32 (0.32)	0.54 (0.56)	0.64 (0.70)	0.64 (0.74)
Redesigned	5%	0.12 (0.12)	0.40 (0.38)	0.63 (0.65)	0.74 (0.79)	0.75 (0.84)
Redesigned	10%	0.16 (0.16)	0.47 (0.46)	0.73 (0.75)	0.84 (0.89)	0.85 (0.94)
Redesigned	50%	0.45 (0.41)	0.89 (0.83)	1.20 (1.18)	1.35 (1.35)	1.38 (1.42)

Table 3.3: PGV thresholds for the exceedance of IO, LS, CP, RT, & CO performance levels in the existing and the redesigned building models with probabilities of 2%, 5%, 10%, and 50%.

Building	Exceedance Probability	S_a [g] (at the two horizontal fundamental translational periods) Threshold				
		IO	LS	CP	RT	CO
Existing	2%	0.02 (0.02)	0.08 (0.08)	0.12 (0.11)	0.14 (0.13)	0.15 (0.13)
Existing	5%	0.03 (0.03)	0.10 (0.09)	0.15 (0.13)	0.18 (0.15)	0.18 (0.16)
Existing	10%	0.04 (0.04)	0.12 (0.11)	0.18 (0.16)	0.21 (0.18)	0.22 (0.19)
Existing	50%	0.13 (0.12)	0.28 (0.24)	0.37 (0.30)	0.42 (0.35)	0.44 (0.36)
Redesigned	2%	0.02 (0.02)	0.12 (0.11)	0.21 (0.18)	0.23 (0.21)	0.24 (0.22)
Redesigned	5%	0.03 (0.03)	0.15 (0.14)	0.25 (0.22)	0.28 (0.25)	0.28 (0.26)
Redesigned	10%	0.05 (0.04)	0.19 (0.17)	0.29 (0.25)	0.32 (0.29)	0.33 (0.31)
Redesigned	50%	0.18 (0.16)	0.38 (0.33)	0.52 (0.44)	0.57 (0.49)	0.58 (0.51)

Table 3.4: S_a (at the two horizontal fundamental translational periods) thresholds for the exceedance of IO, LS, CP, RT, & CO performance levels in the existing [along X (Y)] and the redesigned [along X+Y-(X+Y+)] building models with probabilities of 2%, 5%, 10%, and 50%.

The overall probabilities of the existing and redesigned buildings exceeding any of the FEMA356 limit states (IO, LS, CP) due to southern San Andreas fault earthquakes in the magnitude range of M_w 6.0 − 8.0 over the next three decades (with due consideration to their probabilities of occurrence) based on the scenario simulations are listed in Tab. 3.6. The probability that the existing building model will exceed the CP performance limit state from earthquakes on the southern San Andreas fault

M_w	**IO**	**LS**	**CP**
7.9	75.05 (54.81)	52.33 (35.01)	38.84 (25.29)
7.6	49.75 (48.33)	30.12 (26.58)	21.12 (17.22)
7.2	31.94 (25.59)	15.23 (10.71)	9.13 (5.87)
6.8	19.35 (13.32)	5.74 (2.89)	2.38 (0.91)
6.4	4.98 (3.82)	- (-)	- (-)
6.0	1.36 (0.52)	- (-)	- (-)

Table 3.5: Exceedance probability (%) of IO, LS, and CP performance levels in existing (redesigned) building model(s) conditioned on earthquake magnitude.

over the next 30 years is 7.59%. The corresponding probability for the redesigned building model is 5.23%. This appears quite high, when compared against the building code intent of limiting probability of collapse in code-designed structures to 2% in 50 years (or 10% in an MCE event with return period 2475 years). This is a direct outcome of the disagreement in ground motion prediction between the simulations and the NGA relations that are used in the development of seismic hazard maps. Furthermore, the probabilities of earthquake occurrence used in this study are time-independent. If time-dependent probabilities are used, these building performance limit state exceedance probabilities would likely be significantly higher. This is because earthquake recurrence periods for large earthquakes on the southern San Andreas fault is on the order of 150-300 years and more than 150 years have already passed since the last big earthquake, the 1857 M_w 7.9 Fort Tejon earthquake.

M_w	**IO**	**LS**	**CP**
82 UBC MF	24.40	11.44	7.59
97 UBC MF	19.25	8.40	5.23

Table 3.6: 30-year exceedance probability (%) of FEMA356 limits for IO, LS, and CP performance levels of existing and redesigned buildings in the greater Los Angeles region due to southern San Andreas fault earthquakes in the magnitude range of M_w $6.0 - 8.0$ based on scenario simulations

The characteristics of ground motions from several earthquakes between $M_w 6.0 - 7.9$ occurring on southern San Andreas Fault and their impact on the seismic performance of two 18-story moment frame buildings through rupture-to-rafters simulations have been discussed in this chapter. Nonetheless, it is important to understand the overall nature of these ground motions in context of national/regional seismic hazard maps that are used extensively in the design of new buildings. The following chapter addresses this issue by identifying the conditional and marginal probability distributions of PGV and PGD through a prototype study using Bayesian model class identification for peak ground motions due to large southern San Andreas fault earthquakes considering PGV and PGD at sites within moderate distances of 55-75km from source.

Chapter 4

Characterizing Long-Period Ground Motions Using Bayesian Model Class Selection.

National (or regional) seismic hazard maps, determined from probabilistic seismic hazard analysis, quantify the expected intensity of shaking in a region(s) over the course of one or more desired time interval(s). Building codes use these maps to define the lateral force levels for the design of new structures and the retrofit of existing structures. In the past, the maps depicted the shaking intensity measure of peak ground acceleration (PGA). In recent times, they have switched to depicting short period (0.2 s) and long period (1.0 s) spectral accelerations as these values may be directly used to fully define the code design response spectrum. Two hazard levels are typically of interest to the engineering community, the shaking intensity with a 10% probability of being exceeded in 50 years and the shaking intensity with a 2% probability of being exceeded in 50 years. These two levels of shaking define the Design Basis Earthquake (DBE, an earthquake with a recurrence interval of 475 years) and the Maximum Considered Earthquake (MCE, an earthquake with a recurrence interval of 2475 years) spectra. Typically, the codes' design intent is to avoid loss of life under the DBE and collapse under the MCE.

It is obvious that the vulnerability (or safety) of the building stock hinges quite critically on the veracity of the hazard maps. Ground motion intensities in the maps are determined using ground motion prediction equations or attenuation relations (e.g., Campbell and Bozorgnia 2008), with uncertainty typically being characterized using lognormal distributions. Yamada et al. (2009) argue that while this may be a reasonable assumption for the intensities associated with short periods such as peak ground acceleration and the spectral acceleration at 0.2 s, it is not so for long-period ground motion markers such as peak ground displacement (PGD). It has been known for sometime that PGA tends to saturate for magnitudes greater than about 6 (Rogers and Perkins 1996; Somerville 2003). Using data collected in the near-source region ($\leq 10\ km$) from past earthquakes and a 1906 San Francisco earthquake simulation, Yamada et al. (2009) show that peak ground displacements, on the other hand, do not saturate. In fact, they show that log(PGD) increases linearly with magnitude in the near-source region, a trend that was previously observed by Wells and Coppersmith (1994) and Campbell and Bozorgnia (2008). They then pose the question, "what are the largest expected PGA and PGD at a site within 10 km of a fault capable of producing at least a magnitude 6 earthquake?". Combining the conditional distributions of PGA and PGD given magnitude, which they say are reasonably well-characterized by lognormal distributions, they determine the unconditional distributions of PGA and PGD. They find that for ground motions recorded within 10 km of a fault producing an earthquake with magnitude greater than 6.0, the inferred distribution of PGA is lognormal, whereas the inferred distribution of PGD is approximately uniform within a certain displacement band with unknown points of truncation.

Here, we examine the same question for stations in the Los Angeles and surrounding basins at distances of 60 km-70 km from the southern San Andreas fault, i.e., "what are the expected peak ground motion intensities in the Los Angeles (LA) basin from earthquakes on the southern San Andreas fault with magnitudes in the 6.0-8.0 range?". Specifically, we aim to (i) determine the conditional probability distributions given magnitude for PGD and PGV in the LA and adjacent basins from M_w $6.0 - 8.0$ earthquakes on the southern San Andreas fault and (ii) determine the corresponding unconditional probability distributions (not conditioned on magnitude). We have simulated ground motions from 300 scenario earthquakes [six magnitudes, M_w $6.05, 6.40, 6.80, 7.20, 7.60,$ and 7.90; five stochastic source realization for each magnitude; five rupture locations; and two unilateral rupture directions] for a broader study on the characterization of risk to tall buildings in the Los Angeles region from southern San Andreas fault earthquakes. Here, we use the synthetic data from earthquakes rupturing location 3 alone (i.e., 60 earthquakes), computed for LA basin stations that are within 55-75 km from the source. Location 3 is due north of the LA basin (Fig. 4.1). Of the 636 analysis sites where ground motions are computed, the number of sites in the Los Angeles region that are within 55-75 km of this particular rupture location for all six scenario earthquake magnitudes is similar (243 for M_w 6.05, 248 for M_w 6.40, 246 for M_w 6.80, 246 for M_w 7.20, 249 for M_w 7.60, and 252 for M_w 7.90). Limiting our study to ground motions from location 3 ruptures ensures that there is no bias introduced in the probability distributions due to sample size variations.

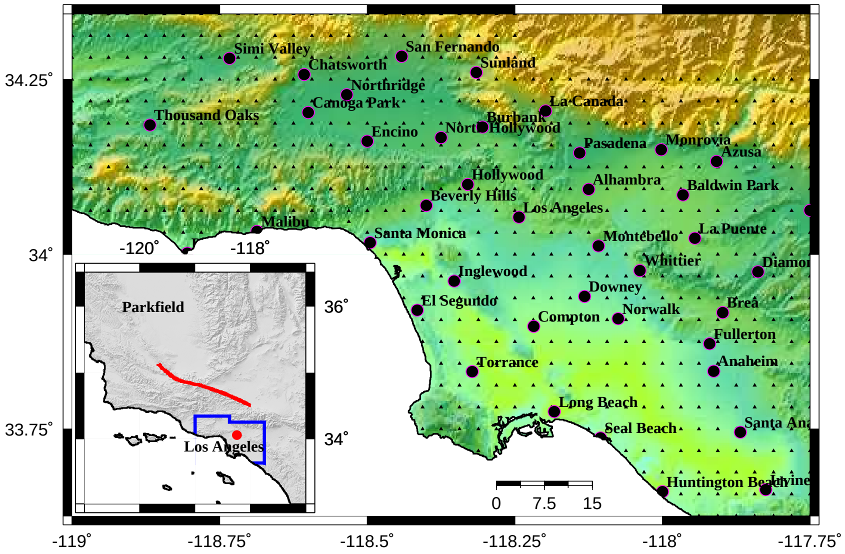
Simi Valley
Chatsworth
San Fernando
Sunland
Northridge
Canoga Park
Thousand Oaks
La Canada
Burbank
Encino
North Hollywood
Pasadena
Monrovia
Azusa
Hollywood
Alhambra
Baldwin Park
Beverly Hills
Los Angeles
Malibu
Santa Monica
Montebello
La Puente
Whittier
Diamo
Inglewood
Downey
El Segundo
Brea
Compton
Norwalk
Fullerton
Torrance
Anaheim
Long Beach
Seal Beach
Santa An
Huntington Beach
Irvine
34.25°
34°
33.75°
-120°
-118°
Parkfield
36°
34°
Los Angeles
0
7.5
15
-119°
-118.75°
-118.5°
-118.25°
-118°
-117.75°

Figure 4.1: The geographical distribution of the 636 southern California sites (shown as triangles) where scenario earthquake ground motions are computed. The spacing between the sites is 3.5 km approximately. The inset shows the southern San Andreas fault rupture extent of a M_w 7.9 earthquake at Location 3.

4.1 Ground Motion Simulation

For each of the six scenario earthquake magnitudes, five stochastic kinematic source models are generated using the algorithm by Siriki et al. (2014). A detailed description of the ground motion simulation is given in Section 2.2. We limit ourselves to long-period ground motion alone in this study and the long-period ground motion markers of the horizontal PGD and PGV as quantified by the vector amplitude. The vector amplitude is defined as the maximum of the square root of the sum of squares of the two horizontal orthogonal components of velocity and displacement time histories. Shown in Fig. 4.2 are the histograms of PGV and PGD for the six different magnitude scenario earthquakes (three shown in each subfigure for clarity), with the PGV/PGD being plotted on a log scale. The scatter in PGV and PGD as a function of magnitude, with a line connecting the median values, is shown in Fig. 4.3. The following observations can be made: (i) The median value of log(PGD) grows linearly with magnitude, with a higher gradient than the near-source ($< 10\ km$) ground motion records studied by Yamada et al. (2009). The slope for log(PGD) as a function of magnitude for the medium-distance basin stations here is 0.98 whereas Yamada et al. (2009) give a slope of 0.60 for the near-source motions (from earthquakes up to magnitude 7.6 and one record from a magnitude 7.8 earthquake) and a range of 0.5-0.75 in the near-source region based on theoretical arguments. The corresponding value for log(PGV) here is 0.89 [Yamada et al. (2009) do not include results for PGV]. (ii) The variance of both log(PGD) and log(PGV) remains more or less the same for all magnitudes, an observation also made for [log(PGD) of] near-source motions by Yamada et al. (2009). (iii) It is conceivable that each of the individual histograms in Fig. 4.2 may be reasonably well characterized by a Gaussian (normal) distribution, which would mean that PGD and PGV may be log-normally distributed individually for each magnitude earthquake. We test this hypothesis using Bayesian model selection in the next section.

4.2 Bayesian Model Selection

Bayesian model selection uses Bayes theorem to answer the question, "Given a set of measurements of a phenomenon or system and some prior knowledge of it (expressed in the form of a probability distribution) which model (or model class) out of a set of proposed probability models (or model classes) is the most plausible?" [e.g., Beck and Yuen (2004)]. Our objectives here are two-fold: (i) to determine the posterior probability distribution function (PDF) for the ground motion intensities of peak ground velocity (PGV) and peak ground displacement (PGD) at basin sites conditional on earthquake magnitude; (ii) to determine the unconditional posterior marginal PDFs for PGV and PGD at basin sites (not conditioned on magnitude). The data consists of observed values of the ground motion intensities $\mathbf{I} =< I_1, I_2, ..., I_N >$ of PGV and PGD at distances in the 55-75 km range from the M_w $6.05, 6.40, 6.80, 7.20, 7.60,$ and 7.90 scenario earthquakes at location 3 of the southern San Andreas fault. For problem (i) (the conditional distributions for PGV and PGD given magnitude), N is the product of the number sites (243 for M_w 6.05, 248 for M_w 6.40, 246 for M_w 6.80, 246 for M_w 7.20, 249 for M_w 7.60, and 252 for M_w 7.90), the number of stochastic source models for each magnitude (5 in our case), and the number of rupture directions (2 in our case). For problem (ii) (the unconditional distributions of PGV and PGD), N is the sum of the data points for all magnitudes (7420). For problem (i) we examine five candidate model classes $\mathbf{Q} =< Q_1, Q_2, ..., Q_5 >$ chosen on the basis of the shapes of the individual histograms corresponding to each magnitude in Fig. 4.2:

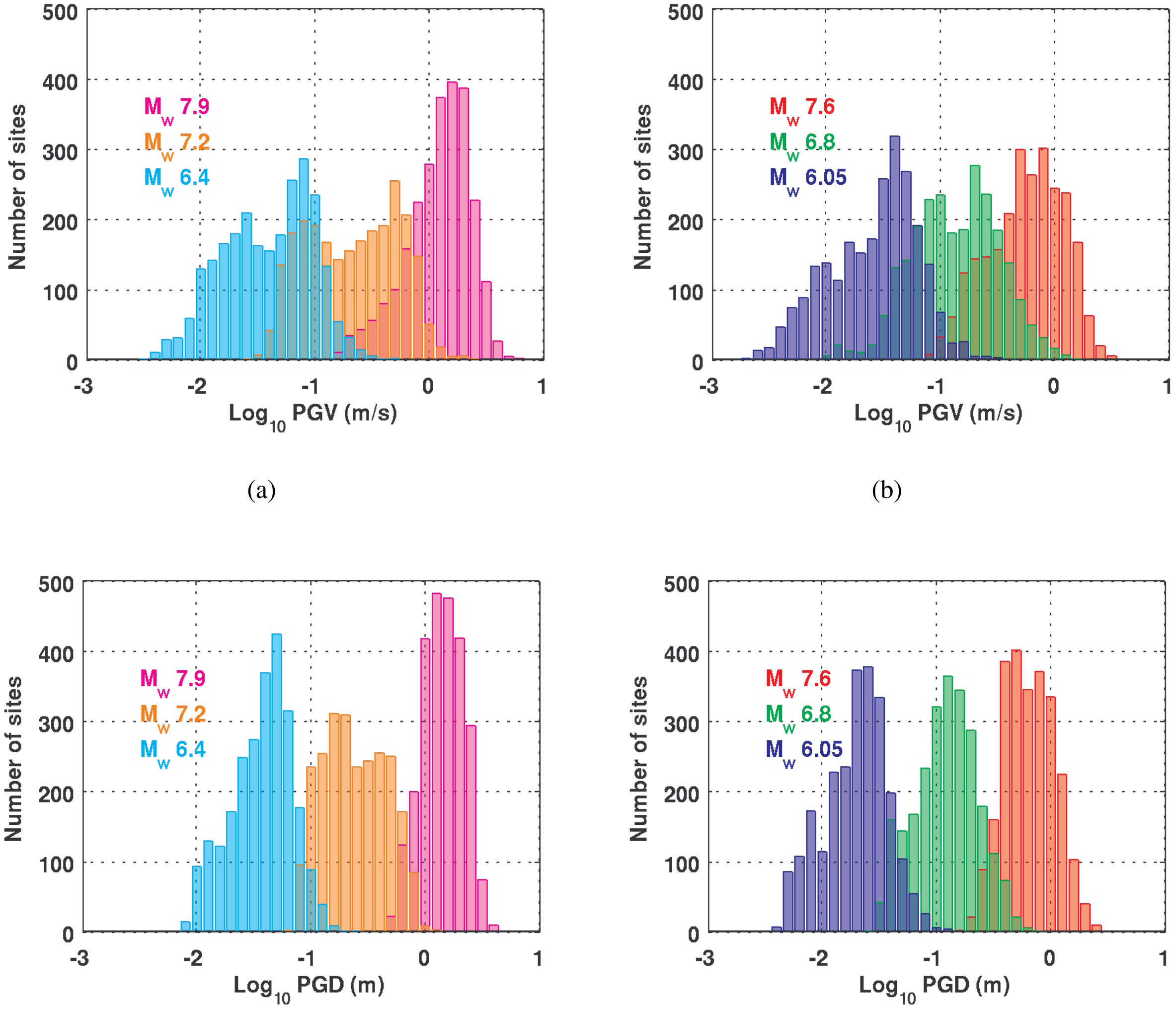

(a) (b)

(c) (d)

Figure 4.2: Horizontal (a), (b) peak ground velocity (m/s) and (c), (d) peak ground displacement (m) histograms for M_w 7.9, 7.6, 7.2, 6.8, 6.4, and 6.05 scenario earthquakes rupturing location 3 of southern San Andreas fault. Synthetic data from all sites within a source-to-site distance of 55 km-75 km in the Los Angeles and adjacent basins are included. The PGV and PGD data are collated into 1.25 m/s and 1.25 m bins, respectively.

lognormal, gamma, exponential, levy and rayleigh distributions. For problem (ii) we examine two candidate model classes $\mathbf{Q} =< Q_1, Q_2 >$, chosen on the basis of the combined histograms of PGV and PGD using data from scenario earthquakes of all magnitudes (Fig. 4.4): lognormal and double pareto uniform. The levy distribution is characterized by shape and location parameters, while the double pareto uniform distribution by two shape parameters, a location parameter and a scale parameter. The remaining distributions are characterized by mean and standard deviation parameters. The

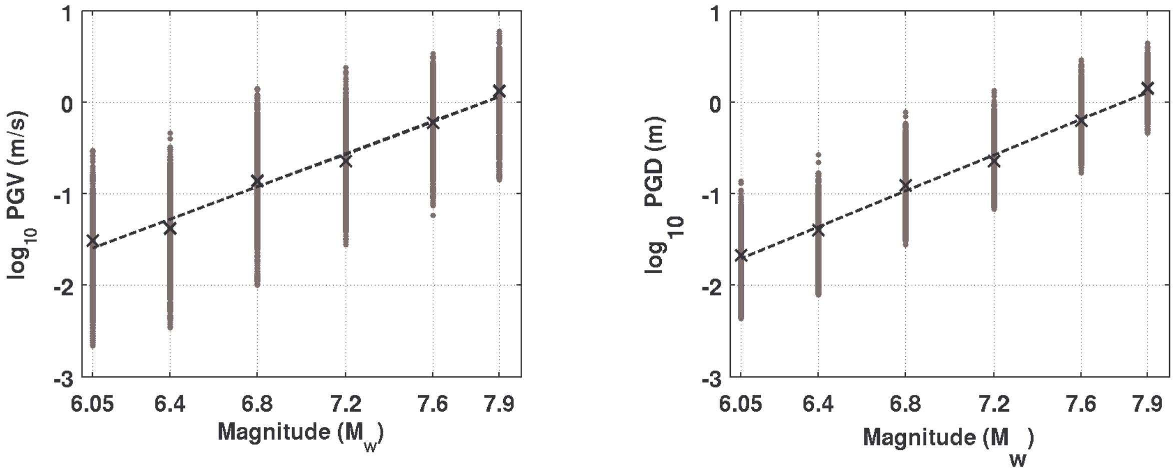

(a) (b)

Figure 4.3: Scatter plot of horizontal (a) peak ground velocity (m/s); and (b) peak ground displacement (m) as a function of magnitude simulated for M_w $7.9, 7.6, 7.2, 6.8, 6.4,$ and 6.05 scenario earthquakes rupturing location 3 of southern San Andreas fault. Note that PGV and PGD are plotted on a log scale. Synthetic data from all sites within a source-to-site distance of 55 km-75 km in the Los Angeles and adjacent basins are included. The median value is indicated by a 'x' for each magnitude. The best fitting lines to the median PGD and PGV values are $log_{10}PGD = 0.98M_w - 7.62$ and $log_{10}PGV = 0.89M_w - 6.77$, respectively.

mathematical expression for the PDFs for all of these distributions are given in Section 4.4 at the end of this chapter. Henceforth, the set of parameters characterizing a distribution will be denoted by the vector $\boldsymbol{\theta}$. It should be noted that, in Bayesian model class selection, the model class parameters are themselves taken to be uncertain with a prior probability density, $p(\theta_j|Q_j)$.

We give a brief outline of Bayesian model selection for the computation of the posterior probability P($Q_j|\mathbf{I}, \mathbf{Q}$) for each model class, given the data **I**, the set of proposed posterior probability models **Q**, the prior probability of each model class Q_j, $P(Q_j|\mathbf{Q})$, and the prior PDFs for the model parameters within each class $p(\theta_j|Q_j)$ from prior knowledge or judgment. The method will allow us to not only identify the model class with the highest posterior probability, but also determine the corresponding parameter vector $\hat{\boldsymbol{\theta}}_j$ (the maximum a posteriori or MAP estimate) that maximizes the posterior PDF for Q_j. The model predictions for the ground motion intensities corresponding to the data at different sites are chosen as independent and identically distributed (i.i.d.) variables. From Bayes' theorem, noting that **I** is a continous variable:

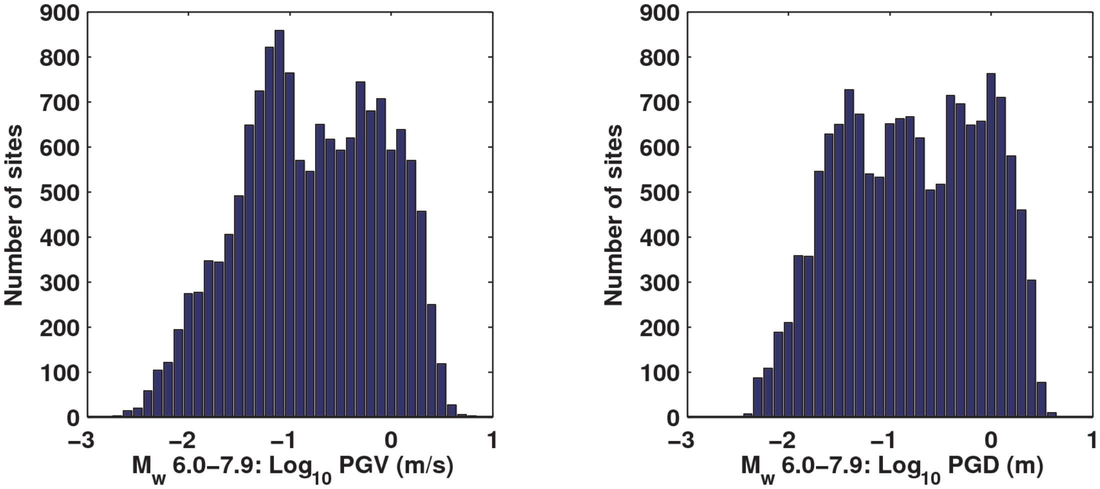

(a) (b)

Figure 4.4: Combined histograms of the (a) PGV (m/s) and (b) PGD (m) for the 60 scenario earthquakes at location 3 on the southern San Andreas fault with magnitudes in the M_w $6.0-7.9$ range. Data from all sites at source-to-site distances of 55-75 km are included. The PGV and PGD data are collated into 1.25 m/s and 1.25 m bins, respectively.

$$\mathrm{P}(\mathrm{Q}_j|\mathbf{I},\mathbf{Q}) = \frac{p(\mathbf{I}|Q_j)P(Q_j|\mathbf{Q})}{\sum\limits_{j=1}^{J} p(\mathbf{I}|Q_j)P(Q_j|\mathbf{Q})} \tag{4.1}$$

In the above equations, the upper limit $J = 5$ for the summation is applicable to problem (i) and the upper limit $J = 2$ is applicable to problem (ii). $p(\mathbf{I}|Q_j)\ dI$ is the probability of realizing intensities in a small neighborhood dI of the dataset $\mathbf{I}$ if the probability model is Q_j and is termed "model class evidence". $p(\mathbf{I}|Q_j)$ is the corresponding probability density. The prior probability for each model Q_j, $P(Q_j|\mathbf{Q})$, is taken to be the inverse of the number of models [1/5 for problem (i) and 1/2 for problem (ii)]. In the absence of any prior knowledge or judgment as is the case here, it would be most reasonable to consider all models to be equally plausible a priori. Substituting the uniform priors into eq. 4.1 we get,

$$P(Q_j|\mathbf{I},\mathbf{Q}) = \frac{p(\mathbf{I}|Q_j)}{\sum\limits_{j=1}^{J} p(\mathbf{I}|Q_j)} \tag{4.2}$$

If we assume a prior distribution for model class Q_j parameters, $p(\theta_j|Q_j)$, then the model class evidence may be determined using the total probability theorem as:

$$p(\mathbf{I}|Q_j) = \int p(\mathbf{I}|\theta_j, Q_j)\ p(\theta_j|Q_j)\mathbf{d}\theta_j \tag{4.3}$$

The last integral in Eq. 4.3 may be evaluated approximately using Laplace's method of asymptotic approximation (Beck 2010):

$$p(\mathbf{I}|Q_j) \approx p(\mathbf{I}|\hat{\boldsymbol{\theta}}_{\boldsymbol{j}}, Q_j)p(\hat{\boldsymbol{\theta}}_{\boldsymbol{j}}|Q_j)(2\pi)^{\frac{N_j}{2}} det[H(\hat{\boldsymbol{\theta}}_{\boldsymbol{j}})]^{\frac{-1}{2}} \tag{4.4}$$

where

$\hat{\boldsymbol{\theta}}_{\boldsymbol{j}}$, the maximum a posteriori (MAP) estimate of model class Q_j parameters, is given by: $\hat{\boldsymbol{\theta}}_{\boldsymbol{j}} = arg\ max_{\boldsymbol{\theta}_{\boldsymbol{j}}}\{\sum\limits_{i=1}^{N} log\ [p(I_i|\boldsymbol{\theta}, Q_j)]\ +\ log\ [p\ (\boldsymbol{\theta}|Q_j)]\ \}.$

This optimization involves evaluating the 2 X 2 Hessian matrix $H(\hat{\boldsymbol{\theta}}_{\boldsymbol{j}})$ of -log[$p(\boldsymbol{I}|\boldsymbol{\theta}_j, Q_j)p(\boldsymbol{\theta}_j|Q_j)$] at the MAP estimate $\hat{\boldsymbol{\theta}}_{\boldsymbol{j}}$. N_j is the number of parameters of model class Q_j (i.e., the dimension of $\boldsymbol{\theta}_j$). $p(\boldsymbol{I}|\hat{\boldsymbol{\theta}}_j, Q_j)$ is the density at the MAP estimate given by $\prod\limits_{i=1}^{N} p(I_i|\hat{\boldsymbol{\theta}}_j, Q_j)$. $p(\hat{\boldsymbol{\theta}}_j|Q_j)$ is the prior at the MAP estimate.

4.3 Conditional and Unconditional Probability Distributions for PGV and PGD

The method above is implemented for the solution to problems (i) and (ii). As mentioned previously, five model classes (lognormal, gamma, exponential, levy and rayleigh) are examined in problem (i) for the PDF of PGV/PGD conditioned on magnitude, and two model classes (lognormal and double pareto uniform) are examined in problem (ii) for the unconditional PDF of PGV/PGD (not conditioned on magnitude). The functional form of all distributions are given in Sec. 4.4. The prior distributions of all parameters in all model classes are assumed uniform in the absence of prior insights/information into/on the problem.

The MAP estimate of the mean and standard deviation of the model classes considered for the conditional distribution (given earthquake magnitude) of PGV and PGD at basin sites at a distance of 55-75 km are given in Tab. 4.1 [problem (i)], along with the sample mean and standard deviation of the ground motion data. The corresponding posterior probabilities of the model classes are given in Tab. 4.2. Tabs. 4.3 and 4.4 show the MAP estimates of the parameters of the model classes considered and the associated posterior probabilities for the unconditional distributions [problem (ii)] of PGV and PGD, respectively. The most probable distributions are graphically illustrated in Fig. 4.5 alongside the unconditional distribution (implicitly taking uniform distribution on magnitude) derived through the summation of the conditional probability distributions followed by normalization.

		Magnitude					
Distribution	**Parameter**	$M_w7.9$	$M_w7.6$	$M_w7.2$	$M_w6.8$	$M_w6.4$	$M_w6.05$
Lognormal	PGV (m/s)	1.47 (1.06)	0.74 (0.64)	**0.32 (0.37)**	**0.19 (0.21)**	**0.05 (0.06)**	0.03 (0.04)
	PGD(m)	**1.54 (0.66)**	**0.73 (0.39)**	**0.29 (0.20)**	**0.14 (0.10)**	0.04 (0.03)	**0.02 (0.01)**
Gamma	PGV (m/s)	1.43 (0.83)	**0.72 (0.49)**	0.31 (0.26)	0.19 (0.15)	0.05 (0.04)	**0.03 (0.02)**
	PGD(m)	1.53 (0.62)	0.73 (0.36)	0.29 (0.18)	0.14 (0.08)	**0.04 (0.02)**	0.02 (0.14)
Exponential	PGV (m/s)	1.43 (1.43)	0.72 (0.72)	0.31 (0.31)	0.19 (0.19)	0.05 (0.05)	0.03 (0.03)
	PGD(m)	1.53 (1.53)	0.73 (0.73)	0.29 (0.29)	0.14 (0.14)	0.04 (0.04)	0.02 (0.02)
Levy	PGV (m/s)	0.10 (0.10)	0.05 (0.05)	0.02 (0.02)	0.00 (0.00)	0.00 (0.00)	0.00 (0.00)
	PGD(m)	0.44 (0.44)	0.16 (0.16)	0.06 (0.06)	0.02 (0.02)	0.00 (0.00)	0.00 (0.00)
Rayleigh	PGV (m/s)	**1.45 (0.76)**	0.77 (0.40)	0.37 (0.19)	0.23 (0.12)	0.06 (0.03)	0.04 (0.02)
	PGD(m)	1.47 (0.77)	0.73 (0.38)	0.31 (0.16)	0.15 (0.08)	0.04 (0.02)	0.02 (0.01)
Sample values	PGV (m/s)	1.43 (0.79)	0.72 (0.50)	0.31 (0.27)	0.19 (0.17)	0.05 (0.04)	0.03 (0.03)
	PGD(m)	1.53 (0.62)	0.73 (0.39)	0.29 (0.19)	0.14 (0.09)	0.04 (0.02)	0.02 (0.01)

Table 4.1: Maximum a Posteriori (MAP) estimates of mean (standard deviation) of the model classes considered for the conditional distributions of PGV and PGD at a distance of 55-75 km given earthquake magnitude. In the case of levy distribution, the values correspond to location (shape) parameters. Bold values correspond to the distribution with greatest posterior probability.

The posterior probabilities of the model classes considered for the [Problem (i)] conditional distributions of PGV and PGD based on simulated ground motion data do indicate that the most probable distributions are typically lognormal. However, there are exceptions. For instance PGV for the

Distribution	**Parameter**	Magnitude					
		$M_w7.9$	$M_w7.6$	$M_w7.2$	$M_w6.8$	$M_w6.4$	$M_w6.05$
Lognormal	PGV (m/s)	0.00	0.00	**1.00**	**1.00**	**1.00**	0.00
	PGD(m)	**0.92**	**1.00**	**1.00**	**1.00**	0.00	**0.51**
Gamma	PGV (m/s)	0.05	**1.00**	0.00	0.00	0.00	**1.00**
	PGD(m)	0.08	0.00	0.00	0.00	**1.00**	0.49
Exponential	PGV (m/s)	0.00	0.00	0.00	0.00	0.00	0.00
	PGD(m)	0.00	0.00	0.00	0.00	0.00	0.00
Levy	PGV (m/s)	0.00	0.00	0.00	0.00	0.00	0.00
	PGD(m)	0.00	0.00	0.00	0.00	0.00	0.00
Rayleigh	PGV (m/s)	**0.95**	0.00	0.00	0.00	0.00	0.00
	PGD(m)	0.00	0.00	0.00	0.00	0.00	0.00

Table 4.2: Posterior probability of the model classes considered for the conditional distributions of PGV and PGD at a distance of 55-75 km given earthquake magnitude. The largest probabilities corresponding to each magnitude are shown in bold.

Distribution	**Parameter**	Magnitude			
		μ		σ	
Normal	$\log_{10}PGV(m/s)$	-0.78		0.69	
	$\log_{10}PGD(m)$	-0.78		0.70	
		m	n	α	β
Double Pareto Uniform	$\log_{10}PGV(m/s)$	**7.50**	**20.75**	**-1.67**	**0.30**
	$\log_{10}PGD(m)$	**10.72**	**31.60**	**-1.77**	**0.34**

Table 4.3: Maximum a Posteriori (MAP) estimates of the parameters of the model classes considered for the unconditional distributions of PGV and PGD at a distance of 55-75 km for earthquakes in the magnitude range of 6.05-7.90. Bold values correspond to the distribution with greatest posterior probability.

Parameter	Distribution	
	Normal	**Double Pareto Uniform**
$\log_{10}PGV(m/s)$	0.00	**1.00**
$\log_{10}PGD(m)$	0.00	**1.00**

Table 4.4: Posterior probability of the model classes considered for the unconditional distributions of PGV and PGD at basin sites at a distance of 55-75 km for earthquakes in the magnitude range of 6.04-7.90. The largest probabilities corresponding to each magnitude are shown in bold.

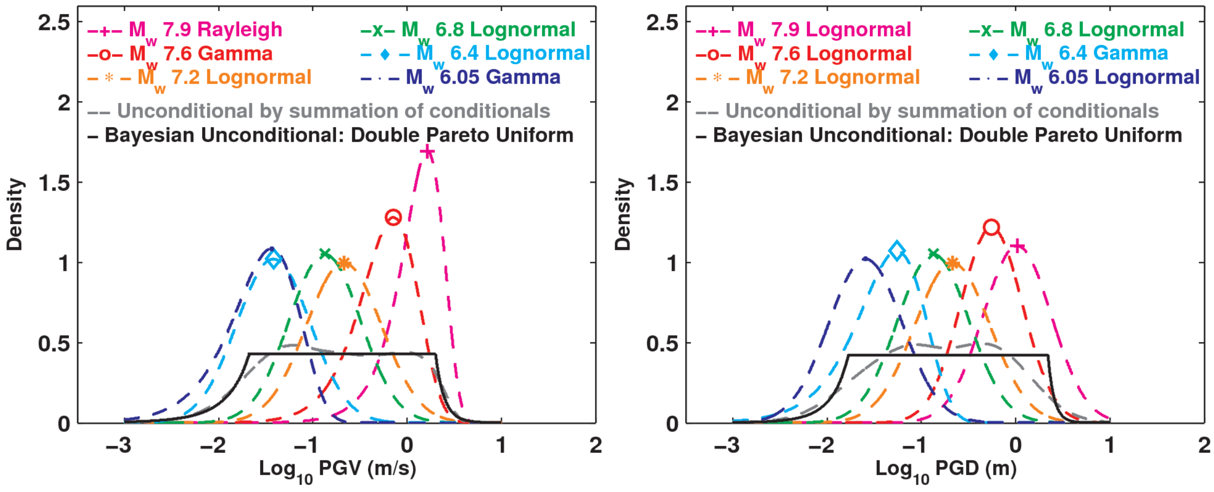

(a) (b)

Figure 4.5: Conditional (given earthquake magnitude, colored dashed lines) and unconditional (solid black line) probability distributions of (a) PGV (m/s) and (b) PGD (m) at basin sites at a distance of 55-75 km for earthquakes in the magnitude range of 6.04-7.90 identified through Bayesian model class selection. The grey dashed lines are the unconditional distributions derived by the summation of conditional distributions followed by normalization, equivalent to assuming an uniform distribution on magnitude.

M_w 7.90 earthquakes is best characterized by a Rayleigh distribution. The posterior probability that PGV or PGD is described by an exponential or a levy distribution is practically zero. The unconditional distribution obtained by the summation of conditional distributions from the Bayesian selection for individual magnitudes to eliminate the conditioning on magnitude is flat over a significant range of PGVs and PGDs [dashed gray lines in Figs. 4.5(a) and 4.5(b)]. This is consistent with the raw data shown in the form of histograms previously in Fig. 4.4. These findings are similar to the conclusion made by Yamada et al. (2009) for near-source ($< 10\ km$) ground motions. Not surprisingly, the Bayesian model selection procedure conclusively picks the double pareto uniform distribution over the normal distribution for the characterization of the unconditional distributions of both the logarithm of PGV and PGD . The identified double pareto uniform distributions [solid gray lines in Figs. 4.5(a) and 4.5(b)] exhibit remarkable agreement with the unconditional distributions derived by the summation of the conditional distributions. The width of the distribution is controlled by the range of magnitudes under consideration. If larger magnitudes are considered, the width of the distribution would increase assuming that the linear trend of Fig. 4.3 holds. It may be concluded that (i) lognormal distributions do not accurately explain the probability of PGV and PGD (at basin sites in the LA region at 55-75 km distances from magnitude 6.05-7.90 earthquakes on the southern San Andreas fault) exceeding a specified value, and (ii) seismic hazard levels for long period ground motion markers such as PGV and PGD defined through lognormal distributions might not accurately represent seismic risk. Shown in Tab. 4.5 is the probability of PGV exceeding 0.5 m/s, 1.0 m/s, 1.5 m/s, 2.0 m/s, and PGD exceeding 0.5 m, 1.0 m, 1.5 m, and 2.0 m from the best fitting lognormal and double pareto uniform distributions derived using MAP estimates for earthquakes between M_w $6.05 - 7.90$. It may be observed that the lognormal distribution consistently under-predicts the probability of PGV and PGD exceeding a specific value up until 2 m/s and 2 m, respectively. For these findings to hold robustly, larger amounts of data must be generated from various source mechanisms and locations, geological settings, source-to-site distances, stochastic source characterization techniques, and ground motion simulation methods. The robustness of the findings with respect to the assumed prior distributions needs to be investigated as well.

Distribution	PGV [m/s] (PGD [m])			
	0.5 m/s (0.5 m)	1.0 m/s (1.0 m)	1.5 m/s (1.5 m)	2.0 m/s (2.0 m)
Lognormal	23.93 (24.11)	12.50 (12.69)	7.88 (8.04)	5.43 (5.57)
Double Pareto Uniform	29.96 (29.93)	17.08 (17.28)	9.54 (9.88)	4.19 (4.64)

Table 4.5: Posteriori probability ($\%$) of the model class exceeding specified peak ground velocity (displacement) value.

4.4 Probability Distributions Used

In the following definitions, "I" represents the intensity of ground motion, namely peak ground velocity and/or displacement.

1. **Lognormal Distribution**

   $f(I;\mu,\sigma) = \frac{1}{I\ \sigma\sqrt{2\pi}} e^{\frac{(log\ I-\mu)^2}{2\sigma^2}}, I\ >\ 0$

   where μ, σ are the location and shape parameters on a logarithmic scale. In other words, they are the mean and standard deviation of the variable's natural logarithm.

2. **Normal Distribution**

   $f(I;\mu,\sigma) = \frac{1}{\sigma\sqrt{2\pi}} e^{\frac{(I-\mu)^2}{2\sigma^2}}$

where μ, σ are the mean and standard deviation of the distribution.

3. **Exponential distribution**

   $f(I;\lambda) = \lambda e^{-\lambda I}, I \geq 0\ and\ \lambda > 0$

   where λ is the rate parameter.

4. **Gamma Distribution**

   $f(I;k,\theta) = \frac{I^{k-1}e^{\frac{-I}{\theta}}}{\theta^k \Gamma(k)}, I > 0\ and\ k,\theta > 0$

   where k, θ are the shape and scale parameters of the distribution and $\Gamma(k)$ is the gamma function evaluated at k.

5. **Levy Distribution**

   $f(I;\mu,c) = \sqrt{\frac{c}{2\pi}}\frac{e^{\frac{-c}{2(I-\mu)}}}{(I-\mu)^{\frac{3}{2}}}, I \geq \mu\ and\ c > 0$

   where μ, c are the location and scale parameters of the distribution.

6. **Rayleigh Distribution**

   $f(I;\sigma) = \frac{I}{\sigma^2}e^{\frac{-I^2}{2\sigma^2}}, I \geq 0\ and\ \sigma > 0$

   where σ is the scale parameter of the distribution.

7. **Double Pareto Uniform Distribution**

   $f(I;m,n,\alpha,\beta) = K(m,n)\frac{(\beta-\alpha)^m}{(\beta-I)^{m+1}} \quad I < \alpha$

   . $\qquad = K(m,n)\frac{1}{\beta-\alpha} \qquad \alpha \leq I \leq \beta$

   . $\qquad = K(m,n)\frac{(\beta-\alpha)^n}{(I-\alpha)^{n+1}} \quad I > \beta$

   where $K(m,n) = \frac{mn}{m+mn+n}; \alpha < \beta; m,n > 0$. m, n denote the shape parameters with α and $(\beta - \alpha)$ denoting the location and scale parameters.

Chapter 5

Conclusions

5.1 Findings

The study presents a framework on how rupture-to-rafters simulations can be conducted to holistically quantify the seismic performance of tall buildings and can provide answers to diverse questions ranging from seismic source modeling to non-linear building response characteristics. A summary on the highlights of the study along with the findings made using rupture-to-rafters simulations in context of large San Andreas fault earthquakes is presented here.

1. A recursive division algorithm for generating stochastic source models of $M_w = 6.0 - 8.0$ strike-slip earthquakes is presented. The algorithm uses observations from laboratory earthquakes to augment the known physics of earthquake ruptures from finite-source inversions of past earthquakes. It is validated through a statistical comparison of long-period (2 s and higher) ground motions generated by stochastic source models and finite-source models of past earthquakes of equivalent magnitude. Its application to several $M_w 7.9$ earthquake simulations at different locations on the southern San Andreas fault has yielded interesting results. First (not surprisingly), the location of strong ground motions is closely related to the location, size and strength of slip asperities on the source. Second, ground motion intensities are higher when a greater proportion of the rupture propagates at sub-Rayleigh speeds, whereas the intensities are lower when a greater proportion of the rupture propagates at super-shear speeds. Third, ground motion intensities in the LA basin are lower when the peak rise-time in the source is higher, although

this anti-correlation is not as strong as the correlation with the percentage of rupture propagating at sub-Rayleigh rupture speeds. Four, median (and variability of) peak ground displacements from the simulations as a function of source-to-site distance agree well with predictions by the Campbell-Bozorgnia NGA relation. Five, median (and variability of) peak ground velocities from the simulations as a function of source-to-site distance are three to six times higher than that predicted by the Campbell-Bozorgnia NGA relation. It is imperative that the differences in the simulations and the NGA predictions be reconciled to ensure that seismic hazard maps based on the NGA relations are credible.

2. The algorithm was applied to generate sixty hypothetical earthquake scenarios for magnitudes varying between 6.0 and 8.0 with varying rupture location and directivity on southern San Andreas fault. The comparison of associated ground motions (at 636 sites in southern California) with ground motion prediction equations (GMPE) indicate that while median spectral acceleration at 3s time period and peak ground velocity of all 636 sites are consistently underestimated by GMPE at times almost by a factor of 3-5, they indicate marginally higher peak ground displacements. Furthermore, the simulated ground motions are significantly affected by fault slip asperity size and intensity, rupture speed (with sub-Rayleigh ruptures resulting in stronger ground motions), peak rise-time (with longer peak rise-times leading to weaker ground motions), proximity to source, and basin configuration (including depth).

3. This algorithm can be implemented for any strike-slip fault in the world for which good estimates of principal stress are available. In the absence of such data, the algorithm can still be implemented with a widely accepted rupture speed of $0.8V_s$ across the fault. However in making this assumption, the findings that in case of large magnitude earthquakes ($M_w7.9$) ruptures traveling primarily in sub-Rayleigh mode produce higher ground motion intensities relative to ones traveling in super-shear mode should be considered. A compelling observation is that such distinct correlation between ground motion intensities and percentage of rupture traveling in sub-Rayleigh mode is not observed for relatively comparable $M_w7.6$ or lower earthquakes.

4. Rupture-to-rafters simulations are incorporated into performance based earthquake engineering for quantifying fault-specific risk to existing (or new) buildings over a target time horizon. Synthetic ground motions from sixty earthquakes (in the magnitude range of 6.0-8.0 rupturing 5

locations along the fault with rupture propagating in one of two directions) have been used for this to quantify the seismic performance of two 18-story moment frame buildings due to southern San Andreas fault earthquakes over the next thirty years. The first is designed according to the 1982 UBC (existing building) while the second is designed according to a new code 1997 UBC (redesigned building). The resulting analysis indicate that the performance of both structures are similar up to earthquakes of $M_w 6.8$ with significant differences observed for higher magnitude earthquakes. The existing building had a median peak inter story drift ratio of approximately 0.06 (corresponds to collapse prevention limit state) while the redesigned building had a median value of 0.025 (corresponds to life safety limit state) for a $M_w 7.9$ earthquake occurring at various sections with two rupture directivities along the southern San Andreas fault. While this has shown that the buildings designed according to new codes perform significantly better on average, a scenario specific analysis such as building response to a hypothetical 1857 Fort Tejon earthquake indicate that the redesigned buildings do not perform adequately.

5. A statistical analysis of the structural response indicates that major damage occurred in both buildings at a predominant ground motion period of $2 - 7$ s, $3 - 6$ s respectively with peak ground velocity of 0.6 m/s and higher, 0.9 m/s and higher for the existing and redesigned buildings respectively . A distinct V-shape transition zone was observed for peak inter story drift ratio in the PGV-PGD plane where the building response transitions between different limit states that indicate the safety level of the building. It is concluded that PGV-PGD combinations of at least 0.4 m/s-0.3 m and 0.8 m/s-0.8 m, approximately, may be necessary to collapse the existing and redesigned buildings, respectively.

6. Fragility curves indicate that the model collapse probability for the redesigned building in the X (EW) direction is lower by factors of 1.75, 1.25, and 1.11 for PGVs of 1.0 m/s, 1.5 m/s, and 2.0 m/s, respectively. The corresponding factors in the Y (NS) direction are 4.33, 1.51, and 1.13 for PGVs of 1.0 m/s, 1.5 m/s, and 2.0 m/s, respectively. There is a 10% probability of collapse that earthquake motion with a PGV of 0.71 m/s in the EW direction or a PGV of 0.59 m/s in the NS direction would collapse the existing building model. Similarly, there is a 10% probability of collapse that earthquake motion with a PGV of 0.85 m/s in the EW direction or a PGV of 0.94 m/s in the NS direction would collapse the redesigned building model. Likewise, there is

a 10% probability of collapse for shaking with a S_a of 0.22 g in the X (EW) direction or a S_a of 0.19 g in the Y (NS) direction for the existing building model. For the redesigned building model, there is a 10% probability of collapse for shaking with a S_a of 0.33 g in the X+Y- direction or a S_a of 0.31 g in the X+Y+ direction . The intent of building codes is to limit the probability of collapse to under 10%. It may thus be inferred that these are the intensities of ground motion that the two buildings have effectively been designed for.

7. Combining this with the likelihood of the earthquake occurring, the existing building indicate a 24.40%, 11.44% and 7.59% probability of exceeding immediate occupancy, life safety and collapse prevention limit states, respectively, due to large southern San Andreas fault earthquakes over the next 30 years. The corresponding result for the redesigned building is 19.25%, 8.40% and 5.23% indicating a marginal improvement in the code based design. The long-period spectral accelerations predicted by the simulations are at least twice as large as the UBC97 MCE spectrum. It is no surprise then that the probabilities of the collapse prevention limit state being exceeded over the next thirty years for the existing (7.59%) and redesigned (5.23%) buildings are much higher than the 2% probability of collapse in 50 years (or 10% probability of collapse in an MCE event with a recurrence period of 2475 years), implicit in building codes.

8. An adjunct analysis of the simulated long-period ground motions for basin sites at moderate distances (55-75 km) from M_w $6.05 - 7.90$ earthquake ruptures using Bayesian model class identification indicate that while the conditional distribution of peak ground velocity and displacement may be typically characterized using a lognormal distribution, the unconditional distribution of log(PGV) and log(PGD) are broader and flatter, and are best classified as double pareto uniform distributions. The broader the range of possible earthquake magnitudes, the broader are the distributions likely to be. This is crucial in understanding the nature of ground motions in future earthquakes and may significantly alter the design of tall buildings that are more affected by such motions .

5.2 Future Work

While the present study tried to address many issues pertaining to rupture-to-rafters simulations, it opened a plethora of opportunities to continue and push the boundaries of current study in the field of earthquake engineering. Further issues that can be addressed by expanding the study include, but are not limited to, the following topics:

1. In order to increase the robustness of the stochastic source model generation algorithm presented, further studies can be conducted using Southern California Earthquake Center broadband platform which allows researchers to compare various stochastic source models and the associated ground motions with historic earthquake data using a wide array of broadband metrics. A key highlight of the proposed algorithm is the use of principal stress data measured near the fault and the inclusion of laboratory earthquake data in modeling seismic sources. However, due to the current limitations, a one-dimensional variation along fault length of rupture velocity is prescribed in the current source models. As more data becomes available the algorithm can be extended to include rupture velocity variation along fault depth producing a more physically accurate seismic source. Furthermore, any study involving the use of laboratory data raises the issue of scaling to address large scale variations that exist in reality. While a self-similarity assumption with necessary justification is provided in the current source models, a more robust analysis can be conducted to address the issue of scaling.
2. While the seismic performance of tall moment frame buildings are quantified in this work using peak inter-story drift ratio, further analysis of the dynamic response of the structure can be conducted to identify the collapse mechanisms of these buildings. This also leads to a pertinent question of whether adding localized braces or other bracing mechanisms improve the performance of these buildings.
3. How does the performance of braced-frame or dual-system buildings designed according to similar codes perform under similar ground motion intensities? Will these buildings behave similarly and are the collapse mechanisms identical to the ones observed from the current study?
4. What are the expected annual economic losses for these tall buildings in southern California or

other regions of interest due to large magnitude earthquakes that pose a relatively great threat?

5. Can the existing simulations be used for disaster preparedness and simultaneously provide a platform for engineers with a ground motion and structural model database? Can those simulations be extended further in the development of a more reliable and accurate seismic hazard maps?

Appendix A

Source Model Generation Algorithm Validation: $M_w 6.05$, 2004 Parkfield-like Earthquake on Southern San Andreas Fault

The validation exercise to ensure that the ground motions produced by the stochastic source models are similar to those produced by finite-source inversion models is repeated for a $M_w = 6.05$ earthquake. As for the $M_w = 7.9$ earthquake, five stochastic source realizations are generated. Each is placed at five locations along the southern San Andreas fault, and ground motions are generated for north-to-south and south-to-north propagating ruptures. The median source model that is determined using the method outlined in the study, is shown in Fig. A.1(a). Also, shown there in Fig. A.1(b), is a finite-source inversion model for the 2004 Mw = 6.0 Parkfield earthquake (Ji 2004). The median ground motion produced by the median model is shown in Fig. A.2. The peak ground velocity and displacement maps generated by the stochastic median and the Parkfield finite-source inversion models rupturing location 3 of the southern San Andreas fault are shown in Figs. A.3 and A.4, respectively. The stronger asperity in the stochastic model leads to more intense ground motions than the Parkfield model. For a north-to-south propagation of the stochastic median model, the location of intense ground motions move gradually southeast of the San Fernando valley as the rupture location shifts south from Parkfield. For south-to-north propagating ruptures, the location of intense ground motions moves gradually northwest of the San Gabriel valley as rupture location shifts north from Bombay Beach. This is similar to the $M_w = 7.9$ earthquake simulations.

The statistical comparison of peak ground velocity (see Figs. A.5 and A.6) and displacement resulting from the two source models indicates significant differences. This can be attributed primarily to the strength of the slip asperity in the stochastic source compared to that in the finite-source inver-

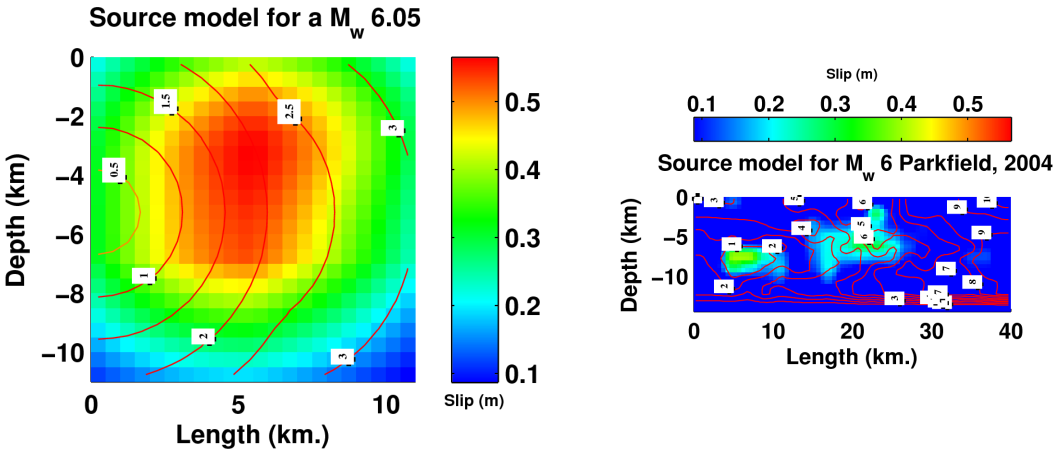

(a)

(b)

Figure A.1: (a) Stochastic median source model with slip in m for a $M_w = 6.05$ earthquake on the San Andreas fault. (b) Finite-source inversion model for the $M_w = 6.0$ Parkfield earthquake of 2004 (Ji 2004). Rupture time (s) contours are overlaid on the slip distribution. The maximum slip rate for the stochastic and inversion models is 1.99 m/s and 1.09 m/s respectively.

sion. The reason for this may be the magnitude-area relation that suggests a rupture area of just 10 km x 10 km for a $M_w = 6.0$ earthquake, whereas the finite-source inversion for the Parkfield earthquake points to a significantly larger area and smaller slips as a result.

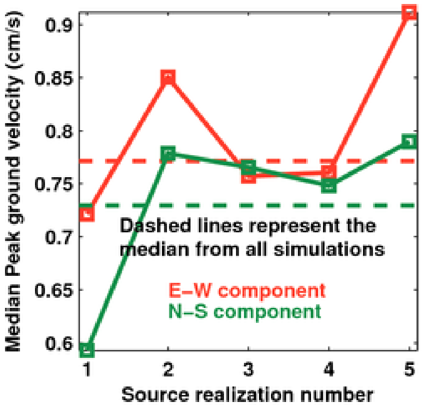

Figure A.2: Solid lines: Median PGV computed at 636 sites in southern California from ten rupture scenarios (five rupture locations along the southern San Andreas fault x two rupture directions) using each of five stochastic source realizations; Dashed lines: The corresponding median PGV from all fifty scenario earthquakes. All earthquakes are of magnitude $M_w = 6.05$.

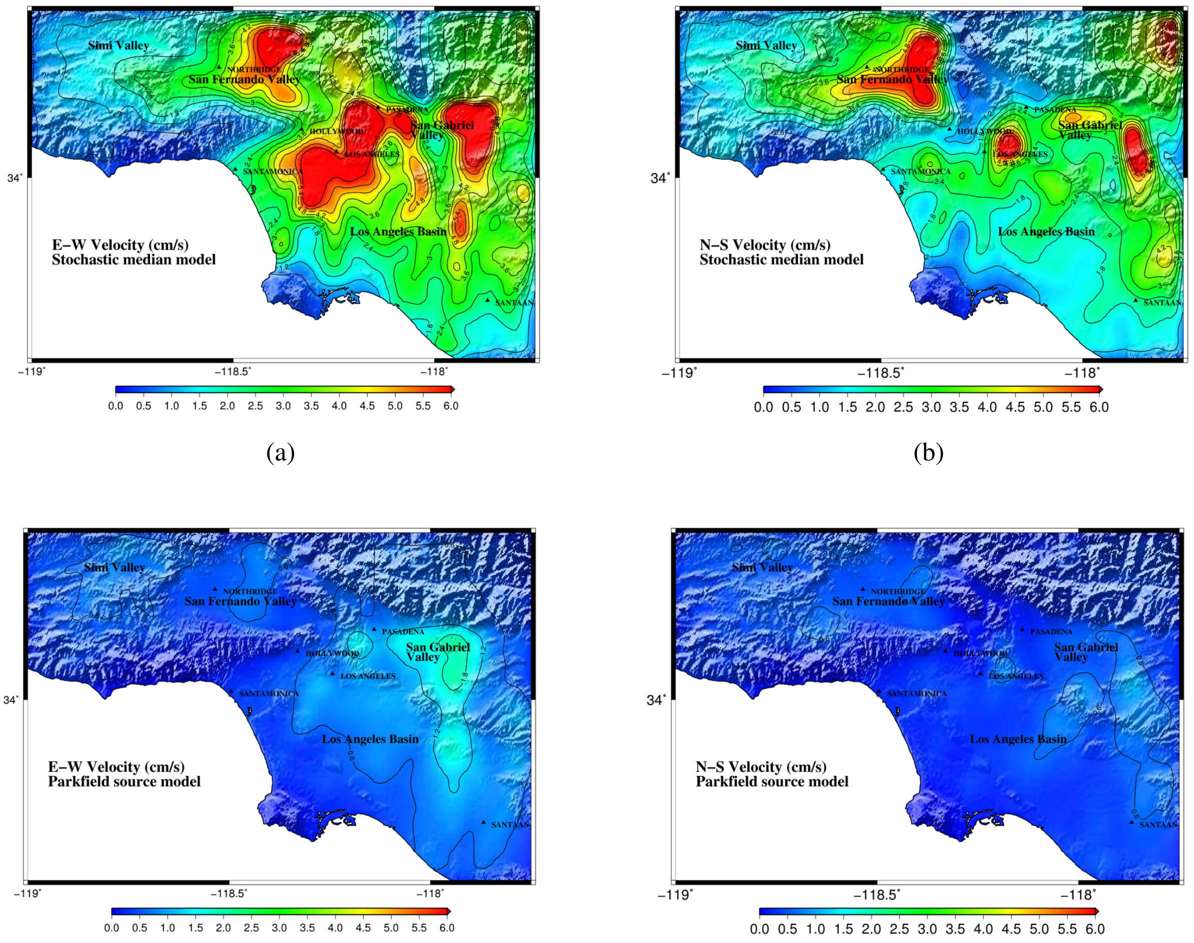
Simi Valley
NORTHRIDGE
San Fernando Valley
PASADENA
HOLLYWOOD
LOS ANGELES
San Gabriel Valley
SANTAMONICA
Los Angeles Basin
SANTAAN
34°
E–W Velocity (cm/s)
Stochastic median model
N–S Velocity (cm/s)
Stochastic median model
E–W Velocity (cm/s)
Parkfield source model
N–S Velocity (cm/s)
Parkfield source model
–119°
–118.5°
–118°
0.0 0.5 1.0 1.5 2.0 2.5 3.0 3.5 4.0 4.5 5.0 5.5 6.0

(a) (b)

(c) (d)

Figure A.3: EW and NS components of PGV (cm/s) from a north-to-south propagating rupture at location 3 on the southern San Andreas fault: (a) and (b) $M_w = 6.05$ stochastic median source model; (c) and (d) $M_w = 6.0$ Parkfield earthquake finite-source inversion model (Ji 2004).

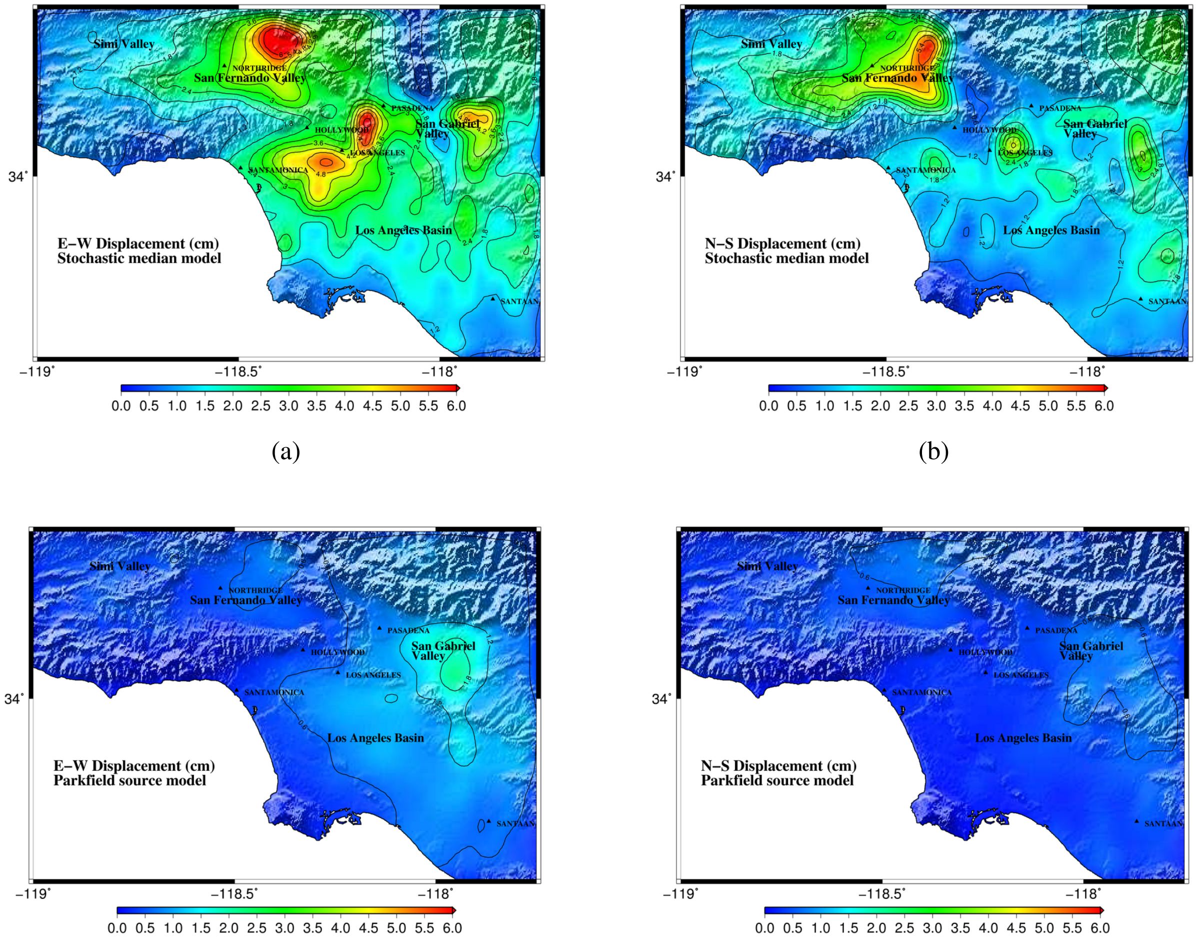
Simi Valley
NORTHRIDGE
San Fernando Valley
PASADENA
HOLLYWOOD
San Gabriel Valley
LOS ANGELES
SANTAMONICA
Los Angeles Basin
SANTAAN
E–W Displacement (cm)
Stochastic median model
N–S Displacement (cm)
Stochastic median model
E–W Displacement (cm)
Parkfield source model
N–S Displacement (cm)
Parkfield source model
34˚
–119˚
–118.5˚
–118˚
0.0 0.5 1.0 1.5 2.0 2.5 3.0 3.5 4.0 4.5 5.0 5.5 6.0

(a) (b)

(c) (d)

Figure A.4: EW and NS components of PGD (cm) from a north-to-south propagating rupture at location 3 on the southern San Andreas fault: (a) and (b) $M_w = 6.05$ stochastic median source model; (c) and (d) $M_w = 6.0$ Parkfield earthquake finite-source inversion model (Ji 2004).

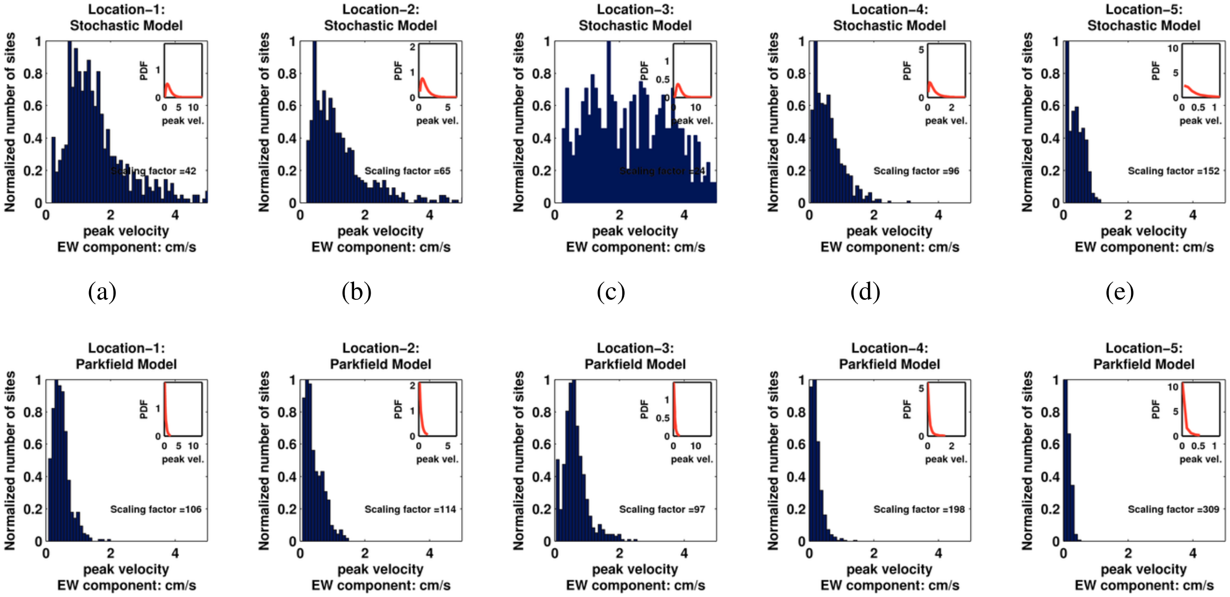

(a) (b) (c) (d) (e)

(f) (g) (h) (i) (j)

Figure A.5: Five $M_w = 6.05$ north-to-south rupture scenarios (at locations $1-5$) on the San Andreas fault using [(a)$-$(e)] the stochastic median model and [(f)$-$(j)] the $M_w = 6.0$ Parkfield earthquake finite-source inversion model: Histograms and best-fit log-normal PDFs (insets) of PGV at 636 stations in southern California. The product of the listed scaling factor and the normalized histogram ordinate at a specific peak velocity gives the total number of stations for that velocity.

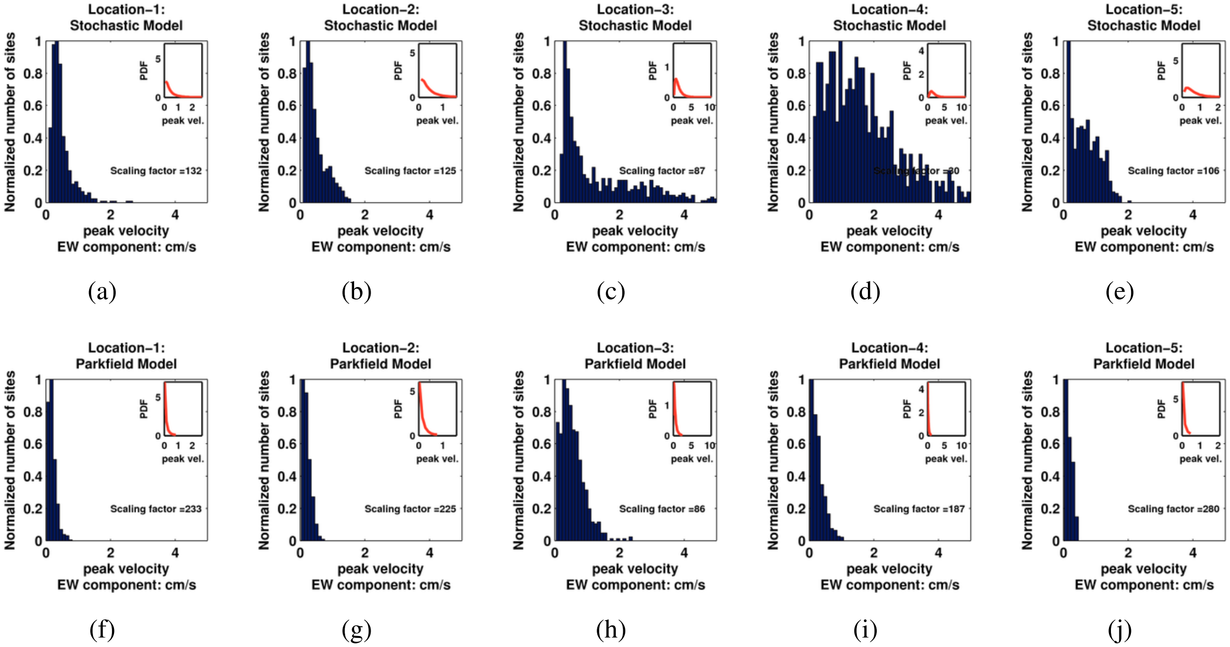

(a) (b) (c) (d) (e)

(f) (g) (h) (i) (j)

Figure A.6: Five $M_w = 6.05$ south-to-north rupture scenarios (at locations $1-5$) on the San Andreas fault using [(a)$-$(e)] the stochastic median model and [(f)$-$(j)] the $M_w = 6.0$ Parkfield earthquake finite-source inversion model: Histograms and best-fit log-normal PDFs (insets) of PGV at 636 stations in southern California. The product of the listed scaling factor and the normalized histogram ordinate at a specific peak velocity gives the total number of stations for that velocity.

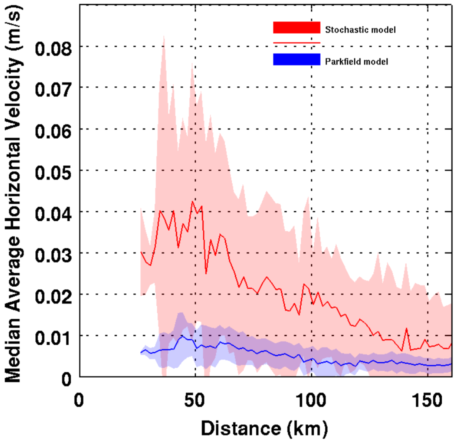

Figure A.7: Median peak average horizontal velocity (m/s) [(red) Stochastic and (blue) Parkfield model] as a function of source-to-site distance, in southern California due to $M_w 6.05$ earthquake occurring along southern San Andreas fault. The shaded region corresponds to median plus/minus one standard deviation. A total of 10 rupture scenarios (5 rupture locations x 2 propagation directivity) are considered.

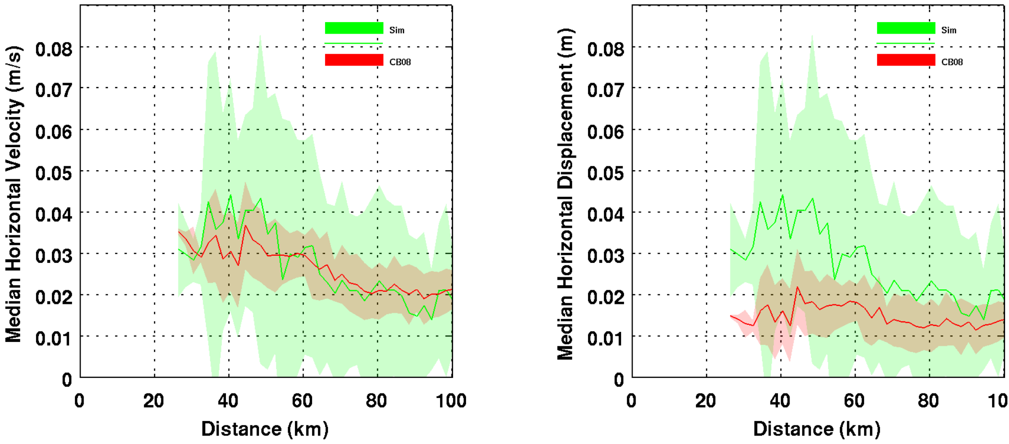

(a)

(b)

Figure A.8: (a) Median peak horizontal velocity (m/s) and (b) median peak horizontal displacement (m) as a function of source-to-site distance for ten $M_w 6.05$ earthquake scenarios on the southern San Andreas fault (five rupture locations and two rupture directions) using the median stochastic source model. Shown in red are the predictions by the Campbell-Bozorgnia NGA relation. The shaded region corresponds to median plus/minus one standard deviation.

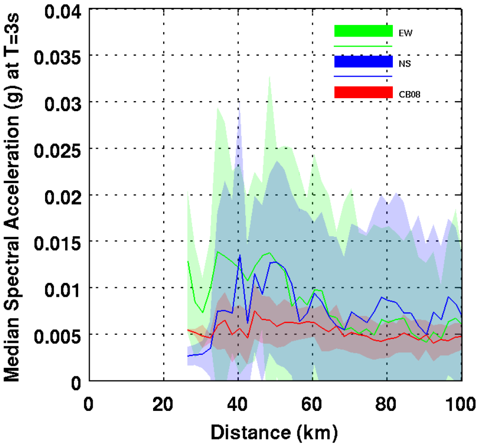

Figure A.9: Spectral acceleration (g) at T = 3 s as a function of source-to-site distance for ten Mw 6.05 earthquake scenarios on the southern San Andreas fault (five rupture locations and two rupture directions). Shown in green and blue are the simulated east-west and the north-south Sa3s components at greater Los Angeles sites using the median stochastic source model, respectively. Shown in red are the predictions by the Campbell-Bozorgnia NGA relation. The shaded region corresponds to median plus/minus one standard deviation.

Appendix B

Ground Motion Maps for $M_w 7.9$ Denali Finite-Source Inversion and Stochastic Source Models Traveling at Sub-Rayleigh and Super-shear Regimes

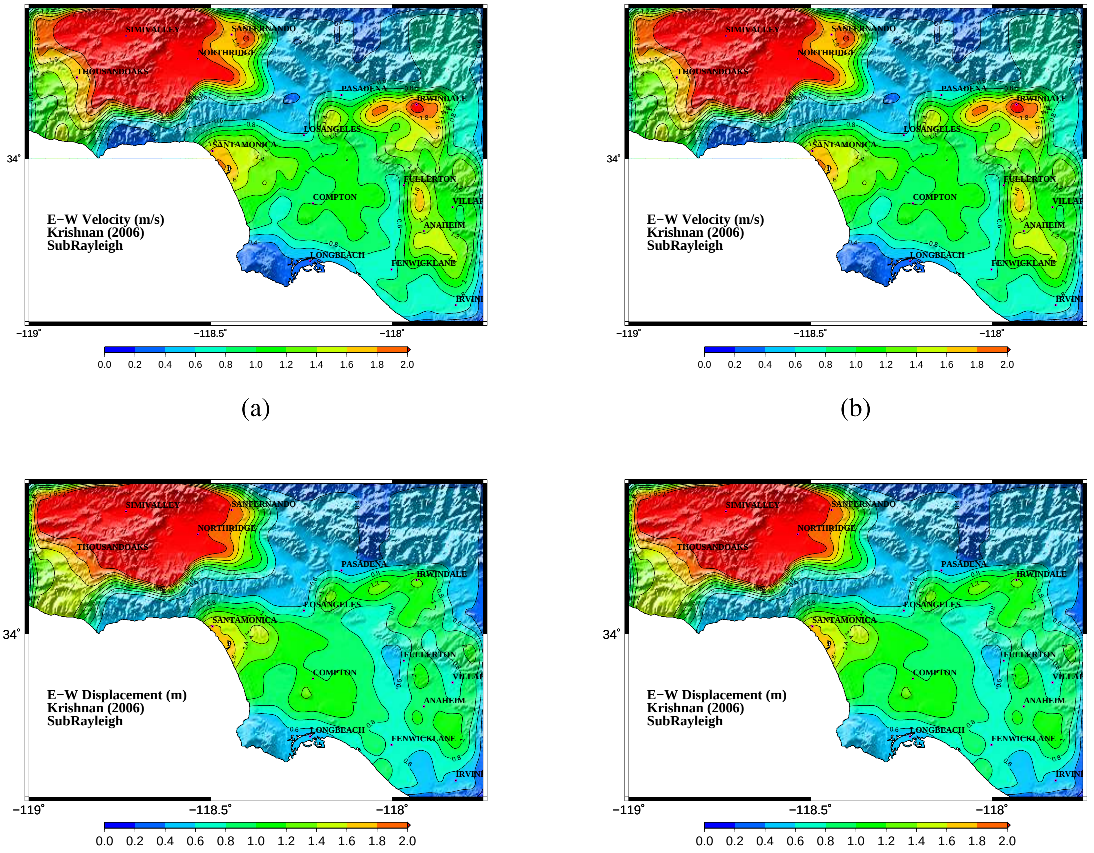
E−W Velocity (m/s)
Krishnan (2006)
SubRayleigh
E−W Displacement (m)
Krishnan (2006)
SubRayleigh
SIMIVALLEY
SANFERNANDO
NORTHRIDGE
THOUSANDOAKS
PASADENA
IRWINDALE
LOSANGELES
SANTAMONICA
FULLERTON
COMPTON
VILLAP
ANAHEIM
LONGBEACH
FENWICKLANE
IRVINE
34°
−119°
−118.5°
−118°
0.0
0.2
0.4
0.6
0.8
1.0
1.2
1.4
1.6
1.8
2.0

(a) (b)

(c) (d)

Figure B.1: EW and NS components of (a) and (b) PGV (m/s); (c) and (d) PGD (m) from a north-to-south propagating rupture at location 1 on the southern San Andreas fault for Denali earthquake finite-source inversion model (Krishnan et al. 2006a) with rupture speed modified to travel in pure sub-Rayleigh mode.

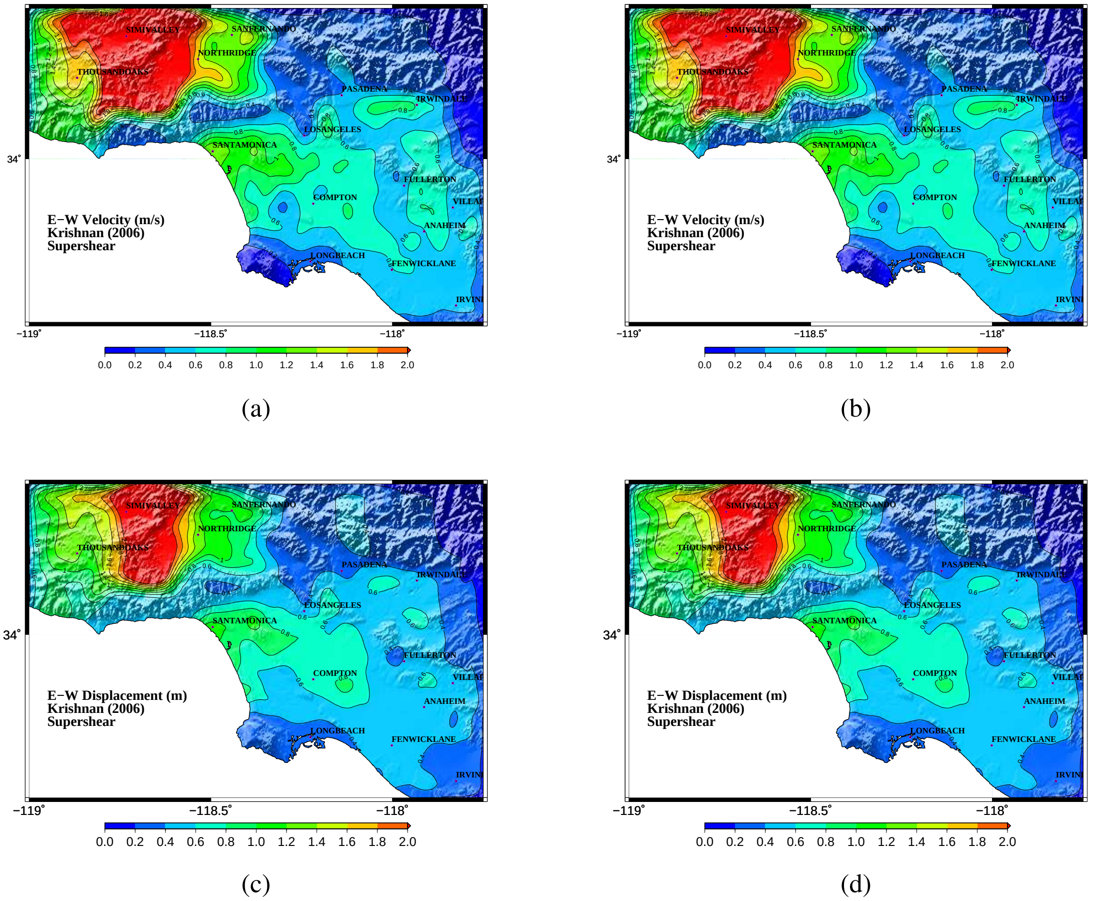
SIMIVALLEY
SANFERNANDO
NORTHRIDGE
THOUSANDOAKS
PASADENA
IRWINDALE
LOSANGELES
SANTAMONICA
FULLERTON
COMPTON
VILLAP
ANAHEIM
LONGBEACH
FENWICKLANE
IRVIN
34°
−119°
−118.5°
−118°
0.0
0.2
0.4
0.6
0.8
1.0
1.2
1.4
1.6
1.8
2.0
E−W Velocity (m/s)
Krishnan (2006)
Supershear
E−W Displacement (m)
Krishnan (2006)
Supershear

(a) (b) (c) (d)

Figure B.2: EW and NS components of (a) and (b) PGV (m/s); (c) and (d) PGD (m) from a north-to-south propagating rupture at location 1 on the southern San Andreas fault for Denali earthquake finite-source inversion model (Krishnan et al. 2006a) with rupture speed modified to travel in pure super-shear mode.

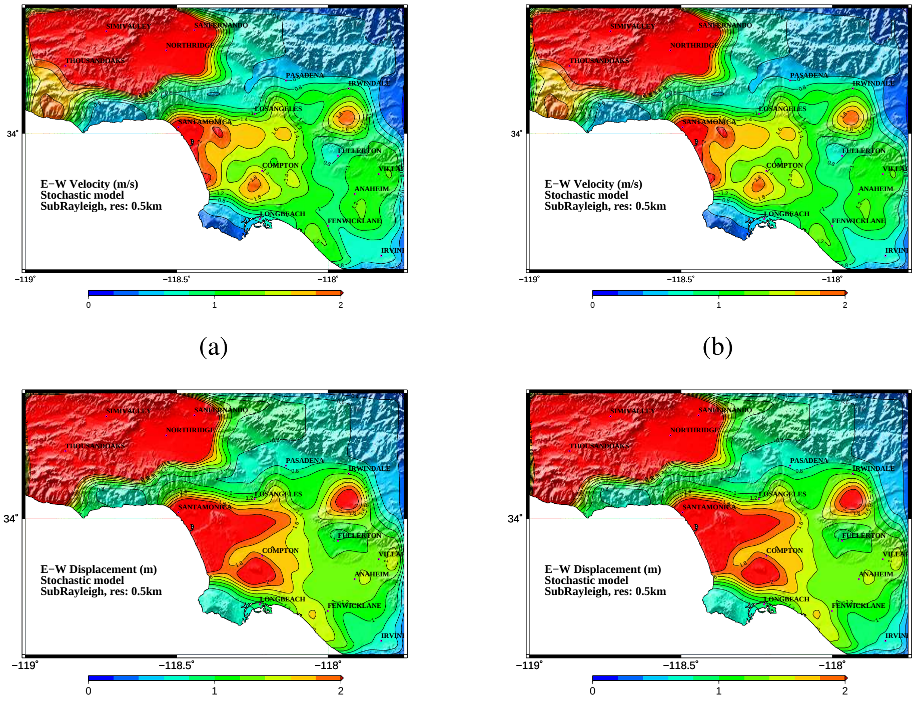
SIMIVALLEY
SANFERNANDO
NORTHRIDGE
THOUSANDOAKS
PASADENA
IRWINDALE
LOSANGELES
SANTAMONICA
FULLERTON
COMPTON
VILLAP
ANAHEIM
LONGBEACH
FENWICKLANE
IRVINE
34°
E−W Velocity (m/s)
Stochastic model
SubRayleigh, res: 0.5km
E−W Displacement (m)
Stochastic model
SubRayleigh, res: 0.5km
−119°
−118.5°
−118°
0
1
2

(a) (b)

(c) (d)

Figure B.3: EW and NS components of (a) and (b) PGV (m/s); (c) and (d) PGD (m) from a north-to-south propagating rupture at location 1 on the southern San Andreas fault for a Stochastic source realization (refer to as model-1) of $M_w 7.9$ earthquake with rupture traveling in pure sub-Rayleigh mode.

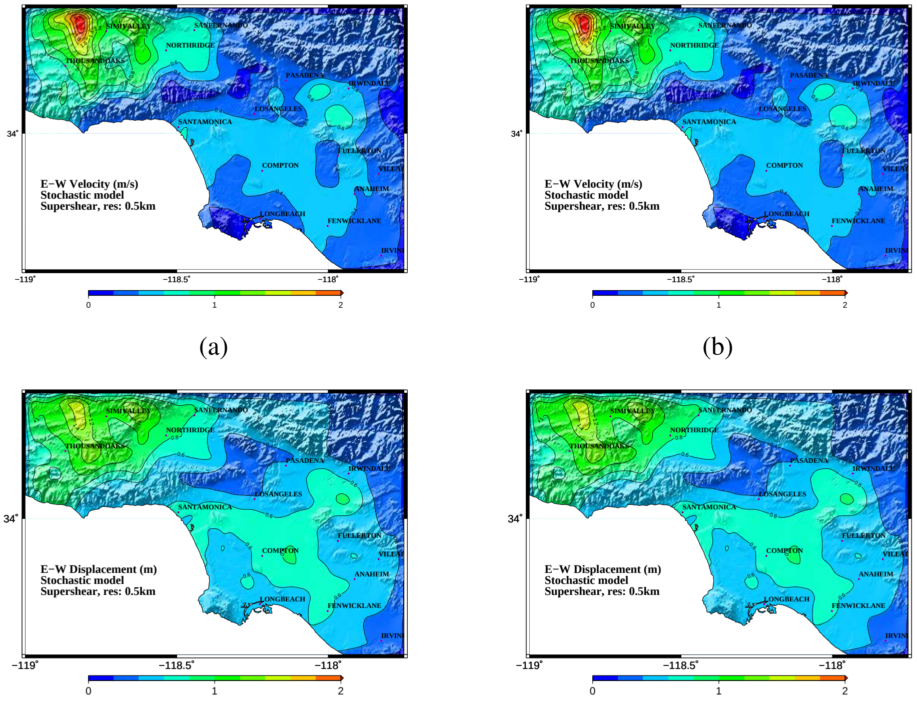
SIMIVALLEY
SANFERNANDO
NORTHRIDGE
THOUSANDOAKS
PASADENA
IRWINDALE
LOSANGELES
SANTAMONICA
COMPTON
FULLERTON
VILLAP
ANAHEIM
LONGBEACH
FENWICKLANE
IRVIN
34°
−119°
−118.5°
−118°
0
1
2
E−W Velocity (m/s)
Stochastic model
Supershear, res: 0.5km
E−W Displacement (m)
Stochastic model
Supershear, res: 0.5km

(a) (b)

(c) (d)

Figure B.4: EW and NS components of (a) and (b) PGV (m/s); (c) and (d) PGD (m) from a north-to-south propagating rupture at location 1 on the southern San Andreas fault for a Stochastic source realization (model-1) of $M_w 7.9$ earthquake with rupture traveling in pure super-shear mode.

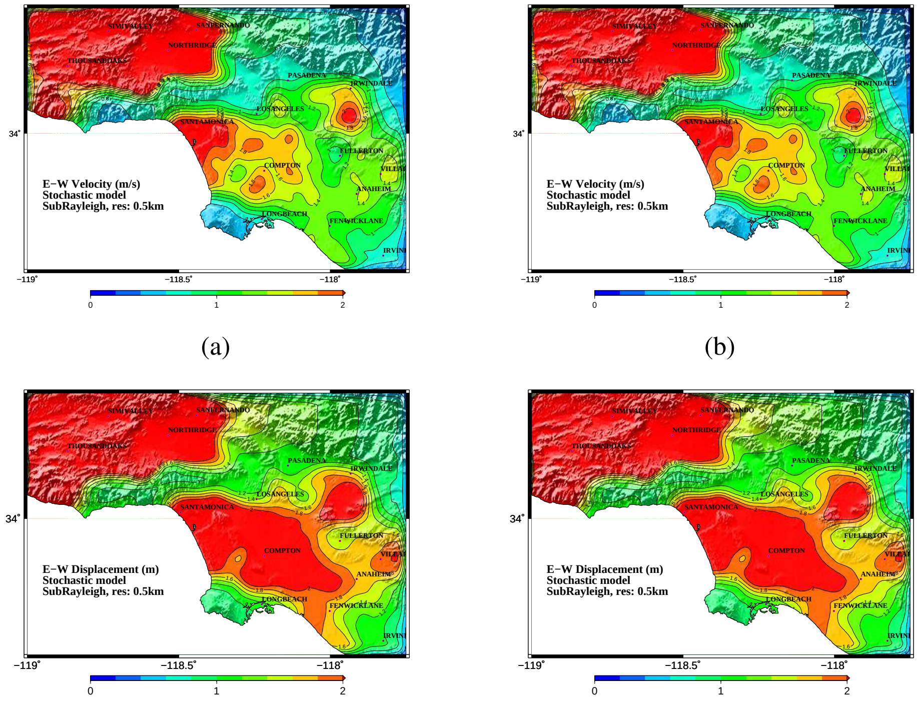
E−W Velocity (m/s)
Stochastic model
SubRayleigh, res: 0.5km
E−W Displacement (m)
Stochastic model
SubRayleigh, res: 0.5km
SIMIVALLEY
SANFERNANDO
NORTHRIDGE
THOUSANDOAKS
PASADENA
IRWINDALE
LOSANGELES
SANTAMONICA
FULLERTON
VILLEP
COMPTON
ANAHEIM
LONGBEACH
FENWICKLANE
IRVINE
34˚
−119˚
−118.5˚
−118˚
0
1
2

(a) (b)

(c) (d)

Figure B.5: EW and NS components of (a) and (b) PGV (m/s); (c) and (d) PGD (m) from a north-to-south propagating rupture at location 1 on the southern San Andreas fault for a Stochastic source realization (refer to as model-2) of $M_w 7.9$ earthquake with rupture traveling in pure sub-Rayleigh mode.

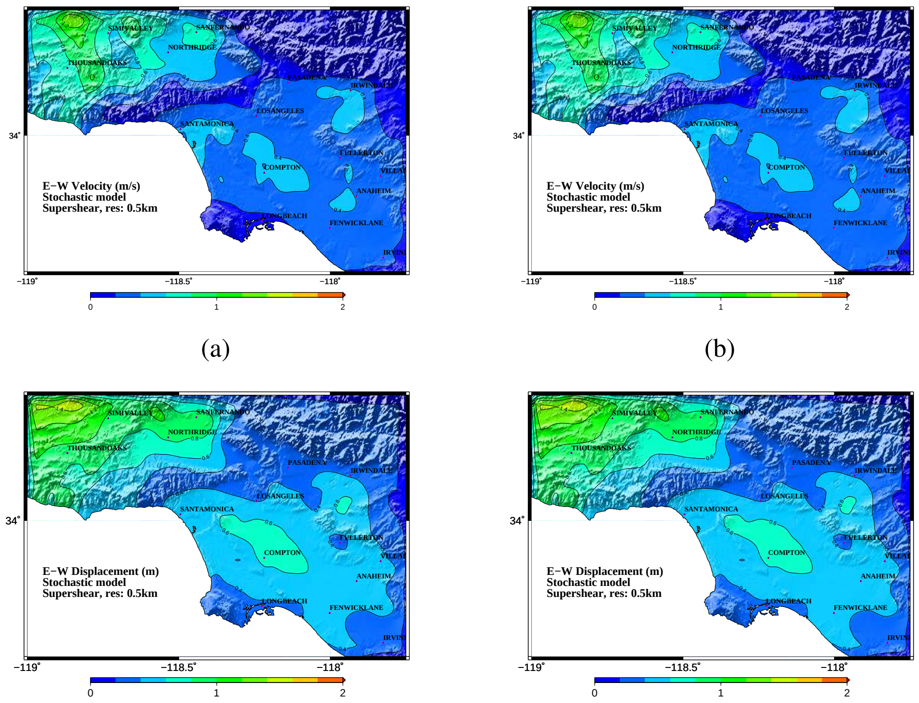
E−W Velocity (m/s)
Stochastic model
Supershear, res: 0.5km
E−W Displacement (m)
SIMIVALLEY
SANFERNANDO
NORTHRIDGE
THOUSANDOAKS
PASADENA
IRWINDALE
SANTAMONICA
LOSANGELES
FULLERTON
COMPTON
VILLAP
ANAHEIM
LONGBEACH
FENWICKLANE
IRVIN
34°
−119°
−118.5°
−118°
0
1
2

(a) (b)

(c) (d)

Figure B.6: EW and NS components of (a) and (b) PGV (m/s); (c) and (d) PGD (m) from a north-to-south propagating rupture at location 1 on the southern San Andreas fault for a Stochastic source realization (model-2) of $M_w 7.9$ earthquake with rupture traveling in pure super-shear mode.

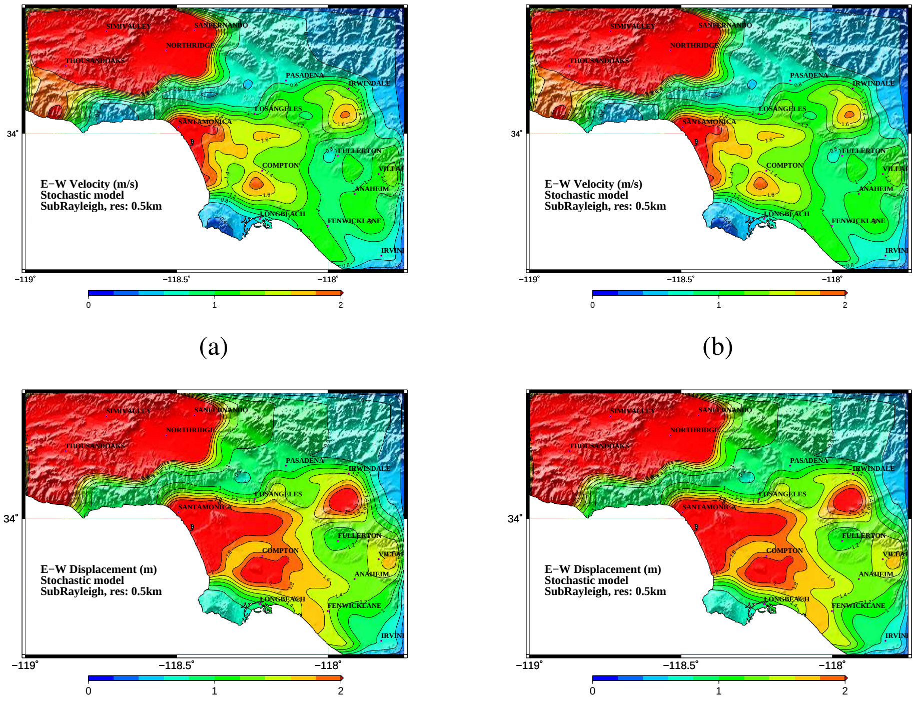

SIMIVALLEY
SANFERNANDO
NORTHRIDGE
THOUSANDOAKS
PASADENA
IRWINDALE
LOSANGELES
SANTAMONICA
FULLERTON
COMPTON
ANAHEIM
LONGBEACH
FENWICKLANE
IRVIN
E−W Velocity (m/s)
Stochastic model
SubRayleigh, res: 0.5km
E−W Displacement (m)
Stochastic model
SubRayleigh, res: 0.5km
34°
−119°
−118.5°
−118°
0
1
2

(a) (b)

(c) (d)

Figure B.7: EW and NS components of (a) and (b) PGV (m/s); (c) and (d) PGD (m) from a north-to-south propagating rupture at location 1 on the southern San Andreas fault for a Stochastic source realization (refer to as model-3) of $M_w 7.9$ earthquake with rupture traveling in pure sub-Rayleigh mode.

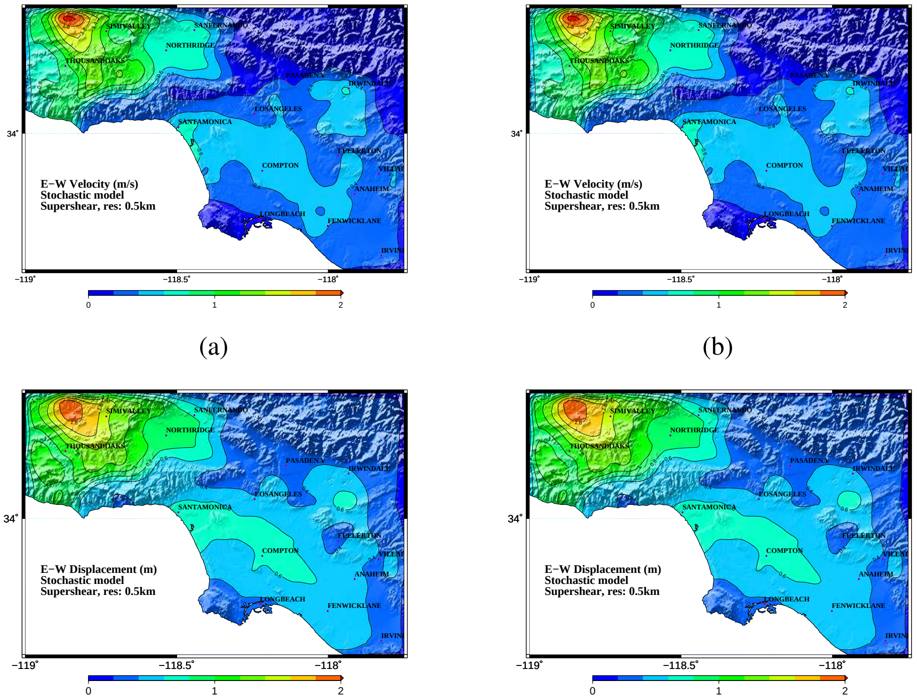

E−W Velocity (m/s)
Stochastic model
Supershear, res: 0.5km
E−W Displacement (m)
Stochastic model
Supershear, res: 0.5km
SIMIVALLEY
SANFERNANDO
NORTHRIDGE
THOUSANDOAKS
PASADENA
IRWINDALE
LOSANGELES
SANTAMONICA
FULLERTON
COMPTON
VILLE
ANAHEIM
LONGBEACH
FENWICKLANE
IRVIN
34˚
−119˚
−118.5˚
−118˚
0
1
2

(a) (b)

(c) (d)

Figure B.8: EW and NS components of (a) and (b) PGV (m/s); (c) and (d) PGD (m) from a north-to-south propagating rupture at location 1 on the southern San Andreas fault for a Stochastic source realization (model-3) with rupture traveling in pure super-shear mode.

Appendix C

Various Stochastic Source Models Generated Through the Algorithm and the Associated Ground Motion Maps

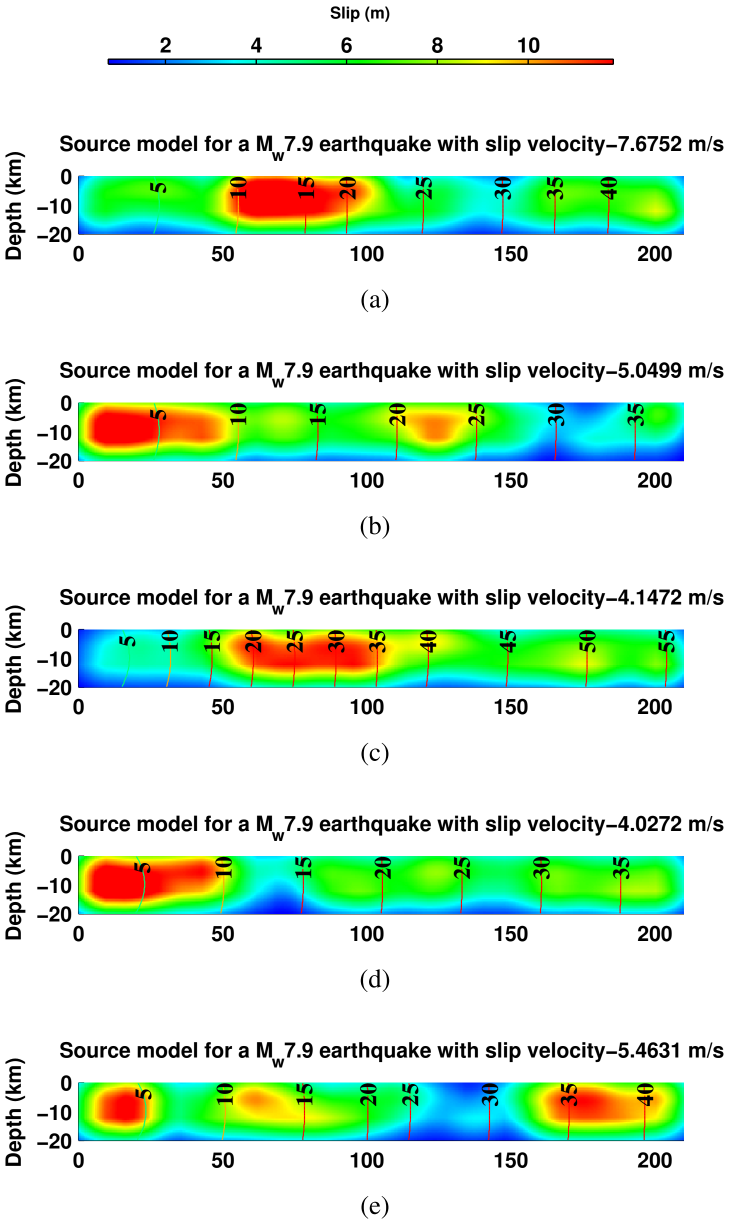

Figure C.1: (a)-(e) Stochastic median source models (here on referred to as models-1, 2, 3, 4, 5) with slip in m for a $M_w = 7.9$ earthquake on the San Andreas fault. Rupture time (s) contours are overlaid on the slip distribution. The rupture contours shown correspond to the stochastic stress conditions at location 1 of the rupture staring at Parkfield. Note that the rupture time contours change for a different location.

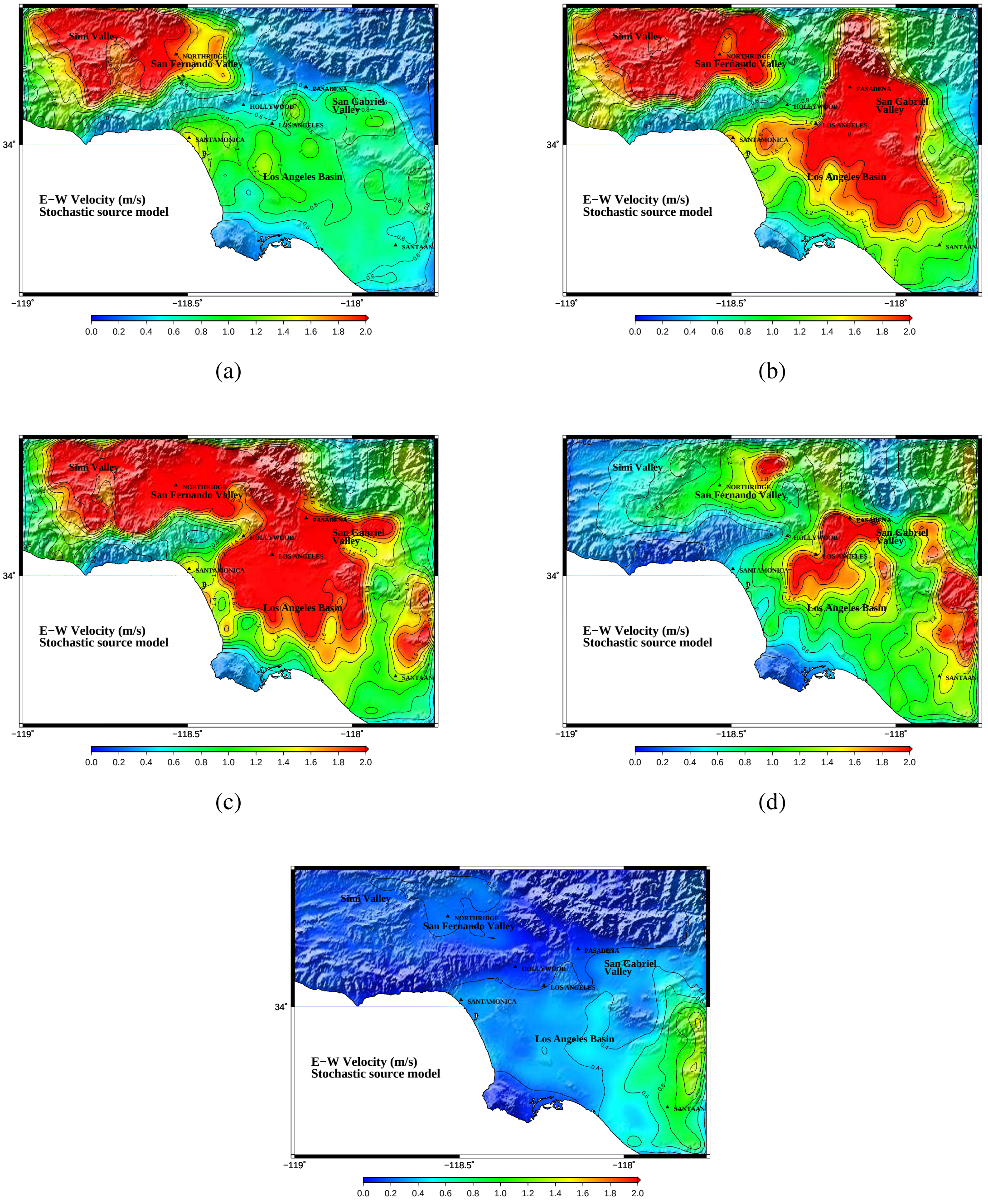
Simi Valley
NORTHRIDGE
San Fernando Valley
PASADENA
HOLLYWOOD
San Gabriel Valley
LOS ANGELES
SANTAMONICA
Los Angeles Basin
SANTAAN
E−W Velocity (m/s)
Stochastic source model
34°
−119°
−118.5°
−118°
0.0
0.2
0.4
0.6
0.8
1.0
1.2
1.4
1.6
1.8
2.0

(a) (b) (c) (d) (e)

Figure C.2: EW component of PGV (m/s) from a north-to-south propagating rupture at (a) - (e) locations 1 - 5 respectively on the southern San Andreas fault for stochastic $M_w 7.9$ model-1 source model. The NS component of PGV has similar characteristics as EW component and the PGD is proportional to PGV in most cases.

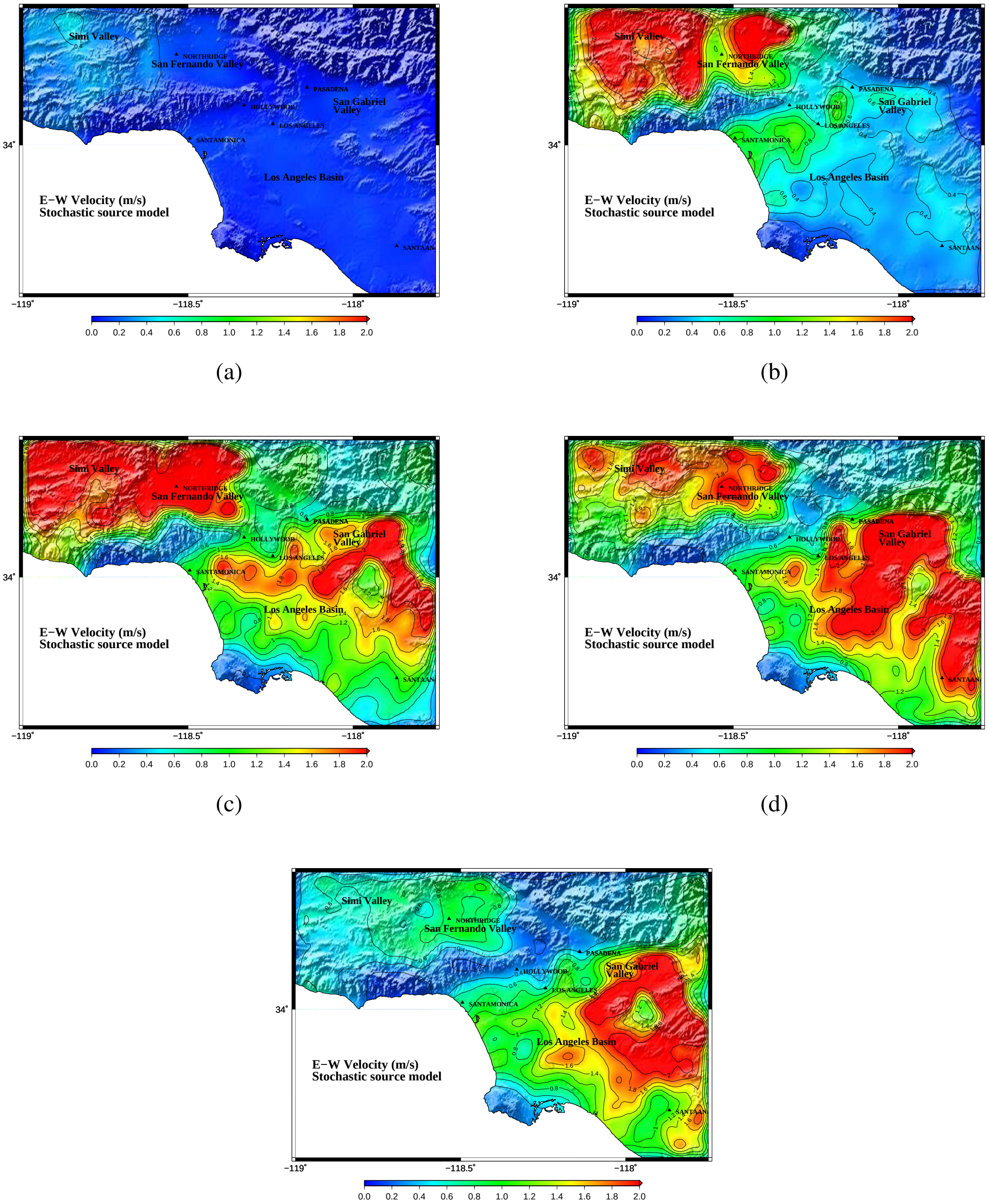
Simi Valley
NORTHRIDGE
San Fernando Valley
PASADENA
San Gabriel Valley
HOLLYWOOD
LOS ANGELES
SANTAMONICA
Los Angeles Basin
SANTAAN
34°
E−W Velocity (m/s)
Stochastic source model
−119°
−118.5°
−118°
0.0
0.2
0.4
0.6
0.8
1.0
1.2
1.4
1.6
1.8
2.0

(a)

(b)

(c)

(d)

(e)

Figure C.3: EW component of PGV (m/s) from a south-to-north propagating rupture at (a) - (e) locations 1 - 5 respectively on the southern San Andreas fault for stochastic $M_w 7.9$ model-1 source model. The NS component of PGV has similar characteristics as EW component and the PGD is proportional to PGV in most cases.

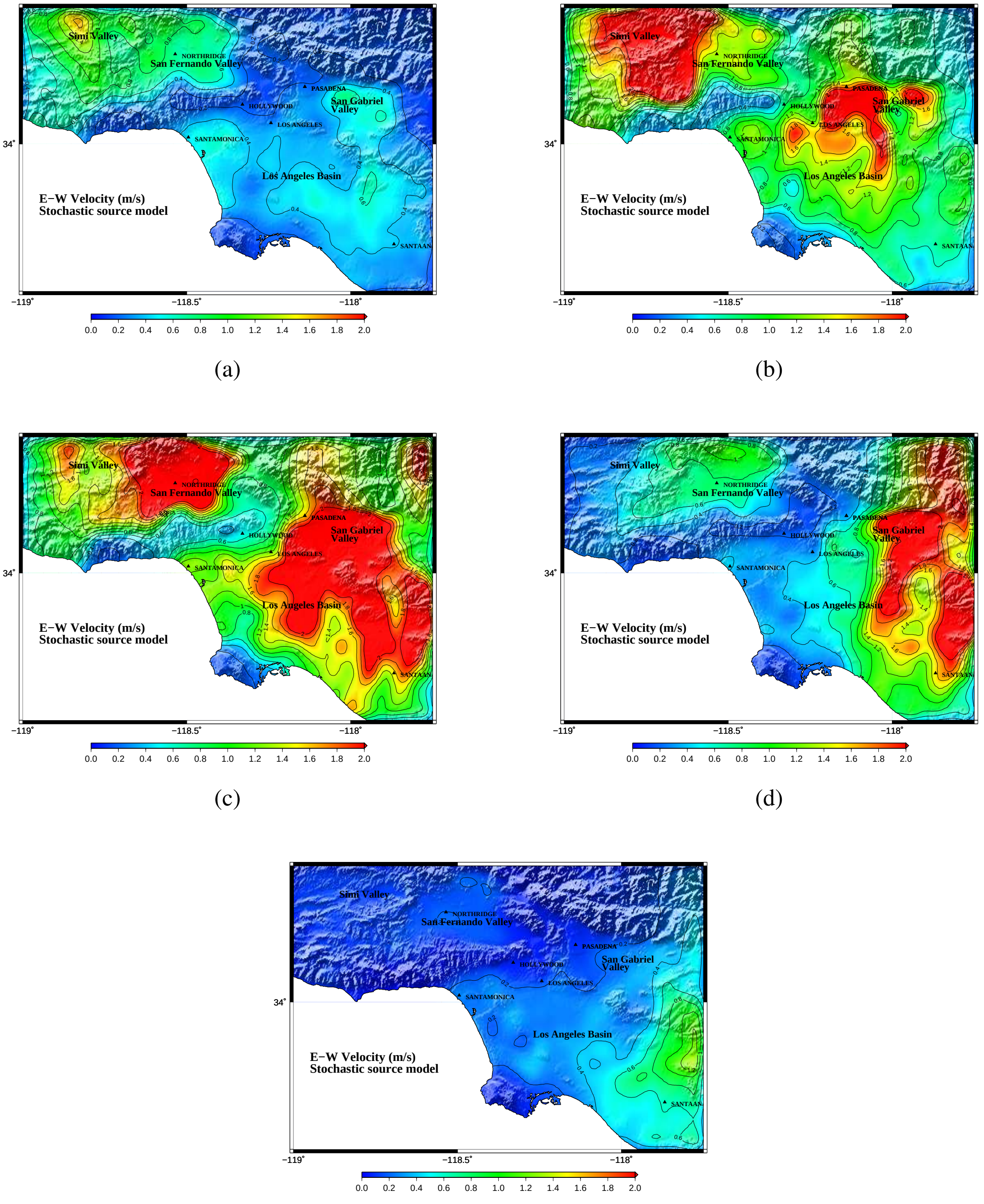
Simi Valley
NORTHRIDGE
San Fernando Valley
PASADENA
San Gabriel Valley
HOLLYWOOD
LOS ANGELES
SANTAMONICA
Los Angeles Basin
SANTAAN
34°
−119°
−118.5°
−118°
E−W Velocity (m/s)
Stochastic source model
0.0
0.2
0.4
0.6
0.8
1.0
1.2
1.4
1.6
1.8
2.0

(a)

(b)

(c)

(d)

(e)

Figure C.4: EW component of PGV (m/s) from a north-to-south propagating rupture at (a) - (e) locations 1 - 5 respectively on the southern San Andreas fault for stochastic $M_w 7.9$ model-2 source model. The NS component of PGV has similar characteristics as EW component and the PGD is proportional to PGV in most cases.

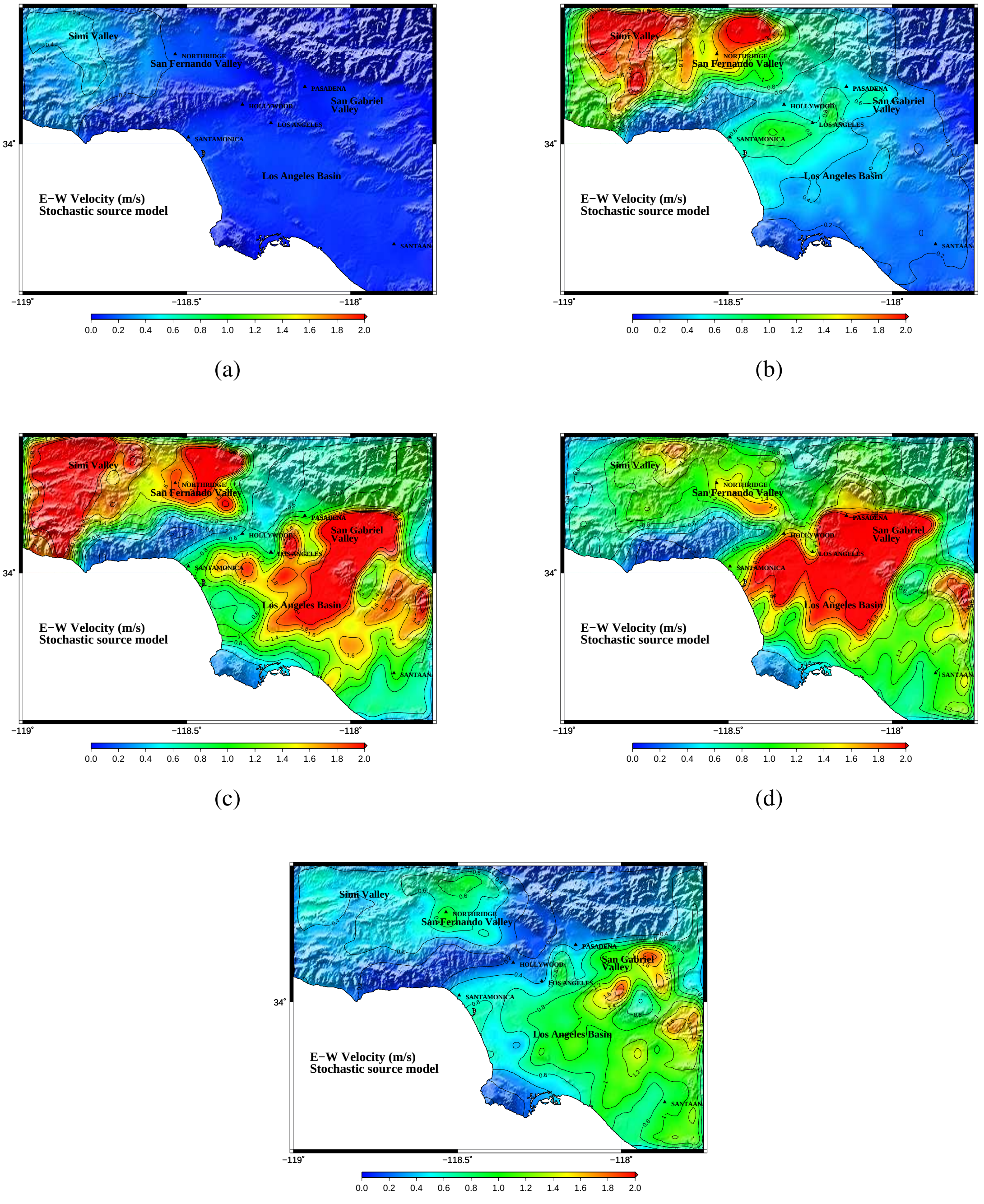
Simi Valley
NORTHRIDGE
San Fernando Valley
PASADENA
San Gabriel Valley
HOLLYWOOD
LOS ANGELES
SANTAMONICA
Los Angeles Basin
SANTAAN
E−W Velocity (m/s)
Stochastic source model
34˚
−119˚
−118.5˚
−118˚
0.0
0.2
0.4
0.6
0.8
1.0
1.2
1.4
1.6
1.8
2.0

(a) (b) (c) (d) (e)

Figure C.5: EW component of PGV (m/s) from a south-to-north propagating rupture at (a) - (e) locations 1 - 5 respectively on the southern San Andreas fault for stochastic $M_w 7.9$ model-2 source model. The NS component of PGV has similar characteristics as EW component and the PGD is proportional to PGV in most cases.

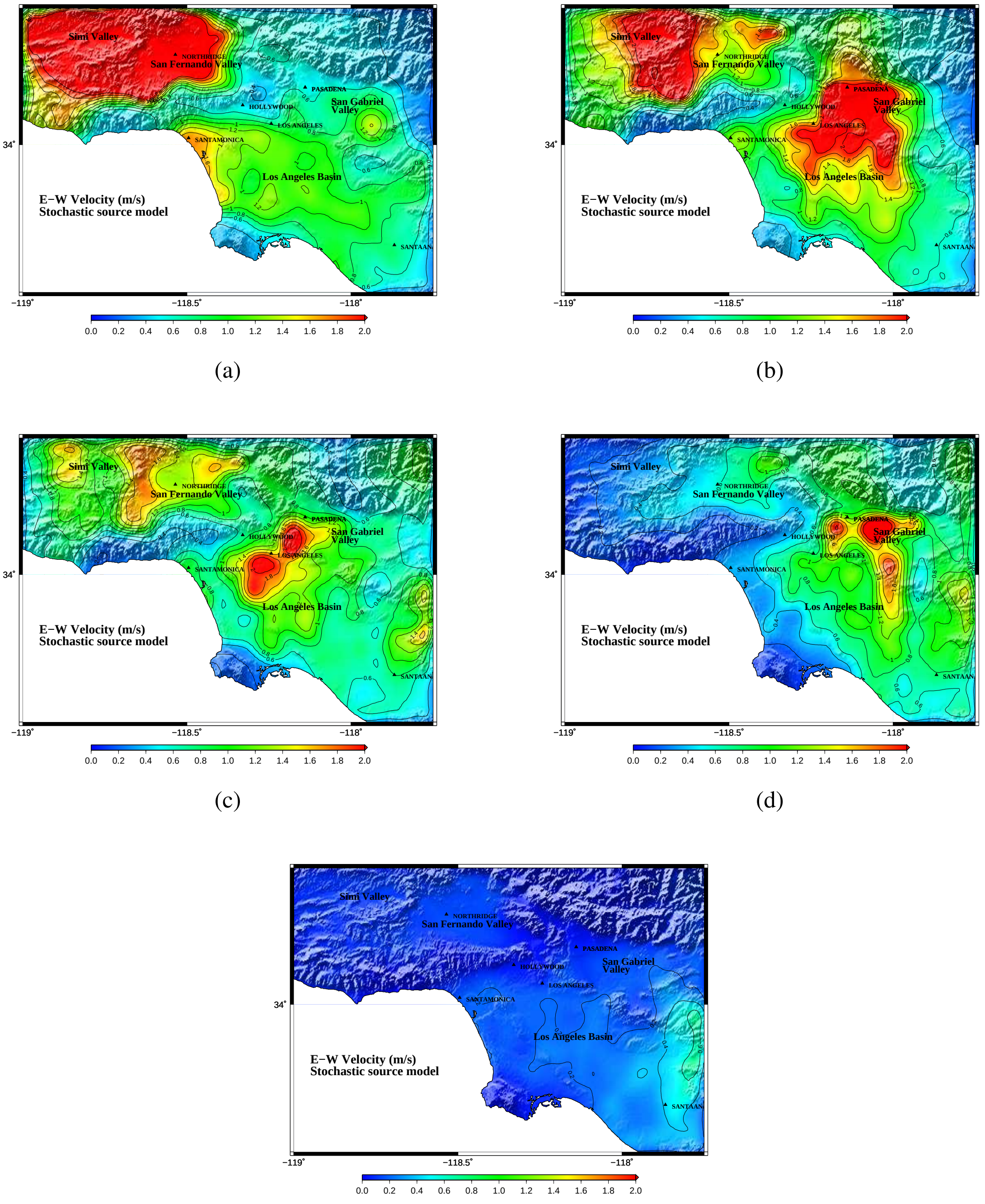

Simi Valley
NORTHRIDGE
San Fernando Valley
PASADENA
HOLLYWOOD
San Gabriel Valley
LOS ANGELES
SANTAMONICA
Los Angeles Basin
SANTAAN
E−W Velocity (m/s)
Stochastic source model
34°
−119°
−118.5°
−118°
0.0
0.2
0.4
0.6
0.8
1.0
1.2
1.4
1.6
1.8
2.0

(a)

(b)

(c)

(d)

(e)

Figure C.6: EW component of PGV (m/s) from a north-to-south propagating rupture at (a) - (e) locations 1 - 5 respectively on the southern San Andreas fault for stochastic $M_w 7.9$ model-3 source model. The NS component of PGV has similar characteristics as EW component and the PGD is proportional to PGV in most cases.

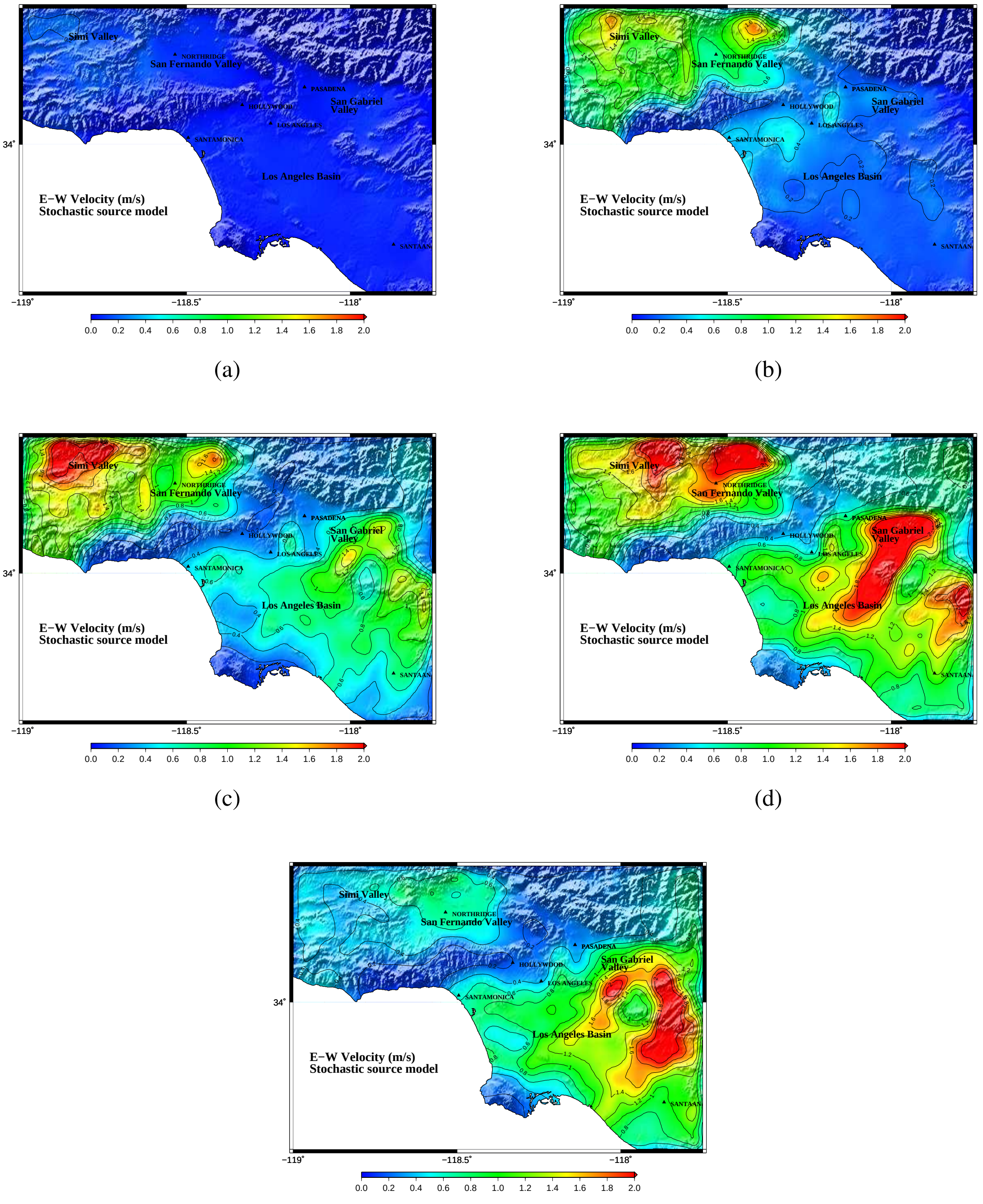
Simi Valley
NORTHRIDGE
San Fernando Valley
PASADENA
San Gabriel Valley
HOLLYWOOD
LOS ANGELES
SANTAMONICA
Los Angeles Basin
SANTAANA
E−W Velocity (m/s)
Stochastic source model
34°
−119°
−118.5°
−118°
0.0
0.2
0.4
0.6
0.8
1.0
1.2
1.4
1.6
1.8
2.0

(a)

(b)

(c)

(d)

(e)

Figure C.7: EW component of PGV (m/s) from a south-to-north propagating rupture at (a) - (e) locations 1 - 5 respectively on the southern San Andreas fault for stochastic $M_w 7.9$ model-3 source model. The NS component of PGV has similar characteristics as EW component and the PGD is proportional to PGV in most cases.

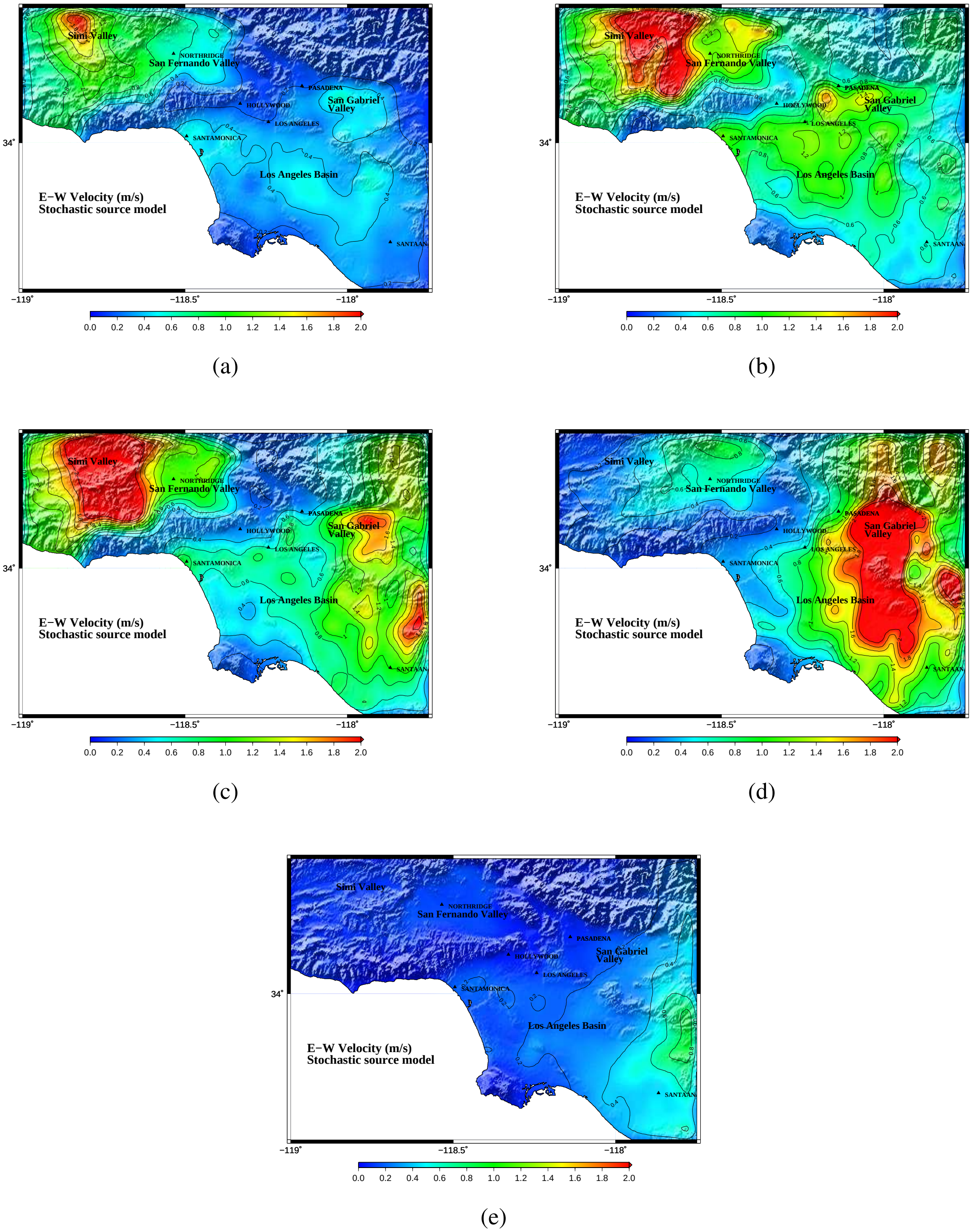
Simi Valley
NORTHRIDGE
San Fernando Valley
PASADENA
HOLLYWOOD
San Gabriel Valley
LOS ANGELES
SANTAMONICA
Los Angeles Basin
SANTAANA
34°
−119°
−118.5°
−118°
E−W Velocity (m/s)
Stochastic source model
0.0
0.2
0.4
0.6
0.8
1.0
1.2
1.4
1.6
1.8
2.0

(a)

(b)

(c)

(d)

(e)

Figure C.8: EW component of PGV (m/s) from a north-to-south propagating rupture at (a) - (e) locations 1 - 5 respectively on the southern San Andreas fault for stochastic $M_w 7.9$ model-4 source model. The NS component of PGV has similar characteristics as EW component and the PGD is proportional to PGV in most cases.

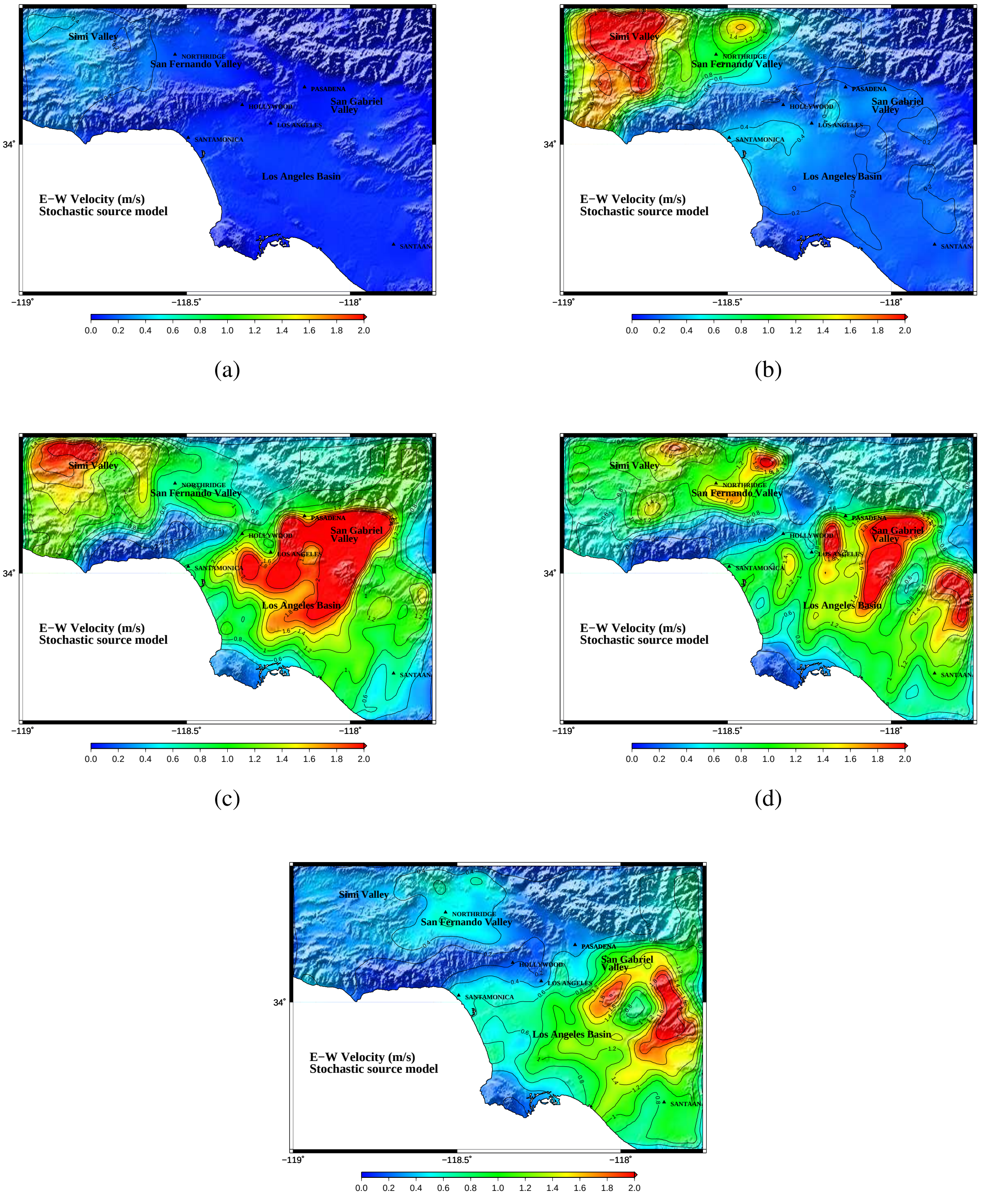
Simi Valley
NORTHRIDGE
San Fernando Valley
PASADENA
San Gabriel Valley
HOLLYWOOD
LOS ANGELES
SANTAMONICA
Los Angeles Basin
SANTAANA
E−W Velocity (m/s)
Stochastic source model
34°
−119°
−118.5°
−118°
0.0
0.2
0.4
0.6
0.8
1.0
1.2
1.4
1.6
1.8
2.0

(a) (b) (c) (d) (e)

Figure C.9: EW component of PGV (m/s) from a south-to-north propagating rupture at (a) - (e) locations 1 - 5 respectively on the southern San Andreas fault for stochastic $M_w 7.9$ model-4 source model. The NS component of PGV has similar characteristics as EW component and the PGD is proportional to PGV in most cases.

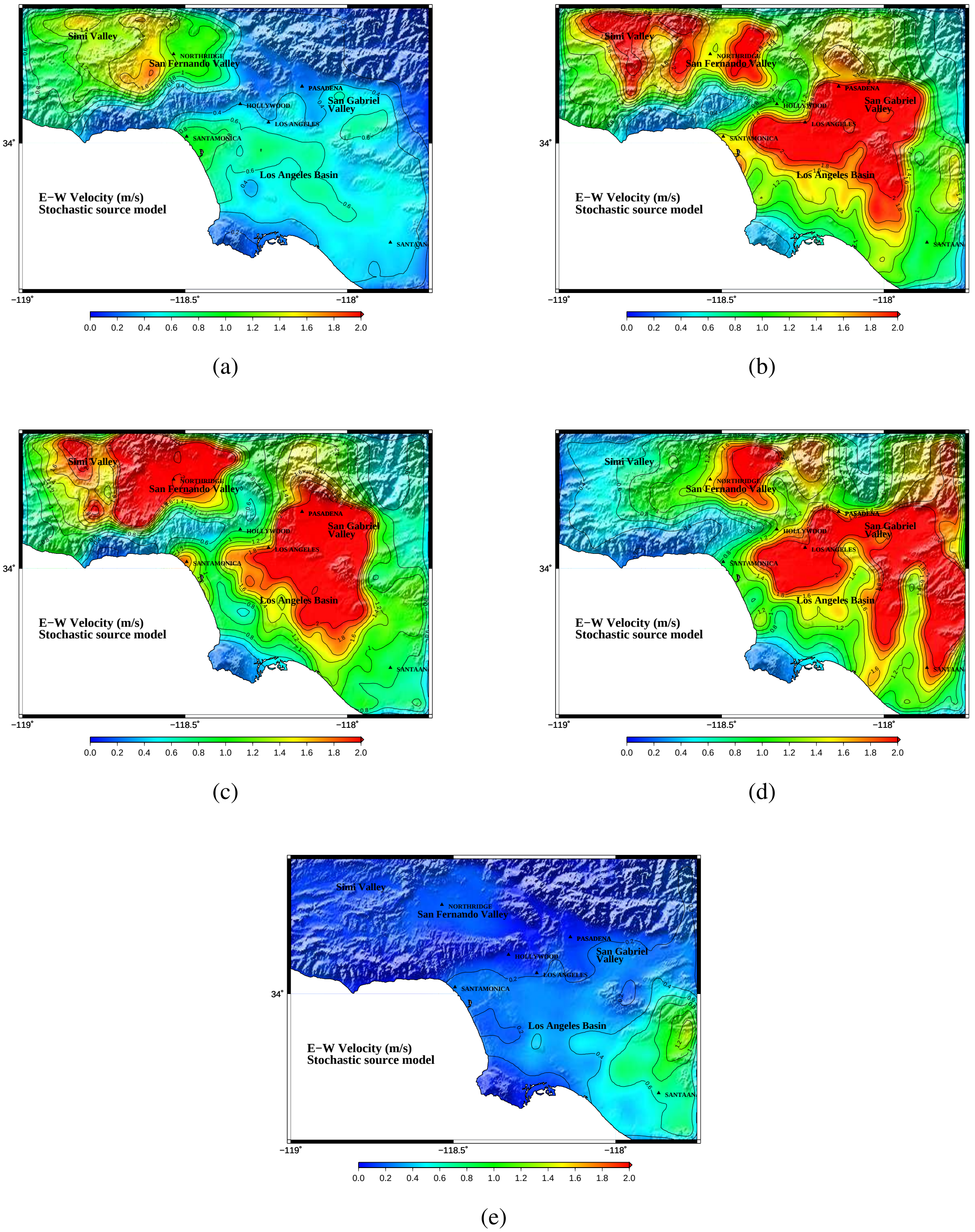
Simi Valley
NORTHRIDGE
San Fernando Valley
PASADENA
San Gabriel Valley
HOLLYWOOD
LOS ANGELES
SANTAMONICA
Los Angeles Basin
SANTAAN
E−W Velocity (m/s)
Stochastic source model
34°
−119°
−118.5°
−118°
0.0
0.2
0.4
0.6
0.8
1.0
1.2
1.4
1.6
1.8
2.0

(a) (b) (c) (d) (e)

Figure C.10: EW component of PGV (m/s) from a north-to-south propagating rupture at (a) - (e) locations 1 - 5 respectively on the southern San Andreas fault for stochastic $M_w 7.9$ model-5 source model. The NS component of PGV has similar characteristics as EW component and the PGD is proportional to PGV in most cases.

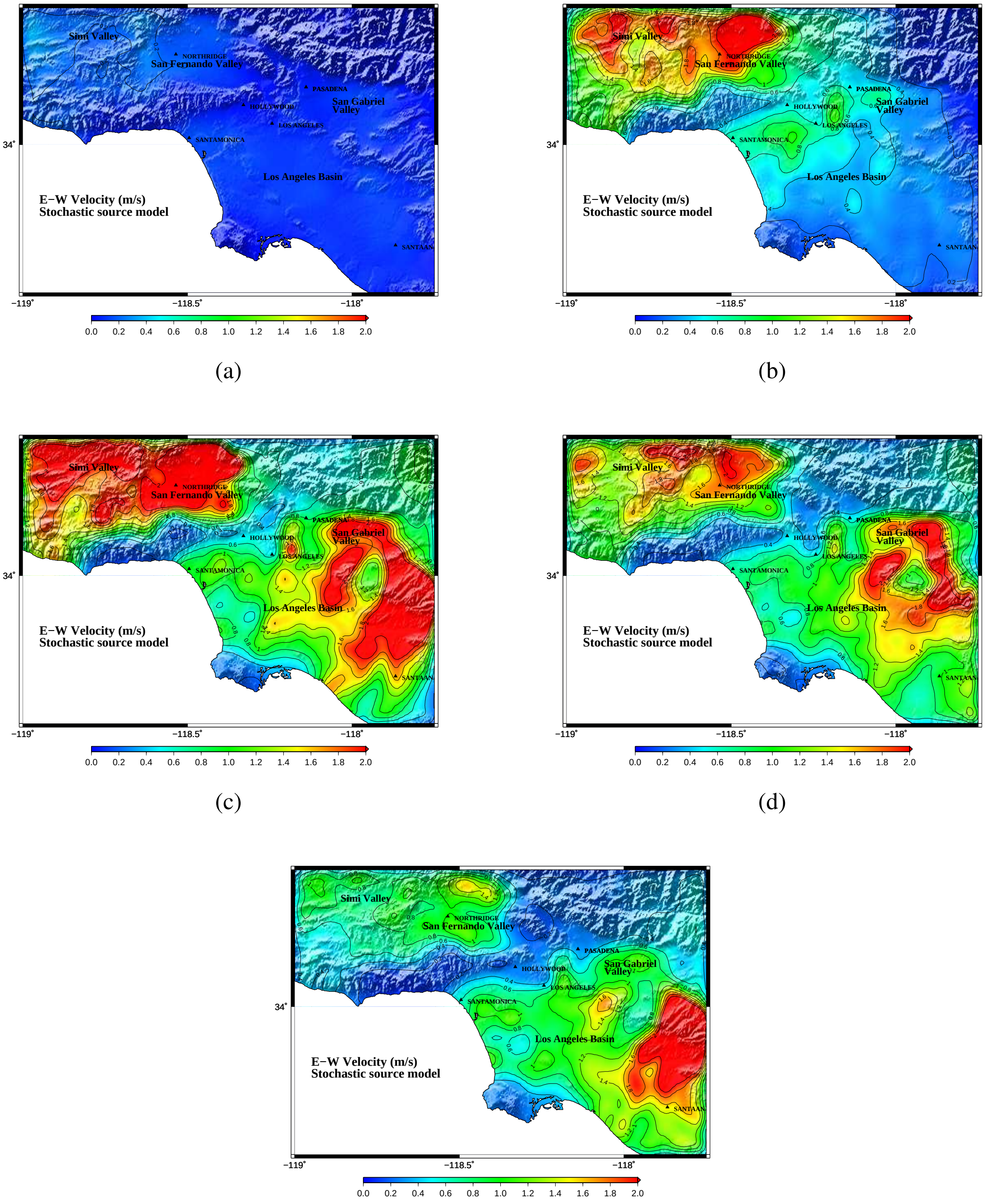
Simi Valley
NORTHRIDGE
San Fernando Valley
PASADENA
San Gabriel Valley
HOLLYWOOD
LOS ANGELES
SANTAMONICA
Los Angeles Basin
SANTAANA
34°
E−W Velocity (m/s)
Stochastic source model
−119°
−118.5°
−118°
0.0
0.2
0.4
0.6
0.8
1.0
1.2
1.4
1.6
1.8
2.0

(a)

(b)

(c)

(d)

(e)

Figure C.11: EW component of PGV (m/s) from a south-to-north propagating rupture at (a) - (e) locations 1 - 5 respectively on the southern San Andreas fault for stochastic $M_w 7.9$ model-5 source model. The NS component of PGV has similar characteristics as EW component and the PGD is proportional to PGV in most cases.

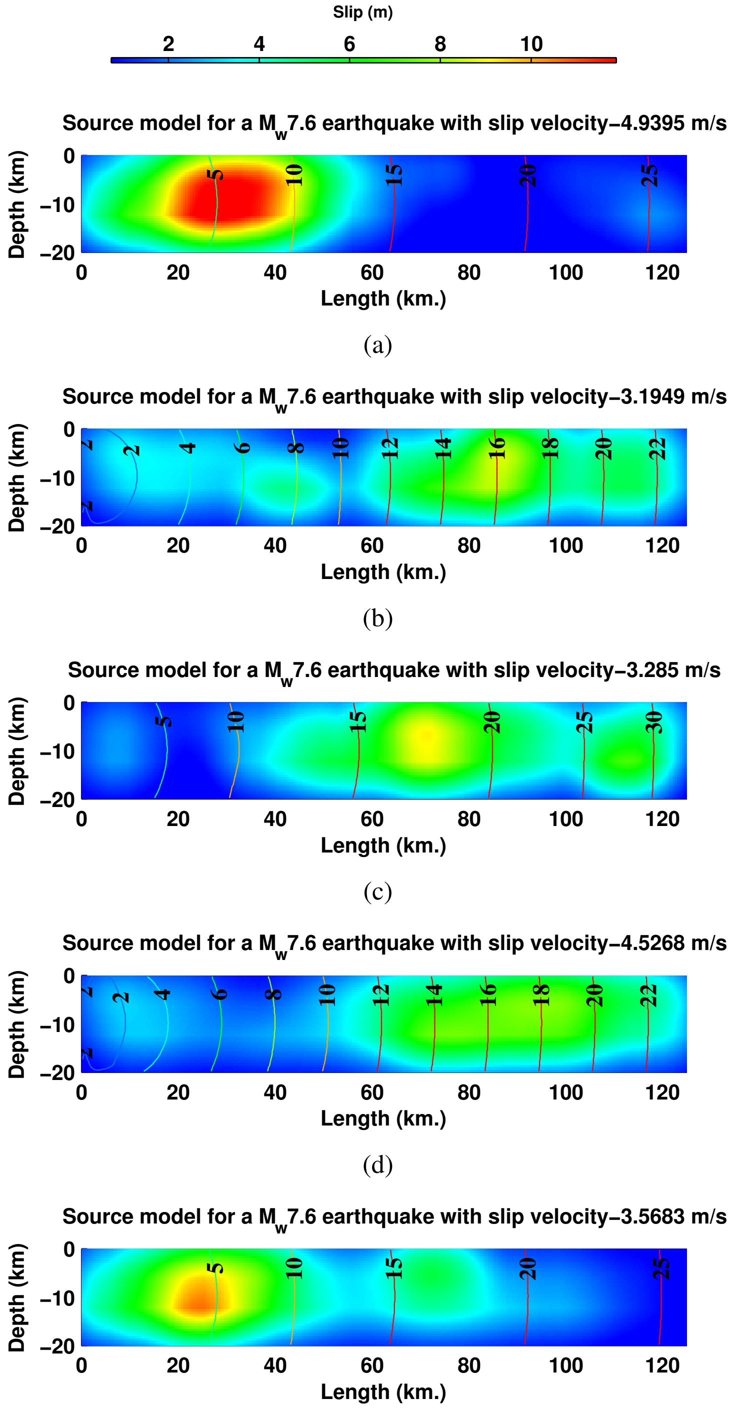

(a)

(b)

(c)

(d)

(e)

Figure C.12: (a)-(e) Stochastic median source models (here on referred to as models-1, 2, 3, 4, 5) with slip in m for a $M_w = 7.6$ earthquake on the San Andreas fault. Rupture time (s) contours are overlaid on the slip distribution. The rupture contours shown correspond to the stochastic stress conditions at location 1 of the rupture staring at Parkfield. Note that the rupture time contours change for a different location.

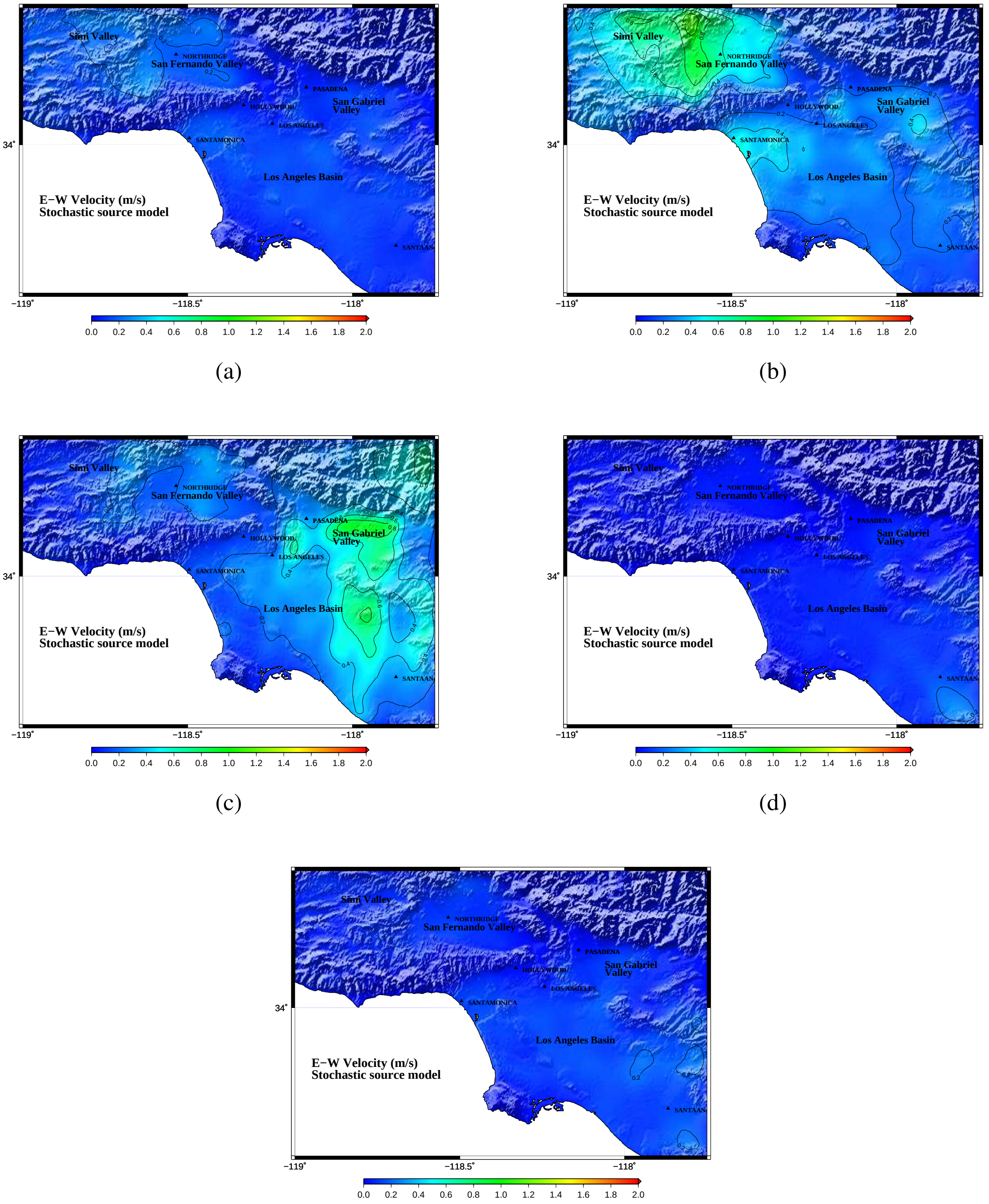

Simi Valley
NORTHRIDGE
San Fernando Valley
PASADENA
San Gabriel Valley
HOLLYWOOD
LOS ANGELES
SANTAMONICA
Los Angeles Basin
SANTAAN
E−W Velocity (m/s)
Stochastic source model
34°
−119°
−118.5°
−118°
0.0
0.2
0.4
0.6
0.8
1.0
1.2
1.4
1.6
1.8
2.0

(a) (b)

(c) (d)

(e)

Figure C.13: EW component of PGV (m/s) from a north-to-south propagating rupture at (a) - (e) locations 1 - 5 respectively on the southern San Andreas fault for stochastic $M_w 7.6$ model-1 source model. The NS component of PGV has similar characteristics as EW component and the PGD is proportional to PGV in most cases.

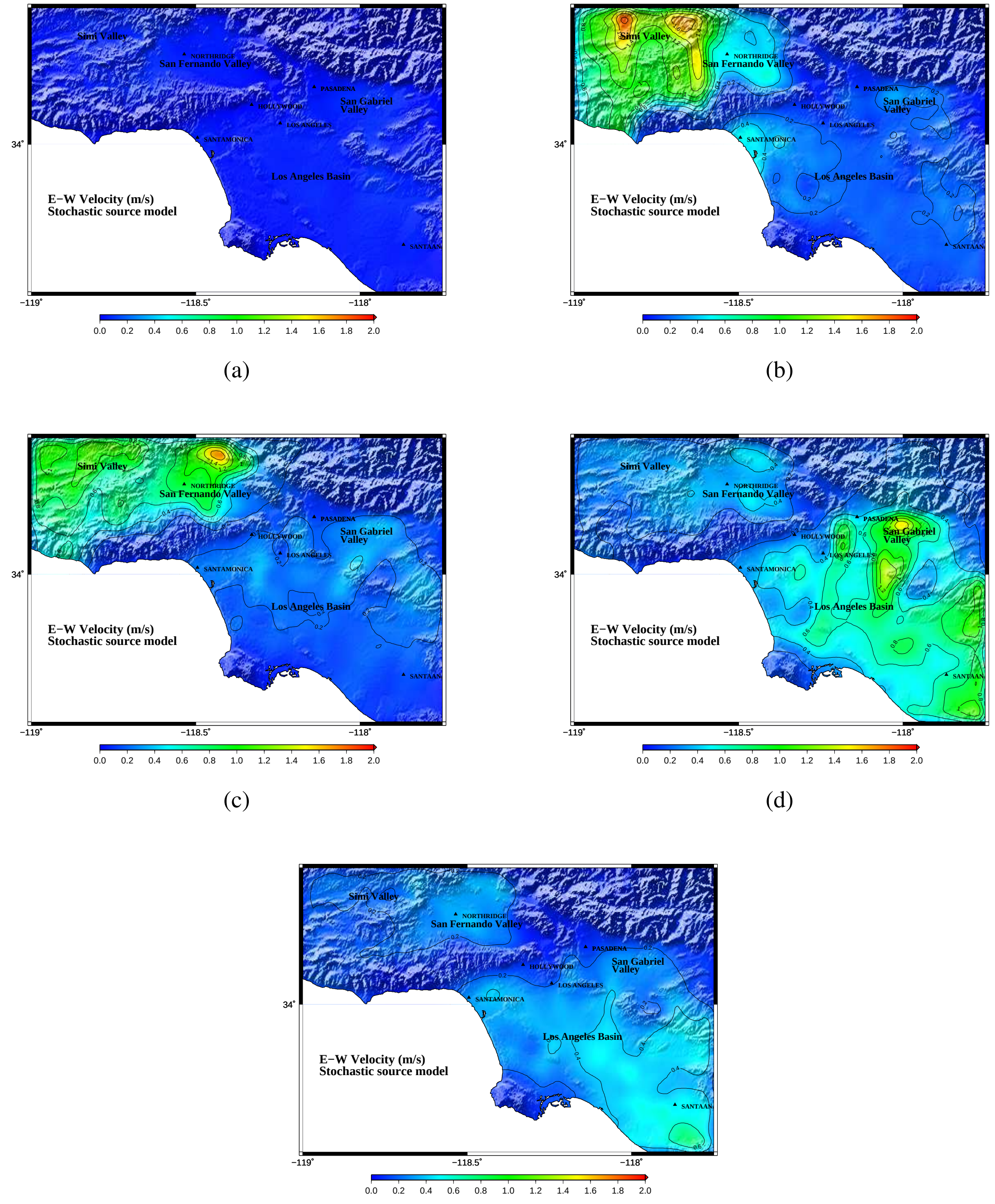
Simi Valley
NORTHRIDGE
San Fernando Valley
PASADENA
San Gabriel Valley
HOLLYWOOD
LOS ANGELES
SANTAMONICA
Los Angeles Basin
SANTAAN
E−W Velocity (m/s)
Stochastic source model
34°
−119°
−118.5°
−118°
0.0
0.2
0.4
0.6
0.8
1.0
1.2
1.4
1.6
1.8
2.0

(a) (b) (c) (d) (e)

Figure C.14: EW component of PGV (m/s) from a south-to-north propagating rupture at (a) - (e) locations 1 - 5 respectively on the southern San Andreas fault for stochastic $M_w 7.6$ model-1 source model. The NS component of PGV has similar characteristics as EW component and the PGD is proportional to PGV in most cases.

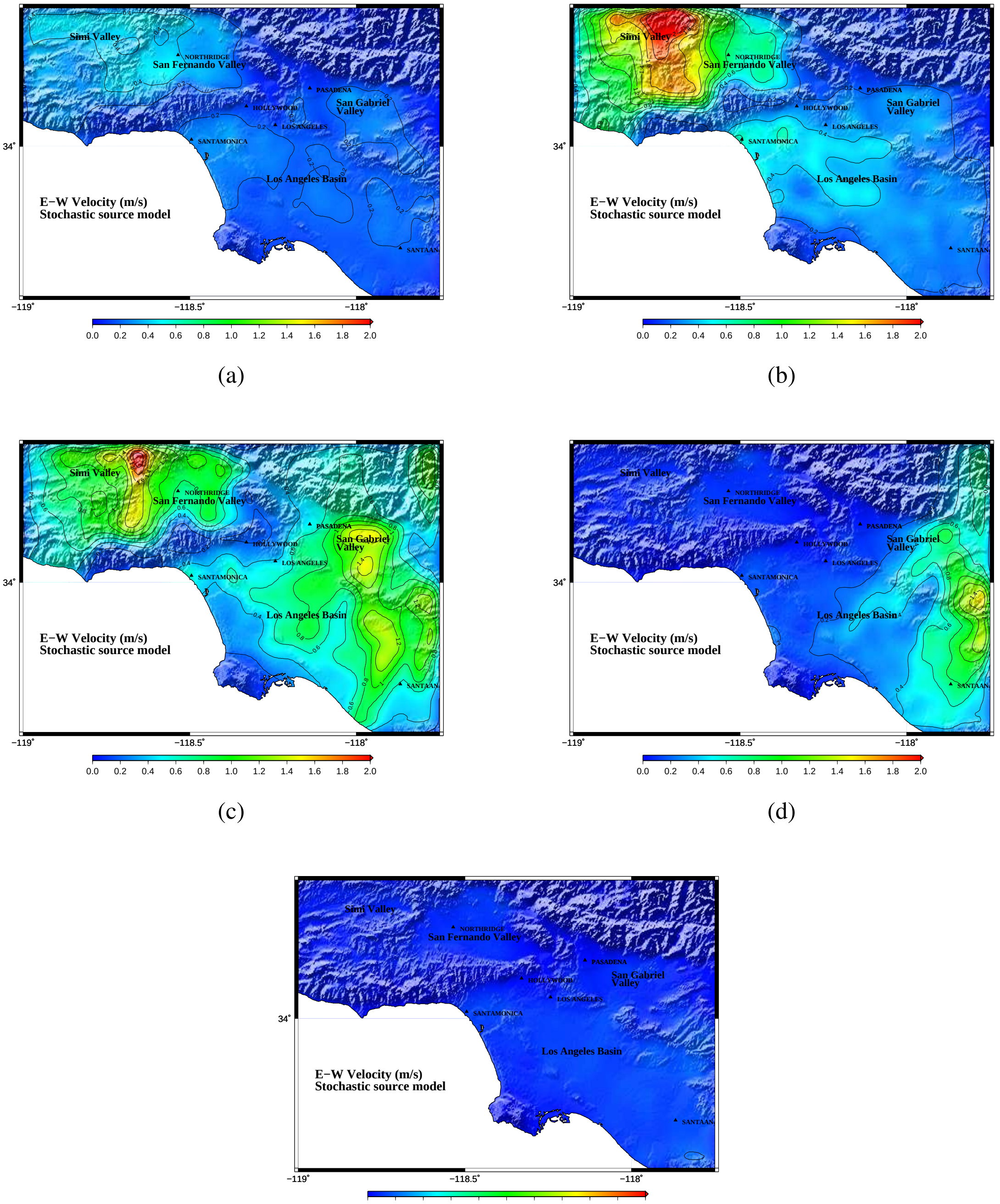
Simi Valley
NORTHRIDGE
San Fernando Valley
PASADENA
San Gabriel Valley
HOLLYWOOD
LOS ANGELES
SANTAMONICA
Los Angeles Basin
SANTAAN
34°
E−W Velocity (m/s)
Stochastic source model
−119°
−118.5°
−118°
0.0
0.2
0.4
0.6
0.8
1.0
1.2
1.4
1.6
1.8
2.0

(a)

(b)

(c)

(d)

(e)

Figure C.15: EW component of PGV (m/s) from a north-to-south propagating rupture at (a) - (e) locations 1 - 5 respectively on the southern San Andreas fault for stochastic $M_w 7.6$ model-2 source model. The NS component of PGV has similar characteristics as EW component and the PGD is proportional to PGV in most cases.

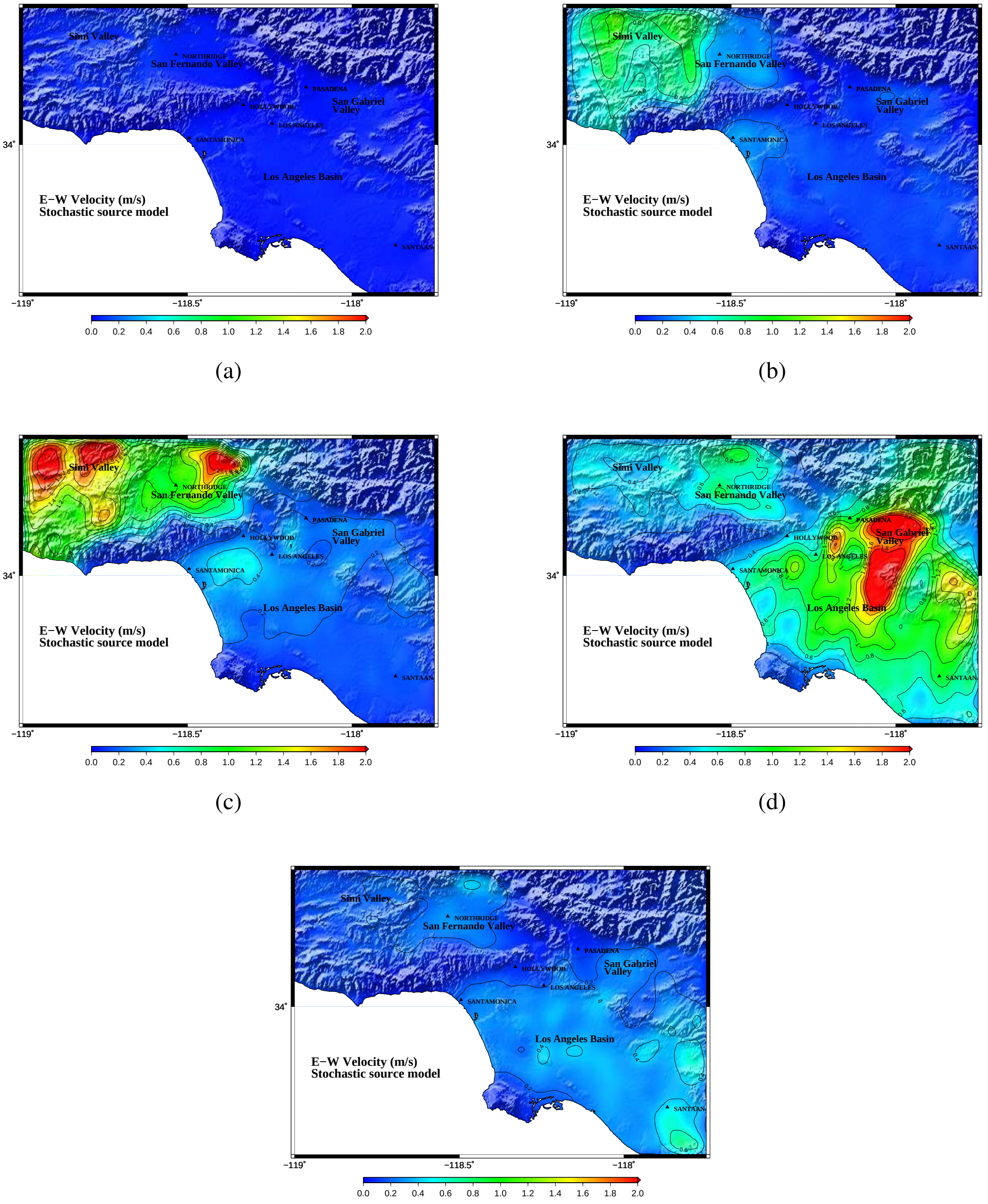
Simi Valley
NORTHRIDGE
San Fernando Valley
PASADENA
San Gabriel Valley
HOLLYWOOD
LOS ANGELES
SANTAMONICA
Los Angeles Basin
SANTAAN
34°
−119°
−118.5°
−118°
E−W Velocity (m/s)
Stochastic source model
0.0
0.2
0.4
0.6
0.8
1.0
1.2
1.4
1.6
1.8
2.0

(a) (b) (c) (d) (e)

Figure C.16: EW component of PGV (m/s) from a south-to-north propagating rupture at (a) - (e) locations 1 - 5 respectively on the southern San Andreas fault for stochastic $M_w 7.6$ model-2 source model. The NS component of PGV has similar characteristics as EW component and the PGD is proportional to PGV in most cases.

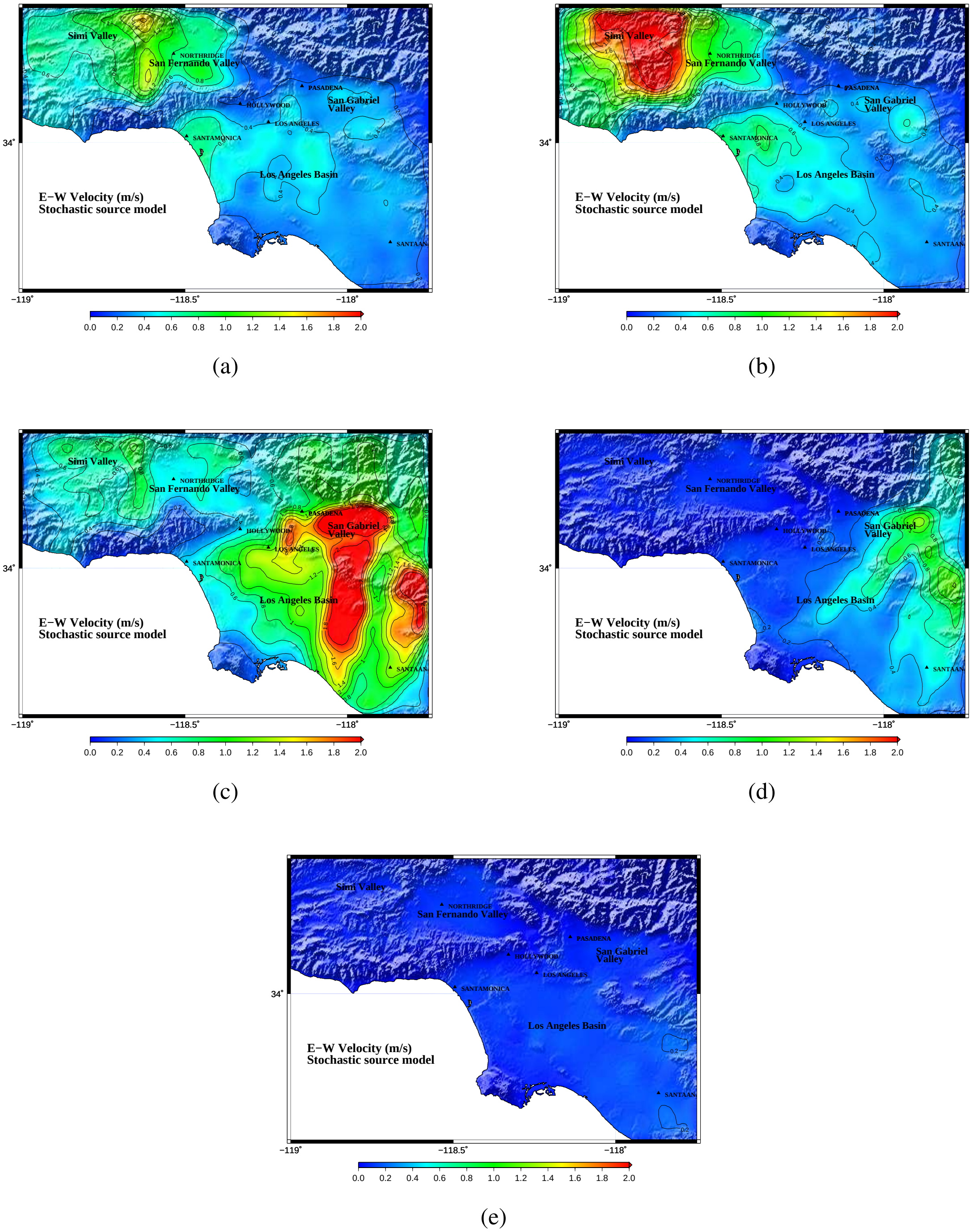
Simi Valley
NORTHRIDGE
San Fernando Valley
PASADENA
HOLLYWOOD
San Gabriel Valley
LOS ANGELES
SANTAMONICA
Los Angeles Basin
SANTAAN
E−W Velocity (m/s)
Stochastic source model
34°
−119°
−118.5°
−118°
0.0
0.2
0.4
0.6
0.8
1.0
1.2
1.4
1.6
1.8
2.0

(a)

(b)

(c)

(d)

(e)

Figure C.17: EW component of PGV (m/s) from a north-to-south propagating rupture at (a) - (e) locations 1 - 5 respectively on the southern San Andreas fault for stochastic $M_w 7.6$ model-3 source model. The NS component of PGV has similar characteristics as EW component and the PGD is proportional to PGV in most cases.

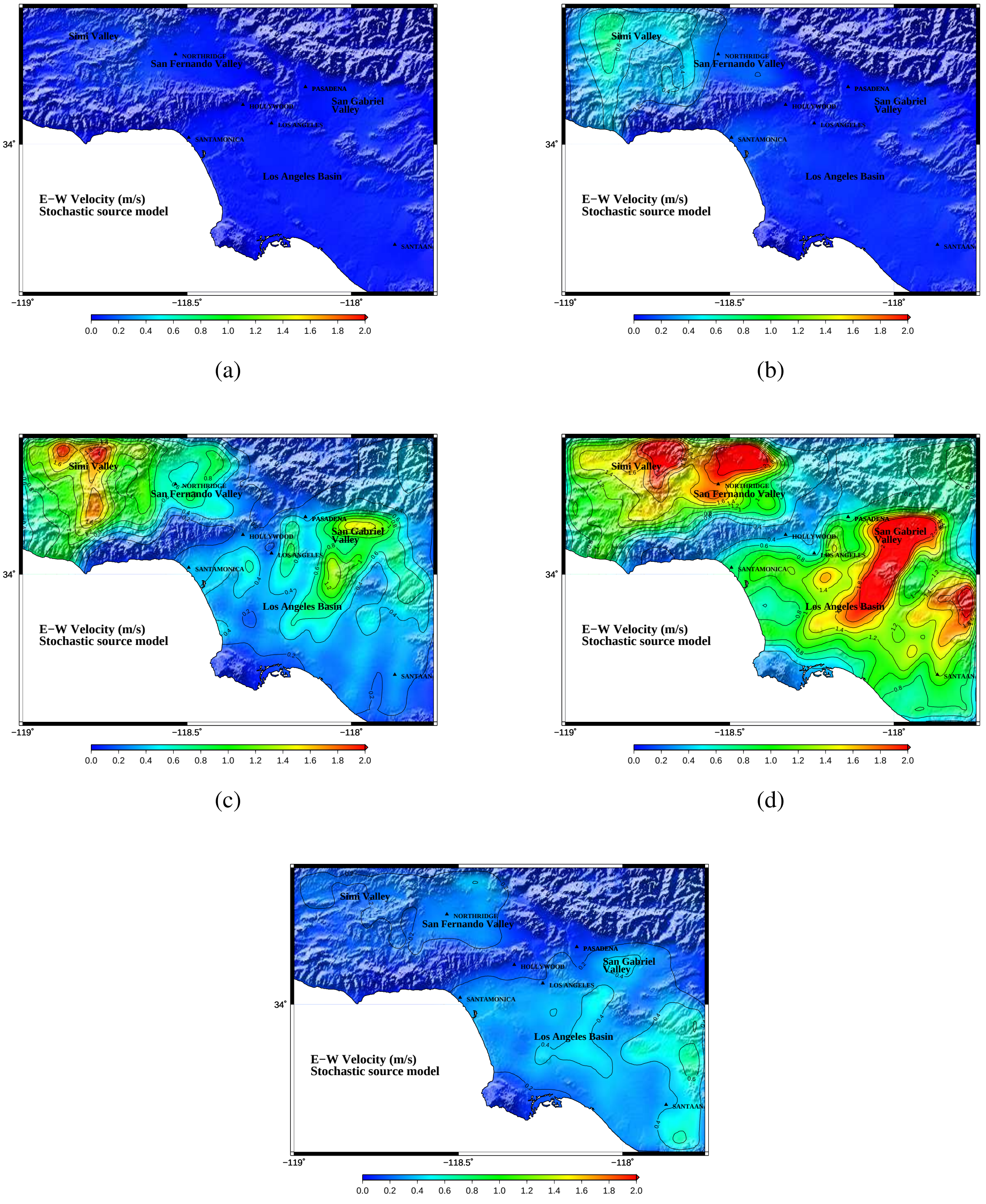
Simi Valley
NORTHRIDGE
San Fernando Valley
PASADENA
San Gabriel Valley
HOLLYWOOD
LOS ANGELES
SANTAMONICA
Los Angeles Basin
SANTAAN
34°
E−W Velocity (m/s)
Stochastic source model
−119°
−118.5°
−118°
0.0
0.2
0.4
0.6
0.8
1.0
1.2
1.4
1.6
1.8
2.0

(a)

(b)

(c)

(d)

(e)

Figure C.18: EW component of PGV (m/s) from a south-to-north propagating rupture at (a) - (e) locations 1 - 5 respectively on the southern San Andreas fault for stochastic $M_w 7.6$ model-3 source model. The NS component of PGV has similar characteristics as EW component and the PGD is proportional to PGV in most cases.

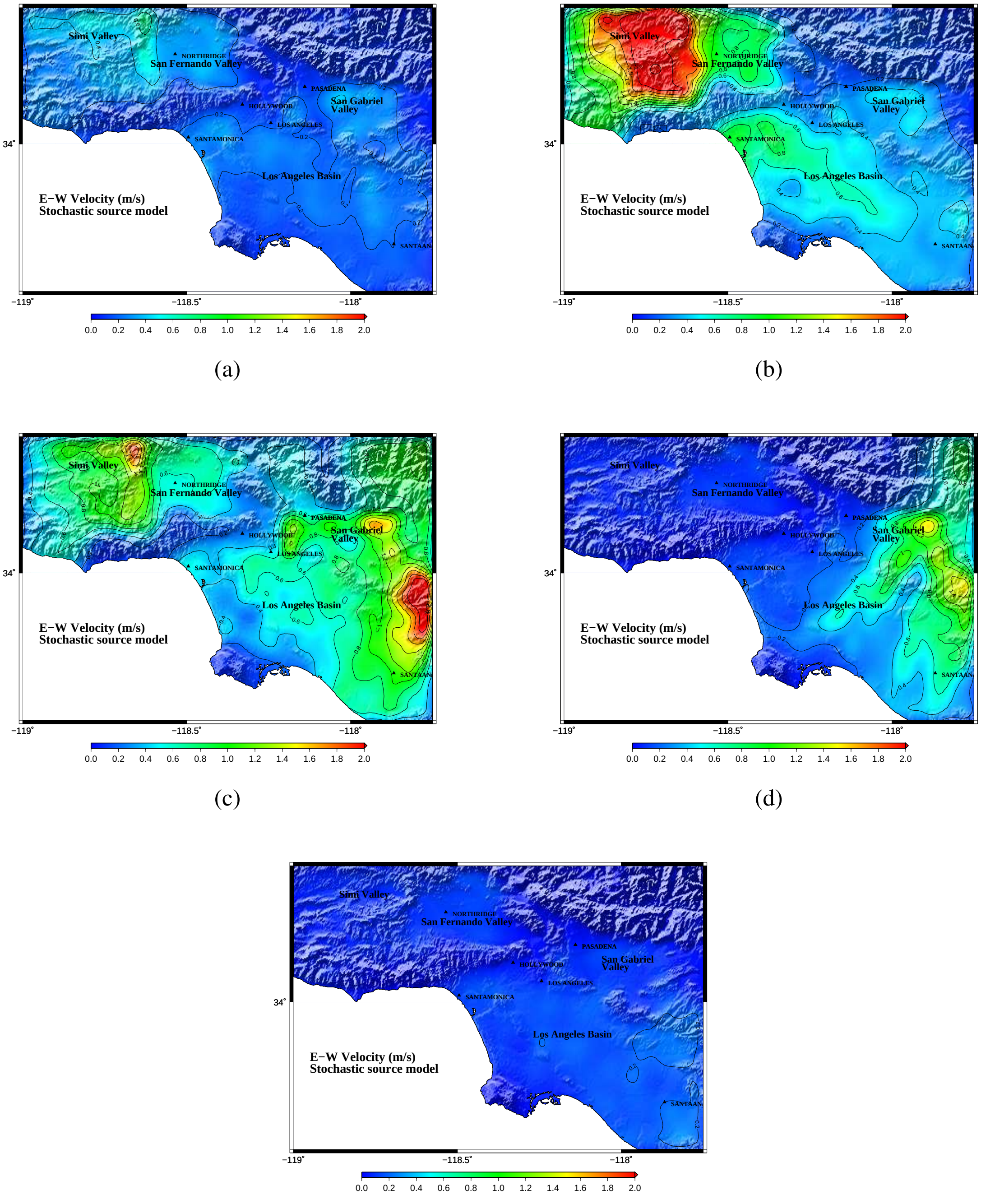
Simi Valley
NORTHRIDGE
San Fernando Valley
PASADENA
HOLLYWOOD
San Gabriel Valley
LOS ANGELES
SANTAMONICA
Los Angeles Basin
SANTAAN
34°
E−W Velocity (m/s)
Stochastic source model
−119°
−118.5°
−118°
0.0
0.2
0.4
0.6
0.8
1.0
1.2
1.4
1.6
1.8
2.0

(a)

(b)

(c)

(d)

(e)

Figure C.19: EW component of PGV (m/s) from a north-to-south propagating rupture at (a) - (e) locations 1 - 5 respectively on the southern San Andreas fault for stochastic $M_w 7.6$ model-4 source model. The NS component of PGV has similar characteristics as EW component and the PGD is proportional to PGV in most cases.

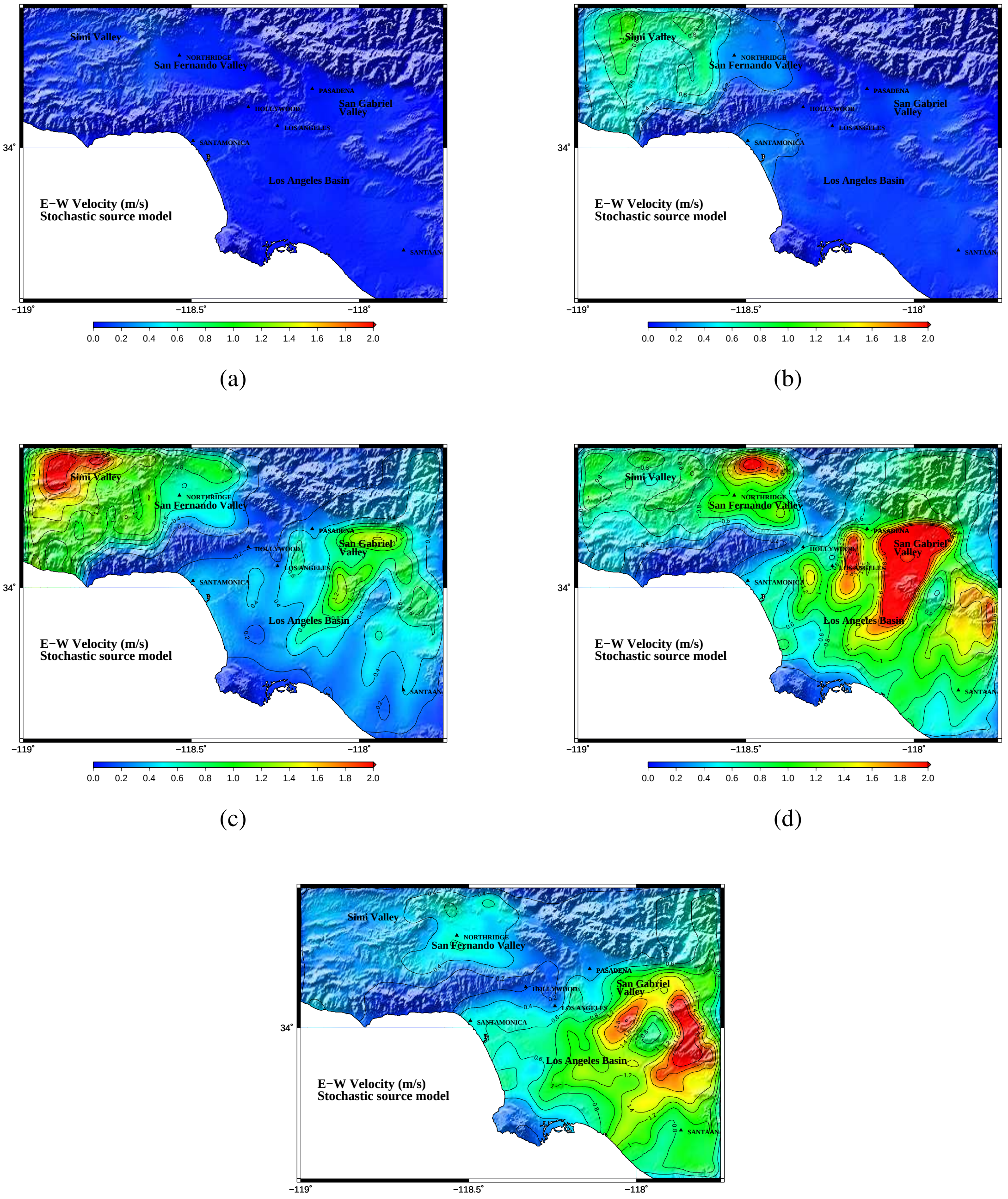
Simi Valley
NORTHRIDGE
San Fernando Valley
PASADENA
San Gabriel Valley
HOLLYWOOD
LOS ANGELES
SANTAMONICA
Los Angeles Basin
SANTAAN
E−W Velocity (m/s)
Stochastic source model
34°
−119°
−118.5°
−118°
0.0
0.2
0.4
0.6
0.8
1.0
1.2
1.4
1.6
1.8
2.0

(a)

(b)

(c)

(d)

(e)

Figure C.20: EW component of PGV (m/s) from a south-to-north propagating rupture at (a) - (e) locations 1 - 5 respectively on the southern San Andreas fault for stochastic $M_w 7.6$ model-4 source model. The NS component of PGV has similar characteristics as EW component and the PGD is proportional to PGV in most cases.

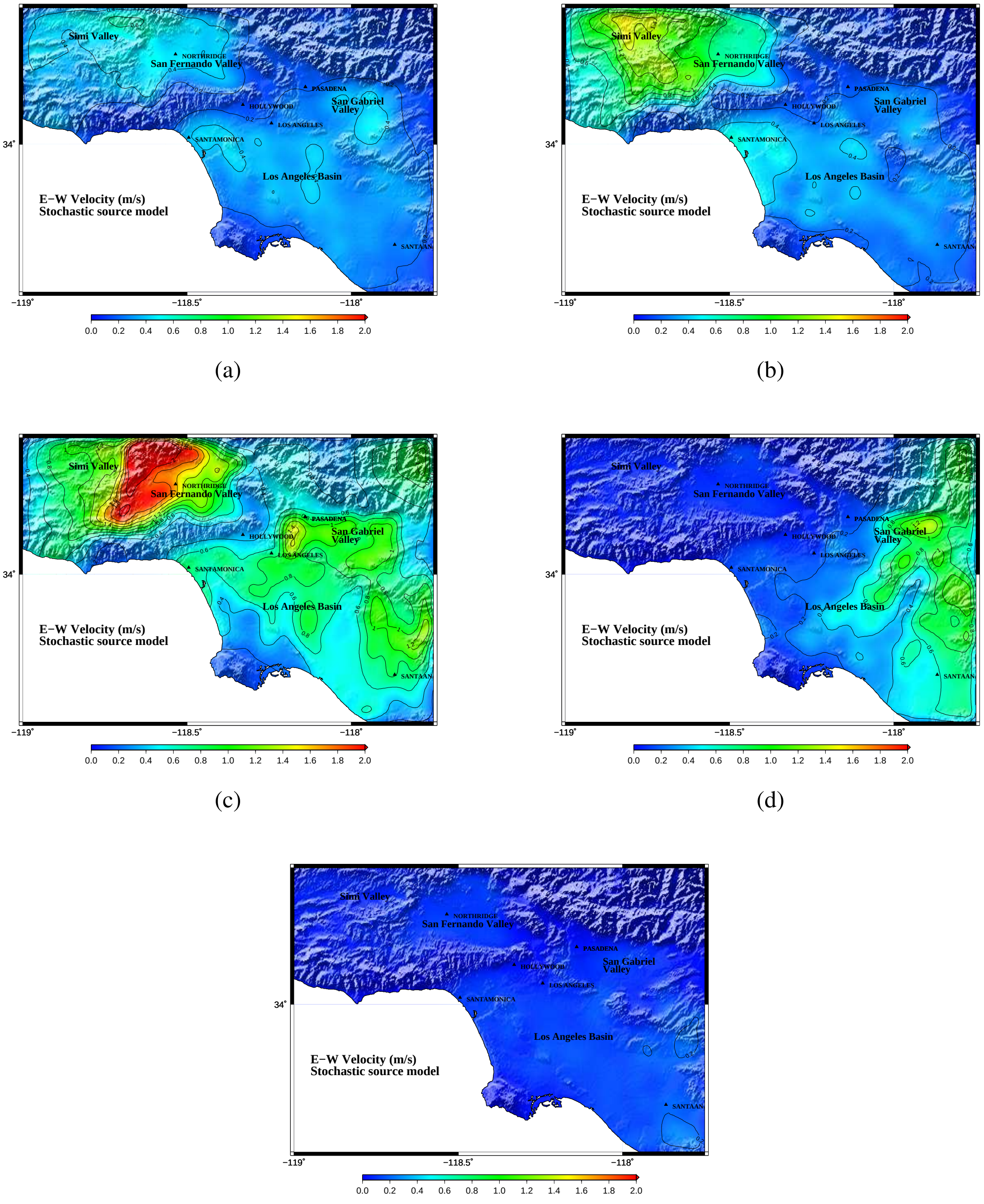
Simi Valley
NORTHRIDGE
San Fernando Valley
PASADENA
San Gabriel Valley
HOLLYWOOD
LOS ANGELES
SANTAMONICA
Los Angeles Basin
SANTAAN
E−W Velocity (m/s)
Stochastic source model
34°
−119°
−118.5°
−118°
0.0
0.2
0.4
0.6
0.8
1.0
1.2
1.4
1.6
1.8
2.0

(a)

(b)

(c)

(d)

(e)

Figure C.21: EW component of PGV (m/s) from a north-to-south propagating rupture at (a) - (e) locations 1 - 5 respectively on the southern San Andreas fault for stochastic $M_w 7.6$ model-5 source model. The NS component of PGV has similar characteristics as EW component and the PGD is proportional to PGV in most cases.

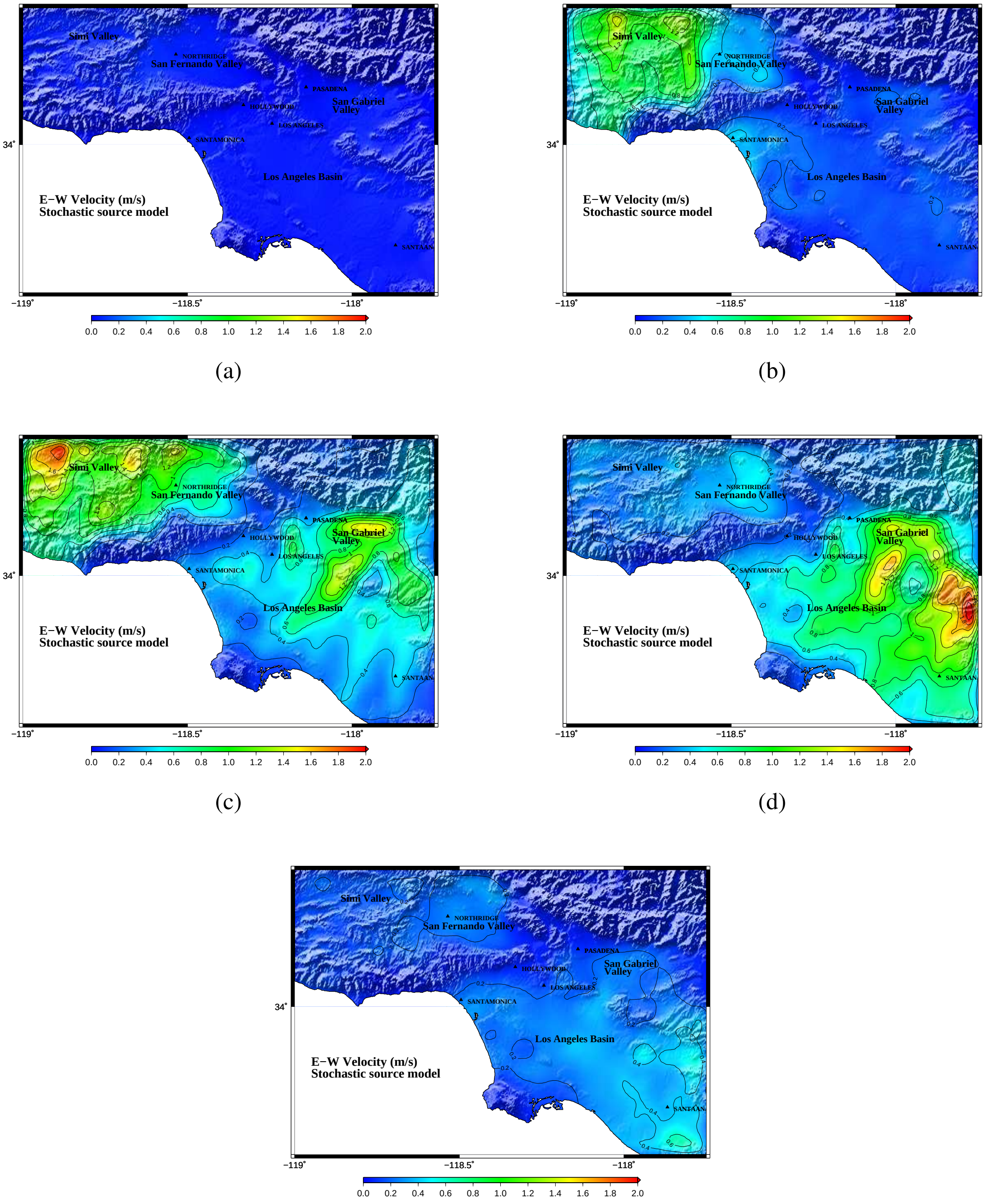
Simi Valley
NORTHRIDGE
San Fernando Valley
PASADENA
San Gabriel Valley
HOLLYWOOD
LOS ANGELES
SANTAMONICA
Los Angeles Basin
SANTAAN
E−W Velocity (m/s)
Stochastic source model
34°
−119°
−118.5°
−118°
0.0
0.2
0.4
0.6
0.8
1.0
1.2
1.4
1.6
1.8
2.0

(a)

(b)

(c)

(d)

(e)

Figure C.22: EW component of PGV (m/s) from a south-to-north propagating rupture at (a) - (e) locations 1 - 5 respectively on the southern San Andreas fault for stochastic $M_w 7.6$ model-5 source model. The NS component of PGV has similar characteristics as EW component and the PGD is proportional to PGV in most cases.

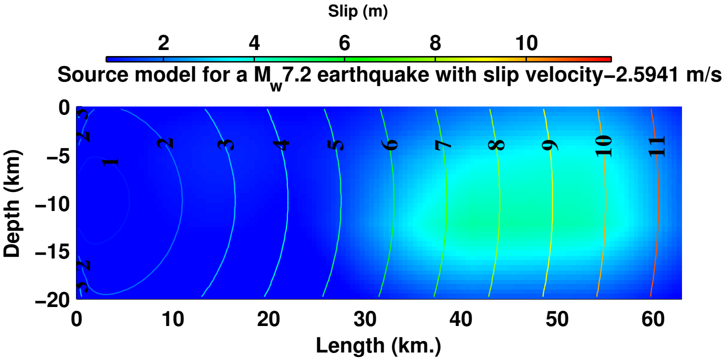
Source model for a M_w7.2 earthquake with slip velocity−2.5941 m/s

(a)

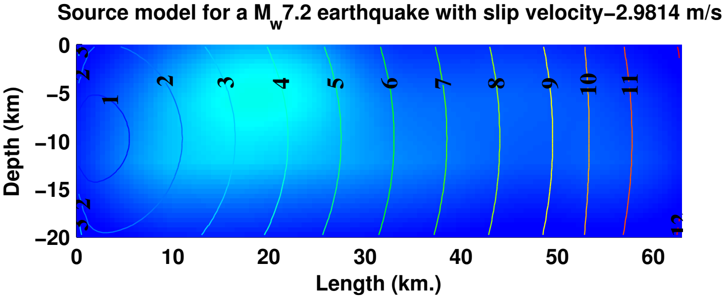
Source model for a M_w7.2 earthquake with slip velocity−2.9814 m/s

(b)

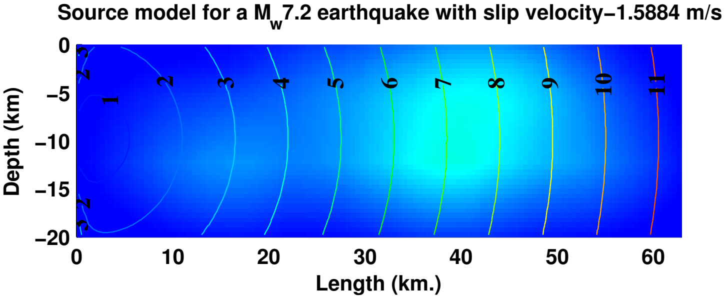
Source model for a M_w7.2 earthquake with slip velocity−1.5884 m/s

(c)

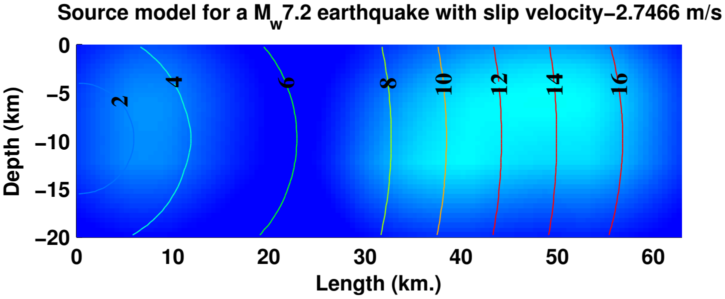
Source model for a M_w7.2 earthquake with slip velocity−2.7466 m/s

(d)

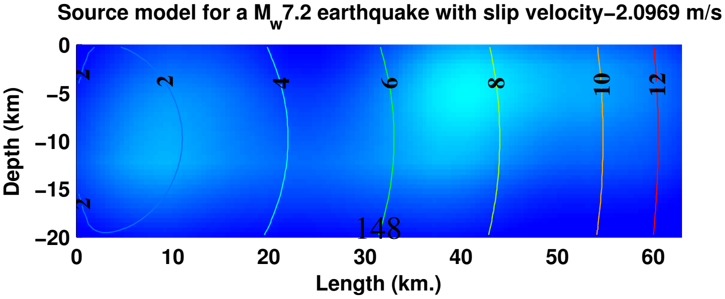
Source model for a M_w7.2 earthquake with slip velocity−2.0969 m/s

(e)

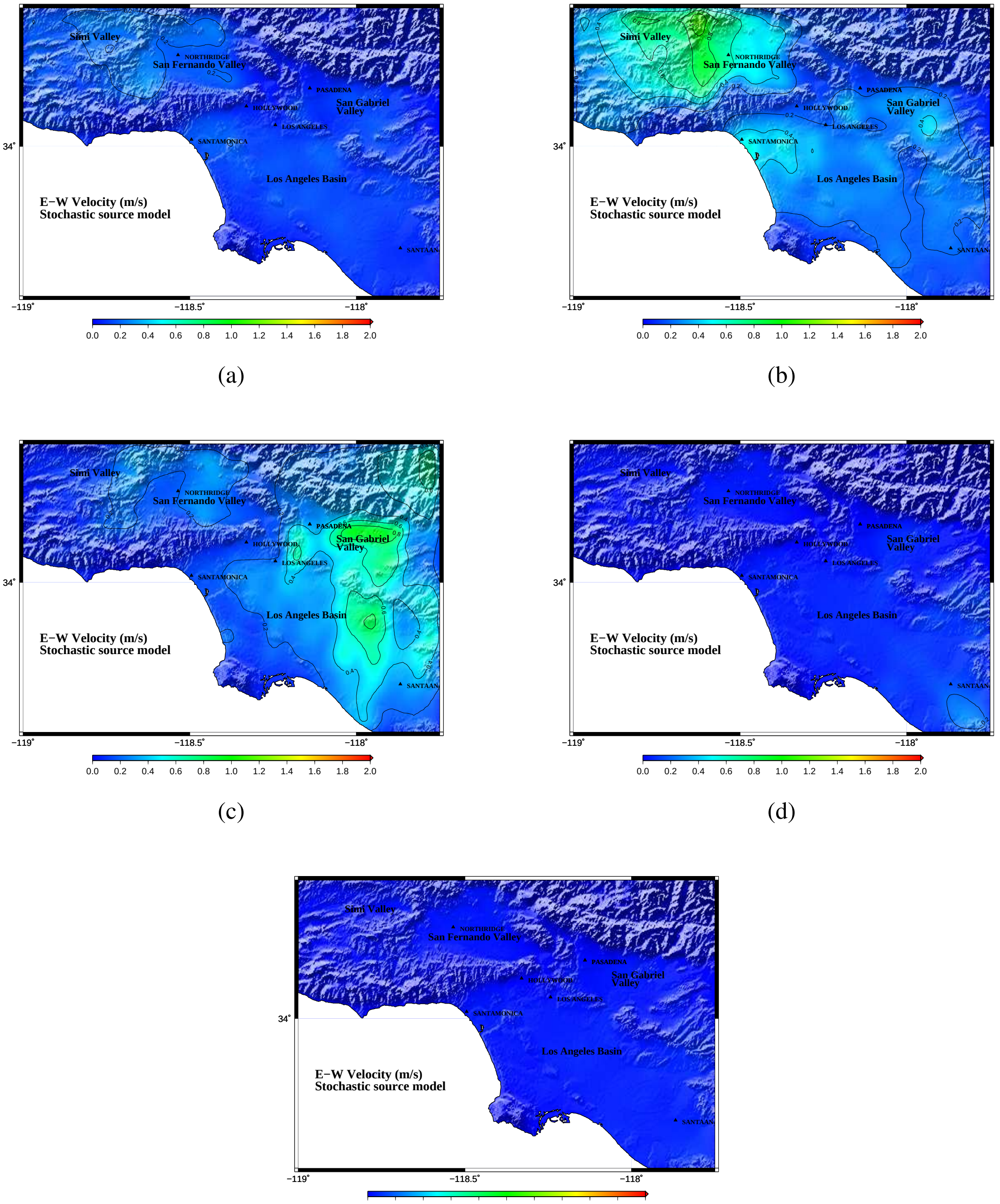
Simi Valley
NORTHRIDGE
San Fernando Valley
PASADENA
San Gabriel Valley
HOLLYWOOD
LOS ANGELES
SANTAMONICA
Los Angeles Basin
SANTAANA
E−W Velocity (m/s)
Stochastic source model
34°
−119°
−118.5°
−118°
0.0
0.2
0.4
0.6
0.8
1.0
1.2
1.4
1.6
1.8
2.0

(a) (b) (c) (d) (e)

Figure C.24: EW component of PGV (m/s) from a north-to-south propagating rupture at (a) - (e) locations 1 - 5 respectively on the southern San Andreas fault for stochastic $M_w 7.2$ model-1 source model. The NS component of PGV has similar characteristics as EW component and the PGD is proportional to PGV in most cases.

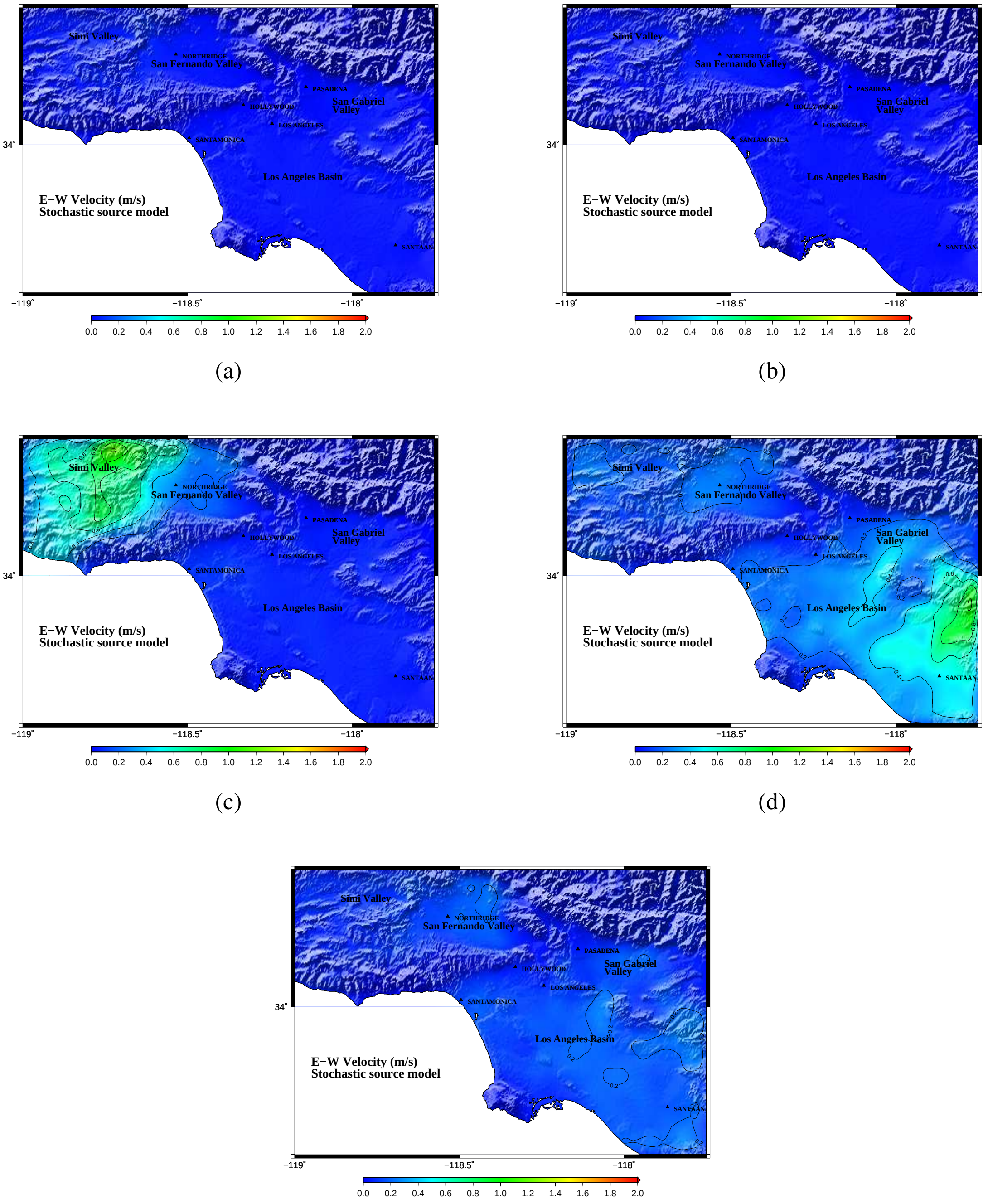
Simi Valley
NORTHRIDGE
San Fernando Valley
PASADENA
San Gabriel Valley
HOLLYWOOD
LOS ANGELES
SANTAMONICA
Los Angeles Basin
SANTAAN
E−W Velocity (m/s)
Stochastic source model
34°
−119°
−118.5°
−118°
0.0
0.2
0.4
0.6
0.8
1.0
1.2
1.4
1.6
1.8
2.0

(a) (b)

(c) (d)

(e)

Figure C.25: EW component of PGV (m/s) from a south-to-north propagating rupture at (a) - (e) locations 1 - 5 respectively on the southern San Andreas fault for stochastic $M_w 7.2$ model-1 source model. The NS component of PGV has similar characteristics as EW component and the PGD is proportional to PGV in most cases.

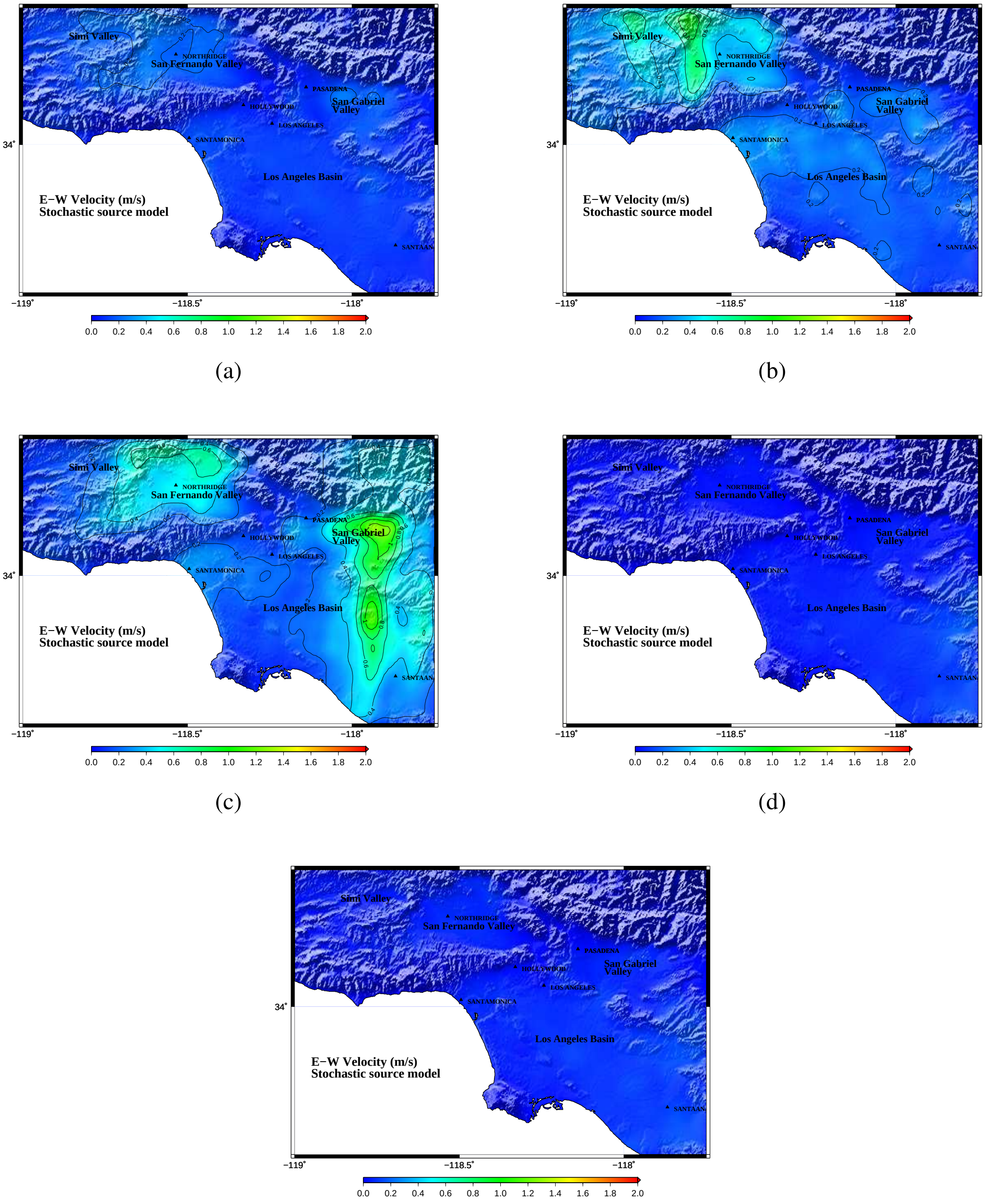
Simi Valley
NORTHRIDGE
San Fernando Valley
PASADENA
San Gabriel Valley
HOLLYWOOD
LOS ANGELES
SANTAMONICA
Los Angeles Basin
SANTAANA
E−W Velocity (m/s)
Stochastic source model
34˚
−119˚
−118.5˚
−118˚
0.0
0.2
0.4
0.6
0.8
1.0
1.2
1.4
1.6
1.8
2.0

(a) (b)

(c) (d)

(e)

Figure C.26: EW component of PGV (m/s) from a north-to-south propagating rupture at (a) - (e) locations 1 - 5 respectively on the southern San Andreas fault for stochastic $M_w 7.2$ model-2 source model. The NS component of PGV has similar characteristics as EW component and the PGD is proportional to PGV in most cases.

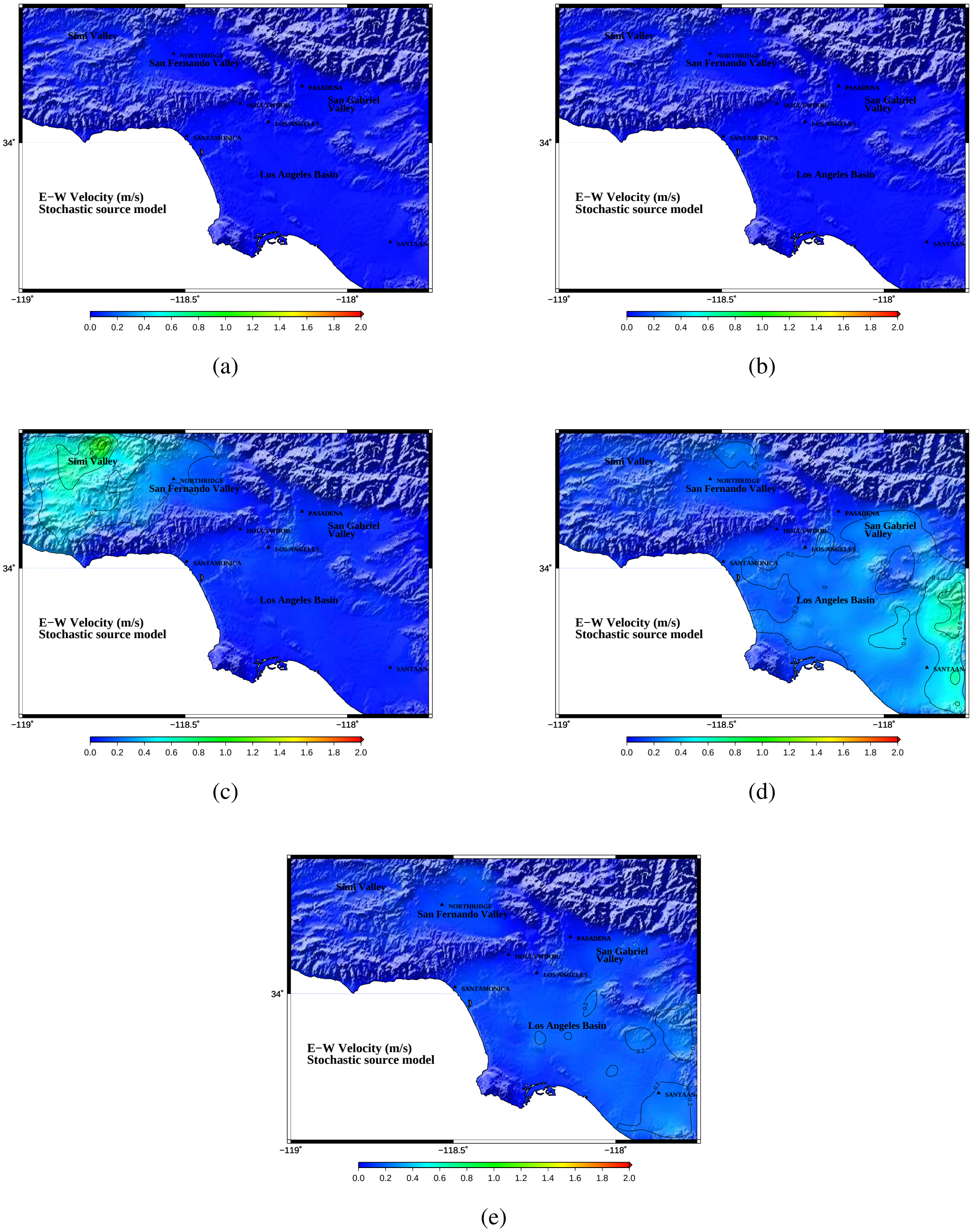
Simi Valley
NORTHRIDGE
San Fernando Valley
PASADENA
San Gabriel Valley
HOLLYWOOD
LOS ANGELES
SANTAMONICA
Los Angeles Basin
SANTAAN
E−W Velocity (m/s)
Stochastic source model
34°
−119°
−118.5°
−118°
0.0
0.2
0.4
0.6
0.8
1.0
1.2
1.4
1.6
1.8
2.0

(a)

(b)

(c)

(d)

(e)

Figure C.27: EW component of PGV (m/s) from a south-to-north propagating rupture at (a) - (e) locations 1 - 5 respectively on the southern San Andreas fault for stochastic $M_w 7.2$ model-2 source model. The NS component of PGV has similar characteristics as EW component and the PGD is proportional to PGV in most cases.

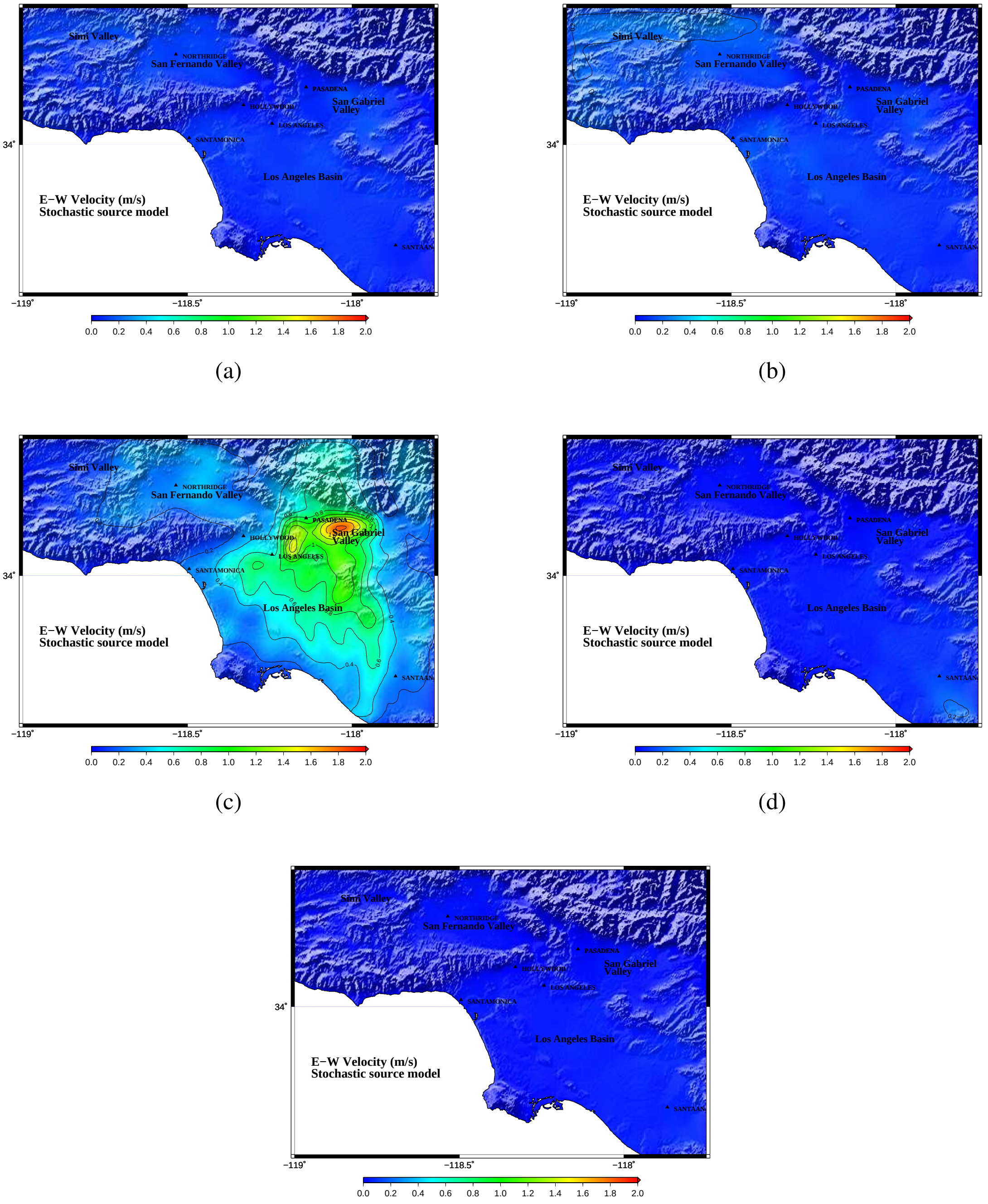
Simi Valley
NORTHRIDGE
San Fernando Valley
PASADENA
San Gabriel Valley
HOLLYWOOD
LOS ANGELES
SANTAMONICA
Los Angeles Basin
SANTAAN
E−W Velocity (m/s)
Stochastic source model
34°
−119°
−118.5°
−118°
0.0
0.2
0.4
0.6
0.8
1.0
1.2
1.4
1.6
1.8
2.0

(a) (b)

(c) (d)

(e)

Figure C.28: EW component of PGV (m/s) from a north-to-south propagating rupture at (a) - (e) locations 1 - 5 respectively on the southern San Andreas fault for stochastic $M_w 7.2$ model-3 source model. The NS component of PGV has similar characteristics as EW component and the PGD is proportional to PGV in most cases.

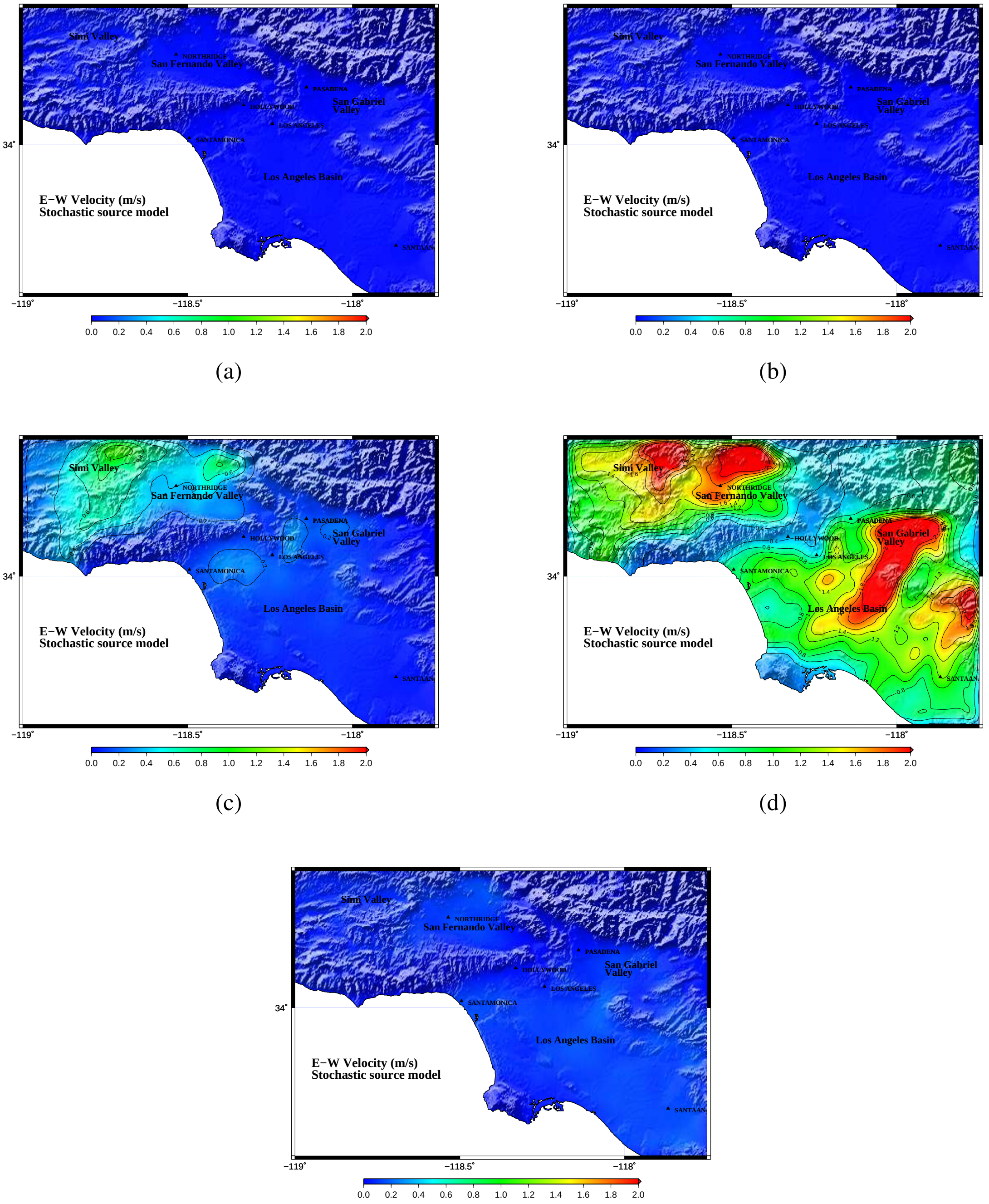

Simi Valley
NORTHRIDGE
San Fernando Valley
PASADENA
San Gabriel Valley
HOLLYWOOD
LOS ANGELES
SANTAMONICA
Los Angeles Basin
SANTAAN
E−W Velocity (m/s)
Stochastic source model
34°
−119°
−118.5°
−118°
0.0
0.2
0.4
0.6
0.8
1.0
1.2
1.4
1.6
1.8
2.0

(a) (b) (c) (d) (e)

Figure C.29: EW component of PGV (m/s) from a south-to-north propagating rupture at (a) - (e) locations 1 - 5 respectively on the southern San Andreas fault for stochastic $M_w 7.2$ model-3 source model. The NS component of PGV has similar characteristics as EW component and the PGD is proportional to PGV in most cases.

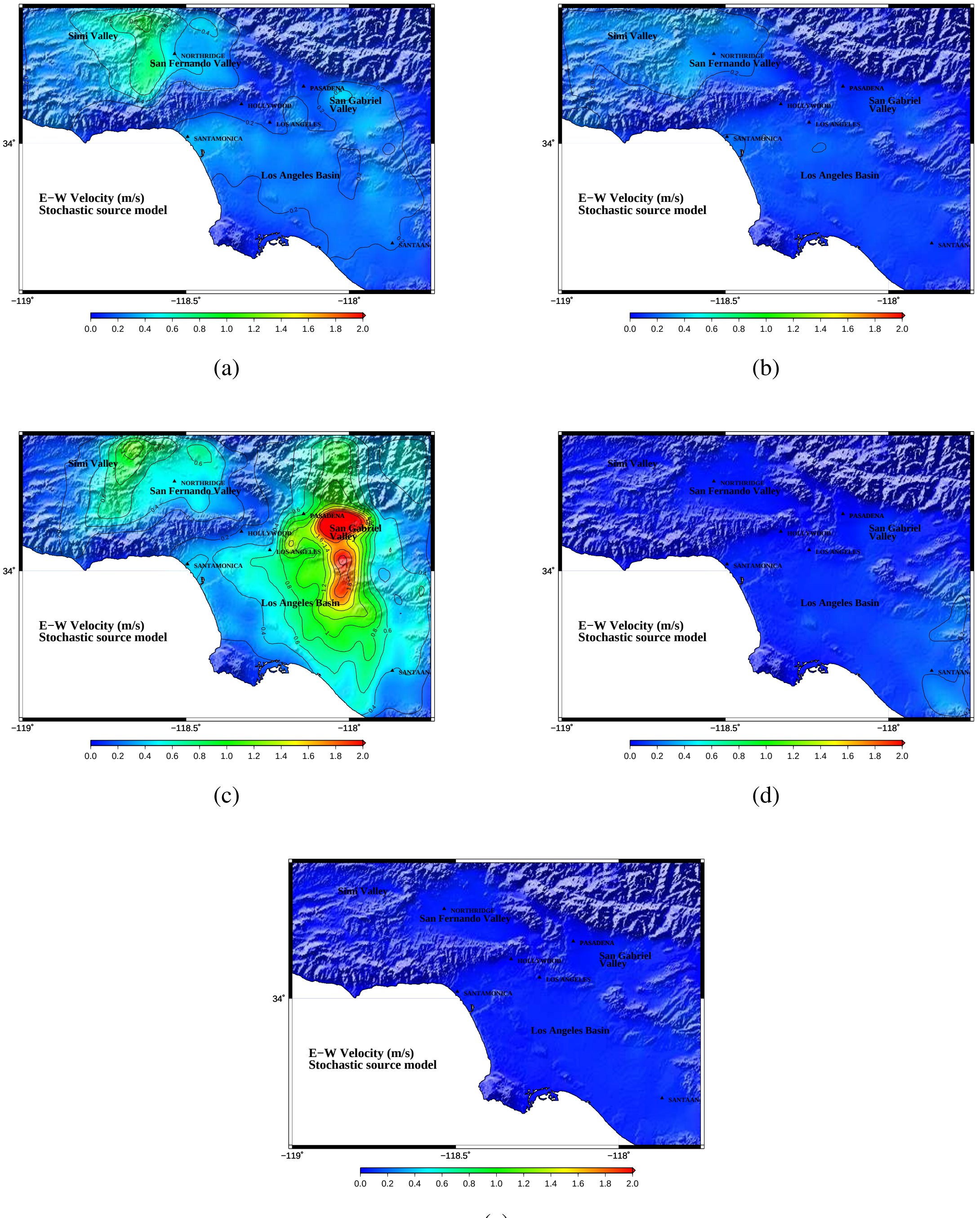
Simi Valley
NORTHRIDGE
San Fernando Valley
PASADENA
San Gabriel Valley
HOLLYWOOD
LOS ANGELES
SANTAMONICA
Los Angeles Basin
SANTAAN
E−W Velocity (m/s)
Stochastic source model
34°
−119°
−118.5°
−118°
0.0
0.2
0.4
0.6
0.8
1.0
1.2
1.4
1.6
1.8
2.0

(a) (b)

(c) (d)

(e)

Figure C.30: EW component of PGV (m/s) from a north-to-south propagating rupture at (a) - (e) locations 1 - 5 respectively on the southern San Andreas fault for stochastic $M_w 7.2$ model-4 source model. The NS component of PGV has similar characteristics as EW component and the PGD is proportional to PGV in most cases.

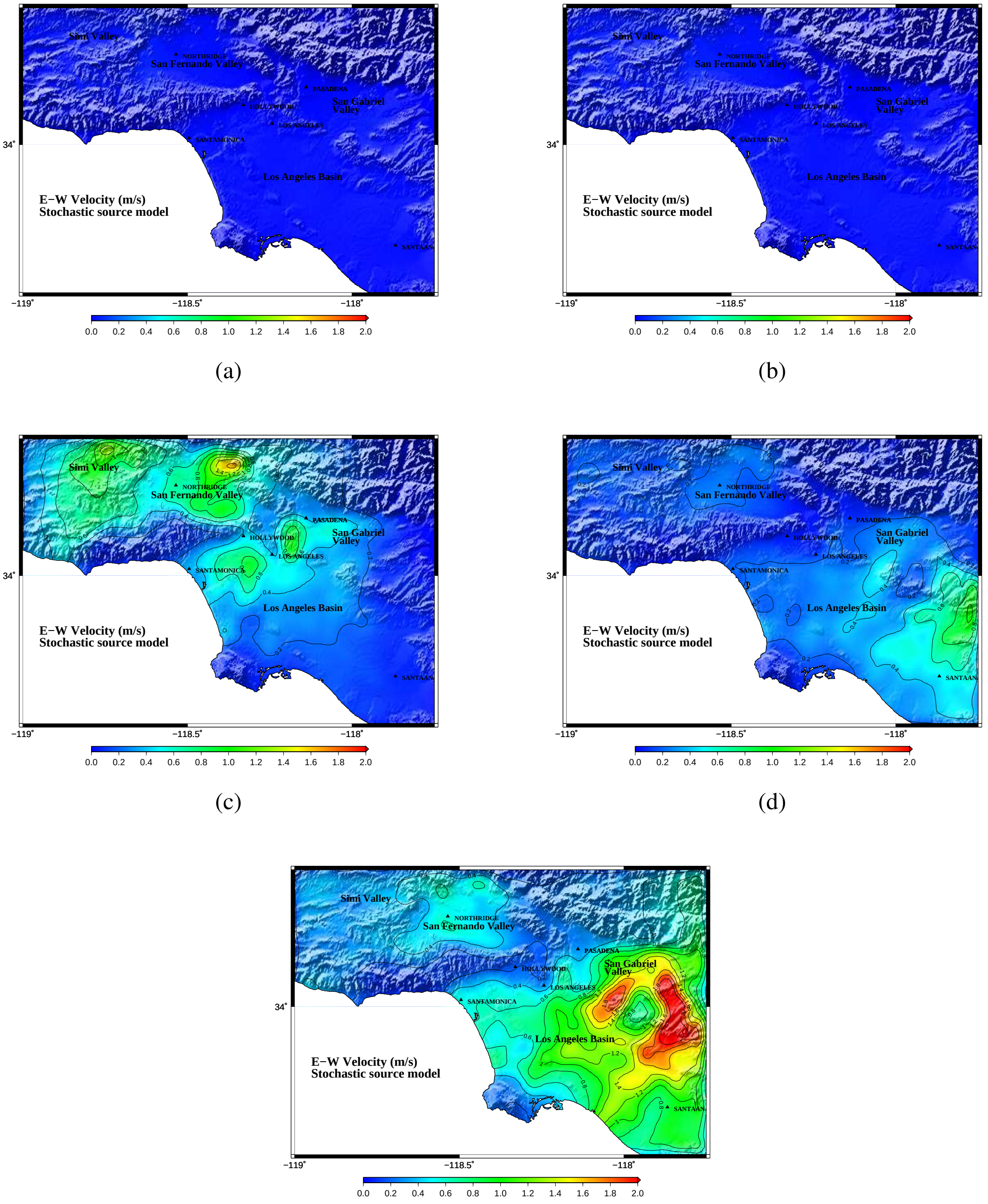
Simi Valley
NORTHRIDGE
San Fernando Valley
PASADENA
San Gabriel Valley
HOLLYWOOD
LOS ANGELES
SANTAMONICA
Los Angeles Basin
SANTAAN
E−W Velocity (m/s)
Stochastic source model
34˚
−119˚
−118.5˚
−118˚
0.0
0.2
0.4
0.6
0.8
1.0
1.2
1.4
1.6
1.8
2.0

(a)

(b)

(c)

(d)

(e)

Figure C.31: EW component of PGV (m/s) from a south-to-north propagating rupture at (a) - (e) locations 1 - 5 respectively on the southern San Andreas fault for stochastic $M_w 7.2$ model-4 source model. The NS component of PGV has similar characteristics as EW component and the PGD is proportional to PGV in most cases.

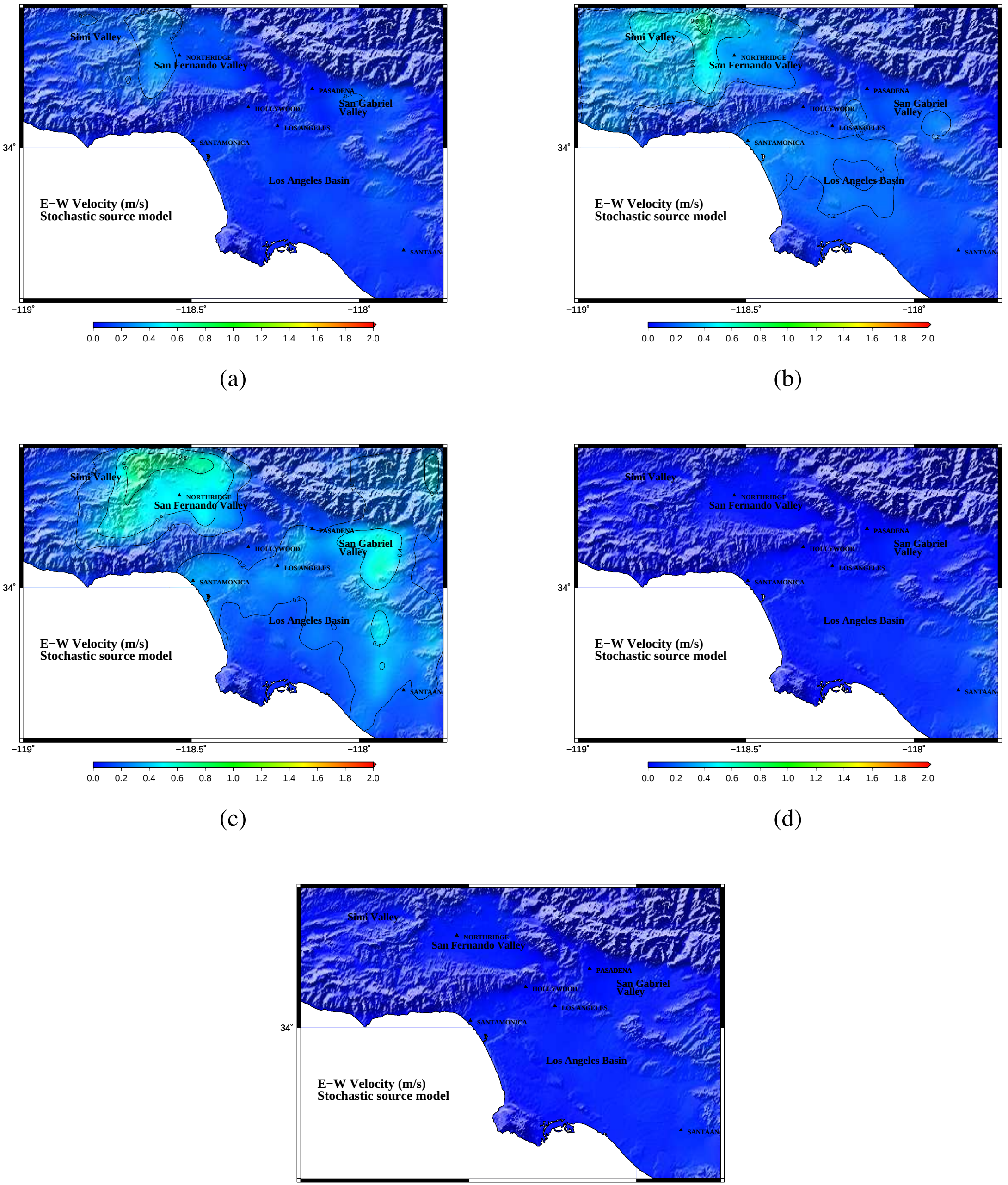
Simi Valley
NORTHRIDGE
San Fernando Valley
PASADENA
San Gabriel Valley
HOLLYWOOD
LOS ANGELES
SANTAMONICA
Los Angeles Basin
SANTAANA
34°
E−W Velocity (m/s)
Stochastic source model
−119°
−118.5°
−118°
0.0
0.2
0.4
0.6
0.8
1.0
1.2
1.4
1.6
1.8
2.0

(a) (b)

(c) (d)

(e)

Figure C.32: EW component of PGV (m/s) from a north-to-south propagating rupture at (a) - (e) locations 1 - 5 respectively on the southern San Andreas fault for stochastic $M_w 7.2$ model-5 source model. The NS component of PGV has similar characteristics as EW component and the PGD is proportional to PGV in most cases.

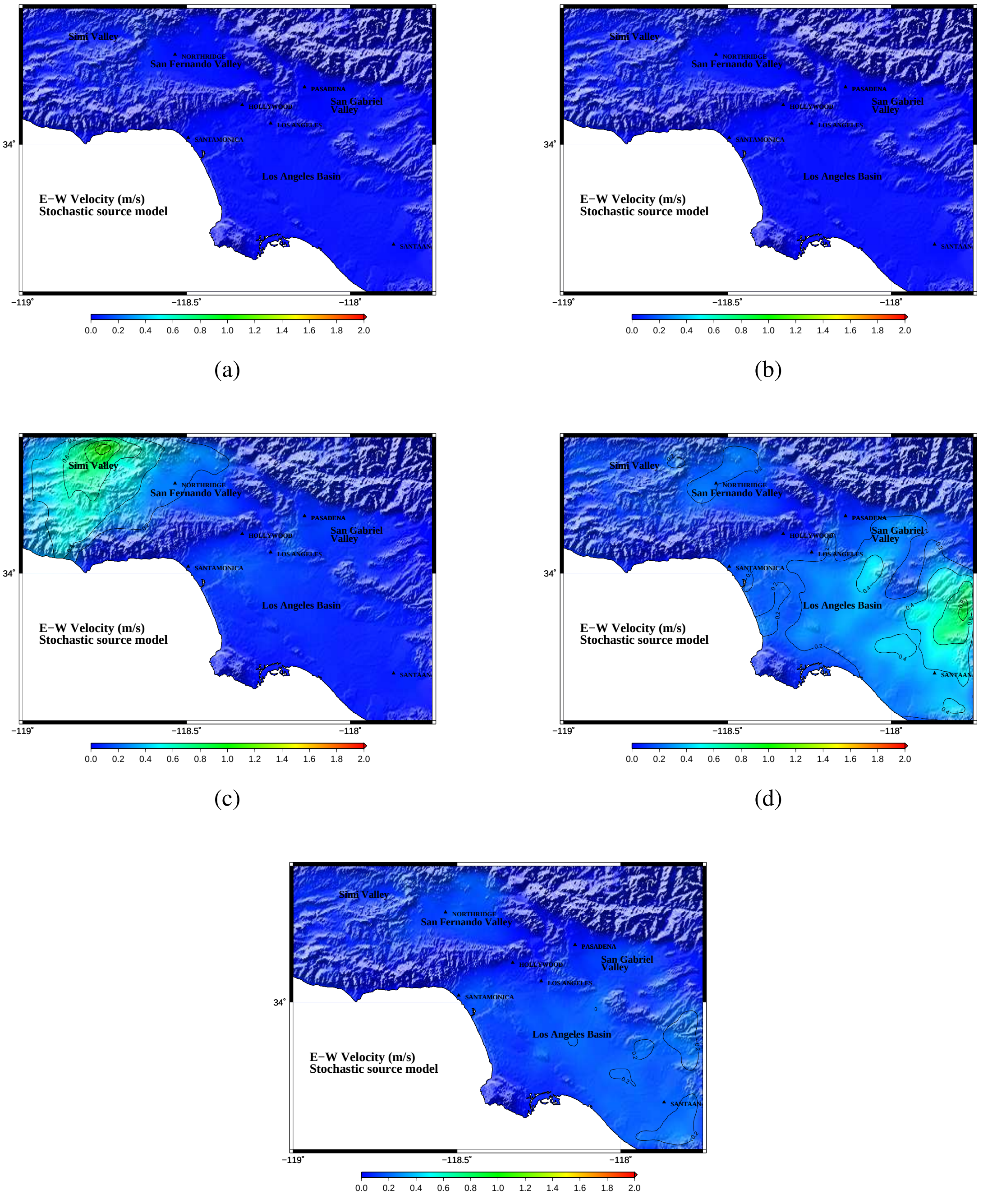
Simi Valley
NORTHRIDGE
San Fernando Valley
PASADENA
San Gabriel Valley
HOLLYWOOD
LOS ANGELES
SANTAMONICA
Los Angeles Basin
SANTAANA
E−W Velocity (m/s)
Stochastic source model
34°
−119°
−118.5°
−118°
0.0
0.2
0.4
0.6
0.8
1.0
1.2
1.4
1.6
1.8
2.0

(a) (b) (c) (d) (e)

Figure C.33: EW component of PGV (m/s) from a south-to-north propagating rupture at (a) - (e) locations 1 - 5 respectively on the southern San Andreas fault for stochastic $M_w 7.2$ model-5 source model. The NS component of PGV has similar characteristics as EW component and the PGD is proportional to PGV in most cases.

Bibliography

Aagaard, B. (2006). Finite-element Simulations of Ground Motions in the San Francisco Bay Area from Large Earthquakes on the San Andreas Fault. *Seism. Res. Lett. 77*.

Aagaard, B. T., R. W. Graves, A. Rodgers, T. M. Brocher, R. W. Simpson, D. Dreger, N. A. Petersson, S. C. Larsen, S. Ma, and R. C. Jachens (2010). Ground-Motion Modeling of Hayward Fault Scenario Earthquakes, Part II: Simulation of Long-Period and Broadband Ground Motions. *Bulletin of the Seismological Society of America 100*(6), 2945–2977.

Aagaard, B. T., R. W. Graves, D. P. Schwartz, D. A. Ponce, and R. W. Graymer (2010). Ground-Motion Modeling of Hayward Fault Scenario Earthquakes, Part I: Construction of the Suite of Scenarios. *Bulletin of the Seismological Society of America 100*(6), 2927–2944.

Aagaard, B. T. and T. Heaton (2004, December). Near-Source Ground Motions from Simulations of Sustained Intersonic and Supersonic Fault Ruptures. *Bulletin of the Seismological Society of America 94*, 2064–2078.

American Society of Civil Engineers (2007). Seismic Rehabilitation of Existing Buildings. ASCE Standard ASCE/SEI 41-06. ASCE, Reston, Virginia, USA.

Andrews, D. (1976). Rupture Velocity of Plane Strain Shear Cracks. *Journal of Geophysical Research 81*(32), 5679–5687.

Andrews, D. and M. Barall (2011). Specifying Initial Stress for Dynamic Heterogenous Earthquake Source Models. *Bulletin of the Seismological Society of America 101*(5), 2408–2417.

Applied Technology Council (2009). Quantification of Building Seismic Performance Factors , prepared for the Federal Emergency Management Agency , FEMA P695, Washington, DC.

Archuleta, R. (1984). A Faulting Model for the 1979 Imperial-Valley Earthquake. *Journal of Geophysical Research 89*, 4559–4585.

Baker, J. W., N. Luco, N. A. Abrahamson, R. W. Graves, P. J. Maechling, and K. B. Olsen (2014). Engineering Uses of Physics-based Ground Motion Simulations. In *Proceedings of the Tenth US Conference on Earthquake Engineering*.

Bao, H., J. Bielak, O. Ghattas, L. F. Kallivokas, D. R. O'Hallaron, J. R. Shewchuk, and J. Xu (1998). Large-scale Simulation of Elastic Wave Propagation in Heterogeneous Media on Parallel Computers. *Computer Methods in Applied Mechanics and Engineering 152*(1), 85–102.

Baumann, C. and L. A. Dalguer (2014). Evaluating the Compatibility of Dynamic Rupture-Based Synthetic Ground Motion with Empirical Ground-Motion Prediction Equation. *Bulletin of the Seismological Society of America*.

Beck, J. L. (2010). Bayesian System Identification Based on Probability Logic. *Structural Control and Health Monitoring 17*(7), 825–847.

Beck, J. L. and K.-V. Yuen (2004). Model Selection Using Response Measurements: Bayesian Probabilistic Approach. *Journal of Engineering Mechanics 130*(2), 192–203.

Bhat, H. S., R. Dmowska, G. C. P. King, Y. Klinger, and J. R. Rice (2007). Off-fault Damage Patterns Due to Supershear Ruptures with Application to the 2001 M_w8.1 Kokoxili (Kunlun) Tibet Earthquake. *Journal of Geophysical Research 112*(B6).

Bielak, J., R. W. Graves, K. B. Olsen, R. Taborda, L. Ramirez-Guzman, S. M. Day, G. P. Ely, D. Roten, T. H. Jordan, P. J. Maechling, J. Urbanic, Y. Cui, and G. Juve (2010, January). The shakeout Earthquake Scenario: Verification of Three Simulation Sets. *Geophysical Journal International 180*(1), 375–404.

Bizzarri, A. (2011). On the Deterministic Description of Earthquakes. *Reviews of Geophysics 49*(3).

Bjornsson, A. and S. Krishnan (2012). A Retrofitting Framework for Pre-Northridge Steel Moment-Frame Buildings. In *Proceedings of the Fifteenth World Conference on Earthquake Engineering*.

Bouchon, M., M. Toksoz, H. Karabulut, M. Bouin, M. Dietrich, M. Aktar, and M. Edie (2002).

Space and Time Evolution of Rupture and Faulting During the 1999 Izmit (Turkey) Earthquake. *Bulletin of the Seismological Society of America 92*(1), 256–266.

Bouchon, M. and M. Vallée (2003). Observation of Long Supershear Rupture During the Magnitude 8.1 Kunlunshan Earthquake. *Science 301*(5634), 824–826.

Brune, J. (1970). Tectonic Stress and Spectra of Seismic Shear Waves From Earthquakes. *Journal of Geophysical Research 75*(26), 4997–5009.

Burridge, R. (1973). Admissible Speeds for Plane-Strain Self-Similar Shear Cracks with Friction but Lacking Cohesion. *Geophysical Journal of the Royal Astronomical Society 35*(4), 439–455.

Campbell, K. W. and Y. Bozorgnia (2008). NGA Ground Motion Model for the Geometric Mean Horizontal Component of PGA, PGV, PGD and 5 % Damped Linear Elastic Response Spectra for Periods Ranging from 0.01 to 10 s. *Earthquake Spectra 24*(1), 139.

Carlson, A. Three-dimensional Nonlinear Inelastic Analysis of Steel Moment Frame Buildings Damaged by Earthquake Excitations. *Tech. Rep. EERL 99-02,Earthquake Engineering Research Laboratory, California Institute of Technology, Pasadena, California, USA, 1999.*.

Carr, A. (2001). RUAUMOKO 3-Dimensional Version. Computer Program Suite for the Dynamic Analysis of Three-dimensional Structures Subjected to Time-varying Excitation http://www.ruaumoko.co.nz (Software).

Casarotti, E., M. Stupazzini, S. J. Lee, D. Komatitsch, A. Piersanti, and J. Tromp (2008). CUBIT and Seismic Wave Propagation Based Upon the Spectral-element Method: An Advanced Unstructured Mesher for Complex 3D Geological Media. In *Proceedings of the 16th International Meshing Roundtable*, pp. 579–597. Springer.

Chi, W.-M., S. El-Tawil, G. G. Deierlein, and J. F. Abel (1998). Inelastic Analyses of a 17-story Steel Framed Building Damaged During Northridge. *Engineering Structures 20*(4), 481–495.

Computers and I. Structures. Perform-3D. http://www.csiamerica.com/products/perform-3d.

Cotton, F. and M. Campillo (1995). Frequency-Domain Inversion of Strong Motions - Application to the 1992 Landers Earthquake. *Journal of Geophysical Research-Solid Earth 100*, 3961–

3975.

Cui, Y., K. B. Olsen, T. H. Jordan, K. Lee, J. Zhou, P. Small, D. Roten, G. Ely, D. K. Panda, A. Chourasia, J. Levesque, S. M. Day, and P. Maechling (2010). Scalable Earthquake Simulation on Petascale Supercomputers. In *High Performance Computing, Networking, Storage and Analysis (SC), 2010 International Conference for*, pp. 1–20.

Dalguer, L. A., H. Miyake, S. M. Day, and K. Irikura (2008). Surface Rupturing and Buried Dynamic-rupture Models Calibrated with Statistical Observations of Past Earthquakes. *Bulletin of the Seismological Society of America 98*(3), 1147–1161.

Das, S. (2010). Earthquake Supershear Rupture Speeds: Preface. *Tectonophysics 493*, 213–215.

Delouis, B., D. Giardini, P. Lundgren, and J. Salichon (2002). Joint Inversion of InSAR, GPS, Teleseismic, and Strong-motion Data for the Spatial and Temporal Distribution of Earthquake Slip: Application to the 1999 Izmit Mainshock. *Bulletin of the Seismological Society of America 92*(1), 278–299.

Di Toro, G., D. L. Goldsby, and T. E. Tullis (2004). Friction Falls Towards Zero in Quartz Rock as Slip Velocity Approaches Seismic Rates. *Nature 427*(6973), 436–439.

Dunham, E. M. and R. J. Archuleta (2004). Evidence for a Supershear Transient During the 2002 Denali Fault Earthquake. *Bulletin of the Seismological Society of America 94*(6B), S256–S258.

Eads, L., E. Miranda, and H. Krawinkler (2013). An Efficient Method for Estimating the Collapse Risk of Structures in Seismic Regions. *Earthquake Engineering & Structural Dynamics 42*(1), 25–41.

Ely, G., T. H. Jordan, P. Small, and P. J. Maechling (2010). A V_s^{30} Derived Near-surface Seismic Velocity Model. In *Proceedings of the American Geophysical Union Fall Meeting, USA*.

Ely, G. P., S. M. Day, and J.-B. Minster (2010). Dynamic Rupture Models for the Southern San Andreas Fault. *Bulletin of the Seismological Society of America 100*(1), 131–150.

FEMA (2000). Prestandard and Commentary for the Seismic Rehabilitation of Buildings, FEMA-356, Federal Emergency Management Agency.

Fialko, Y. (2006). Interseismic Strain Accumulation and The Earthquake Potential on The Southern San Andreas Fault System. *Nature 441*(7096), 968–971.

Fialko, Y., D. Sandwell, M. Simons, and P. Rosen (2005). Three-Dimensional Deformation Caused by the Bam, Iran, Earthquake and the Origin of Shallow Slip Deficit. *Nature 435*(7040), 295–299.

Field, E., G. Biasi, P. Bird, T. Dawson, K. Felzer, D. Jackson, K. Johnson, T. Jordan, C. Madden, A. Michael, K. Milner, M. Page, T. Parsons, P. Powers, B. Shaw, W. Thatcher, I. Weldon, R.J., and Y. Zeng (2013). Uniform California Earthquake Rupture Forecast, Version 3 (UCERF3) – The time-independent model: U.S. Geological Survey Open-File Report 20131165. pp. 97. California Geological Survey Special Report 228, and Southern California Earthquake Center Publication 1792, http://pubs.usgs.gov/of/2013/1165/.

Field, E. H., T. E. Dawson, K. R. Felzer, A. D. Frankel, V. Gupta, T. H. Jordan, T. Parsons, M. D. Petersen, R. S. Stein, R. J. Weldon, and C. J. Wills (2009). Uniform California Earthquake Rupture Forecast, Version 2 (UCERF 2). *Bulletin of the Seismological Society of America 99*(4), 2053–2107.

Frankel, A. (2004). Rupture Process of the M7.9 Denali Fault, Alaska, Earthquake: Subevents, Directivity, and Scaling of High-Frequency Ground Motions. *Bulletin of the Seismological Society of America 94*(6B), S234–S255.

Frankel, A. and W. Stephenson (2000). Three-dimensional Simulations of Ground Motions in the Seattle Region for Earthquakes in the Seattle Fault Zone. *Bulletin of the Seismological Society of America 90*(5), 1251–1267.

Furumura, T. (2005). Large-scale Parallel Simulation of Seismic Wave Propagation and Strong Ground Motions for the Past and Future Earthquakes in Japan. *Journal of the Earth Simulator 3*, 29–38.

Goldsby, D. and T. Tullis (2002). Low Frictional Strength of Quartz Rocks at Subseismic Slip Rates. *Geophys. Res. Lett 29*(17), 25–1 – 25–4.

Goulet, C. A., C. B. Haselton, J. Mitrani-Reiser, J. L. Beck, G. G. Deierlein, K. A. Porter, and J. P. Stewart (2007). Evaluation of The Seismic Performance of a Code-conforming Reinforced-concrete Frame building?from Seismic Hazard to Collapse Safety and Economic Losses. *Earthquake Engineering & Structural Dynamics 36*(13), 1973–1997.

Graves, R. (2006). Broadband Ground Motion Simulations for Earthquakes in the San Francisco Bay Region. *Seism. Res. Lett 77*, 275.

Graves, R. W. (1998). Three-dimensional Finite-difference Modeling of the San Andreas Fault: Source Parameterization and Ground-motion Levels. *Bulletin of the Seismological Society of America 88*(4), 881–897.

Graves, R. W., B. T. Aagaard, and K. W. Hudnut (2011, May). The ShakeOut Earthquake Source and Ground Motion Simulations. *Earthquake Spectra 27*(2), 273–291.

Graves, R. W. and A. Pitarka (2010). Broadband Ground-Motion Simulation Using a Hybrid Approach. *Bulletin of the Seismological Society of America 100*(5A), 2095–2123.

Guatteri, M., P. M. Mai, and G. C. Beroza (2004). A pseudo-dynamic approximation to dynamic rupture models for strong ground motion prediction. *Bulletin of the Seismological* ....

Hanks, T. and W. Bakun (2002). A Bilinear Source-Scaling Model for M-log A Observations of Continental Earthquakes. *Bulletin of the Seismological Society of America 92*(5), 1841–1846.

Hanks, T. C. and W. H. Bakun (2008). M-LogA Observations for Recent Large Earthquakes. *Bulletin of the Seismological Society of America 98*(1), 490–494.

Harris, R., M. Barall, R. Archuleta, E. Dunham, B. Aagaard, J. Ampuero, H. Bhat, V. Cruz-Atienza, L. Dalguer, P. Dawson, et al. (2009). The SCEC/USGS Dynamic Earthquake Rupture Code Verification Exercise. *Seismological Research Letters 80*(1), 119–126.

Hartzell, S., S. Harmsen, A. Frankel, and S. Larsen (1999). Calculation of Broadband Time Histories of Ground Motion: Comparison of Methods and Validation Using Strong-Ground Motion from the 1994 Northridge Earthquake. *Bulletin of the Seismological Society of America 89*(6), 1484–1504.

Hartzell, S., P. Liu, and C. Mendoza (1996). The 1994 Northridge, California, Earthquake: Investigation of Rupture Velocity, Risetime, and High-Frequency Radiation. *Journal of Geophysical Research-Solid Earth 101*, 20091–20108.

Haselton, C. B., A. B. Liel, and G. G. Deierlein (2010). Seismic Collapse Safety of Reinforced Concrete Buildings. I: Assessment of Ductile Moment Frames. *Journal of Structural Engineering 137*(4), 481–491.

Hauksson, E. (2000). Crustal Structure and Seismicity Distribution Adjacent to the Pacific and North America Plate Boundary in Southern California. *Journal of Geophysical Research: Solid Earth (1978–2012) 105*(B6), 13875–13903.

Heaton, T., J. Hall, D. Wall, and M. Halling (1995). Response of high-rise and base-isolated buildings to a hypothetical M_w 7.0 blind thrust earthquake. *Science 267*(5195), 206–211.

Heidbach, O., M. Tingay, A. Barth, J. Reinecker, D. Kurfeß, and B. Müller. The World Stress Map Database Release 2008 doi:10.1594/GFZ.WSM.Rel2008, 2008.

Horikawa, H., K. Mizuno, T. Ishiyama, K. Satake, H. Sekiguchi, Y. Kase, Y. Sugiyama, H. Yokota, M. Suehiro, T. Yokokura, et al. (2003). A Three-dimensional Subsurface Structure Model Beneath the Osaka Sedimentary Basin, Southwest Japan, with Fault-related Structural Discontinuities. *Katsudansou-Kojishin Kenkyu Hhoukoku 3*, 225–259.

Huang, Y., A. Whittaker, N. Luco, and R. Hamburger (2011). Scaling Earthquake Ground Motions for Performance-Based Assessment of Buildings. *Journal of Structural Engineering 137*(3), 311–321.

Ide, S. and M. Takeo (1997). Determination of Constitutive Relations of Fault Slip based on Seismic Wave Analysis. *Journal of Geophysical Research-Solid Earth 102*(B), 27379–27391.

Ji, C. (2004). Slip history the 2004 (M_w5.9) Parkfield Earthquake (Single-Plane Model). http://www.tectonics.caltech.edu/slip_history/2004_ca/parkfield2.html.

Kagawa, T., B. Zhao, K. Miyakoshi, and K. Irikura (2004). Modeling of 3D Basin Structures for Seismic Wave Simulations Based on Available Information on the Target Area: Case Study of the Osaka Basin, Japan. *Bulletin of the Seismological Society of America 94*(4), 1353–1368.

Kellogg, L. (2011, June). Computational Infrastructure for Geodynamics. http://geodynamics.org.

Kohler, M., H. Magistrale, and R. Clayton (2003). Mantle Heterogeneities and the SCEC Three-Dimensional Seismic Velocity Model Version 3. *Bulletin of the Seismological Society of*

America 93(2), 757–774.

Komatitsch, D. (2011). Fluid-solid Coupling On A Cluster of GPU Graphics Cards for Seismic Wave Propagation. *Comptes Rendus de l'Acadmie des Sciences Mcanique 339*, 125–135.

Komatitsch, D., G. Erlebacher, D. Göddeke, and D. Michéa (2010). High-order Finite-element Seismic Wave Propagation Modeling with MPI On A Large GPU Cluster. *Journal of Computational Physics 229*(20), 7692–7714.

Komatitsch, D., Q. Liu, J. Tromp, P. Süss, C. Stidham, and J. H. Shaw (2004). Simulations of Ground Motion in the Los Angeles Basin Based Upon the Spectral-element Method. *Bulletin of the Seismological Society of America 94*(1), 187–206.

Komatitsch, D. and J. Tromp (1999). Introduction to the Spectral Element Method for ThreeDimensional Seismic Wave Propagation. *Geophysical Journal International 139*(3), 806–822.

Krishnan, S. (2003). FRAME3D - A Program for Three-dimensional Nonlinear Time-history Analysis of Steel Buildings: User Guide. *Technical Rep. No. EERL 2003-03*.

Krishnan, S. (2007). Case Studies of Damage to 19Story Irregular Steel MomentFrame Buildings under NearSource Ground Motion. *Earthquake engineering & structural dynamics 36*(7), 861–885.

Krishnan, S. (2009). FRAME3D V2.0 - A Program for the Three-dimensional Nonlinear Time-history Analysis of Steel Structures: User Guide. *Technical Rep. No. EERL 2009-04*.

Krishnan, S. (2010). Modified Elastofiber Element for Steel Slender Column and Brace Modeling. *Journal of Structural Engineering-Asce 136*(11), 1350–1366.

Krishnan, S. and J. F. Hall (2006a). Modeling Steel Frame Buildings in Three Dimensions. I: Panel Zone and Plastic Hinge Beam Elements. *Journal of Engineering Mechanics 132*(4), 345–358.

Krishnan, S. and J. F. Hall (2006b). Modeling Steel Frame Buildings in Three Dimensions. II: Elastofiber Beam Element and Examples. *Journal of Engineering Mechanics 132*(4), 359–374.

Krishnan, S., C. Ji, D. Komatitsch, and J. Tromp (2005). Performance of 18-story steel moment-frame buildings during a large san andreas earthquake - a southern california-wide end-to-end simulation. Technical report, EERL 2005-01, Earthquake Engineering Research Laboratory, California Institute of Technology, Pasadena, CA.

Krishnan, S., C. Ji, D. Komatitsch, and J. Tromp (2006a). Case Studies of Damage to Tall Steel Moment-Frame Buildings in Southern California during Large San Andreas Earthquakes. *Bulletin of the Seismological Society of America 96*(4A), 1523.

Krishnan, S., C. Ji, D. Komatitsch, and J. Tromp (2006b). Performance of Two 18-Story Steel Moment-Frame Buildings in Southern California during Two Large Simulated San Andreas Earthquakes. *Earthquake Spectra 22*(4), 1035–1061.

Krishnan, S. and M. Muto. Analytical and Field Investigations of Buildings Affected by the Northridge Earthquake of January 17, 1994 ? Part 1. *Tech. Rep. SAC 95-04, Part 1,Structural Engineers Association of California, Applied Technology Council, and California Universities for Research in Earthquake Engineering, USA, 1995.*.

Krishnan, S. and M. Muto (2012). Mechanism of Collapse of Tall Steel Moment Frame Buildings Under Earthquake Excitation. *Journal of Structural Engineering 138*(11), 1361–1387.

Krishnan, S. and M. Muto (2013). Sensitivity of the Earthquake Response of Tall Steel Moment Frame Buildings to Ground Motion Features. *Journal Of Earthquake Engineering 17*(5), 673–698.

Krishnan, S., M. Muto, R. Mourhatch, A. B. Bjornsson, and H. Siriki (2011). Rupture-to-Rafters Simulations: Unifying Science and Engineering for Earthquake Hazard Mitigation. *Special Issue on Earthquake Engineering Simulation, IEEE Computing in Science and Engineering Magazine 13*(4), 28–43.

Landes, M., W. Fielitz, F. Hauser, and M. Popa (2004). 3-D Upper Crustal Tomographic Structure Across the Vrancea Seismic Zone, Romania. *Tectonophysics 382*(1), 85–102.

Lavallée, D., P. Liu, and R. J. Archuleta (2006). Stochastic Model of Heterogeneity in Earthquake Slip Spatial Distributions. *Geophysical Journal International 165*(2), 622–640.

Lee, K. and D. A. Foutch (2002). Seismic Performance Evaluation of pre-Northridge Steel Frame Buildings with Brittle Connections. *Journal of Structural Engineering 128*(4), 546–555.

Lee, S.-J., H.-W. Chen, Q. Liu, D. Komatitsch, B.-S. Huang, and J. Tromp (2008). Three-dimensional Simulations of Seismic-wave Propagation in the Taipei Basin with Realistic Topography Based Upon the Spectral-element Method. *Bulletin of the Seismological Society of America 98*(1), 253–264.

Li, H., A. Michelini, L. Zhu, F. Bernardi, and M. Spada (2007). Crustal Velocity Structure in Italy from Analysis of Regional Seismic Waveforms. *Bulletin of the Seismological Society of America 97*(6), 2024–2039.

Lin, G., P. M. Shearer, E. Hauksson, and C. H. Thurber (2007). A Three-dimensional Crustal Seismic Velocity Model for Southern California from a Composite Event Method. *Journal of Geophysical Research: Solid Earth (1978–2012) 112*(B11).

Lindsey, E. and Y. Fialko (2013). Geodetic Slip Rates in The Southern San Andreas Fault System: Effects of Elastic Heterogeneity and Fault Geometry. *Journal of Geophysical Research: Solid Earth 118*(2), 689–697.

Liu, P., R. J. Archuleta, and S. H. Hartzell (2006). Prediction of Broadband Ground-Motion Time Histories: Hybrid Low/High-Frequency Method with Correlated Random Source Parameters. *Bulletin of the Seismological Society of America 96*(6), 2118–2130.

Liu, Q., J. Polet, D. Komatitsch, and J. Tromp (2004). Spectral-element Moment Tensor Inversions for Earthquakes in Southern California. *Bulletin of the Seismological Society of America 94*(5), 1748–1761.

Lu, X. (2009). *Combined Experimental and Numerical Study of Spontaneous Dynamic Rupture on Frictional Interfaces*. Ph. D. thesis.

Lu, X., A. J. Rosakis, and N. Lapusta (2010). Rupture Modes in Laboratory Earthquakes: Effect of Fault Prestress and Nucleation Conditions. *Journal of Geophysical Research 115*(B12).

Madariaga, R. and K. B. Olsen (2002). 12 earthquake dynamics. In P. C. J. William H.K. Lee, Hiroo Kanamori and C. Kisslinger (Eds.), *International Handbook of Earthquake and Engineering Seismology*, Volume 81, Part A of *International Geophysics*, pp. 175 – III. Academic Press.

Magistrale, H., S. Day, R. W. Clayton, and R. Graves (2000). The SCEC southern California reference three-dimensional seismic velocity model version 2. *Bulletin of the Seismological Society of America 90*(6B), S65–S76.

Magistrale, H., K. McLaughlin, and S. Day (1996). A geology-based 3D velocity model of the Los Angeles basin sediments. *Bulletin of the Seismological Society of America 86*(4), 1161–1166.

Mai, P. and G. Beroza (2002). A Spatial Random Field Model to Characterize Complexity in Earthquake Slip. *Journal of Geophysical Research 107*(10.1029), 2001.

Mathiasson, A. and R. A. Medina (2014). Seismic Collapse Assessment of a 20-Story Steel Moment-Resisting Frame Structure. *Buildings 4*(4), 806–822.

McKenna, F., G. Fenves, M. Scott, et al. (2000). Open system for earthquake engineering simulation. *University of California, Berkeley, CA*.

Mello, M., H. S. Bhat, A. J. Rosakis, and H. Kanamori (2010). Identifying the Unique Ground Motion Signatures of Supershear Earthquakes: Theory and Experiments. *Tectonophysics 493*, 297–326.

Mena, B., L. A. Dalguer, and P. M. Mai (2012, August). Pseudodynamic source characterization for strike-slip faulting including stress heterogeneity and super-shear ruptures. *Bulletin of the Seismological Society of America 102*(4), 1654–1680.

Mitrani-Reiser, J., C. Haselton, C. Goulet, K. Porter, J. Beck, and G. Deierlein (2006). Evaluation of the Seismic Performance of a Code-Conforming Reinforced-Concrete Frame Building - Part II: Loss Estimation. In *Proceedings of the Eight National Conference on Earthquake Engineering, San Francisco, CA*.

Miyamoto, H., A. Gilani, and A. Wada (2010). Collapse Risk of Tall Steel Moment Frame Buildings with Viscous Dampers Subjected to Large Earthquakes. *The Structural Design of Tall and Special Buildings 19*(4), 421–438.

Mourhatch, R. (2015). *"Quantifying Earthquake Collapse Risk of Tall Steel Braced Frame Buildings Using Rupture-to-Rafters Simulations "*. Ph. D. thesis, California Institute of Technology.

Mourhatch, R. and S. Krishnan (2014). Simulation of Broadband Ground Motion by Superposing High-Frequency Empirical Green's Function Synthetics on Low-Frequency Spectral-Element Synthetics,under review. *Bulletin of the Seismological Society of America*.

Muto, M. and S. Krishnan (2011). Hope for the Best, Prepare for the Worst: Response of Tall Steel Buildings to the Shakeout Scenario Earthquake. *Earthquake Spectra 27*(2), 375–398.

Muto, M., S. Krishnan, J. Beck, and J. Mitrani-Reiser (2008). Seismic loss estimation based on end-to-end simulation. In *Proceedings of the first international symposium on life-cycle civil engineering, Varenna, Lake Como, Italy*, pp. 215–232.

Nielsen, S. and R. Madariaga (2003). On the Self-Healing Fracture Mode. *Bulletin of the Seismological Society of America 93*(6), 2375–2388.

Olsen, A. H., T. H. Heaton, and J. F. Hall (2014). Characterizing Ground Motions that Collapse Steel, Special Moment-Resisting Frames or Make Them Unrepairable. *Earthquake Spectra*.

Olsen, K., R. Archuleta, and J. Matarese (1995). Three Dimensional Simulation of a Magnitude 7.75 Earthquake on the San Andreas fault. *Science 270*(5242), 1628–1632.

Olsen, K., S. Day, L. Dalguer, J. Mayhew, Y. Cui, J. Zhu, V. Cruz-Atienza, D. Roten, P. Maechling, T. Jordan, et al. (2009). ShakeOut-D: Ground Motion Estimates Using an Ensemble of Large Earthquakes on the Southern San Andreas Fault with Spontaneous Rupture Propagation. *Geophysical Research Letters 36*(4).

Olsen, K. B., S. M. Day, J. B. Minster, Y. Cui, A. Chourasia, D. Okaya, P. Maechling, and T. Jordan (2008). Terashake2: Spontaneous Rupture Simulations of mw 7.7 Earthquakes on the Southern san andreas Fault. *Bulletin of the Seismological Society of America 98*(3), 1162–1185.

Olsen, K. B. and J. E. Mayhew (2010). Goodness-of-fit Criteria for Broadband Synthetic Seismograms, with Application to the 2008 Mw 5.4 Chino Hills, California, Earthquake. *Seismological Research Letters 81*(5), 715–723.

Plesch, A., C. Tape, J. Graves, P. Small, G. Ely, and J. Shaw (2011). Updates for the CVM-H Including New Representations of the Offshore Santa Maria and San Bernardino Basin and a New Moho Surface. In *2011 Southern California Earthquake Center Annual Meeting,* *Proceedings and Abstracts*, Volume 21.

Plesch, A., C. Tape, R. Graves, J. H. Shaw, P. Small, and G. Ely (2011). Updates for The CVM-H Including New Representations Of The Offshore Santa Maria and San Bernardino Basins and A New Moho Surface. In *SCEC 2011 Annual Meeting*, pp. Poster B–128. Southern California Earthquake Center.

Porter, K. A. (2003). An Overview of PEERs Performance-Based Earthquake Engineering Methodology. In *Conference on Applications of Statistics and Probability in Civil Engineering (ICASP9)*, pp. 6–9. Civil Engineering Risk and Reliability Association (CERRA) San Francisco,, California.

Powell, G. H. and S. D. Campbell. DRAIN-3DX: Static and Dynamic Analysis of Inelastic 3D Structures.http://nisee.berkeley.edu/elibrary/getpkg?id=DRAIN3DX .

Pratt, T. L., T. M. Brocher, C. S. Weaver, K. C. Creager, C. M. Snelson, R. S. Crosson, K. C. Miller, and A. M. Tréhu (2003). Amplification of Seismic Waves by The Seattle Basin, Washington State. *Bulletin of the Seismological Society of America 93*(2), 533–545.

Prindle, K. and T. Tanimoto (2006). Teleseismic Surface Wave Study for S-wave Velocity Structure Under an Array: Southern California. *Geophysical Journal International 166*(2), 601–621.

Quinay, P. E. B., T. Ichimura, M. Hori, A. Nishida, and S. Yoshimura (2013). Seismic Structural Response Estimates of a Fault?Structure System Model with Fine Resolution Using Multiscale Analysis with Parallel Simulation of Seismic?Wave Propagation. *Bulletin of the Seismological Society of America 103*(3), 2094–2110.

Raghunandan, M., A. B. Liel, and N. Luco (2014). Collapse Risk of Buildings in the Pacific Northwest Region due to Subduction Earthquakes. *Earthquake Spectra*.

Raileanu, V., A. Bala, F. Hauser, C. Prodehl, and W. Fielitz (2005). Crustal Properties from S-wave and Gravity Data Along a Seismic Refraction Profile in Romania. *Tectonophysics 410*(1), 251–272.

Ramirez, C., A. Gupta, and A. Myers (2012). Detailed Seismic Loss Estimation for a Tall Building in Japan. In *Proceedings of the Fifteenth World Conference on Earthquake Engineering, Lisbon, Portugal*.

Ramirez, M., A. Liel, J. Mitrani-Reiser, C. Haselton, A. Spear, J. Steiner, E. Miranda, and G. Deierlein. Seismic Damage and Monetary Loss Performance of Modern Reinforced Concrete Frame Buildings. *accepted, Earthquake Engineering & Structural Dynamics*.

Rogers, A. and D. Perkins (1996). Monte Carlo Simulation of Peak-Acceleration Attenuation Using a Finite-Fault Uniform-Patch Model Including Isochrone and Extremal Characteristics. *Bulletin of the Seismological Society of America 86*(1A), 79–92.

Rosakis, A., O. Samudrala, and D. Coker (1999). Cracks Faster than the Shear Wave Speed . *Science 284*(5418), 1337–1340.

Rosakis, A., K. Xia, G. Lykotrafitis, and H. Kanamori (2007). Dynamic Shear Rupture in Frictional Interfaces: Speeds, Directionality and Modes. *Treatise in geophysics. Elsevier, Amsterdam*.

Sandia National Laboratory, U. (2011, November). CUBIT: Geometry and Mesh Generation Toolkit. http://cubit.sandia.gov.

Schmedes, J., R. J. Archuleta, and D. Lavallée (2010). Correlation of Earthquake Source Parameters Inferred from Dynamic Rupture Simulations. *Journal of Geophysical Research-Solid Earth 115*(B03304).

Schmedes, J., R. J. Archuleta, and D. Lavallée (2013). A Kinematic Rupture Model Generator Incorporating Spatial Interdependency of Earthquake Source Parameters. *Geophysical Journal International 192*(3), 1116–1131.

Shi, Z. and S. M. Day (2013). Rupture Dynamics and Ground Motion from 3-D Rough-fault Simulations. *Journal of Geophysical Research: Solid Earth 118*(3), 1122–1141.

Sieh, K. E. (1978). Prehistoric Large Earthquakes Produced by Slip on the San Andreas Fault at Pallett Creek, California. *Journal of Geophysical Research: Solid Earth (1978–2012) 83*(B8), 3907–3939.

Siriki, H., H. Bhat, X. Lu, and S. Krishnan (2014). A Laboratory Earthquake-Based Stochastic Seismic Source Generation Algorithm for Strike-Slip Faults and its Application to the Southern San Andreas Fault,in print. *Bulletin of the Seismological Society of America*.

Somerville, P., K. Irikura, R. Graves, S. Sawada, D. Wald, N. Abrahamson, Y. Iwasaki, T. Kagawa, N. Smith, and A. Kowada (1999). Characterizing Earthquake Rupture Models for the

Prediction of Strong Ground Motion. *Seismological Research Letters 70*, 59–80.

Somerville, P. G. (2003). Magnitude Scaling of the Near Fault Rupture Directivity Pulse. *Physics of the earth and planetary interiors 137*(1), 201–212.

Song, S. G., L. A. Dalguer, and P. M. Mai (2014, March). Pseudo-dynamic Source Modelling with 1-point and 2-point Statistics of Earthquake Source Parameters. *Geophysical Journal International 196*(3), 1770–1786.

Song, S. G. and P. Somerville (2010). Physics-Based Earthquake Source Characterization and Modeling with Geostatistics. *Bulletin of the Seismological Society of America 100*(2), 482–496.

Suss, M. P. and J. H. Shaw (2003). P-wave Seismic Velocity Structure Derived from Sonic Logs and Industry Reflection Data in the Los Angeles Basin. *Journal of Geophysical Research 108*(B3), Article no. 2170.

Tape, C., Q. Liu, A. Maggi, and J. Tromp (2009). Adjoint Tomography of The Southern California Crust. *Science 325*(5943), 988.

Tape, C., Q. Liu, A. Maggi, and J. Tromp (2010). Seismic Tomography of The Southern California Crust Based on Spectral-element and Adjoint Methods. *Geophysical Journal International 180*(1), 433–462.

Tinti, E., E. Fukuyama, A. Piatanesi, and M. Cocco (2005). A Kinematic Source-Time Function Compatible with Earthquake Dynamics. *Bulletin of the Seismological Society of America 95*(4), 1211–1223.

Townend, J. (2006). What do Faults Feel? Observational Constraints on the Stresses Acting on Seismogenic Faults. *Goephysical Monograph Series 170*.

Townend, J. and M. Zoback (2000). How Faulting Keeps the Crust Strong. *Geology 28*(5), 399.

Townend, J. and M. Zoback (2004). Regional Tectonic Stress Near the San Andreas Fault in Central and Southern California. *Geophys. Res. Lett 31*(15), L15S11.

Tromp, J., D. Komattisch, and Q. Liu (2008). Spectral-element and Adjoint Methods in Seismology. *Communications in Computational Physics 3*(1), 1–32.

Trugman, D. T. and E. M. Dunham (2014a, February). A 2D Pseudodynamic Rupture Model Generator for Earthquakes on Geometrically Complex Faults. *Bulletin of the Seismological Society* *of America 104*(1), 95–112.

Trugman, D. T. and E. M. Dunham (2014b). A 2D Pseudodynamic Rupture Model Generator for Earthquakes on Geometrically Complex Faults. *Bulletin of the Seismological Society of America 104*(1), 95–112.

Uang, C.-M. and V. V. Bertero (1988). Implications of Recorded Earthquake Ground Motions on Seismic Design of Building Structures. *Report No. UCB/EERC-88/13*.

Wald, D. J. and T. Allen (2007). Topographic Slope as a Proxy for Seismic Site Conditions and Amplification. *Bulletin of the Seismological Society of America 97*(5), 1379–1395.

Wald, D. J. and T. H. Heaton (1994). Spatial and Temporal Distribution of Slip for the 1992 Landers, California, Earthquake. *Bulletin of the Seismological Society of America 84*(3), 668–691.

Weldon, R. J., T. E. Fumal, G. P. Biasi, and K. M. Scharer (2005). Past and Future Earthquakes on the San Andreas Fault. *Science 308*(5724), 966–967.

Wells, D. L. and K. J. Coppersmith (1994). New Empirical Relationships Among Magnitude, Rupture Length, Rupture Width, Rupture Area, and Surface Displacement. *Bulletin of the Seismological Society of America 84*(4), 974–1002.

Yamada, M., A. H. Olsen, and T. H. Heaton (2009). Statistical Features of Short-period and Long-period Near-source Ground Motions. *Bulletin of the Seismological Society of America 99*(6), 3264–3274.

Zeng, Y., J. Anderson, and G. Yu (1994). A Composite Source Model for Computing Realistic Synthetic Strong Ground Motions. *Geophys. Res. Lett 21*(8), 725–728.

Zoback, M. and J. Townend (2001). Implications of Hydrostatic Pore Pressures and High Crustal Strength for the Deformation of Intraplate Lithosphere. In *Tectonophysics*, pp. 19–30. Stanford Univ, Dept Geophys, Stanford, CA 94305 USA.